Tribological Examination of Alkylsilane Monolayer Films via Molecular Dynamics Simulation

By

Andrew Z. Summers

Dissertation

Submitted to the Faculty of the

Graduate School of Vanderbilt University

in partial fulfillment of the requirements

for the degree of

DOCTOR OF PHILOSOPHY

in

Chemical and Biomolecular Engineering

January 31, 2019

Nashville, Tennessee

Approved:

Clare McCabe, Ph.D.

Peter T. Cummings, Ph.D.

G. Kane Jennings, Ph.D.

John T. Wilson, Ph.D.

D. Greg Walker, Ph.D.

To my parents, for their never ending support.

ACKNOWLEDGMENTS

I am extremely grateful to have had the opportunity to interact with many individuals during my time at Vanderbilt that have helped me grow into who I am today. First, I would like to thank Clare McCabe and Peter Cummings for the opportunities they have presented me - advice during weekly meetings and one-on-one interactions, the ability to attend conferences at the local, national, and international level, and funding for my research. I have thoroughly enjoyed learning from my time under your mentorship. I would also like to give a special thanks to Chris Iacovella. Your help was essential in my entry to lab, and I cannot thank you enough for your continued guidance on my various research projects.

Several members of the McCabe and Cummings research groups have also helped make this work possible. I'm especially thankful to Christoph Klein, who helped introduce me to Python and to whom much of my programming and software development knowledge is owed. Thanks also to Tim Moore, Matt Thompson, Remco Hartkamp, Justin Gilmer, Ray Matsumoto, and Alex Yang for the lunch conversations, conference trips, and feedback over the years. Having the opportunity to work alongside you has made my time at Vanderbilt more enjoyable and has been a significant help to my research.

TABLE OF CONTENTS

LIST OF TABLES

LIST OF FIGURES

CHAPTER 1

INTRODUCTION

Micro- and nanoelectromechanical systems (MEMS/NEMS) define a broad and diverse collection of devices that combine both electronic and mechanical components with feature lengths on the order of a few nanometers to hundreds of microns. In the heart of the Digital Age and in an era of miniaturization, MEMS and NEMS have found prominence in a variety of application areas including pressure sensors used in smartphones[1], airbag systems[2], and autonomous vehicles[3], piezoresistive cantilevers for atomic force microscopes[4], and lab on a chip devices for point-of-care diagnostics.[5] However, the lack of a robust lubrication scheme threatens the lifetimes of these devices and often restricts the design of MEMS and NEMS to avoid sliding contact between components, increasing device complexity and limiting their application.[6] As a result of the high surface area-to-volume ratios present in these devices, the viscosity of traditional macroscale lubricants, i.e. oils, is increased by several orders of magnitude[7–9], reducing effectiveness, and introducing a significant tribological barrier. Further compounding this issue is the chemical makeup of the surfaces typically found in MEMS and NEMS, which often consist of high energy silica (a result of the oxidation of silicon, perhaps the most common material for microfabrication); the dominance of interfacial forces in this environment can rapidly lead to surface degradation, which threatens device effectiveness.

Surface functionalization by monolayer films has been proposed as a potential solution to the lubrication issue of MEMS and NEMS. The typical structure of a monolayer film in the context of lubrication features a dense packing of chains, each containing a headgroup (physically or chemically adsorbed to the surface), backbone (typically featuring a hydrocarbon chemistry), and a terminal group (most commonly a methyl group). While monolayer films have been shown to reduce frictional and adhesive forces between surfaces

and provide a means for surface protection, these materials have yet to find widespread use as lubricants for MEMS and NEMS. This is primarily a result of durability issues, where films have typically been shown to feature lifetimes on the order of hours to days under standard operating conditions. Despite this shortcoming, the highly tunable chemistry of monolayer films provides considerable optimism that sufficient chemical optimization can improve the tribological performance these materials and improve their viability as lubricants for MEMS/NEMS.

While experimental approaches are vital for testing monolayer films under conditions comparable to MEMS/NEMS devices, computational techniques, such as molecular dynamics (MD) simulation, have found utility as a tool for understanding the mechanisms influencing monolayer tribology with molecular-level resolution. Through direct control over system variables, MD can help guide experiments towards the discovery of new and promising monolayer chemistries; however, the lack of robust initialization and workflow management tools have prevented MD from realizing its full utility in this regard, hindering the ability to perform large-scale screening over monolayer chemical space.

The work contained herein utilizes MD to broaden the field of knowledge of monolayer tribology and aims to advance the methods by which MD is applied to study these materials. This work can be categorized into three primary thrusts: 1. the use of MD to study molecular-level mechanisms of monolayer friction and degradation (Chapters 3 & 4), 2. large-scale screening of monolayer chemical space (Chapter 5), and 3. the development of a computationally efficient model to facilitate future screening (Chapter 6).

First, in Chapter 3, MD is used to examine the degradation of conventional alkylsilane monolayer films. Particular focus is given to how surface structure influences the degradation of these films, as well as to how the chemistry of the monolayers themselves (in particular the backbone chain length) affects this process. Here, only planar surfaces are considered to provide a baseline understanding of this process; however, in MEMS/NEMS devices surfaces often feature surface irregularities or asperities (characterized by

nanoscale roughness), which may act as focal points for monolayer tribological efficacy. To address this, in Chapter 4, simulations are performed of monolayers under contact by a model nanoscale asperity. Particular emphasis is placed on understanding the various friction mechanisms present in this environment, and how these mechanisms are affected by the chemistry of both the contacting surfaces and the monolayer films.

In addition to providing an atomic level vantage point for examining the mechanisms involved in monolayer friction and wear, MD simulations also allow for precise control over system chemistry, affording the ability for large-scale screening of monolayer chemical space. This is critical to the discovery and design of novel monolayer films that may provide enhanced tribological performance. To date, however, the necessary computational tools have not been available to easily exchange chemical components of systems, perform force field parameterization, and manage simulation execution for large numbers of systems. The Molecular Simulation and Design Framework (MoSDeF) has recently been developed to address these needs (with a portion of this development arising from the work described in this thesis), featuring tools for the facile initialization of parameterized molecular systems in a scriptable and reproducible manner. In Chapter 5, MoSDeF is used to perform large-scale screening of functionalized monolayer films. In addition to providing a case study for applying MoSDeF towards large-scale screening over a chemical parameter space and providing a platform for the future screening of monolayer films, the results of these simulations are examined to uncover links between monolayer terminal group chemistry and optimal tribological performance.

While the benefits of large-scale monolayer screening are showcased in Chapter 5, these simulations come at a significant computational cost. Furthermore, the screening performed in Chapter 5 examines monolayers attached to planar surfaces; however, the examination of monolayers under contact by asperities requires larger system sizes that further increase the computational cost. In Chapter 6, these concerns are addressed through the derivation of a coarse-grained force field for amorphous silica. Here, following work from

the literature, force field development is focused towards application for silica nanoparticles, which themselves feature promising lubricating abilities through possible ball-bearing effects, however, application of this force field to planar surfaces for studies of monolayer films should be straightforward.

Finally, Chapter 7 summarizes the work of the preceding chapters and provides insights into promising future directions.

1.1 Bibliography

[1] Bogue, R. Recent developments in MEMS sensors: a review of applications, markets and technologies. *Sensor Review* **2013**, *33*, 300–304.

[2] Yokota, Y.; Koide, A.; Matsumoto, M.; Hayashi, M. Three-dimensional acceleration sensor and airbag using the same. 1995.

[3] Wendel, J.; Meister, O.; Schlaile, C.; Trommer, G. F. An integrated GPS/MEMS-IMU navigation system for an autonomous helicopter. *Aerospace Science and Technology* **2006**, *10*, 527–533.

[4] Ghodssi, R.; Pinyen, L. MEMS Materials and Processes Handbook. *MEMS Reference Shelf* **2011**,

[5] Ahn, C.; Choi, J.-W.; Beaucage, G.; Nevin, J.; Lee, J.-B.; Puntambekar, A.; Lee, R. Disposable Smart Lab on a Chip for Point-of-Care Clinical Diagnostics. *Proceedings of the IEEE* **2004**, *92*, 154–173.

[6] de Boer, M. P.; Knapp, J. A.; Mayer, T. M.; Michalske, T. A. Role of interfacial properties on MEMS performance and reliability. *Microsystems Metrology and Inspection* **1999**, 2–15.

[7] Klein, J.; Kumacheva, E. Confinement-Induced Phase Transitions in Simple Liquids. *Science* **1995**, *269*, 816–819.

[8] Radhakrishnan, R.; Gubbins, K. E.; Sliwinska-Bartkowiak, M. Effect of the fluid-wall interaction on freezing of confined fluids: Toward the development of a global phase diagram. *The Journal of Chemical Physics* **2000**, *112*, 11048–11057.

[9] Cummings, P. T.; Docherty, H.; Iacovella, C. R.; Singh, J. K. Phase transitions in nanoconfined fluids: The evidence from simulation and theory. *AIChE Journal* **2010**, 842–848.

CHAPTER 2

BACKGROUND

2.1 Tribology in Micro- and Nanoelectromechanical Systems

The functionality of devices featuring sliding contacts may be severely impaired by friction, which gives rise to surface degradation and wear. It has been estimated that economic losses attributed to friction-induced wear may accumulate to more than 4% of the Gross Domestic Product of some developed countries[1], with more conservative estimates still placing this number at greater than 1%.[2] While the adverse effects of friction-induced wear are familiar at the macroscale, such as the need to regularly replace automobile tires, this phenomenon also plagues devices with nanoscale dimensions that feature sliding components - where these effects are magnified by high surface area-to-volume ratios. We live in an age of rapid electronics miniaturization, where device components continue to shrink in an effort to improve efficiency, versatility, and memory storage capacity. The ability for device miniaturization to have considerable societal impacts across a range of application areas has been established for over half a century, perhaps best chronicled by the physicist Richard Feynman in his seminal talk, "There's Plenty of Room at the Bottom".[3] These promises, along with advances in microfabrication techniques, have led to the increasing prevalence of microelectromechanical systems (MEMS), devices that combine mechanical and electronic components with feature lengths on the microscale. More recently, nanoelectromechanical systems (NEMS) have followed as a natural progression in miniaturization, where devices boast feature lengths on the nanoscale. MEMS and NEMS have found applications in a variety of areas including the automotive industry (e.g. accelerometers in airbag sensors[4]), analytical research (e.g. piezoresistive cantilevers in atomic force microscopes[5]), and the biomedical realm (e.g. lab on a chip devices for point-of-care diagnostics[6]). However, the functionality of these devices is threatened by the effects of

friction-induced wear, and as a result MEMS and NEMS are typically designed to avoid conditions where surfaces come into sliding contact.[7] This imposes a significant design constraint that reduces the scope of applications available to these devices. In response, considerable efforts have been made to achieve a better fundamental understanding of the phenomena of friction, wear, and lubrication (collectively termed "tribology", or "nanotribology" when nanoscale feature sizes are involved) under MEMS/NEMS-like conditions, with the goal of resolving these issues.

The tribological barriers for devices featuring sliding components with micro- and nanoscale feature lengths originate from the square-cube law, leading to the arisal of high surface area-to-volume ratios. This results in the enhanced influence of interfacial forces, which both augment the impact of surface-related phenomena, such as friction, adhesion, and wear, as well as hinder the effectiveness of conventional lubricants used at the macroscale, i.e. oils. This is a result of both confinement-induced phase transitions, where compounds like hydrocarbons can exhibit orders-of-magnitude increases in viscosity when confined to nanoscale dimensions[8–15], and the inability for long-chain hydrocarbons to navigate their way to properly fill the interstitial space within these devices. Further compounding these problems is the chemical composition of most surfaces in MEMS and NEMS. As a result of microfabrication technology, most MEMS and NEMS devices are made from silicon, which readily undergoes oxidation, yielding interfaces that are composed of high-energy silica. Contact between silica surfaces, which are coated with hydroxyl groups, yields large adhesive and frictional forces that quickly result in the degradation of the contacting surfaces. By virtue of the small feature lengths of MEMS and NEMS, even modest amounts of surface degradation can have a substantial impact on device performance. As such, lubrication of MEMS/NEMS is essential to extending the lifetimes and maximizing the utility of these devices, yet the lubrication schemes involved will require specialized approaches that differ from those utilized at the macroscale.

2.2 Nanoscale Lubrication using Monolayer Films

It has been expressed that, among other properties, practical lubricants for MEMS/NEMS should be surface-bound, thin, and easily applied.[16] One promising lubrication approach that fulfills these criteria is surface-functionalization by monolayer films. Monolayer films (often referred to as self-assembled monolayers, or SAMs, due to their spontaneous growth process) consist of a layer of physi- or chemisorbed chains which can be constructed from a diverse class of molecules, united by a structure that features a chemically adsorbed headgroup attached to an elongated, multi-atom chain. Dispersion interactions between chains promote the formation of densely packed and well-ordered "brushlike" structures that provide a buffer layer to direct contact between surfaces and can be utilized to modify interfacial properties. The utility of monolayer films as nanoscale lubricants has been recognized for several decades; for example, as early as 1989 it was observed by DePalma et al. that the coefficient of friction (COF) of silicon could be substantially reduced through functionalization by monolayers of alkylsilanes.[17]

The tribology of monolayer films is closely linked to their chemical composition, which can be tuned through modifying the chemistry of the individual chain constituents. The structure of a monolayer chain can generally be subdivided into three components[18]:

1. Headgroup that may be physi- or chemisorbed to the surface
2. Chain backbone
3. Terminal group

The most basic, and most commonly studied, class of monolayers for lubrication of silica surfaces are alkylsilanes (a 2D-depiction of which is shown in Fig. 2.1), which typically feature trichlorosilane ($SiCl_3$) headgroups that are readily hydrolyzed (the result of which is what is shown in Fig. 2.1), along with a hydrocarbon backbone and a methyl terminal group. While head group chemistry is typically dependent on the surface on which the

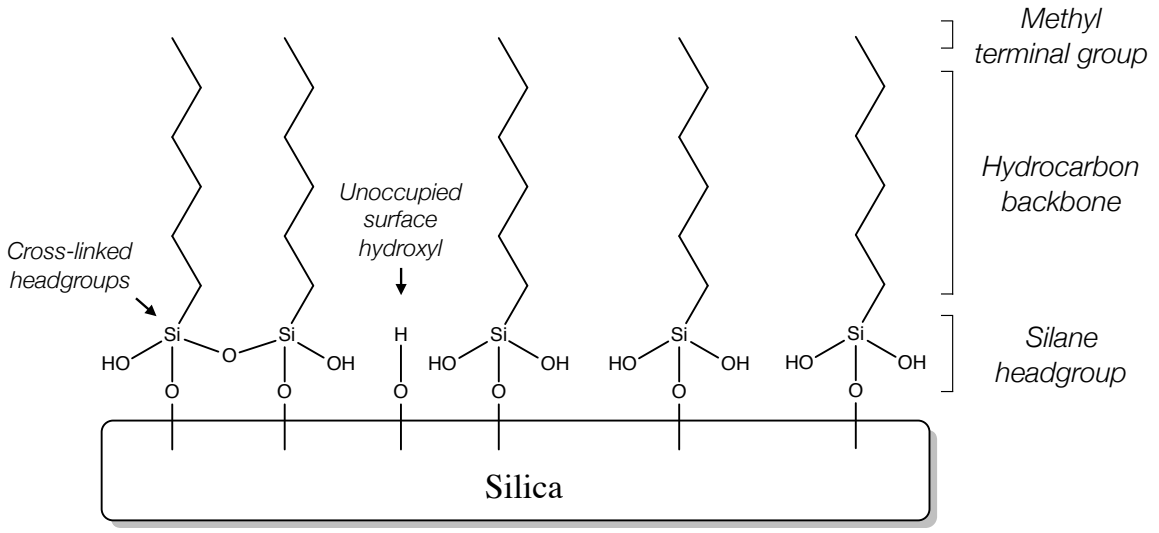

Figure 2.1: Simplified 2D depiction of an alkylsilane monolayer. Each chain shown features a silane headgroup that is chemisorbed to the silica surface, a hydrocarbon backbone, and a methyl terminal group. Chains attach via reactions with surface hydroxyls; however, due to steric hindrance, not all surface sites will be occupied. Additionally, cross-linking between silane headgroups is expected to occur, although the extent to which this is present remains a point of argument.

monolayer will be grown (e.g., thiol head groups are used for gold surfaces), the chemistry of the chain backbone (e.g., number of carbon atoms, functionalization) and terminal group can be modulated to influence the tribology of the resulting film.

It has generally been observed that increasing backbone chain length yields reduced frictional forces.[19–22] This trend has been attributed to an increase in attractive inter-chain van der Waals forces with longer backbones, leading to greater monolayer cohesivity and higher orientational ordering of monolayer chains.[23] However, these more favorable interactions between backbones also make it difficult experimentally to decouple the effects of chain length from those of monolayer density, as longer chains more easily form denser films. This is further compounded by the sensitivity of monolayer structure to preparation conditions; for example, Lee et al. showed that a "critical" temperature exists for monolayer films, below which monolayers form well-ordered structures and above which increasing disorder is present.[24] It was also observed that this critical temperature was de-

pendent on the backbone chain length, with longer chains featuring higher critical temperatures. To obtain an understanding of the interplay between monolayer chain length, density, and tribology, Lee et al. prepared monolayers with backbone chain lengths of 6, 12, and 18 carbons at temperatures ranging from -15 to 60 Celsius (such that both ordered and disordered films of each monolayer were formed).[24] It was observed that for the tightly-packed films formed at lower temperatures the coefficient of friction was independent of chain length. Similarly, simulations by Chandross et al. of alkylsilane monolayers on crystalline silica revealed the coefficient of friction to be independent of chain length.[25] Thus, the effect of chain length on monolayer tribology appears dependent on the conditions of monolayer preparation due to a close coupling with film density.

In addition to chain length, the effects of backbone functionalization, have also received extensive examination, most notably the effect of fluorination.[17,26–33] Despite their lower surface energy, experimentally it has been observed that fluorinated monolayer films feature higher coefficients of friction than hydrogenated films.[17,26,27,31] For example, Brukman et al., in a comparison of hydrogenated and semi-fluorinated monolayers on aluminum oxide, observed that the hydrogenated films consistently featured COFs that were 40-70% of those observed for the semi-fluorinated films.[31] It is possible some these effects are again the result of difficulties in decoupling the effect of monolayer density from other system variables, as fluorinated chains feature larger VDW diameters which will lead to sparser films. However, several studies suggest that the higher friction in fluorinated films may arise as a result of tightly packed terminal groups (again due to larger VDW diameters). While this may appear in contradiction to generally observed trends that denser monolayers yield lower frictional forces, in the case of fluorinated films it appears if the films become too dense they can provide greater resistance to motion and feature collective behavior that yields modes of higher friction. This theory appears to be corroborated by MD studies performed by Park et al. of monolayers where only terminal groups were fluorinated.[28] However, other MD studies suggest density effects likely play a larger role. Lewis

et al. observed via MD that fluorinated monolayers featured lower COFs than hydrogenated monolayers when both were grafted to crystalline silica at a density of 4.0 chains/nm^2.[32] However, when the density of the fluorinated monolayers was reduced to 3.0 chains/nm^2 frictional forces were found to be higher than for the denser hydrogenated films, in agreement with experimental trends.

Changes to the chemistry of chain backbones have significant influence on monolayer structure (e.g. packing density, orientational ordering of chains); however, the interfacial properties of monolayers are more directly influenced by changes to the terminal group chemistry. For example, bulkier functional groups have often been found to yield larger frictional forces than smaller functional groups, such as in the aforementioned study of CF_3-terminated monolayers.[28] In other work, Yu et al. found phenyl-terminated monolayer films to yield higher frictional forces than methyl-terminated films, which was attributed to the presence of additional energy dissipation modes (here defined as mechanisms via which monolayers respond to shear) through the twisting of the phenyl terminal groups.[34] In a more extreme case, Tsukruk et al. observed via AFM that monolayers terminated by fullerenes yielded higher frictional forces than those terminated by methyl groups, which was again suggested to be the result of different mechanisms of energy dissipation.[35] Adhesive forces between monolyers are also strongly influenced by terminal group chemistry. For example, the presence of both hydroxyl (OH) and carboxyl (COOH) moieties has been shown in several studies to lead to increased adhesion as a result of the formation of hydrogen bonds between the two contacting interfaces.[21,36–38] The ability for both backbone and terminal group chemistry to have significant influences over monolayer tribology suggests this may provide a route towards improving the lubricating ability of these materials.

The chemical space afforded by monolayer films can be further expanded when considering monolayers consisting of multiple types of chains, so-called multi-component monolayers. For alkanethiols adsorbed on gold, multi-component films featuring chains of two different lengths have been observed to yield higher frictional forces than single-component

monolayers.[39–42] However, the opposite result was observed by Zhang et al. in a pair of studies of alkylsilane films on silica, where multi-component films with chains of different lengths were found to yield *lower* frictional forces than single-component films.[43,44] In a more recent study by Vilt et al., mixed alkylsilane monolayers of C6 and C18 chains were observed to yield intermediate properties between single-component C6 and C18 films.[37] Thus, it appears the frictional performance of multi-component alkyl monolayers with differing chain lengths is likely influenced by other system variables, such as contact geometry and shear velocity.

In addition to chain length disparity, multi-component monolayers have also been examined in the context of chains of different terminal group and backbone functionalization, which provides a more promising avenue for optimizing the lubricating capacity of these materials. For example, Rivera et al. examined monolayers of mixed hydroxyl and methyl terminal groups via MD simulation, observing intermediate behavior compared to the single-component films.[38] Friction in these systems also revealed a dependence on the chain length of the methyl-terminated chains, whereby lower friction was observed for longer methyl-terminated chains due to the presence of a buffer zone preventing the formation of inter-monolayer hydrogen bonds. In a similar study, Lewis et al. examined systems of mixed fluorinated and hydrogenated alkylsilanes, focusing on both the fractional coverage of each chain as well as the chain length discrepency.[32] It was observed that systems featuring 75% coverage of fluorinated chains (corresponding to film densities expected in experiment) backfilled with 25% hydrogenated chains yielded lower frictional forces when the chain length between these two chain types differed by eight carbons (where the hydrogenated chains were longer). This was attributed to a fluid-like response to shear, whereby the longer hydrogenated chains yielded a liquid-like interface between the two monolayers, providing lowered resistance to shear. This result exemplifies the benefits of multi-component strategies in yielding low-friction mechanisms unavailable to single-component monolayers.

Finally, another route through which the lubricating ability of monolayer films may be altered is through a mixed-lubrication approach, whereby the monolayer films on the two contacting surfaces feature dissimilar chemistry. Such systems have received relatively little attention in the literature; however, several studies have shown that contacting monolayers with dissimilar chemistries may lead to improved tribological behavior over chemically identical systems.[21,27,45,46] In a study by McGuiggan, contact between fluorinated and hydrogenated monolayers was examined, whereby it was observed that while interfacial energies yielded intermediate values, frictional forces were reduced compared to either pure system.[27] Similarly, in several studies it has been observed that contact between hydroxyl or carboxylic acid-terminated monolayers and methyl-terminated monolayers yields lower COFs than either pure system.[21,45,46] However, the lack of a substantial body of literature in this area provides little understanding of the mechanisms behind these results and suggests additional studies are necessary to determine the efficacy of chemically-dissimilar monolayer contact as a means towards improving lubricity.

In summary, many studies exist demonstrating the lubricity of monolayer films and reveal a strong dependency between monolayer chemistry and tribological performance. The chemical parameter space available to monolayer films is vast and affords near infinite possibilities for chemical tuning to optimize performance for tribological applications such as the lubrication of MEMS/NEMS devices. Computational techniques, such as MD, have already provided significant contributions to understanding the underlying mechanisms behind many of the observed trends and will undoubtedly continue to provide aid in helping to screen this parameter space.

2.3 Monolayer Viability

The lubricating ability of monolayer films is recognized through a considerable body of work dating back several decades; however, despite their demonstrated tribological properties, monolayer films have yet to receive widespread use as lubricants for MEMS/NEMS.

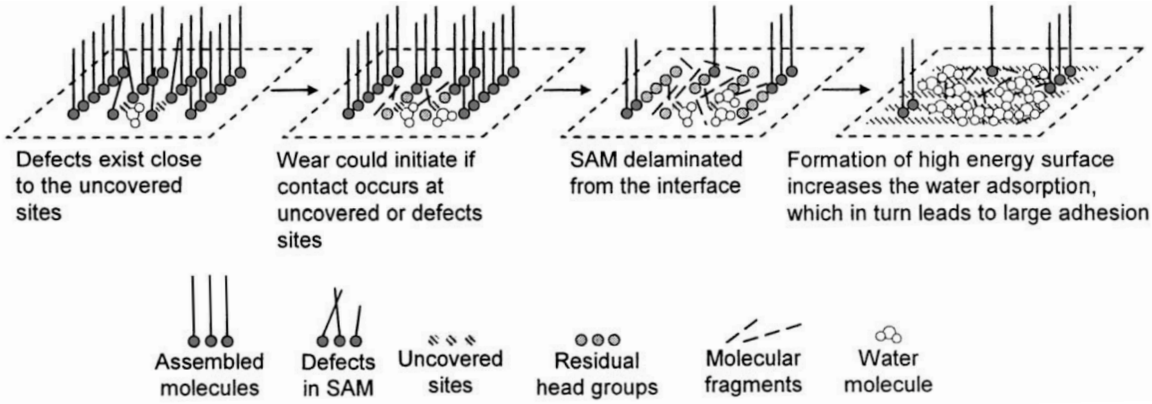

Figure 2.2: Speculated mechanism of monolayer degradation. Reprinted from *Ultramicroscopy*, Vol. 100, Issue 3-4, Liu, H.; Bhushan, B., Nanotribological Characterization of Digital Micromirror Devices Using an Atomic Force Microscope, 391-412, Copyright (2004), with permission from Elsevier.

The reason for this perhaps surprising development is that monolayer films have been found to degrade fairly rapidly under shear. For example, in a study by Booth et al., it was found that although increases in monolayer chain length could provide stability improvements, even long-chain monolayers (C18) had lifetimes of less than 100 hours under shear.[23] In an in situ study of the lubrication of the side wall of a MEMS comb drive, Senft et al. observed a threefold increase in device lifetime through lubrication by a C18 monolayer; however, this still only equated to a lifetime on the order of hours.[47] Similarly, Srinivasan et al. observed wear of fluorinated monolayers on a side wall device after 2100 cycles, leading to a 14x increase in COF.[48] It should be noted that there have been studies of monolayer-coated MEMS devices that have shown lubricant stability over time (Deng. et al observed stable MEMS operation for C18-coated micromotors over a nine-month period[49]), suggesting that monolayer reliability may be closely linked to the specific operating conditions.

To address this viability barrier, a thorough understanding of monolayer wear mechanisms, and the conditions facilitating these mechanisms, is necessary. A proposed mechanism for the monolayer wear process is shown in Fig. 2.2. Several studies have suggested that the onset of the wear of monolayers likely involves scission of interfacial bonds that link chains to the substrate.[50,51] This creates defects in neighboring chains, breaking mono-

layer cohesivity, and facilitating further chain removal propagating from these initial sites. The presence of residual water may further exacerbate this process. This mechanism is supported by several studies that have shown reduced wear resistance for alkanethiols on gold compared to alkylsilanes on silica[36,51], thought to be the result of the weaker S-Au interfacial bond (184 kJ/mol)[52] of alkanethiols compared with the stronger Si-O interfacial bond (242 kJ/mol)[53] of alkylsilanes. The weaker bond strength of the interfacial Si-O bond as compared with other bonds in the alkylsilane chain (Si-C (414 kJ/mol), C-C (426 kJ/mol), and C-H (462 kJ/mol))[54] further supports this mechanism.

The geometry and roughness of the contacting surfaces are also likely to play a key role in the degradation of monolayer films. Surfaces in MEMS/NEMS devices are not likely to be perfectly flat, and may feature both atomic-scale roughness as well as nanoscale roughness in the form of surface asperties. The real area of contact is thus much smaller than the apparent area of contact, with the normal load borne by these asperities, which are likely to act as focal points for monolayer and device failure.[55] This is corroborated in experimental studies using AFM, which serves as an analog to a single asperity contact, where the onset of wear in monolayer films is observed beyond a threshold normal load value (often referred to as the "critical" normal load). It has been shown in a number of both experimental[31,56–62] and simulation[63–69] studies that when contact geometries are small (such as in the case of an asperity or AFM tip) additional modes of energy dissipation arise, which may lead to higher frictional forces. In particular, "plowing"-like modes of energy dissipation may occur when penetration occurs of asperities or tips into monolayer films, as proposed by Flater et al.[58] This has been corroborated by MD studies, such as by Knippenberg et al., who found that the friction coefficient of a buckyball sheared against an alkane monolayer on diamond was considerably higher than that observed for a planar surface sheared against this same monolayer.[66]

The degradation of monolayer films remains the primary obstacle to the full realization of these materials as lubricants for MEMS/NEMS applications. However, the chemical tun-

ability of monolayers provides optimism that these materials can be designed to overcome this shortcoming. Yet, for this dream to become a reality, a more complete characterization of the mechanisms involved in the friction and wear of monolayer films, in particular those associated with surface effects such as roughness, are necessary. Experimental approaches can provide significant insight into friction and wear of bulk monolayers; yet they remain limited in their ability to resolve the underlying behavior at the molecular level. Instruments such as the surface force apparatus (SFA) now have the capacity to resolve separation distance at the angstrom-level; however, the ability to identify specific modes of energy dissipation through experimental analysis remains a difficult, if not impossible, task. Computational techniques, such as MD, hold promise in this regard. MD has been used to provide a better understanding of the mechanisms involved with friction at asperity contacts, yet only a few such studies exist and little is known with respect to how these mechanisms respond to changes in monolayer chemistry. Furthermore, the application of MD to achieve a comprehensive understanding of monolayer wear has remained limited, as classical force fields prohibit bond breaking and reactive force fields come at a signficant computational cost.

The work in this thesis aims to address the viability of monolayer lubricants through a better understanding of friction and wear mechanisms (Chapters 3 & 4), as well as through the development of workflows for chemical-property screening (Chapter 5) and the development of simplified models to further future screening of these materials (Chapter 6).

2.4 Bibliography

[1] Albagachiev, A. Y.; Gurskii, B. E.; Luzhnov, Y. M.; Romanova, A. T.; Chichinadze, A. V. Economic and ecological issues in tribology. *Russian Engineering Research* **2008**, *28*, 959–964.

[2] Jost, H. Tribology — Origin and future. *Wear* **1990**, *136*, 1–17.

[3] Feynman, R. P. There's plenty of room at the bottom [data storage]. *Journal of Microelectromechanical Systems* **1992**, *1*, 60–66.

[4] Yokota, Y.; Koide, A.; Matsumoto, M.; Hayashi, M. Three-dimensional acceleration sensor and airbag using the same. 1995.

[5] Ghodssi, R.; Pinyen, L. MEMS Materials and Processes Handbook. *MEMS Reference Shelf* **2011**,

[6] Ahn, C.; Choi, J.-W.; Beaucage, G.; Nevin, J.; Lee, J.-B.; Puntambekar, A.; Lee, R. Disposable Smart Lab on a Chip for Point-of-Care Clinical Diagnostics. *Proceedings of the IEEE* **2004**, *92*, 154–173.

[7] de Boer, M. P.; Knapp, J. A.; Mayer, T. M.; Michalske, T. A. Role of interfacial properties on MEMS performance and reliability. *Microsystems Metrology and Inspection* **1999**, 2–15.

[8] Gee, M. L.; McGuiggan, P. M.; Israelachvili, J. N.; Homola, A. M. Liquid to solidlike transitions of molecularly thin films under shear. *The Journal of Chemical Physics* **1990**, *93*, 1895–1906.

[9] Klein, J.; Kumacheva, E. Confinement-Induced Phase Transitions in Simple Liquids. *Science* **1995**, *269*, 816–819.

[10] Klein, J.; Kumacheva, E. Simple liquids confined to molecularly thin layers. I. Confinement-induced liquid-to-solid phase transitions. *The Journal of Chemical Physics* **1998**, *108*, 6996–7009.

[11] Kumacheva, E.; Klein, J. Simple liquids confined to molecularly thin layers. II. Shear and frictional behavior of solidified films. *The Journal of Chemical Physics* **1998**, *108*, 7010–7022.

[12] Radhakrishnan, R.; Gubbins, K. E.; Sliwinska-Bartkowiak, M. Effect of the fluid-wall interaction on freezing of confined fluids: Toward the development of a global phase diagram. *The Journal of Chemical Physics* **2000**, *112*, 11048–11057.

[13] Sliwinska-Bartkowiak, M.; Dudziak, G.; Sikorski, R.; Gras, R.; Gubbins, K. E.; Radhakrishnan, R.; Kaneko, K. Freezing Behavior in Porous Materials: Theory and Experiment. **2001**, *75*, 547–555.

[14] Radhakrishnan, R.; Gubbins, K. E.; Sliwinska-Bartkowiak, M. Global phase diagrams for freezing in porous media. *The Journal of Chemical Physics* **2002**, *116*, 1147–1155.

[15] Cummings, P. T.; Docherty, H.; Iacovella, C. R.; Singh, J. K. Phase transitions in nanoconfined fluids: The evidence from simulation and theory. *AIChE Journal* **2010**, 842–848.

[16] Bhushan, B.; Liu, H. Micro-/nanoscale tribological and mechanical characterization for MEMS/NEMS. *Reliability, Testing, and Characterization of MEMS/MOEMS III* **2004**,

[17] DePalma, V.; Tillman, N. Friction and wear of self-assembled trichlorosilane monolayer films on silicon. *Langmuir* **1989**, *5*, 868–872.

[18] Bhushan, B. Self-assembled Monolayers (SAMs) for Nanotribology and Surface Protection. *Nanotribology and Nanomechanics* **2017**, 641–688.

[19] Xiao, X.; Hu, J.; Charych, D. H.; Salmeron, M. Chain Length Dependence of the Frictional Properties of Alkylsilane Molecules Self-Assembled on Mica Studied by Atomic Force Microscopy. *Langmuir* **1996**, *12*, 235–237.

[20] Lio, A.; Charych, D. H.; Salmeron, M. Comparative Atomic Force Microscopy Study of the Chain Length Dependence of Frictional Properties of Alkanethiols on Gold and Alkylsilanes on Mica. *The Journal of Physical Chemistry B* **1997**, *101*, 3800–3805.

[21] Brewer, N. J.; Beake, B. D.; Leggett, G. J. Friction Force Microscopy of Self-Assembled Monolayers: Influence of Adsorbate Alkyl Chain Length, Terminal Group Chemistry, and Scan Velocity. *Langmuir* **2001**, *17*, 1970–1974.

[22] Huo, L.; Du, P.; Zhou, H.; Zhang, K.; Liu, P. Fabrication and tribological properties of self-assembled monolayer of n -alkyltrimethoxysilane on silicon: Effect of SAM alkyl chain length. *Applied Surface Science* **2017**, *396*, 865–869.

[23] Booth, B. D.; Vilt, S. G.; Lewis, J. B.; Rivera, J. L.; Buehler, E. A.; McCabe, C.; Jennings, G. K. Tribological Durability of Silane Monolayers on Silicon. *Langmuir* **2011**, *27*, 5909–5917.

[24] Lee, D. H.; Oh, T.; Cho, K. Combined Effect of Chain Length and Phase State on Adhesion/Friction Behavior of Self-Assembled Monolayers. *The Journal of Physical Chemistry B* **2005**, *109*, 11301–11306.

[25] Chandross, M.; Grest, G. S.; Stevens, M. J. Friction between Alkylsilane Monolayers: Molecular Simulation of Ordered Monolayers. *Langmuir* **2002**, *18*, 8392–8399.

[26] Kim, H.; Koini, T.; Lee, T.; Perry, S. Molecular contributions to the frictional properties of fluorinated self-assembled monolayers. *Tribology Letters* **1998**, *4*, 137–140.

[27] McGuiggan, P. M. Friction and adhesion measurements between a fluorocarbon surface and a hydrocarbon surface in air. *The Journal of Adhesion* **2004**, *80*, 395–408.

[28] Park, B.; Lorenz, C. D.; Chandross, M.; Stevens, M. J.; Grest, G. S.; Borodin, O. A. Frictional Dynamics of Fluorine-Terminated Alkanethiol Self-Assembled Monolayers. *Langmuir* **2004**, *20*, 10007–10014.

[29] Lorenz, C.; Webb, E.; Stevens, M.; Chandross, M.; Grest, G. Frictional dynamics of perfluorinated self-assembled monolayers on amorphous SiO2. *Tribology Letters* **2005**, *19*, 93–98.

[30] Lorenz, C. D.; Chandross, M.; Grest, G. S.; Stevens, M. J.; Webb, E. B. Tribological Properties of Alkylsilane Self-Assembled Monolayers. *Langmuir* **2005**, *21*, 11744–11748.

[31] Brukman, M. J.; Oncins, G.; Dunbar, T. D.; Boardman, L. D.; Carpick, R. W. Nanotribological Properties of Alkanephosphonic Acid Self-Assembled Monolayers on Aluminum Oxide: Effects of Fluorination and Substrate Crystallinity. *Langmuir* **2006**, *22*, 3988–3998.

[32] Lewis, J. B.; Vilt, S. G.; Rivera, J. L.; Jennings, G. K.; McCabe, C. Frictional Properties of Mixed Fluorocarbon/Hydrocarbon Silane Monolayers: A Simulation Study. *Langmuir* **2012**, *28*, 14218–14226.

[33] Xiang, H.; Komvopoulos, K. Effect of fluorocarbon self-assembled monolayer films on sidewall adhesion and friction of surface micromachines with impacting and sliding contact interfaces. *Journal of Applied Physics* **2013**, *113*, 224505.

[34] Yu, B.; Qian, L.; Yu, J.; Zhou, Z. Effects of Tail Group and Chain Length on the Tribological Behaviors of Self-Assembled Dual-Layer Films in Atmosphere and in Vacuum. *Tribology Letters* **2008**, *34*, 1–10.

[35] Tsukruk, V. V.; Everson, M. P.; Lander, L. M.; Brittain, W. J. Nanotribological Properties of Composite Molecular Films: C60 Anchored to a Self-Assembled Monolayer. *Langmuir* **1996**, *12*, 3905–3911.

[36] Booth, B. D.; Vilt, S. G.; McCabe, C.; Jennings, G. K. Tribology of Monolayer Films: Comparison between n-Alkanethiols on Gold and n-Alkyl Trichlorosilanes on Silicon. *Langmuir* **2009**, *25*, 9995–10001.

[37] Vilt, S. G.; Leng, Z.; Booth, B. D.; McCabe, C.; Jennings, G. K. Surface and Frictional Properties of Two-Component Alkylsilane Monolayers and Hydroxyl-Terminated Monolayers on Silicon. *The Journal of Physical Chemistry C* **2009**, *113*, 14972–14977.

[38] Rivera, J. L.; Jennings, G. K.; McCabe, C. Examining the frictional forces between mixed hydrophobic – hydrophilic alkylsilane monolayers. *The Journal of Chemical Physics* **2012**, *136*, 244701.

[39] Beake, B. D.; Leggett, G. J. Variation of Frictional Forces in Air with the Compositions of Heterogeneous Organic Surfaces. *Langmuir* **2000**, *16*, 735–739.

[40] Shon, Y.-S.; Lee, S.; Colorado, R.; Perry, S. S.; Lee, T. R. Spiroalkanedithiol-Based SAMs Reveal Unique Insight into the Wettabilities and Frictional Properties of Organic Thin Films. *Journal of the American Chemical Society* **2000**, *122*, 7556–7563.

[41] van der Vegte, E. W.; Subbotin, A.; Hadziioannou, G.; Ashton, P. R.; Preece, J. A. Nanotribological Properties of Unsymmetricaln-Dialkyl Sulfide Monolayers on Gold: Effect of Chain Length on Adhesion, Friction, and Imaging. *Langmuir* **2000**, *16*, 3249–3256.

[42] Barrena, E.; Ocal, C.; Salmeron, M. A comparative AFM study of the structural and frictional properties of mixed and single component films of alkanethiols on Au(111). *Surface Science* **2001**, *482-485*, 1216–1221.

[43] Zhang, Q.; Archer, L. A. Boundary Lubrication and Surface Mobility of Mixed Alkylsilane Self-Assembled Monolayers. *The Journal of Physical Chemistry B* **2003**, *107*, 13123–13132.

[44] Zhang, Q.; Archer, L. A. Interfacial Friction of Surfaces Grafted with One- and Two-Component Self-Assembled Monolayers. *Langmuir* **2005**, *21*, 5405–5413.

[45] Noy, A.; Frisbie, C. D.; Rozsnyai, L. F.; Wrighton, M. S.; Lieber, C. M. Chemical Force Microscopy: Exploiting Chemically-Modified Tips To Quantify Adhesion, Friction, and Functional Group Distributions in Molecular Assemblies. *Journal of the American Chemical Society* **1995**, *117*, 7943–7951.

[46] Clear, S. C.; Nealey, P. F. Chemical Force Microscopy Study of Adhesion and Friction between Surfaces Functionalized with Self-Assembled Monolayers and Immersed in Solvents. *Journal of Colloid and Interface Science* **1999**, *213*, 238–250.

[47] Senft, D. C.; Dugger, M. T. Friction and wear in surface-micromachined tribological test devices. *Micromachined Devices and Components III* **1997**,

[48] Srinivasan, U.; Foster, J.; Habib, U.; Howe, R.; Maboudian, R.; Senft, D.; Dugger, M. Lubrication of polysilicon micromechanisms with self-assembled monolayers. **1998**,

[49] Deng, K. Performance Impact of Monolayer Coating of Polysilicon Micromotors. *Journal of The Electrochemical Society* **1995**, *142*, 1278.

[50] Liu, H.; Bhushan, B. Nanotribological characterization of digital micromirror devices using an atomic force microscope. *Ultramicroscopy* **2004**, *100*, 391–412.

[51] Bhushan, B.; Kasai, T.; Kulik, G.; Barbieri, L.; Hoffmann, P. AFM study of perfluoroalkylsilane and alkylsilane self-assembled monolayers for anti-stiction in MEMS/NEMS. *Ultramicroscopy* **2005**, *105*, 176–188.

[52] Lio, A.; Morant, C.; Ogletree, D. F.; Salmeron, M. Atomic Force Microscopy Study of the Pressure-Dependent Structural and Frictional Properties ofn-Alkanethiols on Gold. *The Journal of Physical Chemistry B* **1997**, *101*, 4767–4773.

[53] Hoshino, T. Adsorption of atomic and molecular oxygen and desorption of silicon monoxide on Si(111) surfaces. *Physical Review B* **1999**, *59*, 2332–2340.

[54] Lide, D. R. *CRC Handbook of Chemistry and Physics*, 75th ed.; CRC Press: Boca Raton, FL, 1994.

[55] Patton, S.; Zabinski, J. Failure mechanisms of a MEMS actuator in very high vacuum. *Tribology International* **2002**, *35*, 373–379.

[56] Salmeron, M. Generation of Defects in Model Lubricant Monolayers and Their Contribution to Energy Dissipation in Friction. *Tribology Letters* **2001**, *10*, 69–79.

[57] Colburn, T. J.; Leggett, G. J. Influence of Solvent Environment and Tip Chemistry on the Contact Mechanics of Tip-Sample Interactions in Friction Force Microscopy of Self-Assembled Monolayers of Mercaptoundecanoic Acid and Dodecanethiol. *Langmuir* **2007**, *23*, 4959–4964.

[58] Flater, E. E.; Ashurst, W. R.; Carpick, R. W. Nanotribology of Octadecyltrichlorosilane Monolayers and Silicon: Self-Mated versus Unmated Interfaces and Local Packing Density Effects. *Langmuir* **2007**, *23*, 9242–9252.

[59] Knorr, D. B.; Widjaja, P.; Acton, O.; Overney, R. M. Molecular friction dissipation and mode coupling in organic monolayers and polymer films. *The Journal of Chemical Physics* **2011**, *134*, 104502.

[60] Vilt, S. G.; Caswell, C. J.; Tuberquia, J. C.; McCabe, C.; Jennings, G. K. Effect of Roughness on the Microscale Friction of Hydrocarbon Films. *The Journal of Physical Chemistry C* **2012**, *116*, 21795–21801.

[61] Domatti, A.; Stempflé, P.; Carrière, P.; Takadoum, J. Multi-asperity Nanotribology of Self-Assembled Monolayers Grafted on Silicon Wafers Displaying Various Crystallographic Orientations and Nanostructures. *Tribology Letters* **2013**, *51*, 207–218.

[62] Nikogeorgos, N.; Leggett, G. J. The Relationship Between Contact Mechanics and Adhesion in Nanoscale Contacts Between Non-Polar Molecular Monolayers. *Tribology Letters* **2013**, *50*, 145–155.

[63] Tupper, K. J.; Colton, R. J.; Brenner, D. W. Simulations of Self-Assembled Monolayers under Compression: Effect of Surface Asperities. *Langmuir* **1994**, *10*, 2041–2043.

[64] Bonner, T.; Baratoff, A. Molecular dynamics study of scanning force microscopy on self-assembled monolayers. *Surface Science* **1997**, *377-379*, 1082–1086.

[65] Knippenberg, M. T.; Mikulski, P. T.; Dunlap, B. I.; Harrison, J. A. Atomic contributions to friction and load for tip–self-assembled monolayers interactions. *Physical Review B* **2008**, *78*.

[66] Knippenberg, M. T.; Mikulski, P. T.; Harrison, J. A. Effects of tip geometry on interfacial contact forces. *Modelling and Simulation in Materials Science and Engineering* **2010**, *18*, 034002.

[67] Ewers, B. W.; Batteas, J. D. Molecular Dynamics Simulations of Alkylsilane Monolayers on Silica Nanoasperities: Impact of Surface Curvature on Monolayer Structure and Pathways for Energy Dissipation in Tribological Contacts. *The Journal of Physical Chemistry C* **2012**, *116*, 25165–25177.

[68] Ewers, B. W.; Batteas, J. D. Utilizing Atomistic Simulations To Map Pressure Distributions and Contact Areas in Molecular Adlayers within Nanoscale Surface-Asperity Junctions: A Demonstration with Octadecylsilane-Functionalized Silica Interfaces. *Langmuir* **2014**, *30*, 11897–11905.

[69] Ewers, B. W.; Batteas, J. D. The role of substrate interactions in the modification of surface forces by self-assembled monolayers. *RSC Adv.* **2014**, *4*, 16803–16812.

CHAPTER 3

WEAR OF MONOLAYER-BASED LUBRICANTS

In this chapter MD simulations are used to analyze the effects of substrate morphology and backbone chain length on the propensity for monolayer degradation. As a result of the aforementioned problems with studying monolayer wear with MD, a novel approach is taken which allows for the analyzation of several proxy properties to gauge wear propensity. Specifically, after monolayers have reached a steady-state during shear, the interfacial bonds between the silica interface and a fraction of monolayer chains are removed. The mobility of these unbound (free) chains is utilized to measure the viability of the film, whereby systems where these free chains have high mobility and are readily removed from the monolayer suggest greater instability. This approach is utilized to compare degradation propensity between monolayers attached to crystalline silica (a common simplification used in the simulation literature for such materials) with those where chains are arranged in more disordered, realistic patterns, and with systems that feature atomic-scale surface roughness. The effect of monolayer chain length on degradation propensity is also examined to see how these effects couple with those of the underlying substrate morphology.

The work presented in this chapter has been featured in a peer-reviewed publication and is reprinted with permission from Ref. 1.

3.1 Background

Despite the promising tribological properties of monolayer films, widespread application of these materials for MEMS/NEMS lubrication has remained limited due to short lifetimes under shear.[2,3] For example, tribometry tests of alkylsilane durability by Booth et al. revealed monolayer lifetimes on the order of hours to days prior to failure.[4] Likewise, Hook et al. observed rapid wear during tribometry testing of fluorocarbon monolayers on silica,

recording failure after only a handful of cycles.[5] One proposed mechanism for the degradation of monolayers is through scission of the interfacial bonds between individual chains and the substrate.[6] This mechanism has been supported by evidence linking monolayer stability to interfacial bond strength. Specifically, Booth et al. found that alkylsilanes attached through an Si-O bond to silica (bond strength = 242 kJ/mol)[7] could withstand normal loads over 30 times larger than those withstood by alkanethiols, bound through a weaker S-Au bond to gold (bond strength = 184 kJ/mol).[8,9] Similarly, Bhushan and coworkers showed through AFM studies that the critical normal load for failure of alkanethiols was significantly lower than that for alkylsilanes.[7] While this behavior may be somewhat influenced by differences in substrate hardness, in both studies it was concluded that the weak S-Au interfacial bond of alkanethiols likely plays a critical role in determining the degradation characteristics of these films. Further evidence for this theory is provided in work by Pujari et al., who showed that fluoroalkyl monolayers attached to silicon through an Si-C=C bond (bond strength = 360 kJ/mol) featured increased wear resistance as compared to monolayers attached through a weaker Si-O bond.[10] These studies support the degradation mechanism of interfacial bond scission, and thus indicate that conditions precipitating strain of interfacial bonds will be most likely to promote degradation.

Direct control over surface morphology and decoupling of the numerous factors that influence friction and wear in monolayer systems is nearly impossible through a purely experimental approach. As a result, atomistic molecular dynamics (MD) simulations have emerged as a useful tool to analyze monolayer tribology and probe the molecular level behavior. Although the MD simulations performed to date typically utilize a wearless friction model (i.e., a classical force field with permanent bonds), they have helped provide insight into trends in friction force with various monolayer properties, including terminal group composition[11,12], backbone composition[13,14], and shear rate.[15] Many of these studies have examined monolayers attached to substrates featuring an ideal in-plane arrangement of chains and/or surfaces that are atomically smooth. Such surfaces differ from those ex-

pected in experiment and MEMS/NEMS devices, where non-ideality, such as roughness and voids, is likely to influence friction and wear behavior.[16–19] Recently, Black et al. developed a synthesis mimetic scheme that replicates the experimental postsynthesis processing of silica with piranha solution (H_2SO_4/H_2O_2) by allowing silica to react with H_2O_2 to generate more realistic silica substrates and then examined the influence of surface defects (i.e., unoccupied surface sites) and roughness on friction of monolayer-coated surfaces.[20] While the presence of surface defects was shown to yield a slightly larger coefficient of friction, surface roughness was found to have a greater effect, suggesting that roughness on silica surfaces in MEMS/NEMS is likely to play a critical role in the degradation of monolayer films.

MD studies of monolayer degradation have to date been limited, as classical force fields do not allow for bond breakage. Although reactive force fields, such as ReaxFF[21], are available that allow bond status to be dynamic, they are computationally expensive, limiting the practical timescale of an MD simulation. This is further hindered by the fact that relatively long timescales are needed for bond breakage to occur in chemisorbed monolayers. As an alternative approach, Chandross and coworkers have utilized models consisting of physisorbed and partially physisorbed alkylsilane monolayers (i.e., all, or a portion of the chains were not bonded to the substrate) and studied their behavior under shear by nanometer-scale tips, imitating experimental AFM measurements and analogous to asperity contact in a MEMS device with nanometer-scale roughness.[22–24] Physisorbed models account for the possible removal of monolayer chains from the surface through hydrolysis, of which there is some evidence.[23,25] In these studies, localized chain removal and material transfer to the tip (fouling) was observed, providing further evidence that surface conditions, such as asperities, are likely to play a critical role in the process of monolayer wear. Other MD studies, rather than looking at monolayer wear directly, have examined monolayers of reduced density, helping to shed light onto the frictional performance of monolayers at various degradation states, after chains have been removed.[26,27] In one such

study, Mikulski et al. showed that for a monolayer in contact with a flat surface, the greater disorder (i.e., reduced orientational ordering of chains) in less dense monolayers results in an uneven load distribution and a higher friction coefficient under large normal loads.[26] Chandross et al.[27], in an examination of two opposing monolayers of reduced chain density under shear, also found monolayer order to be the primary factor influencing friction and showed that substrate morphology (i.e., amorphous vs. crystalline substrates) had little effect on friction after 10% of the monolayer chains had been removed. This suggests that while surface structure is likely to influence friction and wear of idealized monolayers[20], its effects are eliminated after partial wear has occurred.

Results from Black et al.[20] have suggested that atomistic-scale surface roughness plays a critical role in the tribological behavior of alkylsilane monolayers, yet the extent to which surface morphology influences the onset of wear in these materials remains unclear. Furthermore, as a result of the difficulties of MD to approach the timescales needed to observe monolayer degradation, progress on the identification of wear-inducing conditions through simulation has been limited. Studies from Chandross and co-workers[22–24] of tip-induced wear have shown that wear is likely to be accelerated at large asperity contacts, with localized normal loads, but may not be predictive of conditions for all MEMS/NEMS surfaces, such as those where two monolayer- functionalized surfaces are in contact. Identification of likely surface sites where chain breakage will occur, as well as how monolayer structure, such as chain length, influences the degradation process on realistic surfaces is critical to developing an understanding of how these materials may fail in a MEMS/NEMS environment. In an effort to address these issues and increase understanding of the fundamental factors influencing monolayer degradation in MEMS/NEMS, the work in this chapter builds upon previous MD approaches of chain removal and physisorption. Specifically, through the scission of random interfacial Si-O bonds in alkylsilane monolayers on silica during shear, the influence of normal load, surface structure, and chain length on degradation behavior is examined through the mobility of the broken chains. In this manner

monolayer wear over a molecular dynamics timeframe is observed and conditions that are likely to trigger degradation can be identified.

3.2 Methods

3.2.1 Model

In experiment, the surface chemistry of monolayer films is highly sensitive to the method and conditions of preparation.[28] For simplicity, monolayer models in this study follow the idealized structure described by Stevens of a fully chemisorbed monolayer lacking cross-links between neighboring chains[29], which has been used previously in several simulation studies.[12,13,15,20] This model is analogous to a monolayer generated using an alkyltrichlorosilane precursor, where all chlorines have been hydrolyzed. Although condensation reactions are known to occur, joining adjacent chains, i.e. cross-linking, the extent of cross-linking has not been agreed upon.[29–32] Additionally, for monolayers reaching full coverage, cross-linking cannot occur due to steric effects.[29] Although the presence of cross-links would seem to facilitate stability, some evidence suggests that this may in fact have a negligible effect on friction and wear.[33,34] We also note that our model does not account for the effects of humidity in an ambient environment, which may induce scission of interfacial bonds through hydrolysis even in the absence of shear, leading to monolayers featuring at least partial physisorption.[23] Such effects are likely to influence friction and wear behavior, as evidenced by AFM measurements by Tian et al.;[35] however, simulations by Lane et al. suggest penetration of water molecules through monolayers may be minimal for films featuring high surface coverage.[23]

Several different silica substrates have been used in this work to study the effects of roughness and morphology on monolayer degradation. The internal coordinates of the surfaces are held fixed and thus the surfaces serve primarily as templates for monolayer surface arrangements. The β-cristobalite crystal polymorph of silica is examined as an ex-

ample of an idealized surface, where the size of the lattice is expanded in plane by 27% to yield dimensions of 53.89Å $\times$ 46.67Å , corresponding to a monolayer density of 25.1Å^2 per chain, which agrees with experimental findings for maximum surface coverage.[36] This system size has been previously shown to be large enough to prevent artifacts arising from periodic boundaries.[15] Disordered crystalline surfaces, where surface roughness remains absent but chain attachment sites, i.e. exposed oxygen binding sites on the surface, deviate from their regular arrangement on ideal β-cristobalite, are also considered. These surfaces were generated by performing slight, random displacements to attachment sites in the *xy* plane until a desired hexagonal order was reached. Although this is a non-physical procedure, the absence of intra-substrate bonds (as a result of fixing relative substrate coordinates) alleviates concerns of bond strain, and as the primary interactions affecting chains originate from neighboring chains and the outermost surface layer, contributions from the underlying crystal will be minimal. Thus, this approach simply provides an altered template to isolate the influence of in-plane monolayer ordering. Amorphous substrates, with tunable surface roughness, are also studied and were generated following the procedure described by Black et al.[20] using the ReaxFF reactive forcefield.[21] Briefly, starting with a β-cristobalite structure, monolayer chains are perturbed in the z dimension to obtain a desired nominal roughness value, where roughness corresponds to the standard deviation in attachment height. With the monolayer chains held fixed, the substrate is then melted at 5000K and cooled back to 298K, allowing the substrate to solidify, reforming bonds with the Si attachment site of the immobile chains. Following generation of the amorphous systems, classical, i.e. non-reactive, force fields with permanent bonds are then used.

Systems feature two opposing silica substrates, functionalized by 100 chains of length C6, C10, or C12 (with chain length being uniform within a given monolayer). Systems are described by the classical OPLS all-atom force field of Jorgensen et al.[37] Parameters for the silica substrates have been adapted from those of Lorenz and coworkers[38], altering charges at the attachment site to maintain net charge neutrality. A detailed description of

the OPLS force field, as well as tables of all parameters used in this study, are provided in Appendix A.

3.2.2 Method

Molecular dynamics (MD) simulations were performed using the LAMMPS open-source molecular dynamics code.[39,40] Integration is performed under the canonical ensemble and a Nosé-Hoover thermostat[41,42] is applied to the system to maintain a temperature of 298 K. Thermostatting is not performed in the direction of shear to allow for the possibility of viscous heating, although at the strain rates studied in this work appreciable shear-induced heating is not observed. Long-range electrostatics were calculated using a particle-particle particle-mesh algorithm, applying the slab modification to account for the non-periodic z dimension.[43] The rRESPA timestep algorithm[44] was utilized to aid in computation speed, with timesteps of 0.25fs, 0.5fs, 0.5fs, and 1.0fs defined for bonds, angles, dihedrals, and non-bonded interactions respectively. Production runs begin with a 1ns relaxation period that allows the monolayer to achieve an energetically favorable configuration and is then followed by a compression stage, featuring a compression rate of 1m/s, during which the monolayers are brought into contact. Shearing simulations were then performed under a constant-separation ensemble for 1ns without defects and for an additional 5ns with defects (additional details on the defect scheme are provided below). It should be noted that although a constant normal load ensemble is more common in practical applications, our systems feature a standard deviation in normal force on the order of 1-4%, suggesting that these two ensembles are near equivalent under the conditions of this study.

3.2.3 Monolayer Degradation

A diagram depicting our strategy for observing monolayer wear is provided in Fig. 3.1. Monolayer degradation is imposed by detaching chains from the substrate through the removal of Si-O interfacial bonds (at random) following a 1 ns shearing stage with mono-

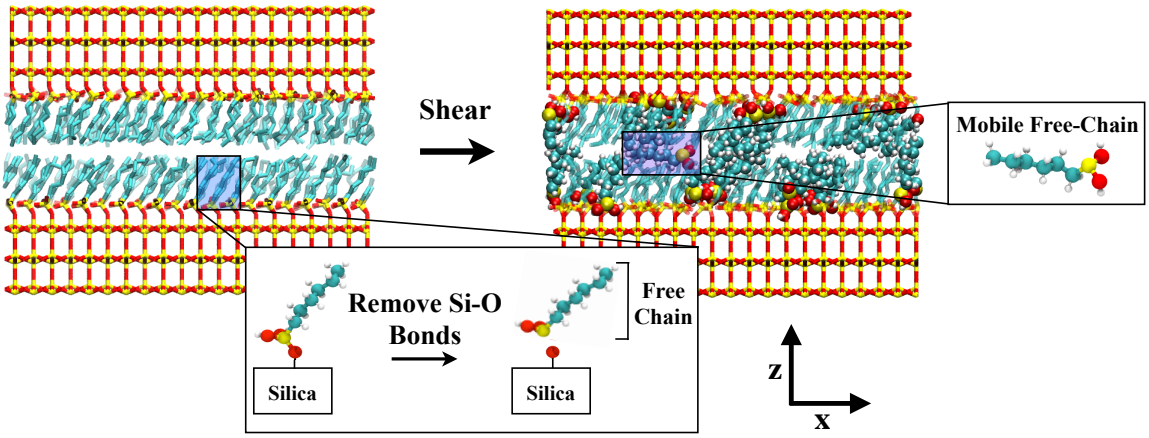

Figure 3.1: Diagram depicting Si-O bond removal yielding a free alkylsilane chain in a C6 monolayer system on crystalline silica under a normal load of 0.5 GPa. Our color scheme depicts silicon in yellow, oxygen in red, carbon in cyan, and hydrogen in white. Free-chains are rendered as van der Waals spheres. Hydrogens have been removed from non-free chains for clarity.

layers intact. To prevent rapid expulsion of free-chains from the monolayer due to overlapping van der Waals radii, nonbonded interactions at the attachment site are slowly turned on over a 1 ps interval. This method allows for retention of the chemisorbed monolayer structure, but with the added ability to now examine degradation characteristics using classical molecular dynamics through analysis of the behavior of the free (nonbonded) chains. In this work, systems with 15% defects, i.e. 15 bonds are removed from each monolayer (30 total free-chains), are studied.

It should be noted that while the aim of utilizing rough, amorphous substrate morphologies is to better represent experimental conditions, several simplifications are made in this work to accelerate the monolayer degradation process to an observable MD timeframe. While the shear rates of 10m/s used in this work are common in MD simulation studies, they are many orders of magnitude larger than those typically used in experiment (such as AFM or tribometry, where shear rates are often on the order of μm/s). We note however, that read/write head speeds in hard disk drives are known to exceed 10 m/s and devices such as micromotors have been proposed that would feature velocities exceeding 500 m/s.[6,45] Additionally, the random removal of bonds differs from experimental expec-

tations, where chains featuring the greatest bond strain are likely to be first removed. The harmonic bond model utilized in the force field yields a narrow bond length distribution, limiting the ability to remove bonds at preferred locations. The use of 15% bond removal provides an adequate sampling of surface locations, with chains removed from monolayers during shear simulations likely representing those more favorably removed in experiment. Keeping these limitations in mind, the goal of this study is to isolate the influence of the silica substrate on monolayer stability as it relates to degradation, so as to identify the effects of various substrate features on monolayer wear.

3.2.4 Analysis

To quantify a monolayer's propensity for wear under a given set of conditions, free-chain mobility is analyzed by counting the number of free-chains that become mobile, or are removed from monolayers, during the course of shear. To achieve this, a boundary is defined for each monolayer located at 80% of the monolayer height, calculated through averaging all chain heights for a given monolayer. The location of the Si atom of the silane group for each free-chain is surveyed every 10 ps over the course of a 5 ns shear simulation. If at any time the z coordinate is located beyond the boundary of the containing monolayer (i.e., towards the dual-monolayer interface), this chain is considered to have become mobile. The percentage of mobile free-chains is observed for monolayers over different sets of conditions, with an increased percentage of mobile chains suggesting a less stable monolayer and a higher likelihood for degradation.

As an additional measure of free-chain mobility, the one-dimensional root-mean-square deviation (RMSD) of free-chain Si atoms (formerly attached to the substrate) is also calculated, following,

$$\mathrm{RMSD}_z = \sqrt{\frac{1}{n}\sum_{i=1}^{n}\left(z_{i,t} - z_{i,t=0}\right)} \tag{3.1}$$

where n represents the number of free-chains and z represents the z coordinate of each

free-chain Si atom. Atomic positions are dumped every 10 ps over a 5 ns shear simulation and deviations in position from the initial frame, in the z dimension only, are surveyed. As RMSD is a tool used to study conformational shifts, although more commonly used in the biomolecular realm, it allows for observation of the deterioration of a monolayer's structure during shear, with increases in RMSD signifying migration of free-chains away from the initial configuration.

Monolayer order is quantified through evaluation of the nematic order parameter, S_2, detailed in Appendix B.2, Eq. B.2, during the 1ns shear period prior to bond removal. In this work, values of S_2 represent an average of the nematic order for the top and bottom monolayers of each system studied.

The global hexagonal order of chain attachment sites on a substrate is quantified through the use of the two-dimensional hexagonal order parameter described in Appendix B.3, Eq. B.3. Using a skin distance of 7.5Å for each attachment site, hexagonal order is examined in the *xy* plane (i.e., the surface plane).

Interdigiation between monolayers is also examined to evaluate the extend of overlap between chains of the two contacting monolayers. Further details on the interdigitation calculation are located in Appendix B.4, Eq. B.5.

3.3 Results and Discussion

First, the wear of monolayers bound to atomically smooth, crystalline silica, featuring an ideal in-plane arrangement of chains, is examined. These results will serve as a baseline for comparison with more complex surface morphologies and allow us to connect with prior simulation studies in which similar surfaces have been used to examine monolayer tribology.[13,15] C6 monolayers, under a constant shear rate of 10 m/s, were exposed to a series of normal loads ranging from 0.5 to 3.1 GPa. The free-chain mobility for each system was quantified by examining the percentage of free-chains that become mobile throughout a 5 ns shear simulation (Fig. 3.2a) and by calculating the one-dimensional root-mean-square

deviation of the Si atoms in free-chain silane groups (Fig. 3.2b). Free-chain mobility is observed to be highest at the lowest normal load, 0.5 GPa (pictured in Fig. 3.2c), with 30% of free-chains becoming mobile, on average. The RMSD of free-chain Si atoms in this low load system is shown to steadily increase over the course of the simulation, as free-chains are removed from the monolayers and migrate toward the interface of contact. Mobility is significantly reduced under normal loads of 1.0 GPa and above, where less than 10% of free-chains are removed from the monolayers, suggesting that for monolayers bound in an ideal arrangement to a flat, crystalline substrate, the propensity for degradation is reduced under higher normal loads. This result indicates that wear and friction are not reciprocal, as friction force is known to increase with normal force for shear of alkylsilane monolayers.[13]

It is likely that the observed load-dependent stability is influenced by increased orientational ordering of chains as load is increased. Fig. 3.2a shows the nematic order of monolayers across the normal load range, and while order is shown to be quite high ($>$0.94) at all normal loads, a transition to a more ordered structure seems to occur as load is increased from 0.5 GPa to 1.0 GPa. Liquid-to-solid structural transitions are known to occur for confined alkanes[46–48], and similar behavior has also been reported for alkane monolayers on crystalline substrates[49,50], comparable to those in this study. Thus, a pressure-induced ordering of monolayer chains may be providing additional stabilization to these systems, helping to prevent the removal of unbound chains. A visual representation of this phenomenon is provided in Figs. 3.2c-d, where monolayers under a load of 0.5 GPa appear to feature reduced order compared to those under a higher normal load of 2.5 GPa, and several free-chains are shown to have escaped from the surface. Another possibility for the observations of reduced free-chain mobility at high normal loads is the effect of reduced volume between surfaces as separation is decreased, leaving less available volume for free-chains to explore, and essentially forcing their confinement within the monolayers. However, the high order present in these films induces a large elastic modulus, such that only a small decrease in separation is necessary to impart a large increase in normal load. As a result,

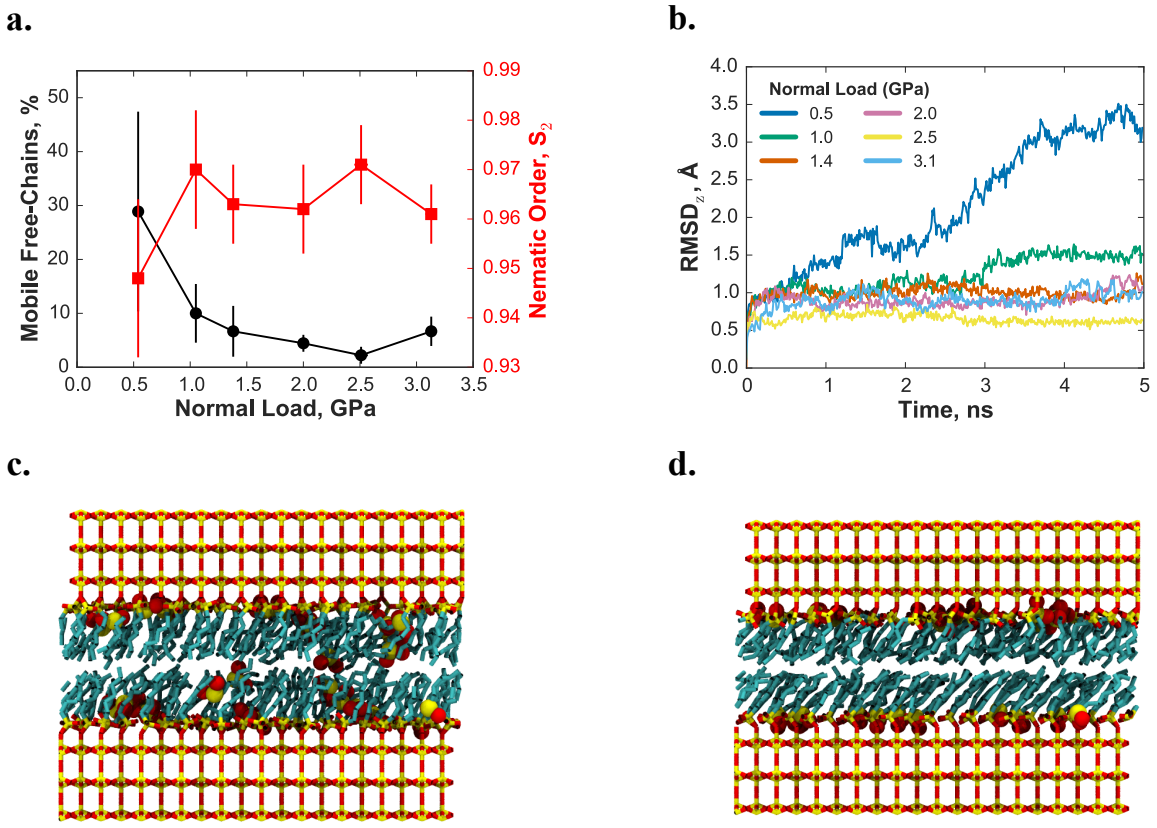

Figure 3.2: a. The percentage of mobile free-chains (black circles) and global nematic order (red squares) for C6 monolayers on crystalline silica sheared at 10 m/s. Error bars indicate one standard deviation. Error in normal force is not shown as it is smaller than plot symbols. b. The average RMSD of free-chain Si atoms (in the z dimension only). c and d. Snapshots of the defected monolayers under normal loads of 0.5 GPa and 2.5 GPa, respectively, revealing stability achieved through pressure-induced order. For clarity, hydrogens have been removed and the silane group atoms of each free-chain are rendered as VDW spheres.

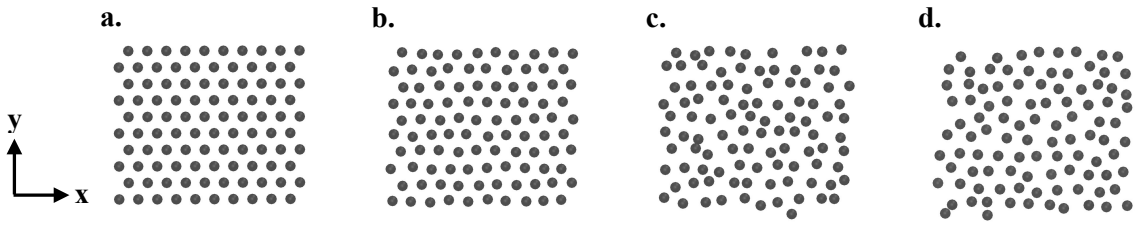

Figure 3.3: Chain attachment site arrangements, in the *xy* plane, on a. crystalline, beta-cristobalite silica (ψ_6 = 1), b and c. crystalline silica with induced hexagonal disorder (b. ψ_6 = 0.9, c. ψ_6 = 0.5), and d. amorphous silica with an RMS surface roughness of 1.2Å (ψ_6 = 0.5)

the reduction in total inter-surface volume is quite small as normal load is increased (ΔV = 5%, 0.5 GPa $\rightarrow$ 1.0 GPa), and its influence on free-chain mobility is likely secondary to that imparted by the increase in orientational order.

One primary difference between amorphous silica surfaces in MEMS/NEMS devices and the ideal, crystalline substrate model often used in simulation studies is the in-plane arrangement of chain attachment sites. While crystalline models place chains in a perfect hexagonal arrangement, chain arrangement on amorphous silica surfaces typically used will likely feature disorder as a result of surface non-idealities such as roughness. To understand the relationship between the in-plane arrangement of chains and monolayer stability, crystalline substrates with reduced attachment site in-plane order have also been considered, with hexagonal orders of 0.9, 0.8, and 0.5, the latter value corresponding to the hexagonal order of amorphous surfaces considered later in this work. Visual representations of chain attachment site arrangements in these systems are provided in Fig. 3.3, where we note that surfaces are still atomistically smooth. Results of the percentage of mobile free-chains as a function of hexagonal order under normal loads of 2.4 ± 0.1 GPa and 0.46 ± 0.05 GPa are displayed in Fig. 3.4a. The RMSD of free-chain Si atoms at both 2.4 GPa (Fig. 3.4b) and 0.46 GPa (Fig. 3.4c) is also provided. At 0.46 GPa, there appears to be a slight trend above ψ_6 = 0.8 where increased hexagonal order correlates with a reduced number of mobile free-chains. The RMSD for this system similarly reveals reduced mobility for $\psi_6 > 0.8$. However, the high variability in mobile free-chain percentage (which appears

to be a consequence of the randomness in free-chain contacts, where mobile chains may induce further mobility in some systems) makes this a relatively weak conclusion. Trends become better illustrated under a higher normal load of 2.4 GPa. Again, high variability in the percentage of mobile free-chains is observed for systems featuring low hexagonal order, however, there is a dramatic increase in mobility as hexagonal order is reduced from 1.0 to 0.9. The RMSD at 2.4 GPa likewise reveals a steady increase for systems with a hexagonal order below 1.0, but relatively little mobility for the ideal system. These trends correspond with values obtained for the nematic order of these systems, shown in Fig. 3.4d, where a substantial reduction in nematic order is found as attachment site hexagonal order decreases from 1.0 to 0.9, again suggesting that orientational monolayer order is a critical factor influencing monolayer stability. Furthermore, Fig. 3.4d shows that pressure-induced order is not present in any of the systems where attachment site hexagonal order has been reduced from the ideal configuration. For these systems, S_2 at 2.4 GPa is reduced by roughly 0.01-0.03 compared to values at 0.46 GPa, whereas for the ideal system S_2 increases by 0.02. These results indicate that only in the presence of a perfect hexagonal chain arrangement will monolayers display enhanced ordering at high normal loads and that even a slight deviation from this configuration will lead to the opposite behavior and significant monolayer instability. This is exemplified by the high number of mobile free-chains observed for systems in which hexagonal disorder has been induced. It should also be noted that while values of S_2 are higher at lower normal loads for systems featuring disordered attachment sites, the percentage of mobile free-chains remains comparable at both normal loads. This likely results from the low magnitude of nematic order for these systems, even at low normal loads, where the highest value of S_2 is 0.86 (for the system with ψ_6 = 0.9 at 0.46 GPa), compared to the values of $S_2 > 0.94$ for ideal, crystalline systems. It appears that at these low values of S_2, the cohesiveness of the monolayer is sufficiently broken to the point that many free-chains are unable to remain intercalated and are removed from monolayers during shear. As such, it appears that the ability for disorder

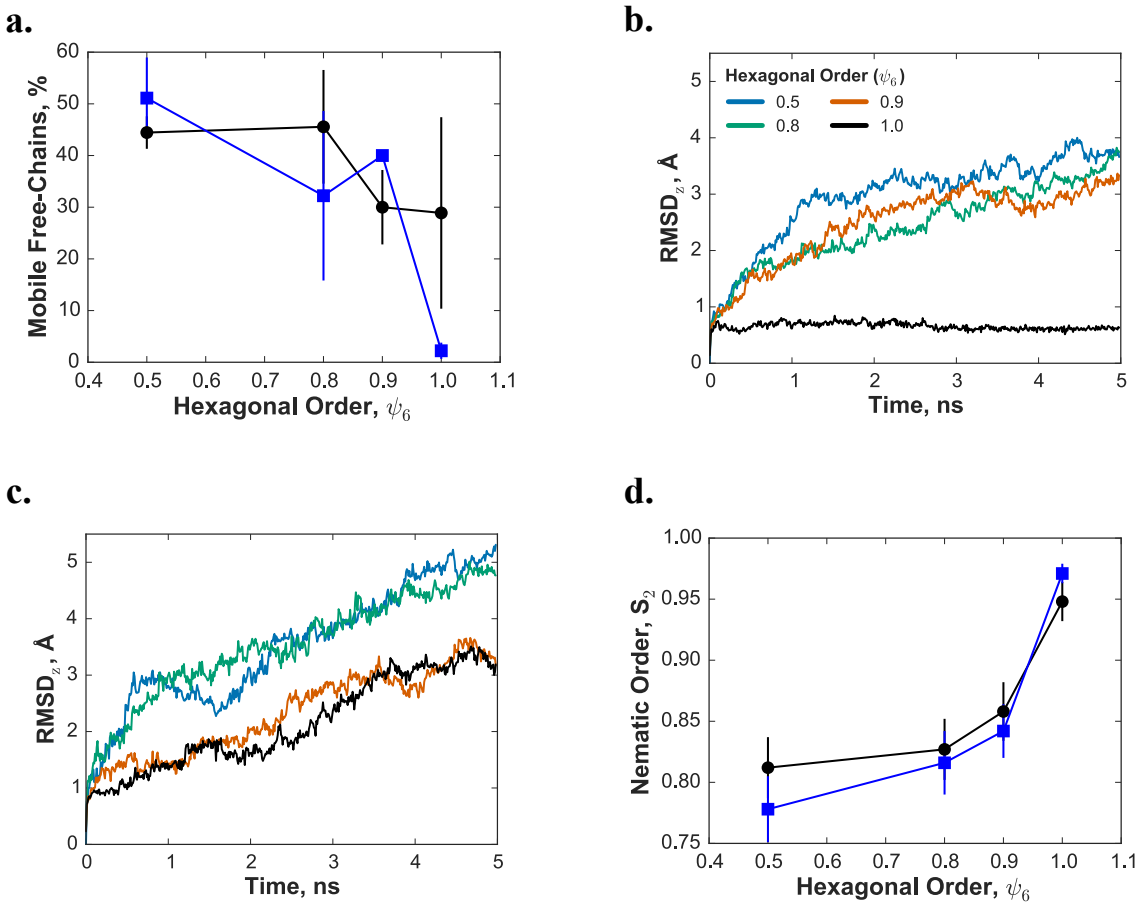

Figure 3.4: a. Effects of attachment site hexagonal order on the percentage of mobile free-chains for C6 monolayers on crystalline silica under normal loads of 2.4 $\pm$ 0.1 GPa (blue squares) and 0.46 $\pm$ 0.05 GPa (black circles). b. and c. Average RMSD trajectories for free-chain Si atoms (in the z dimension only) at b. 2.4 GPa and c. 0.46 GPa. d. The nematic order for each system as a function of hexagonal order. Error bars indicate one standard deviation.

in attachment site locations to facilitate reduced orientational ordering of monolayer chains will lead to enhanced film degradation.

In a prior simulation study, Black et al. generated rough silica surfaces meant to mimic experimental systems that feature an atomic-scale roughness of 1.3Å .[20] In subsequent analysis of alkylsilane monolayers bound to these amorphous silica surfaces under shear, they found that the presence of surface roughness acted as the primary factor leading to increased frictional forces and reduced global nematic order of monolayer coatings,

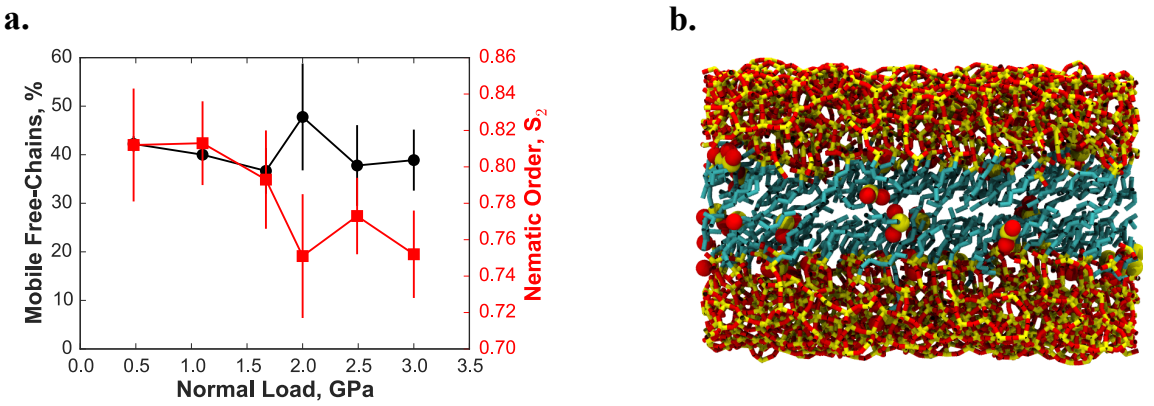

Figure 3.5: a. Free-chain mobility (black circles) and global nematic order (red squares) for C6 monolayers on amorphous silica with an RMS roughness of 1.2Å , sheared at 10m/s. Error bars indicate one standard deviation. b. Snapshot of the defected monolayer under a normal load of 2.5GPa. For clarity, hydrogens have been removed and only atoms of the silane group of each free-chain are rendered as VDW spheres.

suggesting that roughness likely accelerates the wear of monolayer films. To investigate the influence of surface roughness on monolayer degradation, monolayers bound to rough, amorphous surfaces have also been considered. Normal load influence on monolayer stability is examined for monolayers on a surface featuring an RMS roughness of 1.2Å . Results of free-chain mobility and nematic order during shear are shown in Fig. 3.5a. In contrast to what was observed for ideal, crystalline systems over a comparable normal load range, degradation of C6 monolayers bound to the rough, amorphous substrate does not feature a normal load dependence. Monolayers appear to be at a high likelihood for degradation at all normal loads, with roughly 40% of free-chains removed from monolayers during shear. This behavior is similar to that observed for crystalline systems with disordered attachment site arrangements. A comparison between these two systems, as well as with the ideal, crystalline system, is shown in Table 3.1. For the rough, amorphous system, as with the disordered, crystalline system, nematic order is reduced as normal load is increased. Fig. 3.5a shows this in further detail, where a transition appears to take place between 1 and 2 GPa. In both systems, surface non-ideality prevents regular chain spacing, causing monolayers to no longer deform with a uniform tilt under higher normal loads, leading

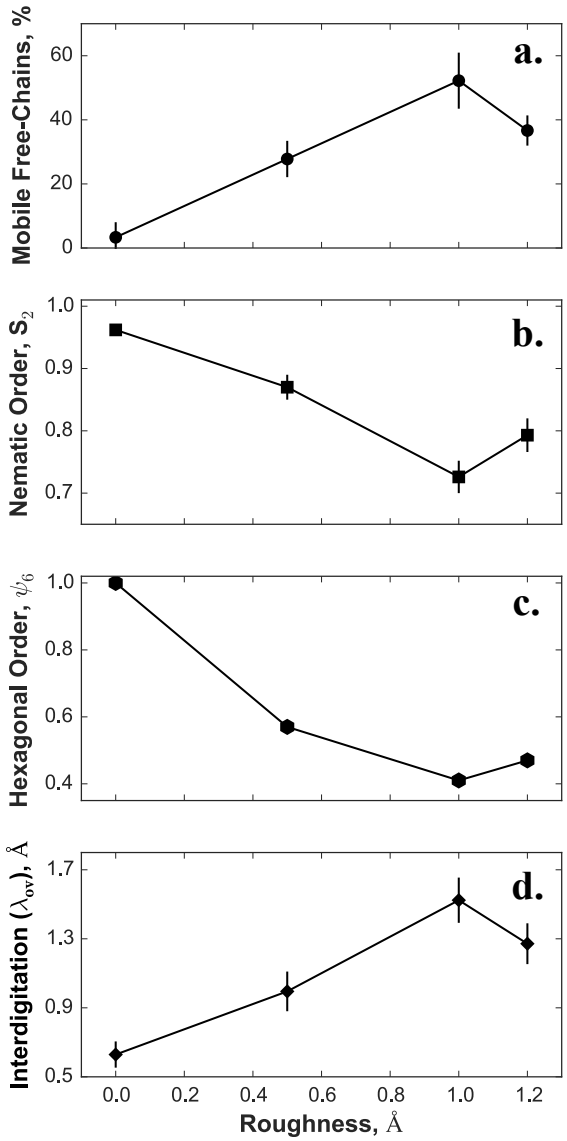

Figure 3.6: Effects of surface roughness on a. free-chain mobility, b. global nematic order, c. attachment site hexagonal order, and d. interdigitation for C6 monolayers sheared at 10m/s under a normal load of 1.71 $\pm$ 0.05 GPa. Error bars indicate one standard deviation.

to more disordered conformations. The similarity between the amorphous and disordered crystalline systems - both exhibiting significant degradation - suggests that the hexagonal arrangement of chains on the surface, as opposed to surface roughness, may act as the primary factor influencing degradation of monolayers.

To further examine the influence of surface roughness on monolayer degradation, two additional amorphous surfaces, featuring RMS roughness values of 0.5Å and 1.0Å were

Table 3.1: Mobility and nematic order of monolayers on surfaces of different morphologies

Surface	Surface Roughness, Å	Attachment Site Hexagonal Order, ϕ_6	0.5 GPa		2.5 GPa	
			Mobile Free-Chains, %	Nematic Order, S_2	Mobile Free-Chains, %	Nematic Order, S_2
Ideal, Crystalline	0.0	1.0	28.9 ± 18.5	0.948 ± 0.016	2.2 ± 1.6	0.971 ± 0.008
Disordered, Crystalline	0.0	0.5	44.5 ± 3.2	0.812 ± 0.025	51.1 ± 7.9	0.778 ± 0.027
Rough, Amorphous	1.2	0.47	42.2 ± 1.6	0.812 ± 0.031	37.8 ± 8.3	0.773 ± 0.021

considered. The free-chain mobility for monolayers bound to each amorphous surface under a normal load of 1.71 ± 0.05 GPa is shown in Fig. 3.6a, with the ideal, crystalline system included as a reference. For all amorphous-bound monolayers, increased free-chain mobility is observed compared to values for monolayers bound to the smooth crystalline surface. Interestingly, however, greater free-chain mobility is observed for the surface featuring an RMS roughness of 1.0Å than is observed for the rougher, 1.2Å , surface. This behavior can again be explained by examining monolayer orientational order and chain arrangement on the surface. Figs. 3.6b and 3.6c display the nematic order and attachment site hexagonal order, respectively, for monolayers on each substrate. Trends in nematic order closely follow those in attachment site hexagonal order, further supporting the strong influence of the in-plane ordering of chains on monolayer cohesivity. Furthermore, both nematic order and hexagonal order follow the inverse of trends in free-chain mobility, again suggesting that rather than surface roughness directly leading to degradation of monolayers, it is the non-ideality in chain spacing, which arises in non-flat surfaces that plays the larger role. As such, a disordered monolayer on a smoother surface will likely feature a re-

duced lifetime compared to a more ordered monolayer on a rougher surface, in the absence of surface-surface contact. This result is reasonable as reduced orientational order is indicative of a disrupted dispersion network within a monolayer, which likely causes monolayers to become highly unstable during shear. The result also agrees with simulations in the literature, where trends between monolayer disorder and friction have been observed.[20,26,27,51] In one such study, Karuppiah et al. showed that the order of alkanethiol monolayers with carboxylic acid headgroups could be tuned by applying a surface voltage.[51] Ordered configurations were found to feature reduced friction, as compared to disordered configurations where exposed chain backbones increased interaction with the countersurface. In another study, Black et al. showed that monolayers on non-ideal, amorphous surfaces featured reduced nematic order compared to those on an ideal, crystalline surface, which resulted in greater frictional forces.[20] Mikulski and coworkers performed simulations of alkane monolayers which showed that at high normal loads, monolayers featuring a 20% lower chain density on a crystalline substrate featured greater disorder, yielding an increase in friction coefficient.[26] Similar observations were made in work by Chandross et al., where greater disorder of alkylsilane monolayers from reduced monolayer density was associated with increased friction.[27] From the results presented herein, it appears that while surface roughness may promote monolayer wear, its effects appear to stem primarily from contributing to greater disorder within the monolayers, achieved through non-ideality of the in-plane arrangement of monolayer chains.

The impact of substrate non-ideality on monolayer stability under shear has been further explored by examining the extent of interdigitation of chains between opposing monolayers during shear. These values, obtained prior to inducing defects, are provided in Fig. 3.6d. Trends in interdigitation are found to closely follow the trends observed for free-chain mobility, and follow the inverse of trends observed for nematic order and attachment site hexagonal order. This suggests that interdigitation is influenced by the extent of a monolayer's orientational order and may play a key role in the degradation process. In-

creased disorder within monolayers appears to allow for greater interdigitation, which in turn may be the cause for higher free-chain mobility under these conditions. Likewise when monolayers are more highly ordered, the more crystalline-like structure helps to prevent interdigitation and free-chain mobility is reduced. The conclusion that interdigitation between monolayers may promote degradation is reasonable, as this will lead to increased chain-chain interactions and provide greater strain on the Si-O attachment bonds. Thus, conditions that facilitate greater interdigitation, such as a low monolayer orientational order, appear likely to result in a higher propensity for degradation.

It is noted as a reminder that in this study, only angstrom-scale roughness, representative of that induced by piranha treatment during substrate preparation, is considered. Silica surfaces in a MEMS device and those studied by experiment are known to feature roughness over several length scales, introducing additional degradation pathways. As an example, work by Chandross et al. and Cheng et al. has shown a plowing-like mechanism of degradation for shear of asperity-like nanoscale tips with monolayer films.[24,52] These mechanisms are not present in this chapter, as the objective is to isolate the influence of substrate non-ideality at the atomic scale; however, an examination of plowing-like mechanisms of friction at asperities can be found in Chapter 4.

Although surface roughness has been shown to only secondarily influence degradation propensity, with the in-plane arrangement of chains being of greater significance, surface roughness may still have a direct influence on the locations where chains are removed during shear. To probe this relationship between surface roughness and chain removal three arrangements of defect locations have been considered on a rough (RMS roughness = 1.2Å), amorphous surface and a new parameter defined, Δz, which represents the deviation (in the z dimension) of an individual chain attachment site location from the mean z value of all surface sites. Deviations toward the interface between the two monolayers are considered as positive and those deeper within the silica substrate are considered to be negative. In the first arrangement (Fig. 3.7a) the 15 chains with Δz values closest

to zero have been broken from each surface, yielding a mean Δz value of 0.05Å . For the second and third arrangements, the 15 chains with the highest (Fig. 3.7b) and lowest (Fig. 3.7c) Δz values are broken from each surface, yielding mean Δz values of 1.63Å and -1.96Å respectively. The evolution of free-chain mobility for each defect arrangement is shown in Fig. 3.7d as the RMSD of free-chain Si atoms over the course of 5 ns of shearing. Rapid removal of chains is observed for the arrangement where defects are induced at locations closest to the monolayer-monolayer interface, corresponding to a steady increase in the RMSD. Conversely, for the arrangement where defects are induced deepest within each

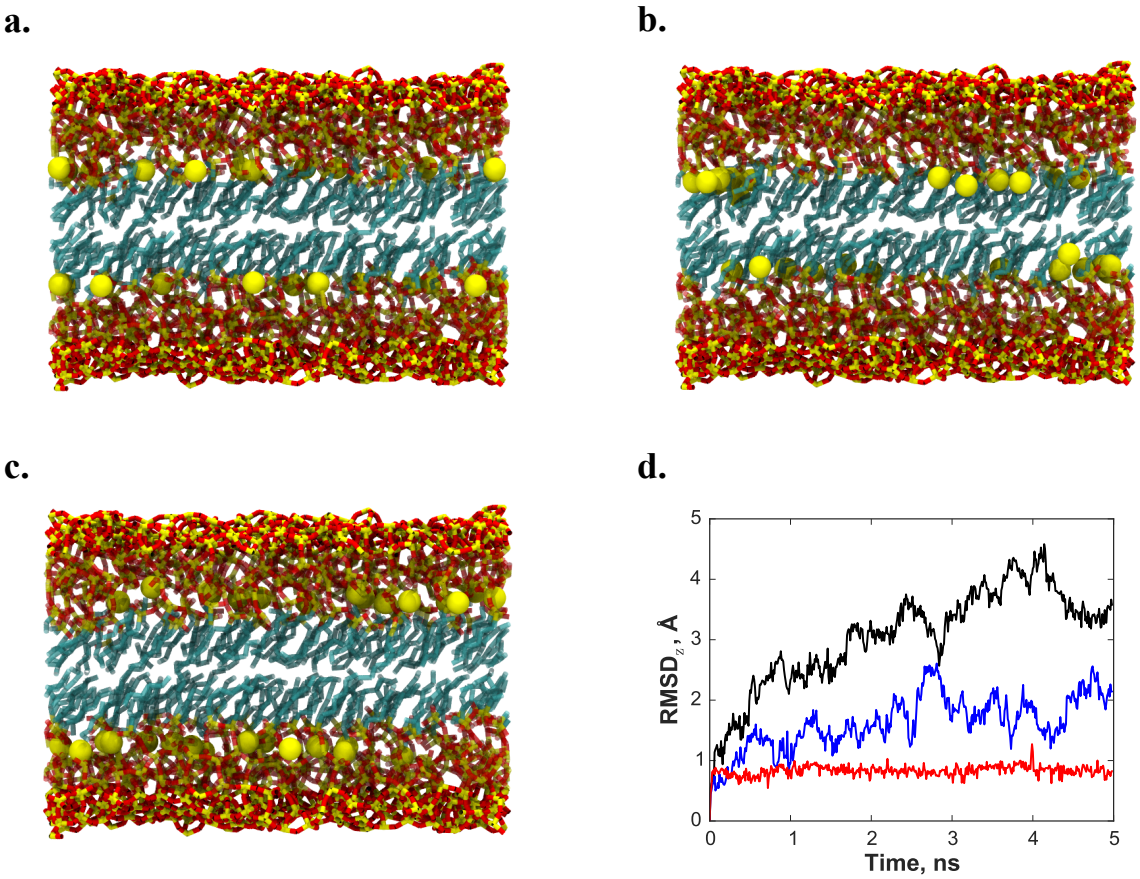

Figure 3.7: Surface locations of defect chains featuring an average Δz of a. 0.05Å , b. 1.63Å , and c. -1.96Å . Yellow spheres are used to represent the Si atom of the silane group on free-chains. d. RMSD of free-chain Si atoms (in the z dimension only) over the course of a 5ns shear run at 10m/s for each system. Average Δz = 0.05Å : blue, 1.63Å : black, -1.96Å : red

surface, no free-chains leave the monolayers during the entirety of the simulation and the RMSD remains level. For the arrangement where defects are induced closest to the surface mean, intermediate behavior is found, with slight free-chain mobility apparent from the RMSD. From these results, it appears that chains located closest to the contact interface are most likely to be removed from monolayers during shear, suggesting that while the extent of monolayer degradation is most likely to be controlled by the in-plane arrangement of monolayer chains, the locations within a monolayer where wear first occurs are likely to be influenced by the surface profile. This result highlights the importance of surface roughness, and models that include it, in capturing wear behavior and suggests that wear initiation at asperities or "peaks" on the surface will occur even with only an atomic-scale roughness and in the absence of surface- surface contact.

Experimentally, monolayers consisting of longer chains have been linked to reduced friction and increased lifetimes under shear.[4,34] As such, the introduction of defects through Si-O bond removal in systems of monolayers with longer chain lengths is expected to yield a reduction in free-chain mobility, which would support greater monolayer stability. Monolayers of C10 (decylsilane) and C12 (dodecylsilane) chains bound to an amorphous surface (RMS roughness = 1.2Å) are therefore now considered. Results of the percentage of mobile free-chains in these systems as a function of normal load are shown in Fig. 3.8a, including results for the C6 system as a reference. Agreeing with expectations, a reduction in the number of free-chains removed from monolayers during shear is observed as chain length is increased, corresponding to an increase in the monolayer's resistance to degradation. Similarly the RMSD of free-chain Si atoms (Fig. 3.8b) is found to decrease for monolayers of longer alkane chains. Interestingly, for C10 and C12 monolayers, the percentage of mobile free-chains appears to exhibit a normal load dependence, unlike observations for C6 monolayers, which were shown to exhibit similar degradation behavior across all normal loads. At 0.5 GPa, free-chains of C10 and C12 remain primarily intercalated within monolayers and degradation of monolayers is minimal. As normal load

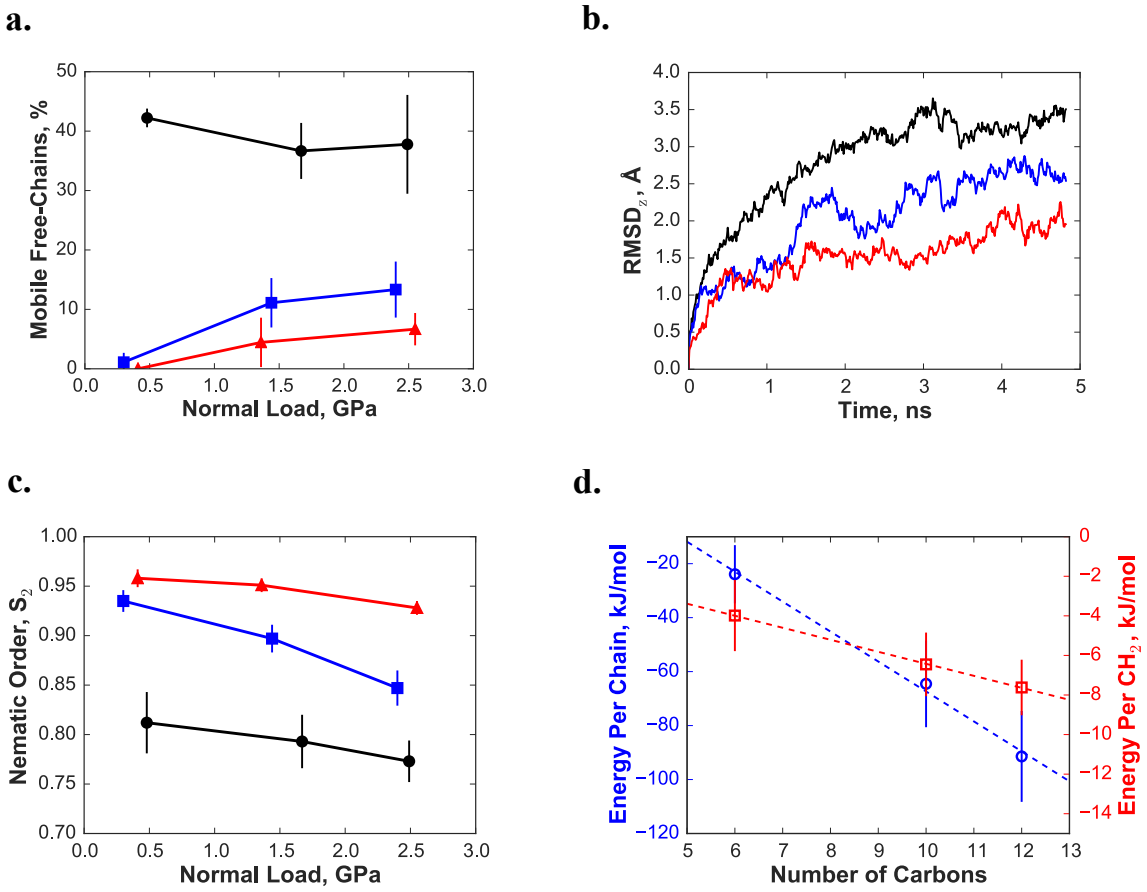

Figure 3.8: a. Percentage of mobile free-chains, b. RMSD of free-chain Si atoms (in the z dimension) at a normal load of 2.48 $\pm$ 0.06GPa, and c. global nematic order of C6 (black circles), C10 (blue squares), and C12 (red triangles) monolayers as a function of normal load, d. Energy per chain (open blue circles) and per CH_2 (open red squares) for each system under a normal load of 2.48 $\pm$ 0.06GPa. Dashed lines indicate linear fits, and solid lines are provided to guide the eye only. Error bars indicate one standard deviation.

is increased, however, the mobility of free-chains is enhanced, although even at roughly 2.5 GPa monolayers remain significantly more stable than those of the C6 system. This behavior is likely to be influenced, in part, by reduced monolayer order as normal load is increased, shown in Fig. 3.8c. Although values of S_2 remain in the crystalline regime across all normal loads for both C10 and C12 systems, a noticeable decrease is apparent for C10 systems and a slight decrease is present for C12 systems, signifying destabilization of monolayer structure and facilitating an increase in free-chain mobility. While also featuring a negative correlation with normal load, the magnitude of nematic order for C6 monolayers

remains sufficiently low that mobility behavior is unchanged across all loads examined. The normal load trend observed for C10 and C12 systems corresponds to experimental reports of C8 and C18 monolayers under shear, where rapid monolayer removal was detected under high normal loads[53,54], and suggests that although increased chain length appears to promote monolayer stability, overcoming the influence of surface non-ideality, long-chain monolayers can still become destabilized under a sufficient pressure.

Booth et al. showed in simulations of monolayers on a crystalline surface that the stabilization achieved through increasing chain length bolsters the dispersion network within the monolayer, with longer-chain monolayers shown to yield a reduction in both energy per chain and per CH_2 group.[4] A similar analysis is performed in this work for monolayers bound to the more realistic, amorphous silica surface, and the energetic contribution per chain and per CH_2 group to the overall energy of the monolayer as a function of chain length is shown in Fig. 3.8d. These values were obtained by isolating the alkane portion of the bottom monolayer following 1 ns of shearing and calculating the difference in non-bonded energy following removal of a single chain, averaging over all possible removal locations. In agreement with the results of Booth et al., as chain length increases, the magnitude of the energy contribution per chain to the overall monolayer energy is shown to increase, signaling a more favorable dispersion network. Furthermore, the magnitude of the energy contribution per methylene group is also shown to increase with increasing chain length, again agreeing with results of Booth et al., and likely a result of the increased tilt and order in monolayers consisting of longer chains. It can thus be concluded that as the length of the monolayer chains is increased, interactions with neighboring chains become more favorable and monolayers become increasingly ordered, such that even in the presence of surface roughness (in this instance, 1.2Å) monolayers of sufficient length are able to resist degradation below a certain normal load threshold.

3.4 Conclusions

The influence of surface morphology on the wear of alkylsilane monolayers is quantified through molecular dynamics simulations using a bond removal approach. Monolayers on atomically flat substrates are observed to feature pressure-induced orientational ordering, which facilitates stability as normal load is increased. This behavior is shown to result from the ideal, hexagonal arrangement of attachment sites on the crystalline surface. Even slight deviations from this ideal chain arrangement result in severely unstable structures, suggesting that the in-plane arrangement of monolayer chains plays a critical role in the susceptibility of a monolayer to wear. Similar instability is found for monolayers bound to amorphous substrates, featuring both reduced attachment site hexagonal order and an atomic-scale roughness. Free-chain mobility, and thus degradation propensity, in these amorphous systems is found to be independent of normal load from 0.5-3.1 GPa (for C6 chains), but follows the inverse of trends in nematic order and attachment site hexagonal order when comparing monolayers attached to substrates with different values of surface roughness. Amorphous surfaces are also shown to feature increased interdigitation, suggesting the mechanism through which the in-plane arrangement of monolayer chains controls monolayer wear is through facilitating increased chain-chain contact between monolayers. The role of surface roughness in the wear process appears primarily in controlling the locations where wear occurs, with rougher surfaces more likely to feature wear at locations farthest from the surface mean, toward the interface of contact between monolayers. Increasing monolayer chain length reduces the influence of substrate non-ideality on degradation behavior, with C10 and C12 monolayers featuring considerably greater stability than C6 monolayers, through an increased dispersion network.

3.5 Bibliography

[1] Summers, A. Z.; Iacovella, C. R.; Billingsley, M. R.; Arnold, S. T.; Cummings, P. T.; McCabe, C. Influence of Surface Morphology on the Shear-Induced Wear of Alkylsilane Monolayers: Molecular Dynamics Study. *Langmuir* **2016**, *32*, 2348–2359.

[2] Åström, R.; Mutikainen, R.; Kuisma, H.; Hakola, A.-H. Effect of alkylsilane coating on sliding wear of silica–silicon contacts with small amplitude motion. *Wear* **2002**, *253*, 739–745.

[3] Kim, S. H.; Asay, D. B.; Dugger, M. T. Nanotribology and MEMS. *Nano Today* **2007**, *2*, 22–29.

[4] Booth, B. D.; Vilt, S. G.; Lewis, J. B.; Rivera, J. L.; Buehler, E. A.; McCabe, C.; Jennings, G. K. Tribological Durability of Silane Monolayers on Silicon. *Langmuir* **2011**, *27*, 5909–5917.

[5] Hook, D. A.; Timpe, S. J.; Dugger, M. T.; Krim, J. Tribological degradation of fluorocarbon coated silicon microdevice surfaces in normal and sliding contact. *Journal of Applied Physics* **2008**, *104*, 034303.

[6] Bhushan, B. Nanotribology and nanomechanics of MEMS/NEMS and BioMEMS/BioNEMS materials and devices. *Microelectronic Engineering* **2007**, *84*, 387–412.

[7] Bhushan, B.; Kasai, T.; Kulik, G.; Barbieri, L.; Hoffmann, P. AFM study of perfluoroalkylsilane and alkylsilane self-assembled monolayers for anti-stiction in MEMS/NEMS. *Ultramicroscopy* **2005**, *105*, 176–188.

[8] Lio, A.; Morant, C.; Ogletree, D. F.; Salmeron, M. Atomic Force Microscopy Study of the Pressure-Dependent Structural and Frictional Properties ofn-Alkanethiols on Gold. *The Journal of Physical Chemistry B* **1997**, *101*, 4767–4773.

[9] Booth, B. D.; Vilt, S. G.; McCabe, C.; Jennings, G. K. Tribology of Monolayer Films: Comparison between n-Alkanethiols on Gold and n-Alkyl Trichlorosilanes on Silicon. *Langmuir* **2009**, *25*, 9995–10001.

[10] Pujari, S. P.; Zuilhof, H. Highly wear-resistant ultra-thin per-fluorinated organic monolayers on silicon(111) surfaces. *Applied Surface Science* **2013**, *287*, 159–164.

[11] Park, B.; Lorenz, C. D.; Chandross, M.; Stevens, M. J.; Grest, G. S.; Borodin, O. A. Frictional Dynamics of Fluorine-Terminated Alkanethiol Self-Assembled Monolayers. *Langmuir* **2004**, *20*, 10007–10014.

[12] Rivera, J. L.; Jennings, G. K.; McCabe, C. Examining the frictional forces between mixed hydrophobic – hydrophilic alkylsilane monolayers. *The Journal of Chemical Physics* **2012**, *136*, 244701.

[13] Lewis, J. B.; Vilt, S. G.; Rivera, J. L.; Jennings, G. K.; McCabe, C. Frictional Properties of Mixed Fluorocarbon/Hydrocarbon Silane Monolayers: A Simulation Study. *Langmuir* **2012**, *28*, 14218–14226.

[14] Lorenz, C. D.; Chandross, M.; Grest, G. S.; Stevens, M. J.; Webb, E. B. Tribological Properties of Alkylsilane Self-Assembled Monolayers. *Langmuir* **2005**, *21*, 11744–11748.

[15] Chandross, M.; Grest, G. S.; Stevens, M. J. Friction between Alkylsilane Monolayers: Molecular Simulation of Ordered Monolayers. *Langmuir* **2002**, *18*, 8392–8399.

[16] Merlijn van Spengen, W. MEMS reliability from a failure mechanisms perspective. *Microelectronics Reliability* **2003**, *43*, 1049–1060.

[17] Romig, A.; Dugger, M. T.; McWhorter, P. J. Materials issues in microelectromechanical devices: science, engineering, manufacturability and reliability. *Acta Materialia* **2003**, *51*, 5837–5866.

[18] de Boer, M. P.; Knapp, J. A.; Mayer, T. M.; Michalske, T. A. Role of interfacial properties on MEMS performance and reliability. *Microsystems Metrology and Inspection* **1999**, 2–15.

[19] Hu, X.; Martini, A. Atomistic simulation of the effect of roughness on nanoscale wear. *Computational Materials Science* **2015**, *102*, 208–212.

[20] Black, J. E.; Iacovella, C. R.; Cummings, P. T.; McCabe, C. Molecular Dynamics Study of Alkylsilane Monolayers on Realistic Amorphous Silica Surfaces. *Langmuir* **2015**, *31*, 3086–3093.

[21] van Duin, A. C. T.; Dasgupta, S.; Lorant, F.; Goddard, W. A. ReaxFF: A Reactive Force Field for Hydrocarbons. *The Journal of Physical Chemistry A* **2001**, *105*, 9396–9409.

[22] Chandross, M.; Lorenz, C. D.; Stevens, M. J.; Grest, G. S. Probe-Tip Induced Damage in Compliant Substrates. *Journal of Manufacturing Science and Engineering* **2010**, *132*, 030916.

[23] Lane, J. M. D.; Chandross, M.; Lorenz, C. D.; Stevens, M. J.; Grest, G. S. Water Penetration of Damaged Self-Assembled Monolayers. *Langmuir* **2008**, *24*, 5734–5739.

[24] Chandross, M.; Lorenz, C. D.; Stevens, M. J.; Grest, G. S. Simulations of Nanotribology with Realistic Probe Tip Models. *Langmuir* **2008**, *24*, 1240–1246.

[25] Baker, M. A.; Li, J. The influence of an OTS self-assembled monolayer on the wear-resistant properties of polysilicon based MEMS. *Surface and Interface Analysis* **2006**, *38*, 863–867.

[26] Mikulski, P. T.; Harrison, J. A. Packing-Density Effects on the Friction ofn-Alkane Monolayers. *Journal of the American Chemical Society* **2001**, *123*, 6873–6881.

[27] Chandross, M.; Webb, E. B.; Stevens, M. J.; Grest, G. S.; Garofalini, S. H. Systematic Study of the Effect of Disorder on Nanotribology of Self-Assembled Monolayers. *Physical Review Letters* **2004**, *93*.

[28] Onclin, S.; Ravoo, B. J.; Reinhoudt, D. N. Engineering Silicon Oxide Surfaces Using Self-Assembled Monolayers. *Angewandte Chemie International Edition* **2005**, *44*, 6282–6304.

[29] Stevens, M. J. Thoughts on the Structure of Alkylsilane Monolayers. *Langmuir* **1999**, *15*, 2773–2778.

[30] Ulman, A. Formation and Structure of Self-Assembled Monolayers. *Chemical Reviews* **1996**, *96*, 1533–1554.

[31] Kessel, C. R.; Granick, S. Formation and characterization of a highly ordered and well-anchored alkylsilane monolayer on mica by self-assembly. *Langmuir* **1991**, *7*, 532–538.

[32] Kim, H. I.; Boiadjiev, V.; Houston, J.; Zhu, X.-Y.; Kiely, J. *Tribology Letters* **2001**, *10*, 97–101.

[33] Liu, H.; Bhushan, B.; Eck, W.; Stadler, V. Investigation of the adhesion, friction, and wear properties of biphenyl thiol self-assembled monolayers by atomic force microscopy. *Journal of Vacuum Science & Technology A: Vacuum, Surfaces, and Films* **2001**, *19*, 1234–1240.

[34] Ruehe, J.; Novotny, V. J.; Kanazawa, K. K.; Clarke, T.; Street, G. B. Structure and tribological properties of ultrathin alkylsilane films chemisorbed to solid surfaces. *Langmuir* **1993**, *9*, 2383–2388.

[35] Tian, F.; Xiao, X.; Loy, M. M. T.; Wang, C.; Bai, C. Humidity and Temperature Effect on Frictional Properties of Mica and Alkylsilane Monolayer Self-Assembled on Mica. *Langmuir* **1999**, *15*, 244–249.

[36] Kojio, K.; Ge, S.; Takahara, A.; Kajiyama, T. Molecular Aggregation State of n-Octadecyltrichlorosilane Monolayer Prepared at an Air/Water Interface. *Langmuir* **1998**, *14*, 971–974.

[37] Jorgensen, W. L.; Maxwell, D. S.; Tirado-Rives, J. Development and Testing of the OPLS All-Atom Force Field on Conformational Energetics and Properties of Organic Liquids. *Journal of the American Chemical Society* **1996**, *118*, 11225–11236.

[38] Lorenz, C.; Webb, E.; Stevens, M.; Chandross, M.; Grest, G. Frictional dynamics of perfluorinated self-assembled monolayers on amorphous SiO2. *Tribology Letters* **2005**, *19*, 93–98.

[39] LAMMPS web page:. http://lammps.sandia.gov.

[40] Plimpton, S. Fast Parallel Algorithms for Short-Range Molecular Dynamics. *Journal of Computational Physics* **1995**, *117*, 1–19.

[41] Nose, S. A unified formulation of the constant temperature molecular dynamics methods. *The Journal of Chemical Physics* **1984**, *81*, 511–519.

[42] Hoover, W. G. Canonical dynamics: Equilibrium phase-space distributions. *Physical Review A* **1985**, *31*, 1695–1697.

[43] Yeh, I.-C.; Berkowitz, M. L. Ewald summation for systems with slab geometry. *The Journal of Chemical Physics* **1999**, *111*, 3155–3162.

[44] Tuckerman, M.; Berne, B. J.; Martyna, G. J. Reversible multiple time scale molecular dynamics. *The Journal of Chemical Physics* **1992**, *97*, 1990–2001.

[45] Mate, C. M.; Marchon, B.; Murthy, A. N.; Kim, S.-H. Lubricant-Induced Spacing Increases at Slider–Disk Interfaces in Disk Drives. *Tribology Letters* **2009**, *37*, 581–590.

[46] Klein, J.; Kumacheva, E. Confinement-Induced Phase Transitions in Simple Liquids. *Science* **1995**, *269*, 816–819.

[47] Klein, J.; Kumacheva, E. Simple liquids confined to molecularly thin layers. I. Confinement-induced liquid-to-solid phase transitions. *The Journal of Chemical Physics* **1998**, *108*, 6996–7009.

[48] Cui, S. T.; Cummings, P. T.; Cochran, H. D. Molecular simulation of the transition from liquidlike to solidlike behavior in complex fluids confined to nanoscale gaps. *The Journal of Chemical Physics* **2001**, *114*, 7189–7195.

[49] Yoshizawa, H.; You-Lung, C.; Israelachvili, J. Recent advances in molecular level understanding of adhesion, friction and lubrication. *Wear* **1993**, *168*, 161–166.

[50] Yoshizawa, H.; McGuiggan, P.; Israelachvili, J. Identification of a Second Dynamic State During Stick-Slip Motion. *Science* **1993**, *259*, 1305–1308.

[51] Karuppiah, K. S. K.; Zhou, Y.; Woo, L. K.; Sundararajan, S. Nanoscale Friction Switches: Friction Modulation of Monomolecular Assemblies Using External Electric Fields. *Langmuir* **2009**, *25*, 12114–12119.

[52] Cheng, S.; Luan, B.; Robbins, M. O. Contact and friction of nanoasperities: Effects of adsorbed monolayers. *Physical Review E* **2010**, *81*.

[53] Kasai, T.; Bhushan, B.; Kulik, G.; Barbieri, L.; Hoffmann, P. Micro/nanotribological study of perfluorosilane SAMs for antistiction and low wear. *Journal of Vacuum Science & Technology B: Microelectronics and Nanometer Structures* **2005**, *23*, 995.

[54] Ren, S.; Yang, S.; Zhao, Y.; Zhou, J.; Xu, T.; Liu, W. Friction and wear studies of octadecyltrichlorosilane SAM on silicon. *Tribology Letters* **2002**, *13*, 233–239.

CHAPTER 4

MONOLAYER LUBRICATION AT A SINGLE-ASPERITY CONTACT

Surfaces in MEMS/NEMS devices are likely to feature, not only non-ideality and roughness at the atomic scale as examined in Chapter 3, but also nanoscale roughness in the form of surface asperities. The classic Bowden and Tabor model points out that the real area of contact between two surfaces is much lower than the apparent area of contact, as the load will be borne and focused at points of surface irregularity (e.g., asperities).[1] Planar surface models, while providing a simplified system for facile examination of structure-property relationships, may preclude relevant friction mechanisms that only arise at asperity-like geometries. Experimentally, monolayer tribology under conditions of nanoscale roughness has been studied extensively using AFM, which serves as a model single-asperity contact. However, many questions remain concerning the friction mechanisms present under these conditions, as few MD studies have been performed in this domain. Several experimental studies have suggested that molecular plowing, characterized by asperity penetration into monolayer films and contortion of chains during shear, may be the dominate friction mechanism in asperity environments[2,3], and this is supported by the simulation studies that have been performed on such systems.[4–7] However, little exploration has been made into how the structure and chemistry of the monolayer film influences the presence of this mechanism; knowledge that is essential for the design of friction and wear-resistant monolayers to withstand these extreme conditions. Here, MD simulation is used to examine a single-asperity contact, where friction mechanisms are compared with more standard systems that utilize planar geometries and are examined as a function of film density. Furthermore, the influence of asperity shape and substrate morphology on single-asperity friction mechanims are explored.

The work presented in this chapter has been featured in a peer-reviewed publication and

is reprinted with permission from Ref. 8. Copyright 2017 American Chemical Society.

4.1 Background

The tribology of monolayer films has been examined extensively via both experiment (e.g. tribometry[9,10], surface force apparatus[11,12], various scanning probe microscopies[11,13]) and molecular dynamics (MD) simulations. These studies have revealed that monolayer response to shear is highly influenced by the structure of the surface contacting the monolayer, where planar geometries (or geometries with low curvature) uniformly increase the tilt angle in the monolayer as a result of compression[4,14], while sharp, tip-like geometries (e.g., an AFM tip) allow penetration of the tip into the monolayer film.[4,7,15] The ability for tip-like geometries to penetrate into monolayer films, creating localized regions of distorted chains, has been shown to result in additional modes of energy dissipation under shear, leading to larger frictional forces and increased monolayer wear.[16,17] This mechanism has been referred to as "molecular plowing,"[2,3,17] as it relates similarly to the more familiar plowing-induced friction (i.e. plastic deformation of surfaces) observed for shear in the absence of a lubricant.[18] Understanding the molecular plowing mechanism is of fundamental importance to the rational design of effective nanoscale lubrication schemes, as even planar MEMS/NEMS systems are likely to feature nanoscale surface asperities that also exhibit plowing, similar to that seen for tips.[19] MD simulation is uniquely suited to examine this problem, as it allows molecular level details to be correlated with system properties. For example, simulations have demonstrated a significant dependence of the frictional response of monolayers on substrate structure (either crystalline[14,20–22] or amorphous[23–25]), where the presence of atomic-scale roughness and disordered chain arrangements (which come naturally from the structure of rough, amorphous surfaces) tend to lead to large increases in the COF[24] and a propensity for monolayer degradation.[25] However, while planar geometries have been widely studied with MD, few studies have considered the impact of asperities and/or tip-like geometries, particularly for monolayers undergo-

ing shear on amorphous silica surfaces with experimentally relevant levels of atomic-scale surface roughness and disorder.

In one simulation study, Tupper et al. compared the compression (in the absence of shear) of monolayers by a planar surface to that of a surface containing an asperity.[4] It was shown that the asperity was able to approach closer to the substrate than a planar surface at the same normal load, a result correlated to localized distortion of chains and an increase in gauche defects in the region of the asperity. Knippenberg et al. compared the friction of a buckyball and a planar surface shearing against an alkane monolayer, finding that shear of the buckyball led to larger frictional forces than planar surfaces, attributed to forces being localized to atoms just in front of the buckyball.[7] In another study, Chandross et al., examined monolayers under shear by hemispherical amorphous silica tips.[17] It was again observed that the COF for the tip geometry was larger than that for planar surfaces, but additionally that these values were largely independent of tip size and monolayer chain length. In contrast, Leng et al. showed that for an alkanethiol monolayer on gold under contact by a sharp gold tip longer chains gave rise to reduced frictional forces, which was attributed to the higher lateral stiffness of the chains.[26] These studies serve to confirm hypotheses from experimental atomic force microscopy (AFM) studies (which serve as a means to isolate the effects of a single-asperity contact) that asperities can induce additional modes of energy dissipation in monolayer films via localized deformation of chains and increased penetration of asperities into monolayer films.[2,3]

The effect of monolayer density on molecular plowing, which would be expected to have a strong influence on the penetration ability of asperities and resistance to lateral motion, remains largely unexplored. Experimentally, Flater et al. observed that friction was higher for octadecyltrichlorosilane (OTS) monolayers in a low-density "liquid expanded" phase compared to the high-density "liquid condensed" phase, with such differences attributed to a decreased propensity for the formation of defects in the denser film.[3] To the best of our knowledge, a similar study of the effect of monolayer density on the frictional

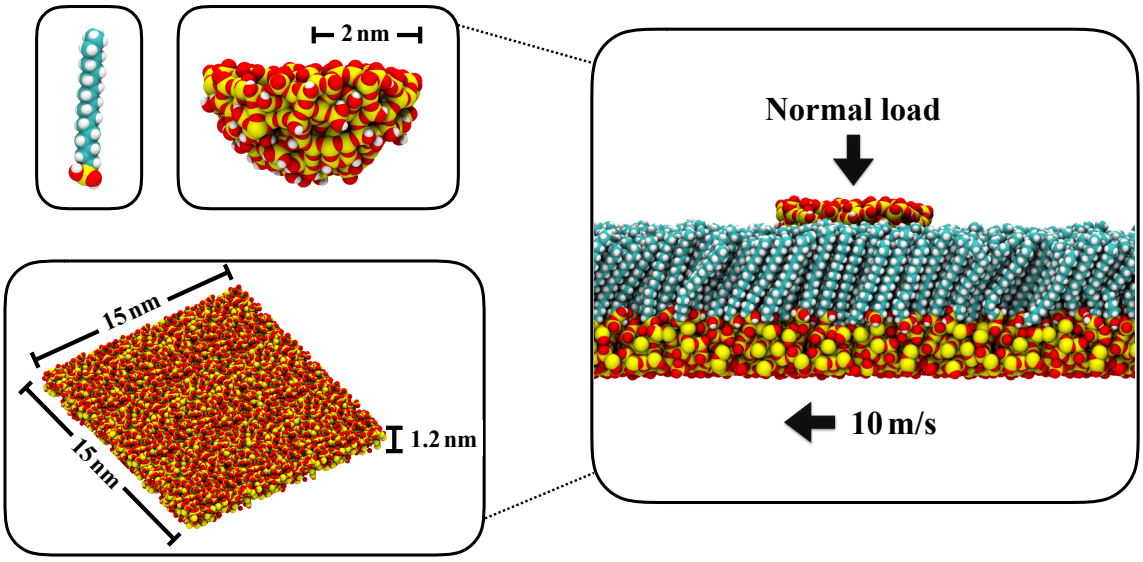

Figure 4.1: Snapshots of the single-asperity model. Systems feature a hemispherical silica tip with a radius of 2nm in contact with an amorphous silica substrate (15nm $\times$ 15nm $\times$ 1.2nm) functionalized by alkylsilane chains with a chain length of 18 carbons.

response and molecular-level structure at a single-asperity contact has not been performed using MD simulation. Thus, in this work, to more robustly understand the molecular plowing mechanism, we examine the behavior of model hemispherical asperities contacting planar surfaces coated with alkylsilane monolayers with various densities, to identify relationships between film structure, monolayer response to shear, and the COF.

4.2 Methods

The systems examined in this work, shown in Fig. 4.1, feature asperities represented by a hemispherical silica tip (of radius 2nm) and a rough, amorphous silica substrate (periodic in plane with dimensions 15nm $\times$ 15nm $\times$ 1.2nm), functionalized by alkylsilane chains 18 carbons long. The substrate size is chosen to avoid any significant self-interaction effects of the tip across the periodic boundaries. Both the tip and substrate are carved from bulk amorphous silica, prepared following the procedure of Litton and Garofalini;[27] however, using the ReaxFF force field to model silicon and oxygen bonding[28] with parameters from

Fogarty et al.[29], as done in our prior work[24] and that of others.[30] Note that ReaxFF is only used to generate the silica bulk, and that the simulations presented in this paper utilize a classical force field where bonds are permanent. Model construction and atom-typing are performed using the mBuild[31,32] and Foyer[33] Python packages, respectively, that are provided as part of the Molecular Simulation and Design Framework (MoSDeF).[34] A Github repository providing access to both initialization scripts, as well as the simulation input files is provided at Ref. 35. Planar surfaces carved from bulk are constructed to feature a hydroxyl density of 5 OH/nm^2, following an analytical approach where hydroxyl density is adjusted by bridging neighboring surface oxygen atoms[36,37], matching expectations from experiment.[38] The planar surfaces feature a surface roughness of 0.11nm, which closely approximates the atomic-scale surface roughness calculated from synthesis mimetic simulations (0.13nm)[24], in which surfaces were exposed to hydrogen peroxide to mimic the "piranha" treatment typical in experiment.[39] Surface monolayers feature densities of 2.0, 3.0, 4.0, and 5.0 chains per nm^2, where the 5.0 chains per nm^2 monolayer fills all available surface sites and 4.0 chains per nm^2 represents the maximum coverage observed in experiment;[40] note, all chains are chemisorbed (i.e. attached to the surface via permanent Si-O bonds) and attachment sites without chains are capped with H atoms. System sizes range from 47,864 to 87,689 atoms for the lowest and highest monolayer densities, respectively. To establish a baseline comparison, periodic planar surfaces in contact with a monolayer on a planar substrate are also examined, although we note that smaller systems of planar dimension 5nm $\times$ 5nm are considered, as prior studies have shown this size to be sufficiently large to avoid self-interaction artifacts.[14]

These simulations follow a similar simulation protocol to that described in Chapter 3 and as reported in our previous work.[22,24,25] All simulations are performed using the LAMMPS molecular dynamics engine.[41,42] The OPLS all-atom force field of Jorgensen et al.[43,44] is used to describe both bonded and non-bonded parameters, with Si-O parameters modeling the surface connection modeled as a Morse potential, fitted to ReaxFF; param-

eters from Lorenz et al. are used to describe the silica interactions.[23] Note that this force field does not allow for bond breaking. The specific force field parameters used in these simulations can be found in Appendix A. Simulations are performed in the NVT ensemble, with the temperature maintained at 298K via a Nosé-Hoover thermostat[45,46], applied to both surfaces and chains, although thermostatting is not performed in the direction of shear. Silica tips are treated as rigid bodies, as deformation is not expected due to the difference in hardness between silica and monolayers. The RESPA multi-timestep integration method[47] is utilized, where bonds are evaluated at 0.25fs, angles and dihedrals at 0.5fs, and all non-bonded interactions at 1fs. The particle-particle particle-mesh (PPPM) Ewald summation method for slab geometries[48] is utilized for the evaluation of long-range electrostatics.

The workflow employed involves first equilibrating monolayers out of contact with the tip for 1ns to achieve a relaxed state. This is followed by a compression stage, in which the tip is lowered onto the monolayer at a constant velocity of 10m/s and snapshots are taken every 10ps. Starting from a snapshot corresponding to a normal load close to that desired for shear, a constant normal load is provided to the tip while the counter-surface is moved at a constant velocity of 10m/s. This velocity corresponds to velocities used in previous simulation studies[14,21,24,25] as well as velocities realized in MEMS/NEMS devices;[49,50] however, it should be noted this is several orders of magnitude larger than typical AFM speeds (O (1) μm/s), thus care must be taken in comparing these results to AFM. It should also be noted that only a single shear direction is considered in this work; however, Appendix C.3 contains additional results for shear in the opposite direction where is it observed that the presented trends are unchanged. Operation is performed under a constant normal load ensemble, where a constant external force is applied to atoms in the silica tip. Loads of 5, 10, 15, 20, and 25nN are considered, which leads to operation in a pressure range of roughly 0.25 to 2.5GPa. While the upper limit of this pressure range is quite high, this is a result of the small contact areas associated with the single-asperity geometry. Comparable normal loads and pressures have been examined in prior simulation

studies[14,51,52] as well as in experimental scanning probe microscopy analysis[53], and tests of actual MEMS devices.[54]

The friction forces reported represent values evaluated by summing the forces in the x-dimension (the direction of shear) on the bottom surface and chains, following our previous work, while normal forces represent the external force added to the asperity in the negative z-dimension (normal to the surface). Unlike friction of monolayers between more idealized, planar surfaces, the tip/surface geometry precludes a steady-state friction force, as forces are localized to the region surrounding the tip. As such, forces represent an averaging over a sampling window from 0.3-1.3ns of shear (see Appendix C.2 for more information), which accounts for a single pass of the tip across the monolayer. Films in some systems are shown to display viscoelastic effects; thus, results would not be reliable beyond a single pass. Several additional metrics are considered to quantify monolayer structure. These include the film thickness, the fraction of dihedral angles featuring gauche defects, the average tilt angle, and the orientational order. These metrics are evaluated over the same sampling window as the friction forces. Additional details on the calculation of these metrics and the associated errors are provided in Appendix C.1.

4.3 Results and Discussion

4.3.1 Planar vs. Tip-like Contact Geometries

To establish a baseline behavior for the specific model and parameters employed in this work, comparisons are made between asperities and planar geometries in contact with a high-density (4.0 chains/nm^2) planar monolayer film. Results for the friction force as a function of normal load for surfaces contacting C18 monolayers are shown in Fig. 4.2. In agreement with trends from the literature, a linear dependence of the friction force as a function of the applied load is observed for both contact geometries.[7,17,55] A linear regression is performed for each system,where the slope of each curve corresponds to the

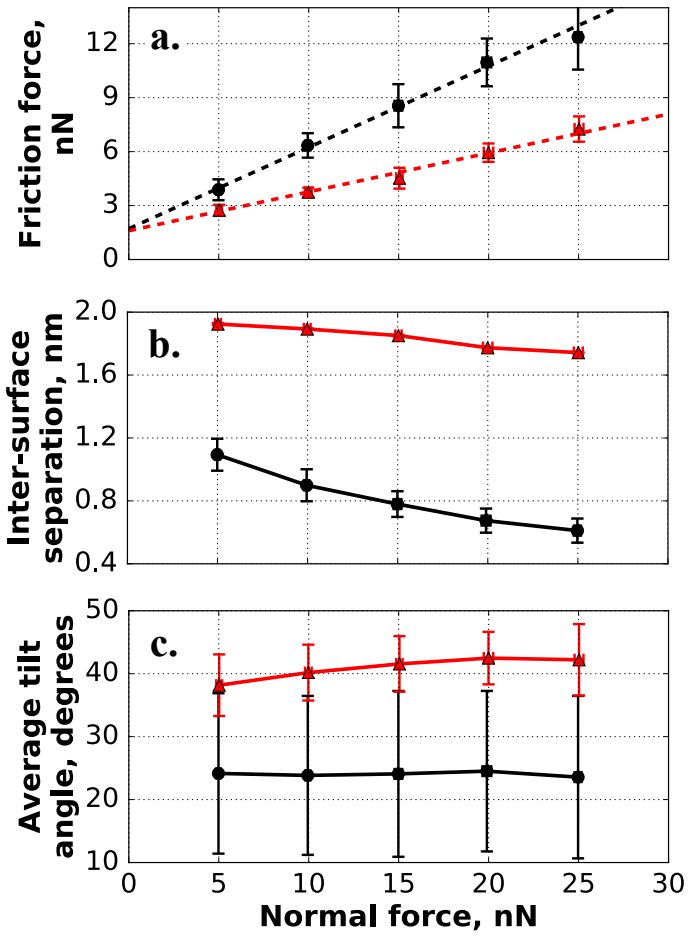

Figure 4.2: Friction force, inter-surface separation, and average tilt angle as a function of normal load for asperity (black, circles) and planar (red, triangles) geometries under shear with a C18 monolayer (at a density of 4.0 chains/nm^2). Dashed lines represent linear regressions, while solid lines are provided only as a guide to the eye. Error bars represent one standard deviation.

coefficient of friction via a modified form of Amontons' Law as used in prior studies[2,17],

$$F_f = \tau_0 \cdot A + \mu \cdot L \tag{4.1}$$

where F_f, τ_0, A, μ, and L represent the friction force, interfacial shear strength at zero normal load, contact area, friction coefficient, and normal load respectively. The linearity of both curves suggests that the first term can be considered a constant for each system. Values for the coefficient of friction are observed to be 0.45 and 0.22 for the asperity and

planar geometries respectively. It should be noted that while these values are larger than those typically reported in experiment for alkylsilane monolayers, they are consistent with values reported in the simulation literature[17], with this difference possibly a result of the higher velocities used in simulation. Similar results to those shown in Fig. 4.2 have been observed in work by Chandross et al., where the COF determined for systems featuring tip-like shear was 3 to 4 times larger than that obtained for planar geometries.[17] While the difference in COF between these two geometries in this work is slightly lower, this can likely be attributed to the higher surface roughness and less ordered substrate used in this work. Knippenberg et al. found similar changes in the COF when comparing shear of a buckyball versus that of a planar amorphous carbon countersurface against a C14 monolayer on diamond.[7] The differences in friction between the buckyball and planar geometries were attributed to the contortion of chains in front of the buckyball via the creation of gauche defects. A similar mechanism likely explains the higher COF observed for the asperity geometry in Fig. 4.2a (examined in detail below, in the context of monolayer density). Figs. 4.2b-c show the inter-surface separation and average tilt angle as a function of normal load for both the asperity and planar systems. A clear trend can be observed where the inter-surface separation is reduced for asperities compared to the planar geometry. That the separation value is lower than the film thickness (2.12nm) indicates penetration of the asperity into the monolayer, as observed from visual inspection of the simulation trajectory. The average tilt angle for the asperity geometry is found to vary little with the applied load, while a slight increase in the average tilt angle is apparent for the planar contact, although we note this increase is small relative to the variation between chains. Furthermore, tilt angles are found to be larger, with less variation, for the planar geometry as opposed to the asperity geometry. This is consistent with the results of prior studies that have shown for tip geometries the monolayer responds to normal loads via localized tilting and contortion of chains in the region of the asperity, while the surrounding film remains essentially unchanged, rather than an increase in tilt angle as for planar geometries.[4] Thus, a clear

Table 4.1: Global Equilibrium Monolayer Properties Prior to Compression [a]

monolayer density (chains/nm^2)	nematic order	avg tilt angle, deg	gauche defects per chain	film thickness, nm
2.0	0.127 + 0.010	54.7 + 18.0	2.4 + 1.6	1.32 + 0.35
3.0	0.549 + 0.007	34.1 + 18.4	1.37 + 1.4	1.78 + 0.36
4.0	0.797 + 0.004	22.8 + 12.0	0.82 + 1.1	2.05 + 0.20
5.0	0.972 + 0.002	7.0 + 3.9	0.16 + 0.5	2.29 + 0.05

[a] Averages are obtained over a 0.5 ns sampling window for the equilibrated film, with values calculated every 1 ps. Values for the nematic order, average tilt angle, and gauche defects per chain represent the mean of all values within this sampling window. Error for nematic order represents one standard deviation of this mean, while error for the average tilt angle and gauche defects per chain is evaluated for each frame and the value reported represents the mean of these error values (thus providing a measure of uniformity within the film as opposed to changes in the global property over time). Film thickness is estimated by voxelizing the surface into a 9×9 grid (each voxel has an area of 2.78 nm^2) where values for each frame equate to the average of the thickness within all voxels. The mean value reported in the table corresponds to the mean of these averages over the sampling window and the error represents the mean of the standard deviations to again allow for error propagation.

distinction in the dominant mechanism of friction between planar and asperity geometries is apparent, whereby molecular plowing appears to lead to higher frictional forces in the system with the asperity geometry, consistent with the literature.

4.3.2 Monolayer Density Effects on Friction at Single-Asperity Contacts

Molecular plowing appears to play a dominant role in the friction forces observed for systems with asperity-like geometries. To better understand how the properties of the monolayer film influence this mechanism the influence of monolayer density on friction at a single-asperity contact is examined. Fig. 4.3 shows snapshots of C18 monolayers with chain densities of 2.0, 3.0, 4.0, and 5.0 chains per nm^2, as well as heatmaps showing the distribution of film thickness, average tilt angle, and orientational order of the chains (i.e., the dot product of chain directors and the average system director). It is found that

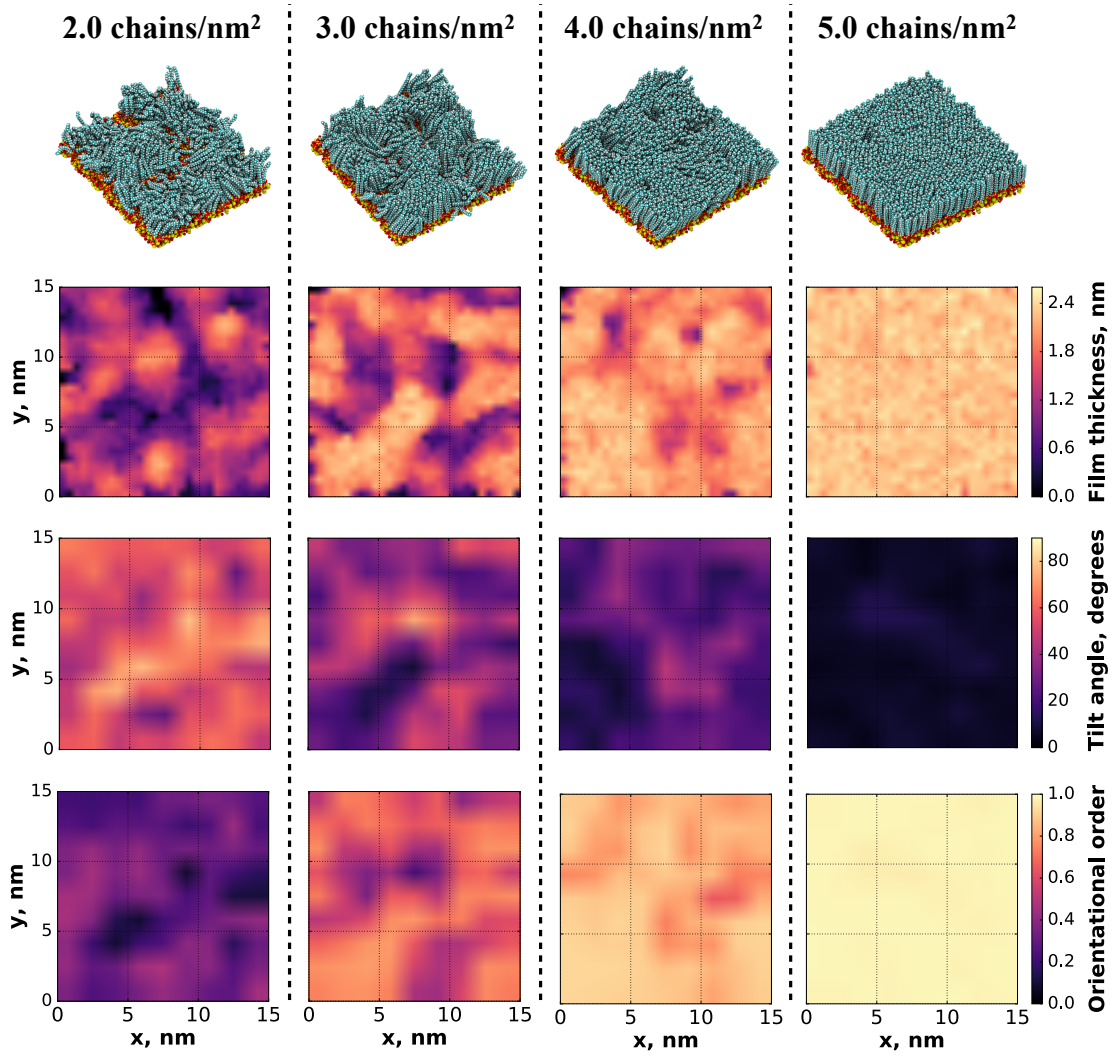

Figure 4.3: Snapshots of monolayers with densities of (left-right) 2.0, 3.0, 4.0, and 5.0 chains per nm^2, and heatmaps of (top-bottom) film thickness, tilt angle, and orientational order for monolayers at equilibrium, prior to compression.

as monolayer density is decreased, monolayers transition from a state where chains are in a highly-ordered, upright configuration (5.0 and 4.0 chains/nm^2) to a state where local domains of order and grain boundaries are apparent (3.0 chain/nm^2), and finally to a state where monolayers feature a complete lack of uniformity and are highly disordered (2.0 chains/nm^2). These observations are consistent with the greater free volume available for chains to explore as monolayer density is decreased, and are further evidenced by several

Table 4.2: Coefficient of Friction (Slope) and y-Intercept for Monolayers under Shear by a Hemispherical Asperity Obtained via Linear Regression of the Data in Figure 4.4, along with Data Obtained for Monolayers under Shear by a Planar Amorphous Silica Surface

	single-asperity		planar	
monolayer density, chains/nm^2	COF	intercept, nN	COF	intercept, nN
2.0	0.34 ± 0.02	1.47 ± 0.27	0.207 ± 0.008	1.25 ± 0.11
3.0	0.37 ± 0.01	1.91 ± 0.12	0.200 ± 0.004	1.85 ± 0.05
4.0	0.45 ± 0.02	1.72 ± 0.21	0.216 ± 0.012	1.60 ± 0.14
5.0	0.56 ± 0.01	1.55 ± 0.16	0.186 ± 0.011	1.71 ± 0.14

global film properties computed for each film, provided in Table 4.1. The large errors present in the global monolayer properties for sparse monolayers are indicative of the lack of uniformity, as can be seen visually in the heatmaps. Note, these measurements are for the monolayers prior to contact by the tip, where values are obtained over a sampling window of 0.5ns for the equilibrated film. From Table 4.1 it is observed that as monolayer density is decreased, the average film thickness and ordering of monolayer chains are reduced while the average tilt angle and number of gauche defects per chain (where a gauche defect is defined as a C-C-C-C dihedral angle $> 270^\circ$ or $< 90^\circ$, following previous work[7]) are increased. These trends are consistent from the visualizations in Fig. 4.3 – where as monolayer density is decreased films appear to transition from a solid-like state to a liquid-like state - and again are likely a result of the increased free volume available for chains to explore as monolayer density is reduced.

A sharp, hemispherical asperity with a radius of 2nm is compressed into each monolayer and shear is performed at normal loads of 5, 10, 15, 20, and 25nN. Friction forces evaluated during the course of these simulations are shown in Fig. 4.4. All systems display a linear relationship between friction force and normal load, consistent with prior simulation studies of monolayers under contact at tip-like geometries.[7,17] A linear regression is performed on each system, with values of the COF (again using Eq. 4.1) shown in Table 4.2, alongside values obtained for systems featuring a planar geometry (the data from

which these fits were calculated is provided in Appendix C.4). For the asperity geometry, a decrease in the COF is observed as monolayer density is decreased, in contrast to the planar geometry where the COF is found to be nearly independent of monolayer density (although we note a small decrease in COF is seen for the well ordered monolayers when density is increased from 4.0 to 5.0 chains/nm^2). This reveals that the difference in the dominant friction mechanisms (i.e. plowing vs. sliding) in systems with asperity vs. planar geometries will alter the response of the COF to monolayer density. Furthermore, the idea that increasing monolayer density will also increase the COF is opposite of typical trends reported in the literature for systems featuring two monolayer films in contact (at a planar geometry). For example, Black et al. showed that the introduction of disorder through the removal of chains (i.e., reducing monolayer density) as well as through the introduction of surface roughness led to increases in the friction force for C10 alkylsilanes on silica.[24] Chandross et al. examined the influence of defects (i.e. reduced monolayer densities) for alkylsilanes of several chain lengths on both crystalline and amorphous substrates, also concluding that the COF increased as defects were introduced, although they did find that

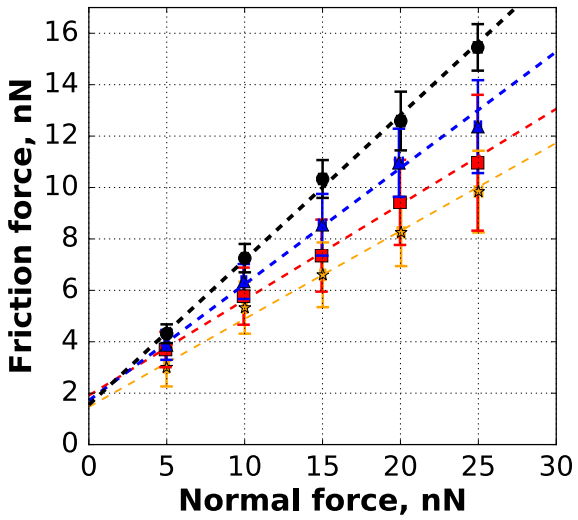

Figure 4.4: Friction force vs. normal force for monolayers with densities of (in chains per nm^2) 5.0 (black, circles), 4.0 (blue, triangles), 3.0 (red, squares), and 2.0 (orange, stars) under shear with a 2nm hemispherical tip. Lines represent linear regressions and error bars represent one standard deviation.

the contributions became negligible beyond a threshold number of defects.[56] The difference in the trend of COF with monolayer density observed in systems with an asperity geometry as compared to that observed for systems with a planar geometry is evidence that the relationship between monolayer density and friction is closely tied to the dominant mechanism of friction.

The molecular plowing mechanism that dominates friction in systems with an asperity geometry is expected to be associated with the depth of tip penetration into the film. An examination of the penetration depth as a function of normal load for each system (Fig. 4.5), reveals that under low normal loads (i.e. 5nN) tips already feature significant penetration (roughly 45% of the tip height for the system with the highest density), further suggesting that under the entire normal load range from 5-25nN molecular plowing should play a significant, if not dominant, role in the measured friction force. At all normal loads, it is observed that as monolayer density is decreased from 5.0 to 3.0 chains per nm^2, penetration depth is increased. This is likely a result of the transition in monolayer structure from a solid-like (high orientational order) to a more liquid-like (low orientational order)

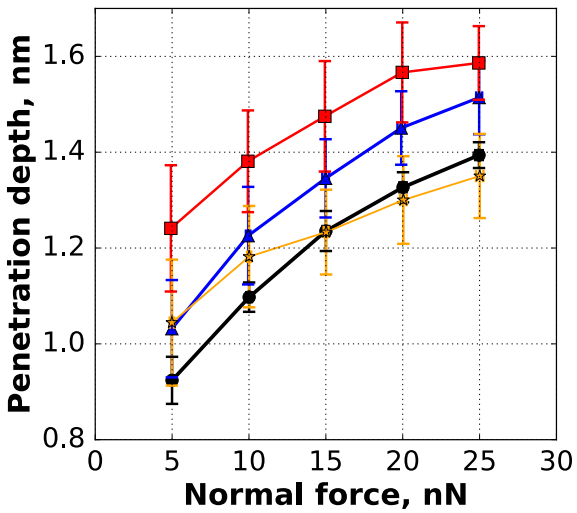

Figure 4.5: Average penetration depth for tips under shear against monolayers with densities of (in chains per nm^2) 5.0 (black, circles), 4.0 (blue, triangles), 3.0 (red, squares), and 2.0 (orange, stars). Error bars represent one standard deviation and lines are provided only as a guide to the eye.

state as monolayer density is reduced, as noted earlier in the text and as evidenced by the visualizations and heatmaps of orientational order in Fig. 4.3, where the more solid-like, higher-density films resist tip penetration. This is an interesting trend, as increased penetration depth would be expected to be associated with an increase in the molecular plowing force, however, Fig. 4.4 shows that lower density films feature reduced COFs. This suggests that penetration depth alone does not determine the extent to which molecular plowing contributes to friction. This idea is further supported by the curve in Fig. 4.5 for the monolayer with the lowest density (2.0 chains per nm^2), which at the highest normal load (i.e. 25nN) yields the lowest penetration depth of the different densities. This can likely be explained by the low value of film thickness calculated for this monolayer (as shown in Table 4.1), which limits the maximum depth of tip penetration. At a normal load of 25nN the penetration depth for this system is comparable to the film thickness, suggesting the system approaches direct contact between the tip and the surface; however, visually, the tip is buffered from direct contact from the surface by at least one chain – often in an elongated configuration parallel to the surface - throughout the entirety of the trajectory. The rigid nature of the silica substrate (i.e. not easily deformed, a consequence of classical MD force fields that prohibit bond breaking) likely also plays a role in the trend of penetration depth vs. normal load observed for the lowest density system. The evidence that as monolayer density is increased, the COF increases while the penetration depth decreases, and that penetration depth in the lowest density system is limited by the thin nature of the film, suggests that friction resulting from molecular plowing is not governed solely by the depth of penetration. Instead the structural characteristics of the monolayer films may play a more dominant role in the extent to which plowing influences friction.

To examine the structure of monolayer films under shear, the time-averaged number density of carbon atoms as a function of their relative position from the tip in the direction of shear (i.e. the x dimension) is shown in Fig. 4.6. Here, values are normalized by the bulk density, i.e. the product of the monolayer chain length and the density of the film,

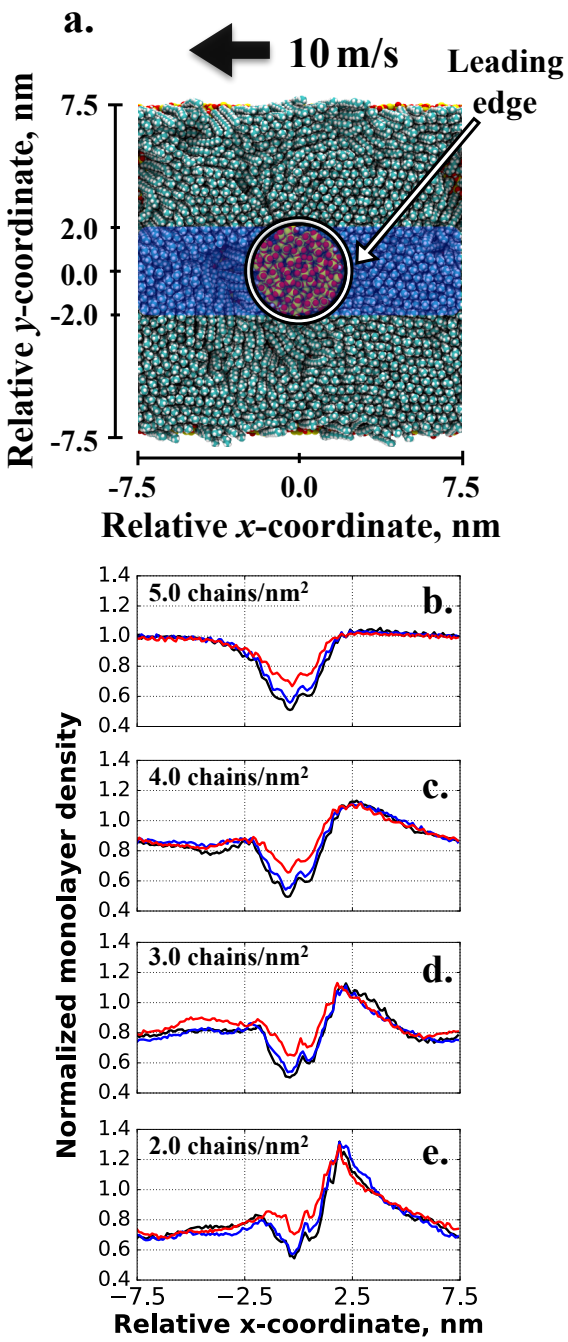

Figure 4.6: Number density of carbon atoms measured as a function of distance relative to the tip apex in the direction of shear (i.e. x) for atoms $\pm$ 2nm from the tip apex (within the shaded region shown in a.). Plots include data for monolayer densities of (in chains per nm^2) b. 5.0, c. 4.0, d. 3.0, and e. 2.0 under normal loads of 5 (red), 15 (blue), and 25nN (black). Number density is normalized by the bulk value, which corresponds to product of the number of carbons per chain (18) and the monolayer density.

so that the four systems can be more directly compared, and only carbon atoms +/- 2 nm in the *y*-dimension from the center of the tip, are considered, as these are the atoms that will be most directly affected by shear. A diagram highlighting this region of interest is shown in Fig. 4.6a. For each system a reduced density of carbons directly beneath the tip is observed, followed by an increase in the number of carbons directly in front of the tip. This is highly suggestive of molecular plowing-induced shear. Material is built-up in front of the tip and chains are then forced to either contort/tilt under the tip, or be displaced in the *y*-dimension (i.e., perpendicular to the direction of shear). Furthermore, a comparison of the extent of "build-up" as a function of monolayer density confirms expectations that monolayer structure will influence the plowing mechanism. Specifically, the normalized density of carbons in the region in front of the tip is shown to be larger (i.e. more build-up) for lower density films. This is consistent with the fluid-like nature of films of reduced density compared to those with higher density, as the chains have more free volume and room to move, thus providing less resistance to being pushed by the tip. At the extreme of a monolayer density of 5.0 chains per nm^2, where all surface sites are filled, there is little available free volume for the chains to move and thus they cannot accumulate in front of the tip, resulting in only a small increase in density is observed. While at the other extreme, for a monolayer density of 2.0 chains per nm^2, chains have significant free volume and mobility and are thus easily built-up in front of the tip and pushed aside as the asperity moves. Thus, while the solid-like nature of higher density films works to reduce tip penetration, these monolayers will feature higher rigidity. In turn, this likely results in greater resistance to shear, leading to higher COFs.

While Fig. 4.6 suggests that chains will be more mobile (i.e. more easily pushed by the tip) in lower density monolayers, this alone does not fully explain the decreased COF observed for these systems. The literature suggests that higher friction forces observed for molecular plowing mechanisms result from the creation of gauche defects in the monolayer films, as additional force is required to contort monolayer chains.[7] To explore this theory,

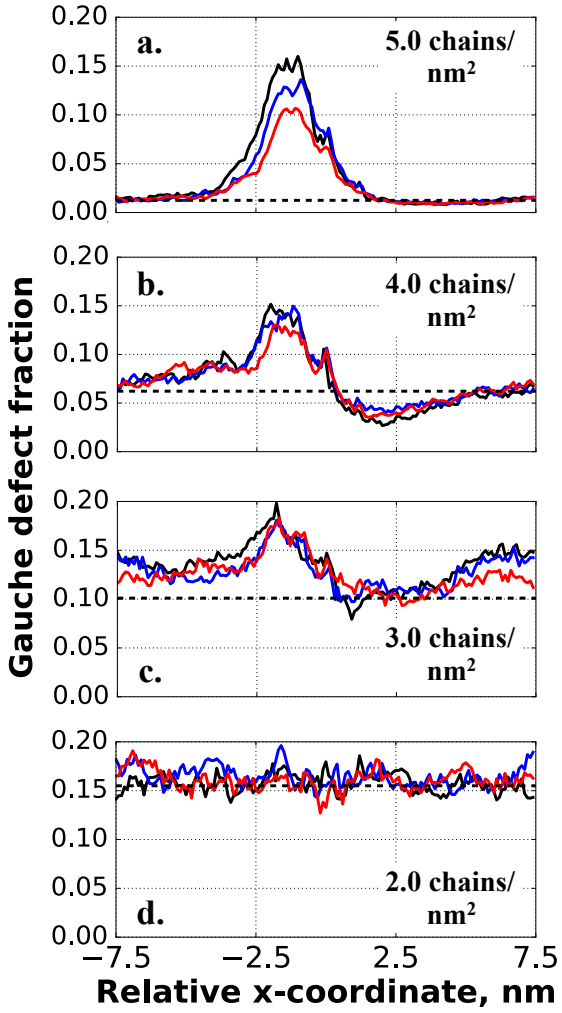

Figure 4.7: Fraction of backbone (C-C-C-C) dihedrals featuring gauche defects as a function of distance from the tip in the direction of shear for dihedrals located ± 2nm in y from the tip apex (within the shaded region shown in Fig. 4.6a). Plots are shown for monolayer densities of a. 5.0, b. 4.0, c. 3.0, and d. 2.0 chains per nm^2 at normal loads of 5 (red), 15 (blue), and 25nN (black). Dashed lines represent average values for the equilibrated films prior to contact.

the fraction of C-C-C-C dihedral angles in gauche configurations (hereafter referred to as the gauche defect fraction) as a function of their relative location from the tip is examined (Fig. 4.7), again focusing on the region highlighted in Fig. 4.6a. The dashed lines in these plots represent the gauche defect fraction in the equilibrated monolayers prior to contact by the tip, to provide a reference so that the impact of the tip can be better interpreted. In Fig. 4.7 a peak is observed for systems with monolayer densities of 3.0, 4.0, and 5.0 chains/nm^2

where the gauche defect fraction increases from the equilibrium value and comes to a maximum in the region just behind the tip. This confirms the expectation from the literature that the molecular plowing mechanism results in the formation of gauche defects in monolayer chains. However, Fig. 4.7 also reveals that as monolayer density is decreased, the difference between the maximum gauche defect fraction and the equilibrium value decreases, indicating that tips induce less gauche defects in sparser films. To provide additional context, for the monolayer with a density of 5.0 chains/nm^2, roughly 1 in 100 dihedrals in the equilibrated film are found in a gauche configuration, whereas in the region just behind the tip in Fig. 4.7a, roughly 1 in 7 dihedrals exhibit a gauche configuration. For a lower density monolayer of 3.0 chains/nm^2, roughly 1 in 10 dihedrals feature a gauche configuration in the equilibrated film, compared to 1 in 5 for the region behind the tip in Fig. 4.7c. This result further clarifies the connection between monolayer structure and plowing induced friction, specifically that increased force will be required to shear tips through denser monolayer films as a result of the formation of a greater number of gauche defects. The extreme of this trend is shown in Fig. 4.7d for the monolayer with a density of 2.0 chains/nm^2, whereby no additional gauche defects are imparted on monolayer chains by the tip. Fig. 4.7 also reveals the interesting trend that the maximum gauche defect fraction observed appears to be nearly independent of monolayer density (ranging from roughly 0.15-0.20 for all systems, or 1 in 7 to 1 in 5 dihedrals). As the gauche defect fraction can be correlated with monolayer fluidity (e.g. the lowest density monolayer features both the most fluid-like behavior and the highest number of gauche defects), it may be that a gauche defect fraction of 0.15-0.20 is required for monolayers to become fluid enough to facilitate movement of the tip during shear.

4.3.3 Discussion on the Linearity of the Friction Force-Normal Load Relationship

Friction forces in this work are observed to be the result of mechanisms related to molecular plowing as determined through analysis of various structural characteristics,

such as gauche defects and local film densities. However, friction force vs. load curves, as shown in Fig. 4.3, still indicate a linear relationship, as is typically observed for shear at planar geometries, which feature different mechanisms of friction. Such linear relationships for friction at tip-like contact with monolayer films have been observed in the literature both via simulation[7,17,55] and experiment[2], yet there is also evidence that suggests that friction forces, when plotted as a function of normal load, will feature a super-linear trend (i.e. greater than first order) when the contacting body is of an asperity or tip-like geometry.[3,57] For example, a study performed by Zhang et al. observed this trend for contact between a blunt, pyramidal gold tip and alkanethiols on a gold surface.[57] This super-linear trend has also been observed experimentally in a study by Flater et al. where OTS monolayers were evaluated via atomic-force microscopy.[3] The contrasting results in trends between friction force and normal load in these various studies make it difficult to determine what friction law best represents single-asperity friction of monolayer films, thus we discuss here a possible solution for these discrepancies.

A thorough examination of the available literature, in conjunction with the results of this study, suggests a two-fold answer can explain many of the aforementioned inconsistencies, both contributing to characteristics of the interface of contact:

1. The shape and size of the asperity/tip

2. The spatial arrangement of monolayer chains on the substrate

In the work of Zhang et al. friction appears to vary linearly with load until a threshold value of load is reached, whereby a dramatic increase in friction is observed, which could be described as a super-linear trend.[57] Examination of the provided snapshots of their systems, reveals that this increase in friction corresponds to the load required for the tip to penetrate the monolayer (i.e. at loads below this threshold value the tip will simply slide on top of the monolayer). Thus, the drastic increase in friction is likely due to contributions from molecular plowing being negligible until this threshold load is reached.

In the work by Flater et al.[3] where molecular plowing was attributed to a super-linear relationship between friction and load, the following friction law was proposed,

$$F_f = \tau \cdot A + F_p(L) \tag{4.2}$$

where a second term (related to forces due to molecular plowing) was suggested to be a nonlinear function of the applied load. However, in the case where the shear strength is linearly related to the normal load, this would not explain the linear trends in friction force vs. normal force observed in this work and others. If, however, we do assume that the plowing force varies linearly with the applied load, then an explanation is achieved. Brukman et al. in considering the effect of molecular plowing on single-asperity friction, suggested that the friction contributions to plowing should be directly proportional to the applied load.[2] This derivation was made by assuming a Hertzian contact geometry, for which it should be noted there is evidence both for[58] and against.[7,17] Substituting a linear relationship into Eq. 4.2 yields (after simplifying):

$$F_f = \tau_0 \cdot A + (\mu + \alpha) \cdot L \tag{4.3}$$

where τ_0, μ, and α represent the interfacial shear stress at zero applied load, the coefficient of friction related to sliding, and the coefficient of friction related to plowing, respectively. The linear friction trends in this study and others suggest that for these systems $\mu + \alpha$ can be treated as a constant, and while contributions from interfacial friction and plowing are not easily decoupled, the sum of both contributions can be compared as essentially a total friction coefficient.

The super-linear relationship observed by Zhang et al. can also be explained by Eq. 4.3. In their systems chains featured an ordered arrangement, as a uniform crystalline substrate was used, and the gold tip was blunted.[57] This likely prevented penetration of the tip into the monolayer until a threshold load was reached. Eq. 4.3 would suggest then that the

value of α in their systems would be zero until this threshold load was reached, at which point plowing would occur and α would then have a non-zero value, leading to a higher total friction coefficient and an apparent super-linear relationship between friction force and load. In contrast, the hemispherical/spherical tips used in the present study, as well as the studies by Knippenberg et al. and Chandross et al.,[7,17] are sharper and have greater adhesion with the monolayer (as evidenced by the y-intercept of the normal vs. shear force), allowing them to penetrate into monolayers even under low normal load. Thus, contribution to the friction force from molecular plowing likely occurs at all normal loads considered in our study. As such, systems where penetration of tips (and thus plowing) is prevented until a threshold load is reached, are likely to exhibit a non-linear relationship between friction force and load, with both tip geometry (i.e. blunt vs. sharp) and substrate structure (i.e. crystalline vs. amorphous, ordered vs. disordered) likely to play a role in governing the penetration ability of tips.

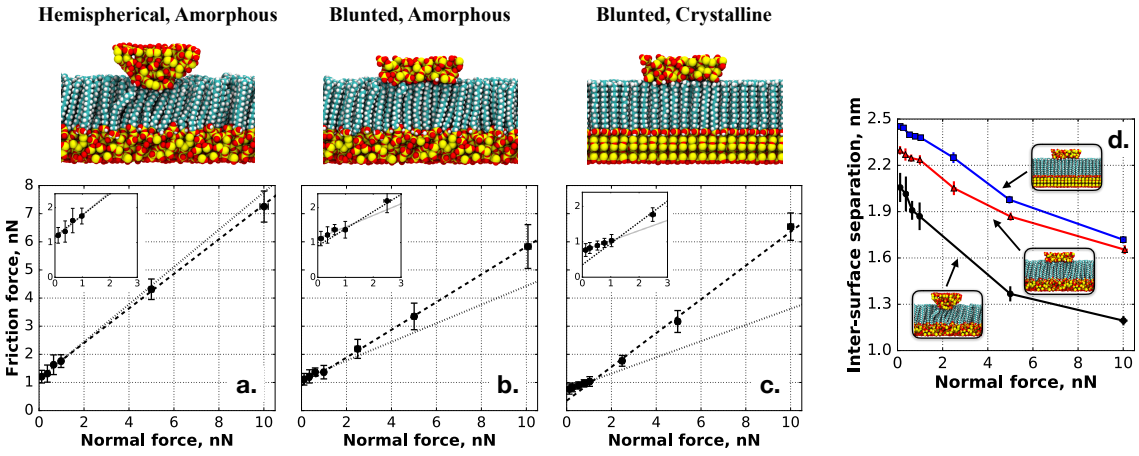

Figure 4.8: Friction force vs. normal load curves and cross-sectional snapshots (at a normal load of 1.0nN) for systems featuring a. a hemispherical tip geometry and amorphous substrate, b. a blunted tip geometry and amorphous substrate, and c. a blunted tip geometry and crystalline substrate. Insets are provided to highlight the low normal load regime (0-3nN). Dotted lines represent a linear regression for points at normal loads from 0-1nN and dashed lines represent a linear regression for points at normal loads from 1-10nN. d. The inter-surface separation for the three systems (black: hemispherical, amorphous; red: blunted, amorphous; blue: blunted, crystalline) during shear, where solid lines are provided only to guide the eye. Error bars in all plots represent one standard deviation.

To test this theory, three systems have been considered, each featuring a unique combination of tip geometry and substrate morphology:

1. A "hemispherical-amorphous" system (snapshot shown in Fig. 4.8a), equivalent to the systems described earlier in this work featuring a hemispherical tip (with a radius of 2nm) in contact with a monolayer attached to a rough, amorphous silica surface

2. A "blunted-amorphous" system, where this tip has been blunted by removing atoms in the bottom 1nm of the tip (snapshot shown in Fig. 4.8b)

3. A "blunted- crystalline" system (snapshot shown in Fig. 4.8c), where the tip has been blunted and monolayer chains are attached to a flat, crystalline silica surface, similar to that utilized in our previous work.[22,25]

Each system features a monolayer density of 5.0 chains/nm^2, where the high monolayer density is expected to better highlight the transition from sliding-dominated friction to plowing- dominated friction. These systems have been sheared under normal loads ranging from 0.1nN to 10nN, and the friction forces plotted as a function of normal load are shown in Fig. 4.8a-c, along with snapshots of each system at a normal load of 1nN. To highlight the possibility of a transition from sliding-dominated friction to plowing-dominated friction linear regressions have been performed in two normal load regimes; one for points at normal loads from 0.1nN to 1.0nN (dotted lines), and another for points at normal loads from 1.0nN to 10nN (dashed lines). The comparable slope for both regression curves for the hemispherical-amorphous system indicates that the friction force vs. normal load relationship remains linear, and that molecular plowing acts as the dominant friction mechanism, for all normal loads examined, as expected. For both the blunted-amorphous and blunted-crystalline systems, the slope of the regression curve for the low normal load regime is lower than that observed for the high normal load regime. This is suggestive of a transition from sliding-dominant to plowing-dominant friction, and follows the idea presented in Eq. 4.3. Furthermore, the difference between these slopes is most evident for the blunted-

crystalline system, which most closely resembles the systems of Zhang et al.[57], supporting our claim that tip geometry and substrate morphology will both play a role in the presence of this transition. Fig. 4.8d shows the average inter-surface separation for each system during shear as a function of normal load. The expected trend is observed whereby inter-surface separation is increased (and thus plowing is reduced) for systems where tips have been blunted, and is further reduced by the use of an idealized, crystalline substrate. Thus, our hypothesis appears supported, such that tip geometry and substrate morphology will both affect the ability of tips to penetrate into monolayer films, influencing the transition from sliding-dominant to plowing-dominant friction, which may yield a linear or apparent super-linear trend between friction force and normal load depending on the normal load regime that is examined.

4.3.4 Discussion on Ideal Lubrication for Single-Asperity Contacts

The results of the present study suggest that the disordered nature (greater free volume) imparted by reduced monolayer densities helps induce a fluid-like shear response, resulting in a lower COF as a result of reduced mechanical stress required by plowing of monolayer chains. However, it is important to note that we have not considered the effects of monolayer wear, where it has been observed that highly ordered chains are typically considered to be more stable, as they exhibit a high degree of stabilizing chain-chain VDW interactions.[9] Similarly, experiments in which monolayer voids are backfilled have been shown to yield increased stability.[59–61] Again, for planar geometries, it has been shown that increased chain disorder also leads to higher COFs[24] and thus low-density states, with reduced structural ordering, might have significant negative impacts for the rest of a system with a predominantly planar geometry, even though they reduce the COF for asperities, where plowing-like mechanisms dominate friction. Mixed monolayer systems may provide a unique route to combine these competing effects; a prior study by Lewis et al. examining planar systems in contact, showed that mixing short perfluoroalkylsilanes with long alkylsi-

lanes results in systems with lower COF than either equivalent single component system.[22] These systems demonstrate a liquid-like layer between the two monolayers, consisting of the ends of the long alkyl chains (i.e., the portion of the chain longer than the short perfluoroalkane). A similar result was found in simulations by Mazyar et al. of monolayers under shear with the addition of an ionic liquid at the contact interface.[62] This liquid-like interfacial region could potentially be designed to mimic the low-density films that are favorable for asperities (by exhibiting sufficient fluidity that asperity do not induce additional gauche defects during shear), while still providing durability and low COF for planar regions of a contacting surface.

4.4 Conclusions

Prior results in the literature comparing the effect of contact geometry on friction of monolayer-coated surfaces have shown that tip-like geometries can induce additional mechanisms of energy dissipation via molecular plowing, resulting in increased COF. These results are corroborated in the present work, as a comparison in the COF between a tip-like and planar geometry shows higher friction for the tip geometry, shown to be a result of penetration of the tip into the monolayer. Examination of the effect of monolayer density on this mechanism has been explored through shear of monolayer coatings of densities of 5.0, 4.0, 3.0, and 2.0 chains per nm^2 by a hemispherical amorphous silica tip. It is observed that lower monolayer densities yield reduced COFs, while COF is shown to be independent of monolayer density for planar geometries. This is found to result from the fluid-like response of lower density monolayer films to shear. Following expectations from the literature, molecular plowing is found to be the dominant mechanism of friction, as gauche defects are shown to be formed in monolayers during tip shear. It is observed that the number of gauche defects induced by the tip is reduced as monolayer density is reduced, with the lowest density film (2.0 chains per nm^2) revealing no additional gauche defects imparted by the tip. However, for this low-density system it is shown that an increased density

of chains exists in the regions surrounding the tip. This is suggestive of two mechanisms contributing to molecular plowing during tip shear:

1. The contortion of chains by the tip through the introduction of gauche defects
2. The displacement of chains to the side of the tip to allow passage through the monolayer

Lower density films contain a higher free volume and thus the second mechanism becomes more likely and requires less additional force. Additionally, it is shown that the relationship between friction force and normal load for systems with an asperity geometry is influenced by the geometry of the tip as well as the ordering of the monolayer chains. Blunted tips and more ordered monolayers are shown to increase the normal load required to transition from sliding-dominated to plowing-dominated shear. While long-chain alkylsilanes would likely feature poor durability in a MEMS/NEMS device, the results of this study suggest that films featuring a liquid-like shear response should provide favorable friction at regions of asperity contact in these devices. Analysis of various mixed monolayers featuring a bound-mobile structure at asperity contacts presents an intriguing area of future research.

4.5 Bibliography

[1] Bowden, F. P.; Tabor, D. The Area of Contact between Stationary and between Moving Surfaces. *Proceedings of the Royal Society A: Mathematical, Physical and Engineering Sciences* **1939**, *169*, 391–413.

[2] Brukman, M. J.; Oncins, G.; Dunbar, T. D.; Boardman, L. D.; Carpick, R. W. Nanotribological Properties of Alkanephosphonic Acid Self-Assembled Monolayers on Aluminum Oxide: Effects of Fluorination and Substrate Crystallinity. *Langmuir* **2006**, *22*, 3988–3998.

[3] Flater, E. E.; Ashurst, W. R.; Carpick, R. W. Nanotribology of Octadecyltrichlorosilane Monolayers and Silicon: Self-Mated versus Unmated Interfaces and Local Packing Density Effects. *Langmuir* **2007**, *23*, 9242–9252.

[4] Tupper, K. J.; Colton, R. J.; Brenner, D. W. Simulations of Self-Assembled Monolayers under Compression: Effect of Surface Asperities. *Langmuir* **1994**, *10*, 2041–2043.

[5] Bonner, T.; Baratoff, A. Molecular dynamics study of scanning force microscopy on self-assembled monolayers. *Surface Science* **1997**, *377-379*, 1082–1086.

[6] Knippenberg, M. T.; Mikulski, P. T.; Dunlap, B. I.; Harrison, J. A. Atomic contributions to friction and load for tip–self-assembled monolayers interactions. *Physical Review B* **2008**, *78*.

[7] Knippenberg, M. T.; Mikulski, P. T.; Harrison, J. A. Effects of tip geometry on interfacial contact forces. *Modelling and Simulation in Materials Science and Engineering* **2010**, *18*, 034002.

[8] Summers, A. Z.; Iacovella, C. R.; Cummings, P. T.; MCabe, C. Investigating Alkylsilane Monolayer Tribology at a Single-Asperity Contact with Molecular Dynamics Simulation. *Langmuir* **2017**, *33*, 11270–11280.

[9] Booth, B. D.; Vilt, S. G.; Lewis, J. B.; Rivera, J. L.; Buehler, E. A.; McCabe, C.; Jennings, G. K. Tribological Durability of Silane Monolayers on Silicon. *Langmuir* **2011**, *27*, 5909–5917.

[10] Booth, B. D.; Vilt, S. G.; McCabe, C.; Jennings, G. K. Tribology of Monolayer Films: Comparison between n-Alkanethiols on Gold and n-Alkyl Trichlorosilanes on Silicon. *Langmuir* **2009**, *25*, 9995–10001.

[11] Salmeron, M. Generation of Defects in Model Lubricant Monolayers and Their Contribution to Energy Dissipation in Friction. *Tribology Letters* **2001**, *10*, 69–79.

[12] Yoshizawa, H.; You-Lung, C.; Israelachvili, J. Recent advances in molecular level understanding of adhesion, friction and lubrication. *Wear* **1993**, *168*, 161–166.

[13] Kim, H. I.; Koini, T.; Lee, T. R.; Perry, S. S. Systematic Studies of the Frictional Properties of Fluorinated Monolayers with Atomic Force Microscopy: Comparison of CF3- and CH3-Terminated Films. *Langmuir* **1997**, *13*, 7192–7196.

[14] Chandross, M.; Grest, G. S.; Stevens, M. J. Friction between Alkylsilane Monolayers: Molecular Simulation of Ordered Monolayers. *Langmuir* **2002**, *18*, 8392–8399.

[15] Tutein, A. B.; Stuart, S. J.; Harrison, J. A. Indentation Analysis of Linear-Chain Hydrocarbon Monolayers Anchored to Diamond. *The Journal of Physical Chemistry B* **1999**, *103*, 11357–11365.

[16] Chandross, M.; Lorenz, C. D.; Stevens, M. J.; Grest, G. S. Probe-Tip Induced Damage in Compliant Substrates. *Journal of Manufacturing Science and Engineering* **2010**, *132*, 030916.

[17] Chandross, M.; Lorenz, C. D.; Stevens, M. J.; Grest, G. S. Simulations of Nanotribology with Realistic Probe Tip Models. *Langmuir* **2008**, *24*, 1240–1246.

[18] Bowden, F. P.; Moore, A. J. W.; Tabor, D. The Ploughing and Adhesion of Sliding Metals. *Journal of Applied Physics* **1943**, *14*, 80–91.

[19] de Boer, M. P.; Knapp, J. A.; Mayer, T. M.; Michalske, T. A. Role of interfacial properties on MEMS performance and reliability. *Microsystems Metrology and Inspection* **1999**, 2–15.

[20] Mikulski, P. T.; Harrison, J. A. Periodicities in the properties associated with the friction of model self-assembled monolayers. *Tribology Letters* **2001**, *10*, 29–35.

[21] Rivera, J. L.; Jennings, G. K.; McCabe, C. Examining the frictional forces between mixed hydrophobic – hydrophilic alkylsilane monolayers. *The Journal of Chemical Physics* **2012**, *136*, 244701.

[22] Lewis, J. B.; Vilt, S. G.; Rivera, J. L.; Jennings, G. K.; McCabe, C. Frictional Properties of Mixed Fluorocarbon/Hydrocarbon Silane Monolayers: A Simulation Study. *Langmuir* **2012**, *28*, 14218–14226.

[23] Lorenz, C.; Webb, E.; Stevens, M.; Chandross, M.; Grest, G. Frictional dynamics of perfluorinated self-assembled monolayers on amorphous SiO2. *Tribology Letters* **2005**, *19*, 93–98.

[24] Black, J. E.; Iacovella, C. R.; Cummings, P. T.; McCabe, C. Molecular Dynamics Study of Alkylsilane Monolayers on Realistic Amorphous Silica Surfaces. *Langmuir* **2015**, *31*, 3086–3093.

[25] Summers, A. Z.; Iacovella, C. R.; Billingsley, M. R.; Arnold, S. T.; Cummings, P. T.; McCabe, C. Influence of Surface Morphology on the Shear-Induced Wear of Alkylsilane Monolayers: Molecular Dynamics Study. *Langmuir* **2016**, *32*, 2348–2359.

[26] Leng, Y.; Jiang, S. Atomic indentation and friction of self-assembled monolayers by hybrid molecular simulations. *The Journal of Chemical Physics* **2000**, *113*, 8800–8806.

[27] Litton, D. A.; Garofalini, S. H. Modeling of hydrophilic wafer bonding by molecular dynamics simulations. *Journal of Applied Physics* **2001**, *89*, 6013–6023.

[28] van Duin, A. C. T.; Strachan, A.; Stewman, S.; Zhang, Q.; Xu, X.; Goddard, W. A. ReaxFFSiOReactive Force Field for Silicon and Silicon Oxide Systems. *The Journal of Physical Chemistry A* **2003**, *107*, 3803–3811.

[29] Fogarty, J. C.; Aktulga, H. M.; Grama, A. Y.; van Duin, A. C. T.; Pandit, S. A. A reactive molecular dynamics simulation of the silica-water interface. *The Journal of Chemical Physics* **2010**, *132*, 174704.

[30] Yeon, J.; van Duin, A. C. T. ReaxFF Molecular Dynamics Simulations of Hydroxylation Kinetics for Amorphous and Nano-Silica Structure, and Its Relations with Atomic Strain Energy. *The Journal of Physical Chemistry C* **2015**, *120*, 305–317.

[31] mBuild: a component-based molecule builder tool that relies on equivalence relations for component composition. http://mosdef-hub.github.io/mbuild/.

[32] Klein, C.; Sallai, J.; Jones, T. J.; Iacovella, C. R.; McCabe, C.; Cummings, P. T. A Hierarchical, Component Based Approach to Screening Properties of Soft Matter. *Molecular Modeling and Simulation* **2016**, 79–92.

[33] Foyer: A package for atom-typing as well as applying and disseminating force fields. http://mosdef-hub.github.io/foyer/.

[34] MoSDeF Github:. http://github.com/mosdef-hub.

[35] Initialization and run scripts for single asperity systems:. http://github.com/summeraz/single_asperity.

[36] Hartkamp, R.; Siboulet, B.; Dufrêche, J.-F.; Coasne, B. Ion-specific adsorption and electroosmosis in charged amorphous porous silica. *Physical Chemistry Chemical Physics* **2015**, *17*, 24683–24695.

[37] Zhuravlev, L. The surface chemistry of amorphous silica. Zhuravlev model. *Colloids and Surfaces A: Physicochemical and Engineering Aspects* **2000**, *173*, 1–38.

[38] Zhuravlev, L. T. Concentration of hydroxyl groups on the surface of amorphous silicas. *Langmuir* **1987**, *3*, 316–318.

[39] Vilt, S. G.; Caswell, C. J.; Tuberquia, J. C.; McCabe, C.; Jennings, G. K. Effect of Roughness on the Microscale Friction of Hydrocarbon Films. *The Journal of Physical Chemistry C* **2012**, *116*, 21795–21801.

[40] Kojio, K.; Ge, S.; Takahara, A.; Kajiyama, T. Molecular Aggregation State of n-Octadecyltrichlorosilane Monolayer Prepared at an Air/Water Interface. *Langmuir* **1998**, *14*, 971–974.

[41] LAMMPS web page:. http://lammps.sandia.gov.

[42] Plimpton, S. Fast Parallel Algorithms for Short-Range Molecular Dynamics. *Journal of Computational Physics* **1995**, *117*, 1–19.

[43] Jorgensen, W. L.; Maxwell, D. S.; Tirado-Rives, J. Development and Testing of the OPLS All-Atom Force Field on Conformational Energetics and Properties of Organic Liquids. *Journal of the American Chemical Society* **1996**, *118*, 11225–11236.

[44] Price, M. L. P.; Ostrovsky, D.; Jorgensen, W. L. Gas-phase and liquid-state properties of esters, nitriles, and nitro compounds with the OPLS-AA force field. *Journal of Computational Chemistry* **2001**, *22*, 1340–1352.

[45] Nose, S. A unified formulation of the constant temperature molecular dynamics methods. *The Journal of Chemical Physics* **1984**, *81*, 511–519.

[46] Hoover, W. G. Canonical dynamics: Equilibrium phase-space distributions. *Physical Review A* **1985**, *31*, 1695–1697.

[47] Tuckerman, M.; Berne, B. J.; Martyna, G. J. Reversible multiple time scale molecular dynamics. *The Journal of Chemical Physics* **1992**, *97*, 1990–2001.

[48] Yeh, I.-C.; Berkowitz, M. L. Ewald summation for systems with slab geometry. *The Journal of Chemical Physics* **1999**, *111*, 3155–3162.

[49] Bhushan, B. Nanotribology and nanomechanics of MEMS/NEMS and BioMEMS/BioNEMS materials and devices. *Microelectronic Engineering* **2007**, *84*, 387–412.

[50] Mate, C. M.; Marchon, B.; Murthy, A. N.; Kim, S.-H. Lubricant-Induced Spacing Increases at Slider–Disk Interfaces in Disk Drives. *Tribology Letters* **2009**, *37*, 581–590.

[51] Mikulski, P. T.; Harrison, J. A. Packing-Density Effects on the Friction ofn-Alkane Monolayers. *Journal of the American Chemical Society* **2001**, *123*, 6873–6881.

[52] Ewers, B. W.; Batteas, J. D. The role of substrate interactions in the modification of surface forces by self-assembled monolayers. *RSC Adv.* **2014**, *4*, 16803–16812.

[53] Burns, A. R.; Houston, J. E.; Carpick, R. W.; Michalske, T. A. Molecular Level Friction As Revealed with a Novel Scanning Probe. *Langmuir* **1999**, *15*, 2922–2930.

[54] Asay, D. B.; Dugger, M. T.; Ohlhausen, J. A.; Kim, S. H. Macro- to Nanoscale Wear Prevention via Molecular Adsorption. *Langmuir* **2008**, *24*, 155–159.

[55] Cheng, S.; Luan, B.; Robbins, M. O. Contact and friction of nanoasperities: Effects of adsorbed monolayers. *Physical Review E* **2010**, *81*.

[56] Chandross, M.; Webb, E. B.; Stevens, M. J.; Grest, G. S.; Garofalini, S. H. Systematic Study of the Effect of Disorder on Nanotribology of Self-Assembled Monolayers. *Physical Review Letters* **2004**, *93*.

[57] Zhang, L.; Leng, Y.; Jiang, S. Tip-Based Hybrid Simulation Study of Frictional Properties of Self-Assembled Monolayers: Effects of Chain Length, Terminal Group, Scan Direction, and Scan Velocity. *Langmuir* **2003**, *19*, 9742–9747.

[58] Ewers, B. W.; Batteas, J. D. Utilizing Atomistic Simulations To Map Pressure Distributions and Contact Areas in Molecular Adlayers within Nanoscale Surface-Asperity Junctions: A Demonstration with Octadecylsilane-Functionalized Silica Interfaces. *Langmuir* **2014**, *30*, 11897–11905.

[59] Zhang, Q.; Archer, L. A. Interfacial Friction of Surfaces Grafted with One- and Two-Component Self-Assembled Monolayers. *Langmuir* **2005**, *21*, 5405–5413.

[60] Zhang, Q.; Archer, L. A. Boundary Lubrication and Surface Mobility of Mixed Alkylsilane Self-Assembled Monolayers. *The Journal of Physical Chemistry B* **2003**, *107*, 13123–13132.

[61] Jones, R. L.; Harrod, B. L.; Batteas, J. D. Intercalation of 3-Phenyl-1-proponal into OTS SAMs on Silica Nanoasperities to Create Self-Repairing Interfaces for MEMS Lubrication†. *Langmuir* **2010**, *26*, 16355–16361.

[62] Mazyar, O. A.; Jennings, G. K.; McCabe, C. Frictional Dynamics of Alkylsilane Monolayers on SiO2: Effect of 1-n-Butyl-3-methylimidazolium Nitrate as a Lubricant. *Langmuir* **2009**, *25*, 5103–5110.

CHAPTER 5

STRUCTURE-PROPERTY SCREENING OF FUNCTIONALIZED MONOLAYER FILMS

In Chapters 3 and 4, MD simulations have been used to gather insights into friction mechanisms present during the shear of monolayer films and to examine how system aspects such as substrate morphology, backbone chain length, and film density influence friction and wear behavior. Such studies are facilitated by the precise control MD simulations provide over system variables, where it is possible to alter one aspect of system chemistry, such as substrate morphology, while keeping the remaining system chemistry the same to examine the direct impact of a single variable on the tribological response. This approach also allows MD simulations to be harnessed for the systematic screening of monolayer films, to determine optimal chemistries for lubrication. To date, however, MD screening of complex systems, such as grafted surfaces, has been limited, as these systems can be difficult to construct (from a software perspective) and are typically not done so in a manner which allows system chemistry to be easily altered. Furthermore, screening over a large chemical space will require parameterization of each system with the appropriate force field parameters, another task where conventional approaches are not general. However, over the past several years the mBuild[1,2] and Foyer[3] Python packages have been developed as pillars of the Molecular Simulation and Design Framework (MoSDeF)[4], a software suite and simulation ideology, which provides a platform for facile tuning of system chemistry and parameterization in a manner that is scriptable, which promotes reproducibility. Here, MoSDeF is utilized to perform screening of functionalized monolayer films where relationships between chain length, terminal group chemistry, and tribology are analyzed. In total, 820 systems were simulated on the Titan supercomputer at Oak Ridge National Laboratory, making this perhaps the most extensive, systematic study of monolayer films to date

in regard to tribological efficacy. Structure-property relationships are examined whereby aspects of terminal group chemistry such as molecular shape, size, and charge distribution are related to tribological variables. The breadth of the data set also facilitates analysis via a machine learning algorithm to develop a predictive model for functionalized monolayers which should aid in discovery of interesting regions of the monolayer chemical parameter space in future studies. Finally, the workflow utilized in this chapter helps provide the framework for the screening of more complex monolayer films.

The work presented in this chapter has been prepared for submission as a peer-reviewed publication.

5.1 Background

The viability of monolayer films for application as nanoscale lubricants requires the design of better-performing materials with improved wear resistance and reduced frictional forces. However, screening the vast chemical space afforded by monolayer films is a difficult, if not impossible, task to perform via experimental means. One significant hurdle is monolayer preparation, where the synthesis of monolayer films may be a non-trivial step; examination of novel chemistries often requires changes to synthesis approaches, which can make it difficult to decouple the effects of chemical changes from the effects of other properties such as monolayer density. Furthermore, comparisons between different experimental studies can be challenging if different synthesis protocols or techniques for measuring tribological properties are used. For example, two common techniques for experimental analysis of monolayer films, atomic force microscopy (AFM) and tribometry, feature probes with radii of curvature that differ by several orders of magnitude, and it has been shown that even slight differences in probe shape can enable different mechanisms of energy dissipation in monolayer films.[5] As a result, molecular dynamics (MD) simulation has become a useful tool for examining the tribological properties of monolayers, affording atomic-level resolution and fine control over system variables. MD can be utilized for sys-

tematic variation of monolayer chemistry, in order to identify both tribologically-favorable chemistries as well as chemistry-property relationships that can provide insight used for the design of more favorable films.

Despite these advantages, typical MD workflows often lend themselves better to screening over thermodynamic space (e.g., varying temperature or normal force) as opposed to chemical space (e.g., terminal group chemistry), with the majority of studies examining chemical influences on tribology reserving themselves to a comparison between only a small number of systems/chemistries. This can be associated, in part, with the lack of tools designed to enable screening; i.e., that provide the ability to systematically vary chemistry during model setup, to apply force field parameters to these models, and to manage the execution of the simulation workflow on large numbers of systems. Instead, the current state of MD simulation typically involves system setup in an ad-hoc manner, often using in-house scripts and human manipulation, which makes large-scale screening studies intractable and limits reproducibility of published results. As a means to resolve these issues, the Molecular Simulation and Design Framework (MoSDeF)[4] has been designed as a Python framework for generating molecular systems as objects with exchangeable chemical parts and for automatically applying force field parameters.

Here, we use the MoSDeF toolkit, along with the Signac framework[6] for workflow management, to enable large-scale, non-equilibrium MD screening simulations of lubricating monolayer films. Focus is specifically placed on the monolayer chain length and terminal group chemistry, where 5 chain lengths and 16 unique terminal group chemistries are compared. Along with chemically-identical films, 84 unique combinations of chemically-dissimilar films are considered, where the two contacting monolayers feature different terminal groups. In total, 164 unique system chemistries are examined. Both the coefficient of friction (COF) and the force of adhesion are examined for each system to evaluate tribological efficacy. The scope of the monolayer chemical space examined in this work is sufficient such that machine learning is utilized in the derivation of quantitative structure-

property relationship (QSPR) models for each variable, to aid in exploring links between chemistry and tribology. These models, which take as an input a SMILES[7] representation of a molecular terminal group, can also aid in the further screening of monolayer chemical space, by identification of regions that may have favorable tribological properties, as well as excluding those with potentially unfavorable tribological properties. While previous experimental and simulation studies have examined the effects of terminal group chemistry on friction, the work herein presents, to the best of our knowledge, the most comprehensive single study to date of these relationships, where we note that all simulations follow the same exact procedures and methods, allowing for direct cross examination.

5.2 Methods

5.2.1 Molecular Model

Systems in this work consist of two opposing monolayer films, attached to amorphous silica substrates, as in prior studies.[8,9] Our procedure for carving the amorphous surfaces builds upon procedures found in the literature[10,11], with further details provided in Chapter 4.2. In particular, our procedure yields an atomic-scale roughness of approximately 0.12nm, found to closely match prior studies that explicitly considered surface oxidation treatment typical of experiment.[8] The majority of prior simulation studies of monolayer films have considered either crystalline silica or amorphous silica substrates that are atomically smooth, which prior work suggests may influence the behavior and trends.[5,8,9] We have utilized the mBuild Python package[1,2], a component of the MoSDeF toolkit[4], to construct our dual-monolayer systems. These systems are constructed in a hierarchical manner, whereby (1) a prototype for each chain is constructed, (2) duplicates are attached to assigned sites on the surface, and (3) the monolayer is duplicated, rotated by 180^{o}, and shifted to yield the complete system. Chain prototypes are created by instantiating a Python class with two tunable, top-level parameters: the backbone chain length (excluding the ter-

minal group) and the functional group used to terminate the chain. This approach, shown graphically in Fig. 5.1a, is designed such that both the backbone chain length and terminal group chemistry can be trivially modified, making these scripts easily extensible to other chemistries not considered here. Furthermore, due to the hierarchical, component-based framework of mBuild, these routines can be modified to allow for screening over additional chemical degrees of freedom, such as backbone monomer, film chemistry, etc.

The pool of terminal group chemistries examined in this work is shown in Fig. 5.1a and was constructed to meet two primary criteria:

1. The functional group should be able to be described using existing parameters within the OPLS force field (described in further detail below).

2. The pool should span a wide range of chemical characteristics (e.g. size, shape, polarity) to facilitate structure/property analysis.

It is worth noting that several of the chosen functionalities would likely not be synthesizable, or would readily react following synthesis [12]. However, as reactions are not considered in our simulations, such groups remain stable. Furthermore, as our goal is simply to study a chemically-diverse range of terminal group chemistries, such systems still provide valuable data for the development of property-prediction models.

Screening of dual-monolayer systems is performed over two distinct parameter spaces:

1. Chemically-identical systems (Fig. 5.1b), where the top and bottom monolayer films feature the same chemistry

2. Chemically-dissimilar systems (Fig. 5.1c), where the top and bottom monolayer films feature different chemistries

The motivation for including chemically-dissimilar systems in this study is two-fold. First, in the context of performing a structure-property analysis between terminal group chemistry and monolayer tribology, the inclusion of chemically-dissimilar systems provides increased sampling of unique interfacial chemistries without the need to expand the pool of

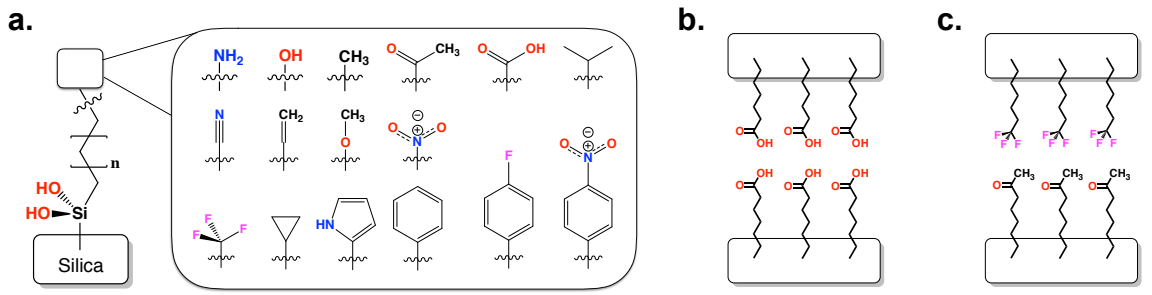

Figure 5.1: a. Overview of the chemical parameter space examined in this work. The pool of terminal group chemistries consists of (row 1) amino, hydroxyl, methyl, acetyl, carboxyl, isopropyl; (row 2) nitrile, vinyl, methoxy, nitro; (row 3) perfluoromethyl, cyclopropyl, 2-pyrrole, phenyl, fluorophenyl, and nitrophenyl. Dual-monolayer systems include both b. chemically-identical and c. chemically-dissimilar compositions.

terminal group chemistries. This provides a significant advantage, as it reduces the number of unique force field parameters necessary to perform the study. The second motivation for examining chemically-dissimilar systems concerns findings in the literature of favorable tribological properties for such systems, outperforming their chemically-identical counterparts.[13,14]

For each chemistry, five systems have been generated, each corresponding to a unique arrangement of chains on the silica surface. Structural and tribological properties are evaluated for each of the five replicas and are averaged to obtain values for each chemistry that are independent of chain arrangement. For systems featuring chemically-identical films, all 16 terminal group chemistries from Fig. 5.1a are considered along with five chain lengths (5, 8, 11, 14, and 17 backbone carbons, excluding the terminal group), equaling 80 unique chemistries and 400 systems in total. Chemically-dissimilar films considered feature backbone chain lengths of 17 carbons and include all combinations of seven select terminal groups (carboxyl, fluorophenyl, hydroxyl, isopropyl, methyl, nitro, and perfluoromethyl) with the 16 terminal groups in Fig. 5.1a, leading to an additional 84 unique chemistries (after removing duplicates) and 420 total systems. In total, 820 systems are examined, with 164 unique monolayer chemistries, and 100 unique terminal group combinations with a chain length of 17 carbons.

5.2.2 Force Field

After construction of the monolayer structures, the systems are atom-typed, i.e., the appropriate force field parameters are determined for the bonded and non-bonded interactions of the system. Atom-typing is handled by the Foyer library[3] as part of MoSDeF. In Foyer, forcefield parameters and their usage rules are encoded within a single XML-formatted file that builds upon the OpenMM[15] XML forcefield file format. Usage rules are encoded using SMARTS[16], along with overrides statements to set rule precedents, making these definitions both human and machine readable, and contained within a single unambiguous format. In Foyer, each molecular model is treated as a graph, and atom-types are determined by matching chemical environments to the patterns defined by the SMARTS usage rules. This file format also provides digital object identifiers (DOIs) corresponding to the source of the parameters, to aid in reproducibility. Further details on Foyer can be found online[3] and in Ref. 17.

The OPLS all-atom force field[18–24] has been employed in this work for all systems examined, and all parameters are located in Appendix A. The specific OPLS version used was provided with the Gromacs 5.1 distribution[25] in addition to parameters for silica which were obtained from Lorenz et al.[26] It should be noted that for several systems, certain parameters were not available (most commonly dihedrals including either alpha, beta, or gamma carbons neighboring the terminal group). In these cases, additional parameters were introduced according to sensible conventions; for example, in the case of missing dihedrals including alpha, beta, or gamma carbons, standard C-C-C-C alkane dihedrals were used, which was found to be the convention within the rest of the OPLS force field. These additions are, again, detailed in the Appendix A.

5.2.3 Molecular Dynamics Simulations

Molecular dynamics simulations were performed using the Gromacs molecular dynamics engine (version 5.1.0).[25] An initial, short, distance-limited NVE simulation was performed using the LAMMPS molecular dynamics engine[27,28] to remove overlaps between terminal groups from the initial configuration. After converting the final structure from the initial LAMMPS simulation to Gromacs format, simulations were executed in four stages: (1) energy minimization, (2) equilibration, (3) compression, and (4) shear. Energy minimization was performed using a steepest descent algorithm. Following energy minimization, equilibrium molecular dynamics simulations were performed, whereby monolayers and surfaces (excluding the outer 4Å) were allowed to relax over 1ns to reach a low-energy state, using a timestep of 1fs. Following equilibration, a force of 5nN was applied to the bottom surface in the $+z$ direction (i.e. towards the top monolayer) to bring the two monolayers into contact, where they were compressed over 0.5ns, allowing the inter-surface distance to reach a steady-state value. Beginning from snapshots from the end of the compression stage, three independent simulations were performed where monolayers were sheared under normal loads of 5, 15, and 25nN (corresponding to pressures of 200, 600, and 1000MPa, respectively), consistent with normal loads used for such systems in the literature.[29–31] To maintain a constant normal load, a constant force was applied to the bottom silica surface in the $+z$ direction. Shear was introduced by coupling the top surface to a ghost particle by a harmonic spring (with a spring constant of 1e5$\frac{\text{kJ}}{\text{mol}\cdot\text{nm}^2}$) and pulling the ghost particle in the $+x$ direction at a rate of 10$\frac{\text{m}}{\text{s}}$. Shear was performed for 10ns, whereby over the first 5ns monolayers reach a steady-state configuration where chains tend to align in the direction of shear, and the final 5ns was used for sampling. All MD simulations were performed under the NVT ensemble using a Nose-Hoover thermostat[32,33] to maintain a system temperature of 298.15K. Hydrogen bonds were constrained using the LINCS algorithm[34], removing high-frequency atomic motions, and affording a time step of 2fs to be used for the compression and shear stages. The Particle-Mesh Ewald method[35,36] was

used for long-range electrostatics, using a force and pressure correction in the z-dimension to support slab geometries.

The molecular dynamics workflow was maintained and executed using the Signac workflow manager (v0.5.4), a part of the Signac framework.[6] With Signac-flow, individual molecular dynamics operations (e.g., equilibration) were wrapped into Python functions. These operations were then performed on each state point (i.e., each system), where Signac-flow kept track of all operations that had been performed on each state point.

All simulations were performed on the Titan supercomputer located at Oak Ridge National Laboratory.

5.2.4 Tribological and Structural Analysis Methods

As with the molecular dynamics workflow, management and execution of analysis routines was governed by the Signac (v0.8.5) and Signac-flow (v0.5.4) Python packages within the Signac framework.[6] Monolayer tribology is evaluated via calculation of the coefficient of friction (COF) and adhesive force as defined by the Derjaguin form of Amontons' Law of Friction detailed in Appendix B.1, Eq. B.1. For each dual-monolayer system, shear simulations are performed under a series of normal loads (5, 15, and 25nN), and the average friction force is measured for each simulation, allowing the COF and force of adhesion to be determined from Eq. B.1 through linear regression. Values reported for each interfacial chemistry (i.e. unique combination of terminal groups) represent the average of the five systems with different chain configurations on the surface.

In addition to tribological metrics, monolayer structure is also examined through use of a nematic order parameter, as defined in Appendix B.2, Eq. B.2.

5.2.5 QSPR Modeling

Monolayers are also examined via the development of topological quantitative structure-property relationship (QSPR) models relating characteristics of the monolayer chemistries

to their tribological response. These models are given as an input a "fingerprint" for each system, which represents each system as a series of numerical values. These numerical values are referred to as "molecular descriptors" and characterize a variety of molecular aspects such as size (e.g. approximate surface area), shape (e.g. asphericity), and charge distribution (e.g. topological polar surface area). Calculation of molecular descriptors is facilitated through use of the RDKit Python package.[37] While the majority of these descriptors are topological, meaning they are inferred from the molecular graph, several additional descriptors are considered that require a 3D molecular conformation. These conformations are generated by RDKit using the Experimental-Torsion Distance Geometry approach with "basic knowledge" terms (ETKDG), as proposed by Riniker and Landrum.[38] For descriptors requiring information concerning molecular charge, charges are assigned via RDKit to the molecular graph using the approach of Gasteiger and Marsili.[39] Along with the descriptors calculated via RDKit, we have introduced an additional descriptor, which we call the "hydrogen bond factor" that provides a relative estimate of the availability for intermonolayer hydrogen bonding. The descriptor is calculated using counts of the number of

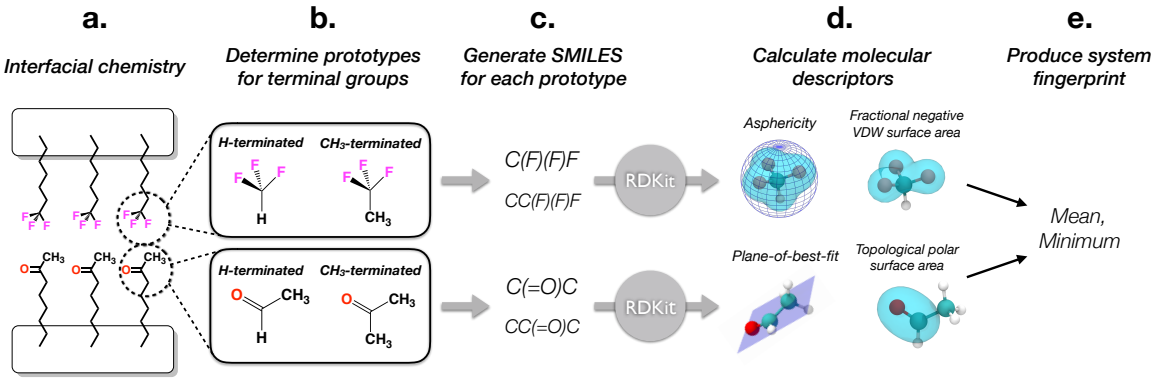

Figure 5.2: Workflow of the process used to fingerprint each interfacial chemistry. a. For a given interfacial chemistry (a perfluoromethyl-acetyl system is shown as an example), H-terminated and CH_3 prototypes are utilized for each terminal group (b.). These prototypes are converted to SMILES representations (c.), which are fed to the RDKit Python package used to calculate a variety of molecular descriptors (d.). e. The fingerprint for the interfacial chemistry is then described by the mean and minimum values for all molecular descriptors calculated for the two terminal groups.

hydrogen bond donor and acceptor atoms in the two terminal groups of a dual monolayer system via:

$$hb_{tb} = \begin{cases} 0 & min(0, max(d_t, a_b)) = 0 \\ max(d_t, a_b) & min(0, max(d_t, a_b)) > 0 \end{cases} \tag{5.1}$$

$$hb_{bt} = \begin{cases} 0 & min(0, max(d_b, a_t)) = 0 \\ max(d_b, a_t) & min(0, max(d_b, a_t)) > 0 \end{cases} \tag{5.2}$$

$$hbonds = hb_{tb} + hb_{bt} \tag{5.3}$$

where d and a represent the number of hydrogen donor and acceptor atoms present in terminal groups for the top (t) or bottom (b) monolayers. A complete list of all descriptors used, including brief descriptions of each, is provided in Appendix D.1.

The strategy used in this work for performing fingerprinting of dual monolayer systems is shown in Fig. 5.2, where the primary challenge concerns how to properly design a system fingerprint that can be used for both chemically-identical and chemically-dissimilar systems (where the contributions of both terminal groups must be accounted for). First, as shown in Fig. 5.2a-d., "molecular fingerprints" (i.e. fingerprints for individual molecules rather than the complete dual monolayer system) are calculated for the terminal groups of each monolayer. In molecular fingerprinting, a decision must be made concerning the molecule used to represent each terminal group. Here, we utilize two separate molecules to represent terminal groups (as shown in Fig. 5.2b), calculating a subset of molecular descriptors on each. Specifically, molecules featuring terminal groups capped by hydrogen atoms (where the hydrogen atom is attached at the location where the terminal group is attached to the chain backbone in the complete chain) are used in the calculation of descriptors that relate to molecular shape, while molecules featuring terminal groups capped by methyl groups are used in the calculation of the remaining descriptors. The methyl group is chosen as this chemistry is comparable to that of the chain backbone, and thus

these molecules should provide a reliable distribution of charge (as again, we use Gasteiger charges for fingerprinting as opposed to OPLS charges to simplify data inputs).

Our approach to molecular fingerprinting relies only upon information of the molecular bond graph as an input. As such, molecules are provided to RDKit in the notation of the simplified molecular-input line-entry system (SMILES)[7], shown in Fig. 5.2c. This provides a concise input syntax that allows the QSPR models in this work to be easily extensible to additional terminal group chemistries beyond those considered here. After providing RDKit with SMILES representations of the two molecules representing each terminal group in a given system, molecular fingerprints are generated for each terminal group, shown in Fig. 5.2d. System fingerprints are then created from the two molecular fingerprints by using the mean and minimum values of each component (descriptor) of the molecular fingerprint (shown in Fig. 5.2e). While other combinations of these values (such as the maximum and absolute difference) were considered, analysis of correlations with the target variables (COF and adhesion) suggested only the mean and minimum values were needed, which also helps reduce complexity of the QSPR models.

A random forest regression algorithm[40,41] is used for QSPR models, as implemented in the scikit-learn Python package.[42] Random forest is an ensemble method that utilizes a forest of decision trees obtained from bootstrap sampling of the training data and produces a prediction based on the average values obtained for each tree. This algorithm is a popular choice in the literature for machine learning models; for example, Ballester et al. used random forest to predict binding affinities of protein-ligand complexes.[43] Predictions from random forest converge for a large number of decision trees[44], thus, a large number of 1000 trees are used in this work. One reason for the choice of the random forest algorithm is that contributions to the model from the various molecular descriptors can be easily extracted, and furthermore, interaction terms are implicitly included by the nature of the algorithm. Evaluation metrics for these models consist of the root-mean-square error (RMSE), mean absolute error (MAE), and the coefficient of determination (R^2) between the predicted and

expected target values within both the training set and a 20% holdout test. Additional model evaluation is accomplished via out-of-bag (OOB) sampling, whereby predictions are made on subsets of the data held out for each tree. The RMSE, MAE, and R^2 on the out-of-bag estimates of each sample are provided as an additional measure of model efficacy.

5.3 Results and Discussion

5.3.1 Chemically-Identical Monolayer Films

As a test of model accuracy and to serve as a baseline for the examination of more complex monolayers, relationships between chemistry and tribology are first examined be-

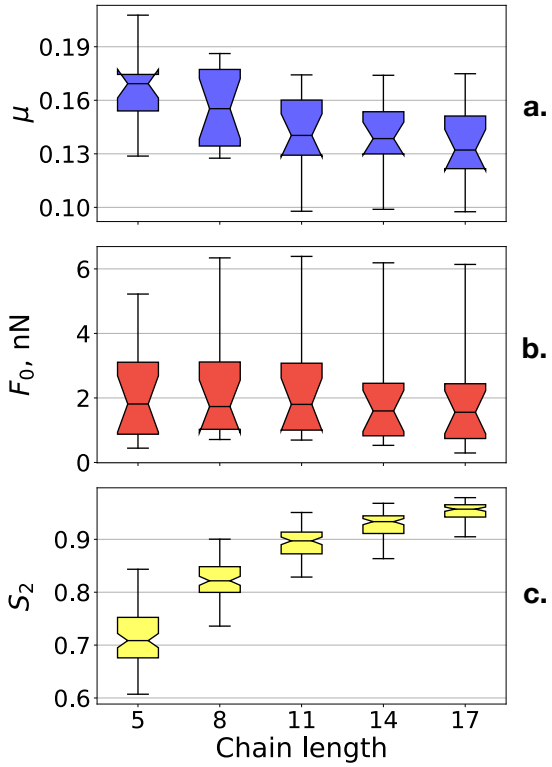

Figure 5.3: Box plots showing a. coefficient of friction (μ), b. adhesive force (F_0), and c. nematic order (S_2, measured during shear under a normal load of 15nN) as a function of backbone chain length for systems of two chemically-identical monolayer films. Filled regions correspond to the interquartile range (IQR), while whiskers extend from the minimum and maximum values of the data. Notches are present, along with a line, to denote the median.

tween contacting monolayers with identical chemistries. The effect of backbone chain length is explored by calculating both tribological properties (COF and adhesion force) and structural properties (nematic order) for systems with chain lengths ranging from 5 to 17 backbone carbons, shown in Figure 5.3 in the form of box plots (where data for all chemically-identical systems has been included). The effects of backbone chain length on friction have been explored extensively in the literature[14,45–50] and a comparison to these results helps verify that our model produces similar trends. It has been noted in several studies that the addition of carbons to the chain backbone should correlate with a reduction in the COF.[14,45,46,50] Fig. 5.3a reveals this expected trend, where the COF decreases as the backbone chain length is increased from 5 to 8 to 11 carbons, at which point further increases in chain length appear to have little additional effect. It should be noted that while the range of the COF data is shown to overlap for all chain lengths examined, this is due to effects of the chain terminal groups (examined in detail later in this chapter) on each property, and that for any given chemistry the trend is more pronounced (see individual plots provided in Appendix D.2). Furthermore, the decrease in COF with increased chain length has often been attributed to an increased ordering of monolayer chains[46], due to an increase in favorable VDW forces between neighboring chain backbones. Here, monolayer order is quantified via the nematic order parameter and is shown in Fig. 5.3c as a function of chain length. The expected trend is observed, whereby the monolayer nematic order is found to increase as the backbone chain length is increased. Again, the range of the data is the result of influence by the terminal group chemistry, and this range is found to decrease as backbone chain length increases; suggesting, as one might expect, that terminal group chemistry has diminishing effects on monolayer structure as the backbone chain length is increased. The ability to capture the expected trends of decreased COF and increased nematic order as chain length is increased helps verify the efficacy of our model.

Additionally, the effect of backbone chain length on the adhesive force between the monolayers during shear, quantified via the Derjaguin offset, F_0 in Eq. B.1, has been ex-

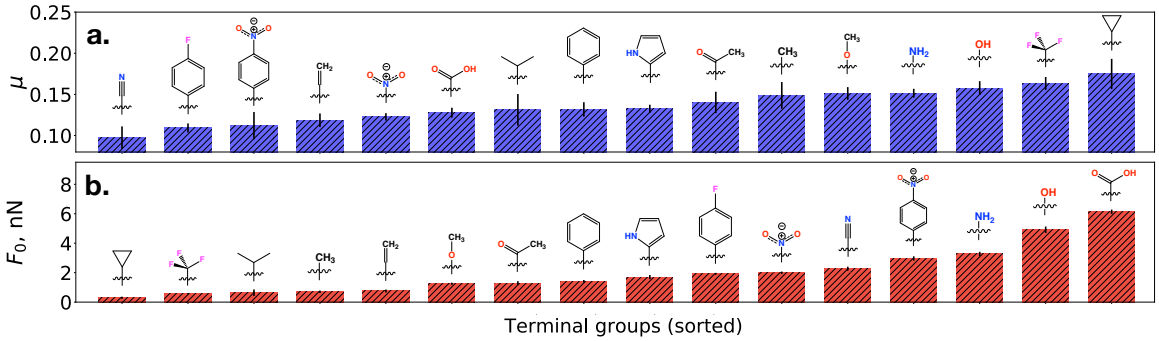

Figure 5.4: Bar graphs displaying a. coefficient of friction and b. adhesive force as a function of terminal group chemistry for monolayers with a backbone chain length of 17 carbons.

amined, shown in Fig. 5.3b. It is found that for the data as a whole, chain length has little effect on the adhesive force, particularly relative to the effects of the terminal group chemistry (apparent in Fig. 5.3b by the large range of the data). A slight increase in the maximum adhesion value in the data set is observed as chain length is increased from five to eight carbons, after which successive increases in chain length appear to have no influence. The systems with the largest adhesive force are found to be the carboxyl-terminated films, with the large value of adhesion the result of inter-monolayer hydrogen bonding, as has been observed in the literature.[14] Interestingly, it appears the system's ability to form hydrogen bonds is impaired for the lowest chain length, likely due to disorder in chain orientations. As monolayer order increases when the backbone chain length is increased to eight carbons, chains become better able to orient themselves to form inter-monolayer hydrogen bonds and adhesion increases. Plots showing COF, the force of adhesion, and nematic order for each individual terminal group chemistry as a function of chain length are provided in Appendix D.2.

The range of the data in Fig. 5.3 for both COF and the force of adhesion for all chain lengths suggests that terminal group chemistry influences both properties. To isolate the effects of terminal group chemistry, Figure 5.4 shows, in the form of bar charts, the COF and adhesion force calculated for systems with only a backbone chain length of 17 carbons.

From Fig. 5.4 it is indeed observed that terminal group chemistry influences both COF and adhesion, although the effects on adhesion are more profound. Specific trends between terminal group properties and COF from the results of Fig. 5.4a are not immediately obvious. COF appears to be independent of the size of the terminal group, as large terminal groups are shown to yield both low (fluorophenyl) and high (cyclopropyl) COFs. Terminal group polarity also does not appear to influence COF, as polar and nonpolar groups are shown to yield both high and low values of COF. Thus, a direct comparison between systems appears insufficient at unearthing the specific terminal group characteristics that influence COF. Instead, a more comprehensive approach is required and will be addressed further in this chapter via the development of QSPR models.

In contrast to COF, trends between terminal group chemistry and adhesion, shown in Fig. 5.4b, are fairly clear. It appears there is a strong correlation between terminal group polarity and adhesion, as might be expected, as the terminal groups with the largest adhesion forces are all polar molecules and the groups with the smallest forces are all nonpolar. Furthermore, the three terminal groups yielding the highest adhesive forces are all groups that can participate in inter-monolayer hydrogen bonding, again agreeing with results from the literature.[51] In fact, the results shown in Fig. 5.4b further support the link between hydrogen bonding and adhesion, as the order of the three systems with the highest adhesive forces (carboxyl, hydroxyl, and amino, from highest to lowest) corresponds with expected hydrogen bond strengths.

5.3.2 Chemically-Dissimilar Monolayer Films

Although Fig. 5.4 provides some insight into the relationships between terminal group chemistry and both COF and adhesion values, such analysis still relies upon one's chemical intuition. Furthermore, no apparent trends are present between terminal group chemistry and COF, yet the range of the data, while smaller relative to that of adhesion, suggests that there is indeed a relationship. As a means to collect data for additional interfacial

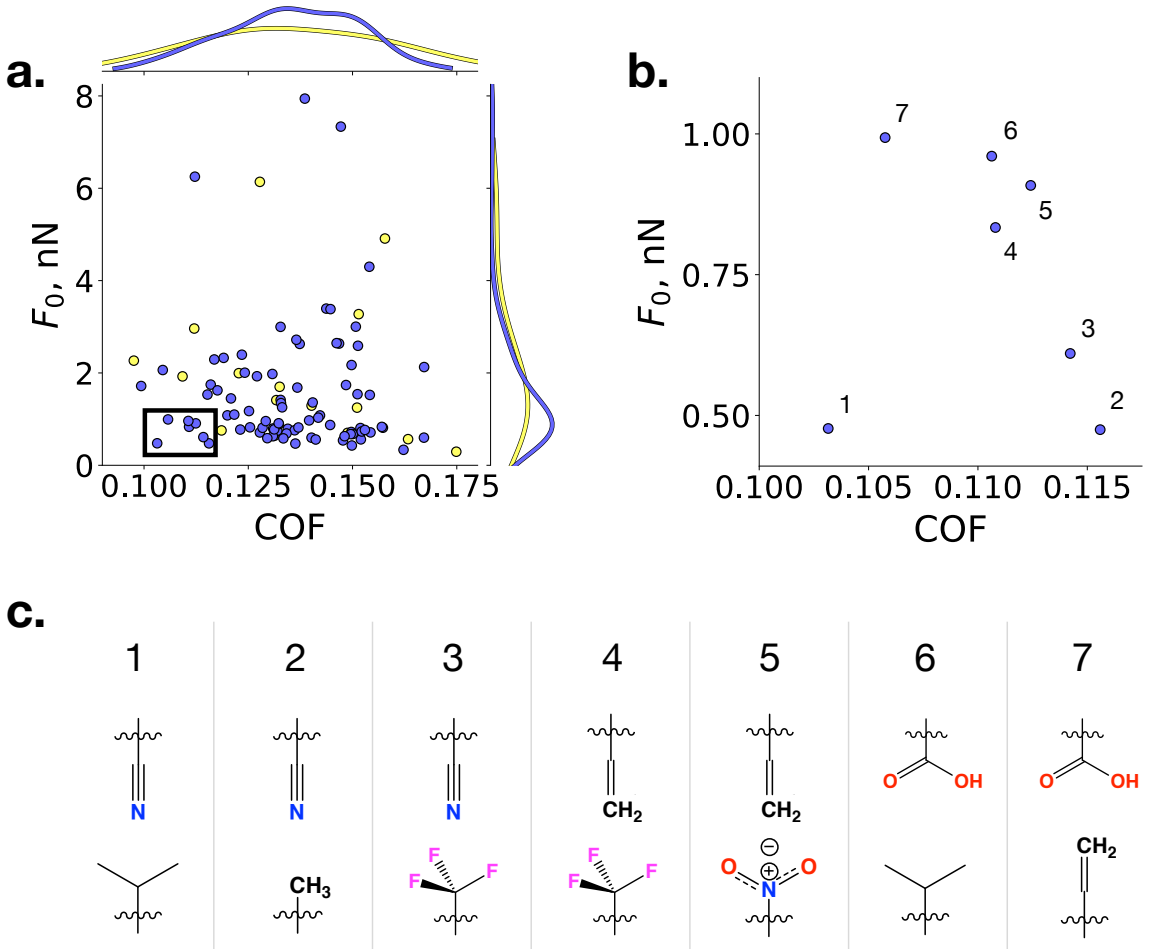

Figure 5.5: a. Scatter plot of COF and adhesion force data for chemically-identical systems (yellow) and chemically-dissimilar systems (blue). Distributions of these two variables are also shown. The boxed region highlights the area featuring the most tribologically favorable systems and is enlarged in b., where the seven systems in this region are annotated and the corresponding terminal group chemistries are shown in c.

compositions, without the need to introduce new terminal group chemistries, a collection of simulations featuring systems of chemically-*dissimilar* monolayer films has been performed, using the model shown in Fig. 5.1c. Specifically, 420 chemically-dissimilar systems, all with a backbone chain length of 17 carbons, are examined, corresponding to 84 unique interfacial chemistries (as the results of five different monolayer surface configurations are averaged for each interfacial chemistry). This helps expand the dataset, as, e.g. a "hydroxyl-methyl" system should provide unique tribological properties distinct from either a "hydroxyl-hydroxyl" or "methyl-methyl" system. With the increased size of

the data set, QSPR models can be developed to provide both greater insight into relationships between terminal group chemistry and tribology (through extraction of the relative contributions of the various components of the models), along with predictive capacity for terminal groups not included in this study. The information garnered from these models can be utilized to aid in further exploration of the monolayer chemical parameter space by identifying regions of interest and regions where tribological properties are predicted to be poor. However, first, the results of these chemically-dissimilar monolayer systems are compared with the chemically-identical results to see if the mixing of monolayer chemistries yields tribological benefit, as has been suggested by experimental results.[13,14,52,53]

In Fig. 5.5a the COF and adhesion results for all systems, both chemically-identical and chemically-dissimilar, are shown alongside the distributions of both of these properties for the complete dataset. The ideal monolayer chemistry should feature both a low COF and low adhesive force. As such, systems with favorable chemistries would exist in the lower left hand corner of the plot. From Fig. 5.5a, the distribution observed for both COF and adhesion of the chemically-dissimilar systems is similar to that observed for the chemically-identical systems, suggesting that simply mixing chemistries is not sufficient enough to provide substantially improved lubricity across the whole range. Nonetheless, there are several chemically-dissimilar systems that do appear to provide favorable tribological properties, as highlighted in Fig. 5.5b and c. Interestingly, the majority of these systems feature one monolayer that is polar/hydrophilic and another that is nonpolar/hydrophobic. This helps highlight the potential advantages of using a lubrication scheme where the two contacting surfaces feature different lubricant molecules. For example, two of the systems shown in Fig. 5.5b and c. feature one monolayer that is terminated by carboxyl groups. Carboxyl-terminated monolayers are found to yield the highest adhesive forces for chemically-identical systems (Fig. 5.4b), yet when paired with a nonpolar countermonolayer the ability to form inter-monolayer hydrogen bonds is eliminated, and these combinations of terminal groups are able to provide favorable COF and adhesion values.

This agrees with results in the literature that have observed reduced COF and adhesion for polar-nonpolar systems[14,52,54], although we note that the effects on COF here are weaker than observed in the cited experimental studies. Along with carboxyls, several other terminal group chemistries are found to appear in multiple systems in Fig. 5.5b and c. In fact, the three systems observed to have the lowest adhesive forces, including the system that also features the lowest COF, all feature one monolayer that is terminated by a nitrile group. Additionally, vinyl-terminated monolayers are also present in several of these systems. While these two groups (nitrile and vinyl) have several differences (e.g., chemical composition, polarity), they share many features as well. Both groups are linear and feature a cylindrical shape with a small VDW radius. It appears possible that these aspects, combined with the more rigid nature owed to these groups by the presence of a double or triple bond, lends towards more favorable tribological properties.

To further explore how the mixing of monolayer chemistries alters tribological response, the COF and adhesion of chemically-dissimilar monolayers has been predicted from the results calculated for chemically-identical systems using a simple arithmetic mean. For example, the COF and adhesion of a "hydroxyl-methyl" system is estimated by taking the average of the COF and adhesion calculated for the "hydroxyl-hydroxyl" and "methyl-methyl" systems. If the estimation over-predicts the actual value, that would suggest that the mixing of monolayer chemistries provides an advantageous route to improving monolayer tribological performance. The actual vs. expected values for both COF and adhesion using this approach are shown in Fig. 5.6. Interestingly, from Fig. 5.6a it is observed that the COF of chemically-dissimilar systems is reasonably-approximated by the averaging of values from the chemically-identical systems, as the COF of nearly all chemically-dissimilar systems is predicted correctly within error of the measurement. This result suggests that the use of chemically-dissimilar surfaces does not provide a route towards directly reducing COF, at least for the subset of systems considered here.

Conversely, Fig. 5.6b shows that the force of adhesion is not well predicted by this

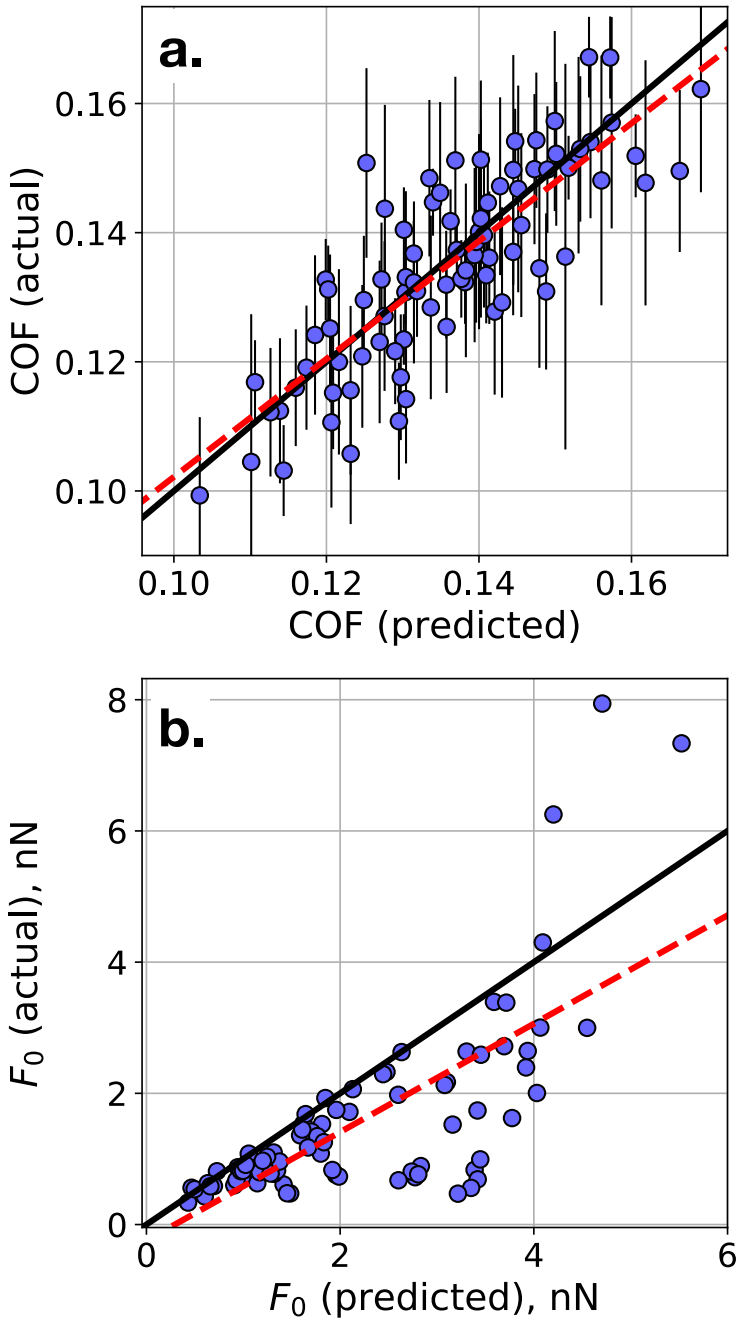

Figure 5.6: Predicted values of a. COF and b. adhesive force for chemically-dissimilar monolayer systems, as calculated by the mean of the values obtained for chemically identical systems, compared to the actual values. The y=x line is drawn in black for reference, while the dashed red line represents a linear regression of the data. Each unique surface chemistry (averaged over five monolayer surface configurations) is represented by a single point, and errors bars represent a single standard deviation calculated from the estimation of these five configurations.

approach, as was expected from the systems shown in Fig. 5.5. This follows similar reasoning to that given for the presence of several carboxyl-containing systems in Fig. 5.5c, namely that if one monolayer in a system is terminated by a polar functional group and the other is terminated by a nonpolar functional group, the adhesive force will be most similar to that of the pure nonpolar system, rather than an average of the two. As a result, when predicting the adhesive force for chemically-dissimilar systems featuring a mixture of polar and nonpolar groups using mean data from chemically-identical systems, adhesion values are over-estimated, as evidenced by the high concentration of points below the y=x line in Fig. 5.6b.

While COF appears to not be lowered through the mixing of monolayer chemistries, the ability to reduce adhesion in the case of polar-nonpolar systems still presents an advantage of this approach. For example, in Fig. 5.4a, nitrile-terminated monolayers were observed to feature the lowest COF for chemically-identical films, yet the adhesive force for these films (2.27nN $\pm$ 0.14nN) is prohibitively high due to their polarity. However, when paired with a countermonolayer that is hydrophobic, the adhesion force is decreased while the COF is largely unaffected. *Thus, the use of chemically-dissimilar surfaces provides a means to utilize terminal groups that yield low COFs, even if they would normally feature a large adhesive force, provided the other monolayer is hydrophobic.*

While the difference in COF between nitrile-terminated films, and other, hydrophobic films (such as vinyl), is found to be slight, there may be polar terminal groups not included within this study that yield lower COFs, and the use of chemically-dissimilar monolayers would provide a route to take advantage of that property. It should be noted again, however, that the result of Fig. 5.6a, suggests that the lower bound of COF is not reduced by the mixing of monolayer chemistries (i.e. the COF of the mixed system will not be lower than the lowest COF of either of the chemically-identical systems). Thus, if seeking to reduce COF, it appears that additional modifications to the monolayer would be necessary; either using a functional group not included in the pool of this study or through some other means

such as the use of multicomponent films to expose different friction mechanisms.

5.3.3 QSPR Modeling

While Fig. 5.6a suggests that the use of chemically-dissimilar monolayers does not provide a route to directly reducing COF from a pure system, the data collected for the 100 unique interfacial chemistries (considering only systems with backbone chain lengths of 17 carbons) does provide adequate sampling to develop QSPR models for the prediction of COF and adhesion for systems of arbitrary chemistry and can be used to aid in further exploration of the monolayer chemical parameter space in future studies. Furthermore, if systems are properly fingerprinted through the use of ample molecular descriptors, aspects of terminal group functionality that contribute most strongly to these properties can be extracted from these models and exploited in the design of better-performing monolayers. Using the freely-available RDKit Python package over 30 descriptors can be calculated for each terminal group (a complete list of the descriptors used is available in the Appendix D.1) and dual-monolayer systems can be fingerprinted using this information following the workflow shown in Fig. 5.2. To aid in model interpretation, we have categorized these molecular descriptors into those that aid in characterization of molecular shape, size, complexity (such as degree of branching), and charge distribution. These clusters are visualized in Fig. 5.7.

Models for COF and adhesion were derived using a random forest algorithm, and Table 5.1 details the RMSE, MAE, and the coefficient of determination (R^2) between the predicted and expected target values within both the training set and a 20% holdout test set for QSPR models of COF and adhesion, along with metrics for out-of-bag samples. In addition to our primary model (Model 1 in Table 5.1), four additional models (Models 2-5) were developed to provide further insight into performance dependence on test-train splits. It is observed from Table 5.1 that the models for both COF and adhesion perform consistently well. Random forest is known to overfit to the training data, so the high R^2

values observed for the training data sets are expected, and do not alone provide a great metric for the model's performance. However, R^2 values above 0.6 are observed for both the test data as well as for the out-of-bag samples for both models, providing more reliable estimates of model performance, and suggesting respectable predictive power. In particular, the out-of-bag results should be emphasized, as for the small data set considered here (100 total samples, only 20 of which are included within the test set) evaluation metrics on the test data set for the five models shown in Table 5.1 are shown to feature moderate fluctuation. This suggests that for some models the small test set does not provide a good representation of the overall population (or at least, the feature distributions within the train and test sets differ). However, the evaluation metrics obtained for out-of-bag samples are found to remain mostly stable between the five models, providing greater confidence in these results and in the models' predictive power. Although R^2 values of 0.6 may not appear exceptional at first, these results are in fact quite remarkable when considering the simplicity of the inputs required. The simulations in this work were performed using the OPLS force field, while molecular descriptors were calculated for terminal group moieties

Charge distribution	*Complexity*	*Shape*	*Size*
H-bond factor	*Balaban's J*	*Asphericity*	*Approximate surface area*
logP	*Bertz C_T*	*Eccentricity*	*Molar refractivity*
Relative maximum charge (+ and -)	*Chi indices*	*HK alpha*	*Molecular weight (w/ and w/o H)*
Topological polar surface area	*Information content, I_{pc}*	*HK kappa indices*	*# heavy atoms*
Total and fractional VDW surface area contributions		*Inertial shape factor*	*# rotatable bonds*
		Normalized principal moments ratios	*# valence electrons*
		Principal moments of inertia	
		Radius of gyration	
		Spherocity	

Figure 5.7: Features considered for QSPR models, grouped into clusters describing charge distribution, complexity (i.e., degree of connectivity/branching), shape, and size. Additional descriptions of these features can be found in Appendix D.1.

Table 5.1: Evaluation of random forest regression models for COF and F_0 [†]

Model	Target Variable	Training set			Out-of-bag			Test set		
		R^2	RMSE	MAE	R^2	RMSE	MAE	R^2	RMSE	MAE
1	COF	0.9496	0.0037	0.0029	0.6306	0.0100	0.0079	0.6524	0.0090	0.0068
	F_0 (nN)	0.9600	0.2644	0.1383	0.6985	0.7259	0.3782	0.6905	0.9530	0.4237
2	COF	0.9473	0.0036	0.0027	0.6067	0.0099	0.0074	0.6049	0.0110	0.0086
	F_0 (nN)	0.9539	0.3067	0.1473	0.6586	0.8351	0.4046	0.9422	0.3252	0.2439
3	COF	0.9418	0.0037	0.0028	0.5594	0.0101	0.0078	0.6571	0.0114	0.0087
	F_0 (nN)	0.9747	0.2283	0.1233	0.7978	0.6452	0.3410	0.4066	1.0031	0.5579
4	COF	0.9471	0.0038	0.0029	0.6029	0.0104	0.0081	0.8204	0.0062	0.0048
	F_0 (nN)	0.9435	0.2974	0.1406	0.5740	0.8165	0.3844	0.7787	0.8453	0.6076
5	COF	0.9484	0.0038	0.0030	0.6043	0.0106	0.0081	0.5199	0.0096	0.0069
	F_0 (nN)	0.9613	0.2642	0.1388	0.7119	0.7213	0.3797	0.6367	1.0031	0.4699
Average	COF	0.9468 ± 0.0027	0.0037 ± 0.0001	0.0029 ± 0.0001	0.6008 ± 0.0230	0.0102 ± 0.0003	0.0079 ± 0.0003	0.6509 ± 0.0980	0.0094 ± 0.0018	0.0072 ± 0.0014
	F_0 (nN)	0.9587 ± 0.0102	0.2722 ± 0.0278	0.1377 ± 0.0079	0.6882 ± 0.0729	0.7488 ± 0.0693	0.3776 ± 0.0206	0.6909 ± 0.1759	0.8259 ± 0.2569	0.4606 ± 0.1261

[†] The following metrics are used for evaluation; R^2: coefficient of determination between predicted and actual values, RMSE: root-mean-square error, MAE: mean absolute error

provided to the models in the form of SMILES, where Gasteiger charges were assigned in place of OPLS charges and 3D conformations were generated through a stochastic method. If OPLS charges and 3D structures generated using OPLS had been provided to the models, their ability to predict values of COF and adhesion *would have been limited* to only those chemical moieties that could be described by OPLS. However, by using generic SMILES as inputs, arbitrary molecules that may not be parameterized for use with OPLS can still have values of COF and adhesion predicted. Thus, the models should have utility in future studies with the aim of further exploring the monolayer chemical parameter space.

To provide visual evaluation of the models for COF and adhesion, Fig. 5.8 shows both the training data and the test data used to generate and evaluate each model (Model 1 from Table 5.1). It is found that for COF, the majority of the test data sits close to the y=x line, with no significant deviations, further corroborating the positive evaluation from Table 5.1. Meanwhile, for adhesion, it is shown in Fig. 5.8b that the model's predictive capacity is best for systems with low values of adhesion. Particularly for systems with adhesion forces greater than 4nN the model appears to under-predict these values. Systems in this region correspond to those that feature inter-monolayer hydrogen bonds. Fortunately, this regime is of least concern, as interfacial chemistries featuring large adhesive forces would feature

poor performance as lubricants. Thus, the fact that the model still properly acknowledges the large adhesion values for these systems, despite under-predicting them, allows for these

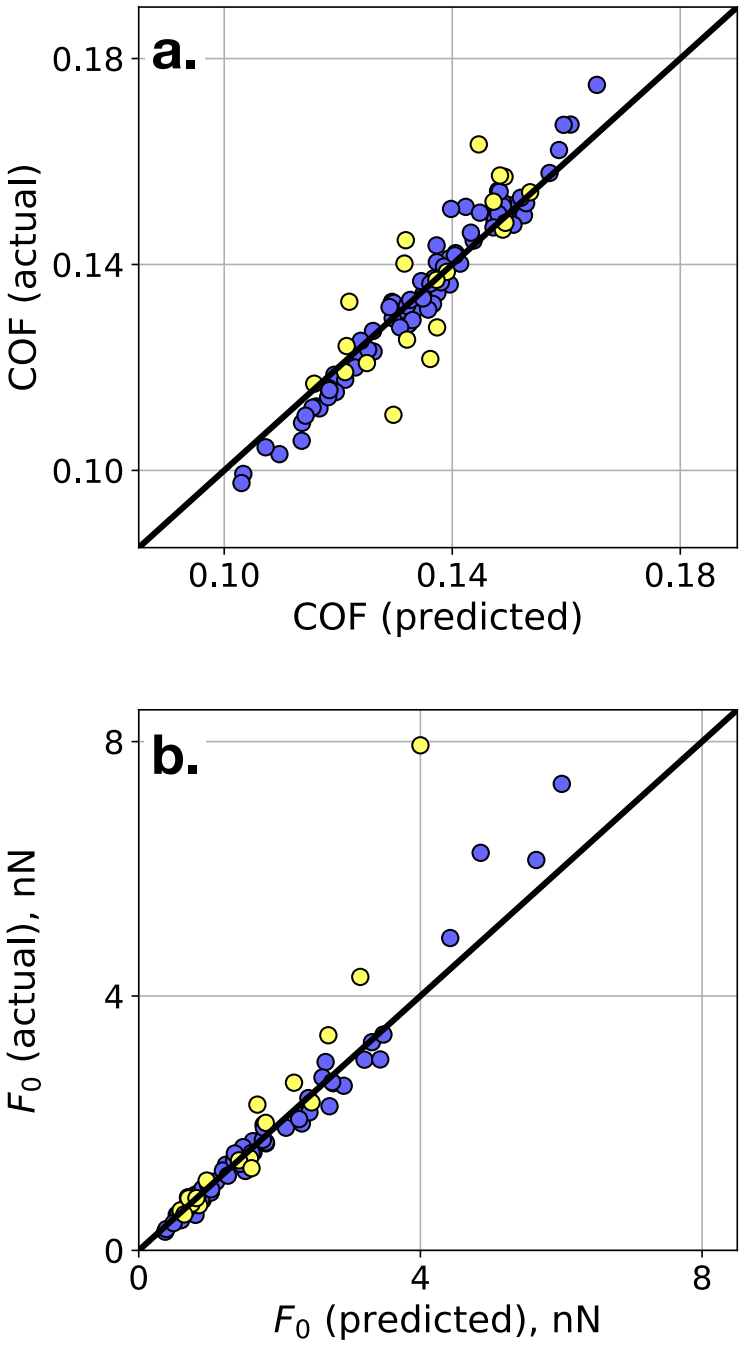

Figure 5.8: Values predicted by QSPR models (Model 1 in Table 5.1) for a. COF and b. adhesive force compared to the actual values. The y=x line is drawn in black for reference. Points in blue denote data used as part of the training set, while points in yellow denote data that was part of the test set.

systems to be properly screened out.

Following establishment from Table 5.1 and Fig. 5.8 that the random forest models perform well at predicting COF and adhesion, the relative contributions to the performance of each model, the "feature importances", can be extracted to evaluate which elements of the system fingerprint have the most influence over each variable. Fig. 5.9 provides the

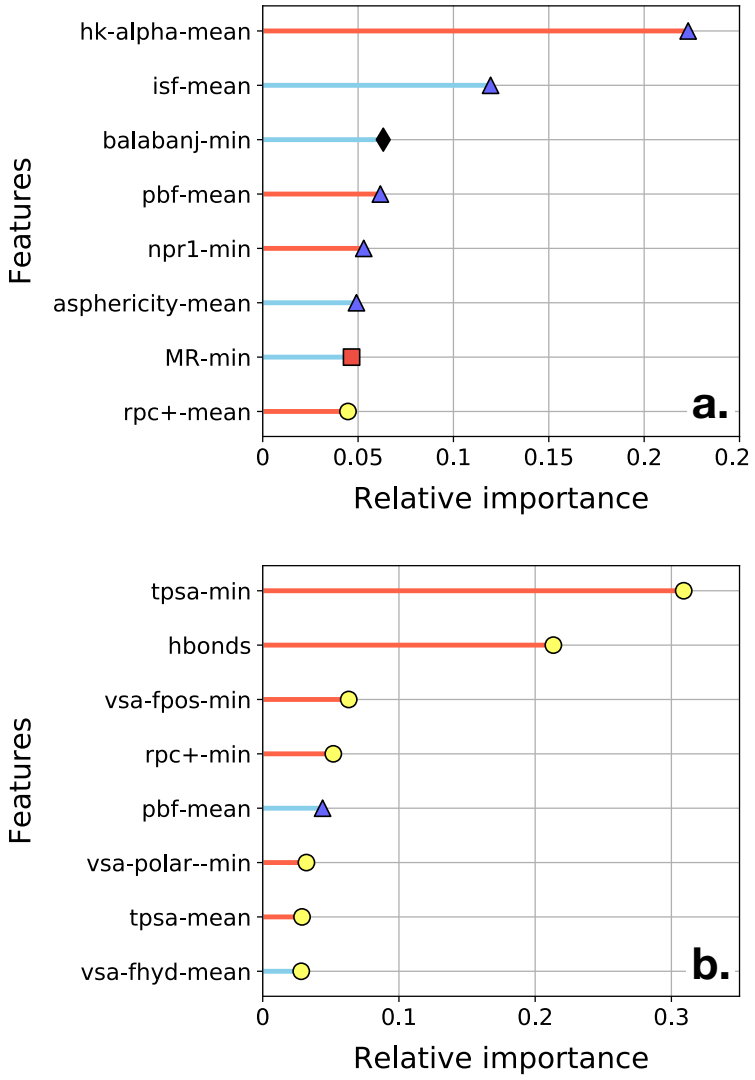

Figure 5.9: Relative feature importances extracted from the random forest regression models for a. COF and b. adhesion. Symbols represent the molecular aspect characterized by each feature from the cluseters defined in Fig. 5.7 (yellow circles: charge distribution, blue triangles: shape, red squares: size, black diamonds: complexity). Stick colors represent whether each feature correlates positively (red) or negatively (light blue) with the target variable.

relative contributions of the eight molecular descriptors with the highest contributions to the prediction of COF and adhesion. The "-mean" or "-min" in the descriptor name indicates whether this corresponds to the mean or minimum value, respectively, of the descriptor for the two terminal groups in the system (refer back to Fig. 5.2e). For COF, it is observed that the majority of features with high contributions to the model are those which describe molecular shape. In particular, the molecular descriptor with the largest contribution is the mean Hall-Kier alpha value between the two terminal groups in the system. The Hall-Kier alpha is described by[55]:

$$\alpha = \sum_{i=1}^{A} \left(\frac{R_i}{R_{C_{sp^3}}} - 1 \right) \tag{5.4}$$

where A is the number of (non-hydrogen) atoms in the molecule, $R_{C_{sp^3}}$ is the covalent radius of sp^3 carbon, and R_i is the covalent radius of atom i. From this definition, the Hall-Kier alpha is shown to provide a measure of hybridization, where contributions to alpha decrease from $sp^3 > sp^2 >$ sp hybridized atoms. Thus, planar (such as aromatic, carboxyl, and vinyl) and linear (such as nitrile) groups will feature lower alpha values. Furthermore, as alpha is not normalized, larger molecules will have larger values of alpha. From Fig. 5.9a it is observed that a positive correlation between the Hall-Kier alpha and COF exists. Thus, COF will be minimized for terminal group moieties that are both small and planar or linear. This result helps explain the low COFs observed for systems featuring at least one monolayer terminated by a nitrile group, as shown in Fig. 5.5c. Furthermore, this finding agrees with results from the literature which have suggested that bulky terminal groups may lead to higher frictional forces through introduction of collective energy dissipation modes.[30,56,57] Smaller, linear groups, such as nitriles, will feature less steric overlap, which promotes reduced COFs. Furthermore, the majority of the top contributing descriptors to predictions of COF, shown in Fig. 5.9a, are found to be those which describe mean values between the two contacting monolayers in the system. This is consistent with the results of Fig. 5.6a, which showed that the COF of chemically-dissimilar systems is well-predicted by the mean values of the chemically-identical systems relating to the two terminal groups

in the system.

Feature contributions to the QSPR model for the prediction of adhesion are shown in Fig. 5.9b. Following expectations, nearly all of the top contributing molecular descriptors provide measures of the distribution of charge on the terminal group. Furthermore, nearly all of these descriptors are found to be those that correspond to the minimum value between the two terminal groups, rather than the mean value. The top contributing feature is found to be the minimum topological polar surface area between the two terminal groups. That this feature is a strong predictor of adhesion is sensible, as large adhesive forces will require both terminal groups in the system to feature significant charge imbalances (i.e., large dipole moments). For such systems, the larger the area of charge imbalance, the stronger the adhesive force will be. However, if one of the monolayers features a terminal group with a low polar surface area (a nonpolar molecule such as a hydrocarbon), the adhesion force between the two monolayers will be low. This agrees with the findings of Fig. 5.5c and Fig. 5.6b. The second top contributing feature to adhesion is observed to be the "hbonds" descriptor, developed in this work and described by Eqs. 5.1-5.3. This descriptor characterizes a system's ability to form inter-monolayer hydrogen bonds. While systems featuring inter-monolayer hydrogen bonding are found to not have their adhesive forces predicted with high accuracy, as evidenced by Fig. 5.8b, the addition of the "hbonds" descriptor does allows the model to a qualitatively correct prediction that such systems will feature high adhesion. Thus, for future exploration of the monolayer chemical parameter space, such systems can be successfully filtered out with this model.

In addition to providing insight into aspects of terminal group chemistry that have the greatest influence on COF and adhesion, the models generated in this work should also have utility in predicting values for these variables for systems with arbitrary terminal group chemistry, which should aid in further exploration of the monolayer chemical parameter space. These models have been developed to require only a molecular bond graph, which can be provided in a SMILES representation, making predictions easily accessible.

The models themselves are hosted on GitHub *, along with all of the code related to this work.[58,59] As emphasized in the Introduction, the monolayer chemical parameter space is vast, and brute force exploration is costly. Each system in this work required roughly 16 real hours of computing time to perform all MD simulations and analysis, despite GPU acceleration. Thus, expanding such a study to 1000s or 10000s of systems would be intractable through a purely brute force approach. The models derived here should find utility in filtering areas of this parameter space where exploration is unnecessary (large values of COF or adhesion). The use of these models in such a predictive capacity will be explored in future work.

5.4 Conclusions

In this work, the screening of functionalized monolayer films, enabled by use of the MoSDeF software suite and Signac framework, has been performed using MD simulations. In agreement with prior literature, increases in the length of the chain backbone are found to reduce COF and increase monolayer order. Adhesion between monolayer films is observed to be relatively insensitive to backbone chain length. The effects of terminal group chemistry on monolayer tribology are examined for both chemically-identical systems (i.e., where both monolayers feature the same chemistry) and chemically-dissimilar systems. It is observed that combinations of polar and nonpolar terminal groups in chemically-dissimilar films yield favorable tribological properties (i.e., low COF and low adhesion). However, the COF of chemically-dissimilar films is found to be well-predicted from a simple mean of the COF values for each of the two terminal groups individually, suggesting that the mixing of monolayer films does not provide a route towards reducing COF beyond pure systems. The utility of chemically-dissimilar systems appears primarily in the reduction of adhesion through the inclusion of at least one nonpolar terminal group.

*GitHub repositories have been set to private until submission of the related manuscript at which point they will be made public.

The breadth of the data in this study has afforded the ability to generate QSPR models, which require a simple SMILES representation as an input, and are found to yield reasonable predictive capability. Feature extraction from these models reveals that COF is most sensitive to terminal group shape, whereby small, planar or linear groups result in the lowest COF values. Adhesion is found to be most sensitive to charge distribution on the terminal group, whereby both the polar surface area and ability for the formation of inter-monolayer hydrogen bonding are found to be strong predictors of adhesion. The models generated in this work should have utility in narrowing the scope of the monolayer parameter space for future screening. Furthermore, the workflow utilized in this study should be readily extensible to the examination of more complex monolayer films (e.g., multi-component films) which may provide even more favorable tribological properties.

5.5 Bibliography

[1] Klein, C.; Sallai, J.; Jones, T. J.; Iacovella, C. R.; McCabe, C.; Cummings, P. T. A Hierarchical, Component Based Approach to Screening Properties of Soft Matter. *Molecular Modeling and Simulation* **2016**, 79–92.

[2] mBuild: a component-based molecule builder tool that relies on equivalence relations for component composition. http://mosdef-hub.github.io/mbuild/.

[3] Foyer: A package for atom-typing as well as applying and disseminating force fields. http://mosdef-hub.github.io/foyer/.

[4] MoSDeF Github:. http://github.com/mosdef-hub.

[5] Summers, A. Z.; Iacovella, C. R.; Cummings, P. T.; MCabe, C. Investigating Alkylsilane Monolayer Tribology at a Single-Asperity Contact with Molecular Dynamics Simulation. *Langmuir* **2017**, *33*, 11270–11280.

[6] Adorf, C. S.; Dodd, P. M.; Ramasubramani, V.; Glotzer, S. C. Simple data and workflow management with the signac framework. *Computational Materials Science* **2018**, *146*, 220–229.

[7] Weininger, D. SMILES, a chemical language and information system. 1. Introduction to methodology and encoding rules. *Journal of Chemical Information and Computer Sciences* **1988**, *28*, 31–36.

[8] Black, J. E.; Iacovella, C. R.; Cummings, P. T.; McCabe, C. Molecular Dynamics Study of Alkylsilane Monolayers on Realistic Amorphous Silica Surfaces. *Langmuir* **2015**, *31*, 3086–3093.

[9] Summers, A. Z.; Iacovella, C. R.; Billingsley, M. R.; Arnold, S. T.; Cummings, P. T.; McCabe, C. Influence of Surface Morphology on the Shear-Induced Wear of Alkylsilane Monolayers: Molecular Dynamics Study. *Langmuir* **2016**, *32*, 2348–2359.

[10] Zhuravlev, L. The surface chemistry of amorphous silica. Zhuravlev model. *Colloids and Surfaces A: Physicochemical and Engineering Aspects* **2000**, *173*, 1–38.

[11] Hartkamp, R.; Siboulet, B.; Dufrêche, J.-F.; Coasne, B. Ion-specific adsorption and electroosmosis in charged amorphous porous silica. *Physical Chemistry Chemical Physics* **2015**, *17*, 24683–24695.

[12] Labukas, J. P.; Drake, T. J. H.; Ferguson, G. S. Compatibility of omega-Functionality in the Electrochemically Directed Self-Assembly of Monolayers on Gold from Alkyl Thiosulfates. *Langmuir* **2010**, *26*, 9497–9505.

[13] Clear, S. C.; Nealey, P. F. Chemical Force Microscopy Study of Adhesion and Friction between Surfaces Functionalized with Self-Assembled Monolayers and Immersed in Solvents. *Journal of Colloid and Interface Science* **1999**, *213*, 238–250.

[14] Brewer, N. J.; Beake, B. D.; Leggett, G. J. Friction Force Microscopy of Self-Assembled Monolayers: Influence of Adsorbate Alkyl Chain Length, Terminal Group Chemistry, and Scan Velocity. *Langmuir* **2001**, *17*, 1970–1974.

[15] Eastman, P.; Friedrichs, M. S.; Chodera, J. D.; Radmer, R. J.; Bruns, C. M.; Ku, J. P.; Beauchamp, K. A.; Lane, T. J.; Wang, L.-P.; Shukla, D.; et al., OpenMM 4: A Reusable, Extensible, Hardware Independent Library for High Performance Molecular Simulation. *Journal of Chemical Theory and Computation* **2012**, *9*, 461–469.

[16] SMARTS - A Language for Describing Molecular Patterns. http://www.daylight.com/dayhtml/doc/theory/theory.smarts.html.

[17] Klein, C. Towards Rational Design of Nanoscale Lubricants and Elucidation of the Hydration Lubrication Mechanism using Molecular Simulation. Ph.D. thesis, Vanderbilt University, 2017.

[18] Jorgensen, W. L.; Maxwell, D. S.; Tirado-Rives, J. Development and Testing of the OPLS All-Atom Force Field on Conformational Energetics and Properties of Organic Liquids. *Journal of the American Chemical Society* **1996**, *118*, 11225–11236.

[19] McDonald, N. A.; Jorgensen, W. L. Development of an All-Atom Force Field for Heterocycles. Properties of Liquid Pyrrole, Furan, Diazoles, and Oxazoles. *The Journal of Physical Chemistry B* **1998**, *102*, 8049–8059.

[20] Price, D. J.; Roberts, J. D.; Jorgensen, W. L. Conformational Complexity of Succinic Acid and Its Monoanion in the Gas Phase and in Solution: Ab Initio Calculations and Monte Carlo Simulations. *Journal of the American Chemical Society* **1998**, *120*, 9672–9679.

[21] Rizzo, R. C.; Jorgensen, W. L. OPLS All-Atom Model for Amines: Resolution of the Amine Hydration Problem. *Journal of the American Chemical Society* **1999**, *121*, 4827–4836.

[22] Price, M. L. P.; Ostrovsky, D.; Jorgensen, W. L. Gas-phase and liquid-state properties of esters, nitriles, and nitro compounds with the OPLS-AA force field. *Journal of Computational Chemistry* **2001**, *22*, 1340–1352.

[23] Watkins, E. K.; Jorgensen, W. L. Perfluoroalkanes: Conformational Analysis and Liquid-State Properties from ab Initio and Monte Carlo Calculations. *The Journal of Physical Chemistry A* **2001**, *105*, 4118–4125.

[24] Jorgensen, W. L.; Ulmschneider, J. P.; Tirado-Rives, J. Free Energies of Hydration from a Generalized Born Model and an All-Atom Force Field. *The Journal of Physical Chemistry B* **2004**, *108*, 16264–16270.

[25] Abraham, M. J.; Murtola, T.; Schulz, R.; Páll, S.; Smith, J. C.; Hess, B.; Lindahl, E. GROMACS: High performance molecular simulations through multi-level parallelism from laptops to supercomputers. *SoftwareX* **2015**, *1-2*, 19–25.

[26] Lorenz, C.; Webb, E.; Stevens, M.; Chandross, M.; Grest, G. Frictional dynamics of perfluorinated self-assembled monolayers on amorphous SiO2. *Tribology Letters* **2005**, *19*, 93–98.

[27] LAMMPS web page:. http://lammps.sandia.gov.

[28] Plimpton, S. Fast Parallel Algorithms for Short-Range Molecular Dynamics. *Journal of Computational Physics* **1995**, *117*, 1–19.

[29] Chandross, M.; Webb, E. B.; Stevens, M. J.; Grest, G. S.; Garofalini, S. H. Systematic Study of the Effect of Disorder on Nanotribology of Self-Assembled Monolayers. *Physical Review Letters* **2004**, *93*.

[30] Park, B.; Lorenz, C. D.; Chandross, M.; Stevens, M. J.; Grest, G. S.; Borodin, O. A. Frictional Dynamics of Fluorine-Terminated Alkanethiol Self-Assembled Monolayers. *Langmuir* **2004**, *20*, 10007–10014.

[31] Devaprakasam, D.; Biswas, S. K. Molecular damping: Mechanical response of self-assembled monomolecular layer to compression. *Physical Review B* **2005**, *72*.

[32] Nose, S. A unified formulation of the constant temperature molecular dynamics methods. *The Journal of Chemical Physics* **1984**, *81*, 511–519.

[33] Hoover, W. G. Canonical dynamics: Equilibrium phase-space distributions. *Physical Review A* **1985**, *31*, 1695–1697.

[34] Hess, B.; Bekker, H.; Berendsen, H. J.; Fraaije, J. G. LINCS: a linear constraint solver for molecular simulations. *Journal of computational chemistry* **1997**, *18*, 1463–1472.

[35] Darden, T.; York, D.; Pedersen, L. Particle mesh Ewald: An Nlog(N) method for Ewald sums in large systems. *The Journal of Chemical Physics* **1993**, *98*, 10089–10092.

[36] Essmann, U.; Perera, L.; Berkowitz, M. L.; Darden, T.; Lee, H.; Pedersen, L. G. A smooth particle mesh Ewald method. *The Journal of Chemical Physics* **1995**, *103*, 8577–8593.

[37] RDKit: Open-source cheminformatics. http://www.rdkit.org, [Online; accessed 11-April-2013].

[38] Riniker, S.; Landrum, G. A. Better Informed Distance Geometry: Using What We Know To Improve Conformation Generation. *Journal of Chemical Information and Modeling* **2015**, *55*, 2562–2574.

[39] Gasteiger, J.; Marsili, M. Iterative partial equalization of orbital electronegativity—a rapid access to atomic charges. *Tetrahedron* **1980**, *36*, 3219–3228.

[40] Breiman, L. Random Forests. *Machine Learning* **2001**, *45*, 5–32.

[41] Geurts, P.; Ernst, D.; Wehenkel, L. Extremely randomized trees. *Machine Learning* **2006**, *63*, 3–42.

[42] Pedregosa, F. et al. Scikit-learn: Machine Learning in Python. *Journal of Machine Learning Research* **2011**, *12*, 2825–2830.

[43] Ballester, P. J.; Mitchell, J. B. O. A machine learning approach to predicting protein–ligand binding affinity with applications to molecular docking. *Bioinformatics* **2010**, *26*, 1169–1175.

[44] Svetnik, V.; Liaw, A.; Tong, C.; Culberson, J. C.; Sheridan, R. P.; Feuston, B. P. Random Forest: A Classification and Regression Tool for Compound Classification and QSAR Modeling. *Journal of Chemical Information and Computer Sciences* **2003**, *43*, 1947–1958.

[45] Xiao, X.; Hu, J.; Charych, D. H.; Salmeron, M. Chain Length Dependence of the Frictional Properties of Alkylsilane Molecules Self-Assembled on Mica Studied by Atomic Force Microscopy. *Langmuir* **1996**, *12*, 235–237.

[46] Lio, A.; Charych, D. H.; Salmeron, M. Comparative Atomic Force Microscopy Study of the Chain Length Dependence of Frictional Properties of Alkanethiols on Gold and Alkylsilanes on Mica. *The Journal of Physical Chemistry B* **1997**, *101*, 3800–3805.

[47] Chandross, M.; Grest, G. S.; Stevens, M. J. Friction between Alkylsilane Monolayers: Molecular Simulation of Ordered Monolayers. *Langmuir* **2002**, *18*, 8392–8399.

[48] Lee, D. H.; Oh, T.; Cho, K. Combined Effect of Chain Length and Phase State on Adhesion/Friction Behavior of Self-Assembled Monolayers. *The Journal of Physical Chemistry B* **2005**, *109*, 11301–11306.

[49] Booth, B. D.; Vilt, S. G.; Lewis, J. B.; Rivera, J. L.; Buehler, E. A.; McCabe, C.; Jennings, G. K. Tribological Durability of Silane Monolayers on Silicon. *Langmuir* **2011**, *27*, 5909–5917.

[50] Huo, L.; Du, P.; Zhou, H.; Zhang, K.; Liu, P. Fabrication and tribological properties of self-assembled monolayer of n -alkyltrimethoxysilane on silicon: Effect of SAM alkyl chain length. *Applied Surface Science* **2017**, *396*, 865–869.

[51] Rivera, J. L.; Jennings, G. K.; McCabe, C. Examining the frictional forces between mixed hydrophobic – hydrophilic alkylsilane monolayers. *The Journal of Chemical Physics* **2012**, *136*, 244701.

[52] Noy, A.; Frisbie, C. D.; Rozsnyai, L. F.; Wrighton, M. S.; Lieber, C. M. Chemical Force Microscopy: Exploiting Chemically-Modified Tips To Quantify Adhesion, Friction, and Functional Group Distributions in Molecular Assemblies. *Journal of the American Chemical Society* **1995**, *117*, 7943–7951.

[53] McGuiggan, P. M. Friction and adhesion measurements between a fluorocarbon surface and a hydrocarbon surface in air. *The Journal of Adhesion* **2004**, *80*, 395–408.

[54] Frisbie, C. D.; Rozsnyai, L. F.; Noy, A.; Wrighton, M. S.; Lieber, C. M. Functional Group Imaging by Chemical Force Microscopy. *Science* **1994**, *265*, 2071–2074.

[55] Hall, L. H.; Kier, L. B. The Molecular Connectivity Chi Indexes and Kappa Shape Indexes in Structure-Property Modeling. *Reviews in Computational Chemistry* **2007**, 367–422.

[56] Brukman, M. J.; Oncins, G.; Dunbar, T. D.; Boardman, L. D.; Carpick, R. W. Nanotribological Properties of Alkanephosphonic Acid Self-Assembled Monolayers on Aluminum Oxide: Effects of Fluorination and Substrate Crystallinity. *Langmuir* **2006**, *22*, 3988–3998.

[57] Yu, B.; Qian, L.; Yu, J.; Zhou, Z. Effects of Tail Group and Chain Length on the Tribological Behaviors of Self-Assembled Dual-Layer Films in Atmosphere and in Vacuum. *Tribology Letters* **2008**, *34*, 1–10.

[58] Signac workflow for screening systems of chemically-identical functionalized monolayer films:. http://github.com/summeraz/terminal_group_screening.

[59] Signac workflow for screening systems of chemically-dissimilar functionalized monolayer films:. http://github.com/summeraz/terminal_groups_mixed.

CHAPTER 6

A COARSE-GRAINED MODEL FOR AMORPHOUS SILICA

With the use of a MoSDeF-driven workflow, the previous chapter has demonstrated that screening of monolayer-based lubricants over a large chemical space is tractable. However, such simulations come at a significant computational cost, which will be further increased if screening simulations consider monolayers under contact by asperities, which is likely more relevant to MEMS/NEMS conditions, but requires larger system sizes. One avenue to reduce computational cost in molecular dynamics is through coarse-graining, whereby several neighboring atoms are combined into a single interaction site. To this end, this chapter will explore the derivation of a coarse-grained model for amorphous silica. While the model in this chapter is derived for application to silica nanoparticles, the optimization scheme proposed should be extensible to planar surfaces.

The work in this chapter has been motivated by the work of Lee and Hua[1], who developed a coarse-grained model for amorphous silica nanoparticles. While the model developed by Lee and Hua matched several properties of bulk silica, no comparison was made to all-atom data for nanoparticles and pseudo-atoms in their model are of a fixed size. The model derived in this chapter is motivated to extend the concept of Lee and Hua's model to one that is (1) transferable to nanoparticles of arbitrary size, (2) features tunable coarse-grained fidelity, and (3) is derived directly through potential-matching to data for all-atom nanoparticles.

In addition to the possible extension of the optimization scheme provided in this chapter to the derivation of parameters for coarse-grained silica interfaces, this work also relates to tribology as nanoparticles themselves have been shown to provide promise as lubricants for MEMS-based devices.[2–6] For example, Ko et al. observed lifetime increases for MEMS switches through lubrication by gold nanoparticles, thought to be facilitated by in-plane

movement of nanoparticles redistributing mechanical load over time.[6] Likewise, Hu et al. observed via MD that under a load of 500 MPa and a shear velocity of 10 m/s both diamond and silica nanoparticles yielded low friction forces when confined between two iron surfaces through the introduction of ball-bearing-like friction mechanisms.[5] Thus, while the primary goal of the model developed in this chapter is to enable large-scale studies of nanoparticle self-assembly with a fast, chemically-derived model, this work also has utility in facilitating studies of nanoparticle-based lubricants for MEMS/NEMS.

The work presented in this chapter has been prepared for submission as a peer-reviewed publication.

6.1 Background

Molecular simulations have played a critical role in providing an understanding of a wide range of phenomena related to nanoparticle systems[7–17], with a large body of literature focused on the behavior of nanoparticles with oligomer/polymer coatings.[8,17–23,23–35] While systems can be examined with atomistic-level detail for very small nanoparticles, e.g. molecular nanoparticles such silsesquioxanes[36–39], detailed atomistic simulations of even moderately sized systems become difficult, and even impractical, as nanoparticle size increases. In practice, atomistic simulations for even relatively small diameters (e.g. 5-10nm) have been typically limited to a single or pair of nanoparticles due to the large number of atoms required to model these systems (e.g. around 35000 atoms needed for a nanoparticle with a diameter of 10nm), especially when including solvent and/or coatings.[8,30] As a result, non-atomistic, coarse-grained (CG) models have been widely used to access the larger system sizes and longer time scales required to better understand nanoparticle behavior and more directly compare with experiment.

Many of the CG models used for nanoparticles are generic, often featuring simple functional forms, such as the Lennard-Jones (LJ) or square-well potentials, to model the interactions between nanoparticle cores or between subunits that describe a nanoparticle (e.g.

beads used to construct generic rod-like[40,41], cubic nanoparticles[42], or spherical shells[43]). Often, these parameters are not tuned to experimental or atomistic data, and are instead utilized to gather qualitative relationships between nanoparticle properties/behavior and features of the interactions (e.g., the depth of the potential well). While generic models are often highly effective at capturing the phenomenological behavior[9,15,16,27,28], more specific models that attempt to recoup details of the underlying nanoparticle chemistry may be needed to more directly and accurately capture experimental behavior.

Although few models exist in the literature, several different approaches have been considered for developing chemically-specific CG nanoparticle models. For example, accurate single-site CG C_{60} nanoparticle models have been constructed based on integrating the interactions between the underlying atoms in the nanoparticles, as in the work of Girfalco[44], and through the use of a force-matching comparison with atomistic molecular dynamics (MD) simulations, as in the work of Izvekov et al.[45] However, in single-site nanoparticle models, interactions are typically not transferable between different sizes, and thus a unique set of interactions must be derived for each nanoparticle size one wishes to study, including cross-interactions with solvent species and coatings. CG nanoparticles can also be constructed of smaller pseudo-atoms (i.e. CG beads) with intermediate fidelity between all-atom and single-site models. Chan, et al. developed a CG model of a polyoligomeric silsesquioxane (POSS) nanocube, including interactions with oligomer coatings, using the iterative Boltzmann inversion method.[46] The silsesquioxane cube was represented by 8 pseudo atoms (each pseudo-atom represented a Si atom and half of each of the three O atoms it was bonded to), where the interactions of the pseudo atoms were optimized to match the radial distribution functions derived from corresponding atomistic simulations of POSS. While this CG POSS nanocube model would likely be transferrable to systems with other oligomer coatings, it is unclear whether the psuedo-atoms in the nanocube could be effectively transferred to other silica nanoparticles, since the underlying chemical structure would be different (i.e., each Si in POSS has 3 bonds with O, while most Si atoms in

amorphous silica have 4 bonds with O) and the fact that the iterative Boltzmann inversion method often leads to potentials that are state/system specific.[47] Other approaches have specifically been design with the idea of transferrability in mind, developed such that the underlying pseudo-atoms would not need to change if the nanoparticle size is changed. For example, Lee and Hua developed a model for silica nanoparticles, whereby a LJ potential was used to model the interactions between CG pseudo-atoms representing Si_6O_{12} subunits.[1] Si_6O_{12} subunits were chosen through a screening procedure over various silica substructures of the form Si_nO_{2n}, where bulk Si_6O_{12} clusters were found to best reproduce the density and heat capacity of amorphous silica; CG pseudo-atom interactions were modeled using the LJ potential and optimized to reproduce the radial distribution function of a bulk atomistic simulation of Si_6O_{12}. While this approach yielded a CG model that could be transferred to different sized nanoparticles without rederivation, the CG nanoparticles were not directly validated against atomistic or experimental amorphous silica nanoparticle data. That is, while Si_6O_{12} subunits were shown to reproduce the density and heat capacity of bulk amorphous silica, they were not directly shown to reproduce the energetic interactions between atomistically detailed amorphous silica nanoparticles. Additionally, in the approach of Lee and Hua, the fidelity of the pseudo-atoms was fixed, which may impose practical limits on the maximum size of the nanoparticles that can be considered, as large nanoparticles would still feature a large number of interaction sites that could make their study computationally infeasible, even with a CG model.

Given the ubiquity of nanoparticles in experiment, it is of fundamental importance to develop a general approach for the optimization and validation of transferrable CG nanoparticle potentials, along with cross-interaction parameters between nanoparticles an solvent/-coating species, where the fidelity of the CG model can be adjusted. Herein, we introduce a general approach for the derivation of transferrable CG nanoparticles through the construction of a CG model for amorphous silica nanoparticles. Interactions are derived directly from all-atom nanoparticle models via a simplified version of the potential-matching

scheme proposed by Toth[48], and similar to the force-matching approach taken by Izvekov et al. for C_{60}.[45] Rather than using only a single nanoparticle size to perform the fitting, parameters are derived such that a single pseudo-atom can simultaneously reproduce the behavior of a range of nanoparticle diameters, with the goal of increasing transferability as a function of nanoparticle size. For general applicability, pseudo-atom interaction parameters are fitted to a Mie potential, allowing the shape and range to be tuned. The model does not prescribe a specific mapping (i.e., the all-atom equivalents to the coarse-grained beads are intentionally ambiguous), thus allowing the fidelity of the pseudo-atoms to be tuned for the nanoparticle size of interest. Furthermore, fits are applied such that parameters can be derived for nanoparticle models with arbitrary pseudo-atom size and surface packing. Validation is performed by comparing against the target data as well as larger nanoparticles not used in the optimization. The same potential-matching approach is utilized in the derivation of cross-interactions with linear alkanes, to enable further validation of the approach via the examination of of polymer grafted nanoparticles. Validation is performed by comparing CG to all-atom models of the nanoparticles in the polymer grafted systems. The optimization framework is wrapped into an open-source Python package to facilitate usage and extension by interested parties. *

6.2 Methods

6.2.1 Coarse-Grained Nanoparticle Model

Coarse-grained nanoparticles are constructed using mBuild[39], a package within the Molecular Simulation and Design Framework (MoSDeF).[49] The nanoparticle model consists of a spherical shell of pseudo-atoms (i.e., CG beads), similar to the model of Lee and Hua[1] and In't Veld[43]; however, it should be noted that the pseudo-atoms in our model are not defined to have a direct all-atom equivalent. A golden section spiral algorithm is

*The Python package, hosted on GitHub, has been set to private pending submission of the forthcoming manuscript at which time it will be made public.

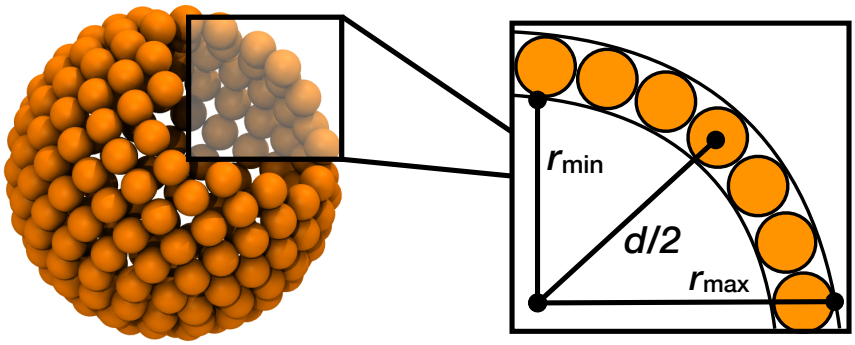

Figure 6.1: Diagram of the coarse-grained nanoparticle model where pseudo-atoms are arranged into a spherical shell. The inset highlights the spherical shell which will feature a width equal to the diameter of the pseudo-atoms, σ_b. The volume fraction of pseudo-atoms within the spherical shell is defined as ϕ_b.

used to distribute these pseudo-atoms in a roughly uniform distribution. This algorithm is a common solution for constructing spheres out of smaller spheres and helps to facilitate reproducibility, as compared to other approaches which may use stochastic processes for sphere distribution. Additionally, this algorithm allows for a uniform surface density for all nanoparticle diameters. Additional details on the golden section spiral algorithm can be found in Appendix E.1.1. The pseudo-atom diameter is defined by σ_b, where σ_b is also used in the non-bonded interaction potential (Eq. 6.1). Thus, the model's resolution can be tuned by altering σ_b, where larger values result in a coarser nanoparticle model. The spherical shell is constructed such that each pseudo-atom's center is placed at radial separation, a distance of $\frac{1}{2}[d-(\sigma_b+\sigma_{silica})]$ from the nanoparticle center, where d is the diameter of the atomistic nanoparticle and $\sigma_{silica} = 0.40323$nm is the arithmetic average of σ_{Si} and σ_O. This ensures that the van der Waals diameter of the nanoparticle remains nominally independent of the size of the pseudo-atoms.

Pseudo-atoms are arranged at fixed values of ϕ_b, where ϕ_b represents the volume fraction of pseudo-atoms within the spherical annulus described by $(d \pm \sigma_b)/2$, as depicted in Fig. 6.1. Thus, depending on the specified value of ϕ_b pseudo-atoms may feature overlaps (large ϕ_b, Fig. 6.2b-c.) or void space may be present between neighboring beads (small ϕ_b, Fig. 6.2d.). Preliminary work tested a maximum packing algorithm, where pseudo-atoms

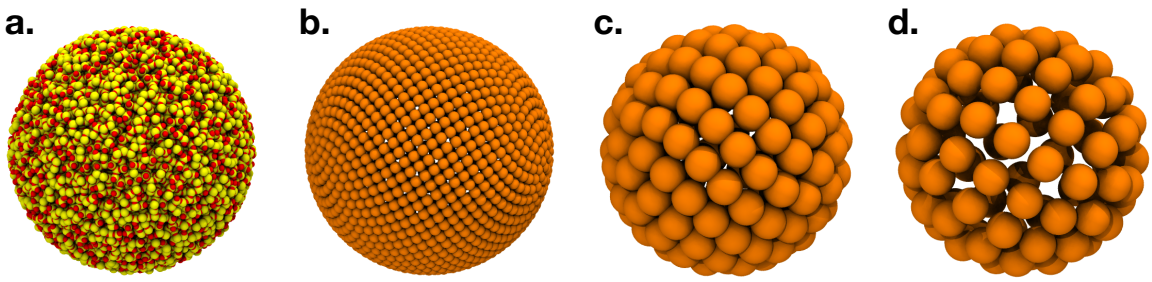

Figure 6.2: Amorphous silica nanoparticles ($d = 10$nm) modeled using a. an all-atom representation (carved as a sphere from an amorphous silica bulk; silicon is shown in yellow and oxygen in red) and b-d. coarse-grained representations featuring b. $\sigma_b = 0.5$nm, $\phi_b = 0.6$, c. $\sigma_b = 1.5$nm, $\phi_b = 0.6$, and d. $\sigma_b = 1.5$nm, $\phi_b = 0.4$ (coarse-grained silica beads are shown in orange). The nanoparticles feature particle counts of a. 34674, b. 1441, c. 131, and d. 85, respectively.

were placed so as to achieve the maximum ϕ_b without overlaps. However, it was found that the value of ϕ_b was strongly dependent on the ratio of the nanoparticle diameter to the diameter of the pseudo-atoms; this variability in ϕ_b resulted in issues regarding the transferability of the optimized interaction parameters between nanoparticle sizes (further details provided in Appendix E.1.2). It should be noted that certain restrictions exist on the value of ϕ_b that should be used for constructing nanoparticles. Values of ϕ_b above $\approx$0.6 will yield regions within the spherical shell where three neighboring spheres intersect; as the overlap volume is difficult to calculate in such instances, ϕ_b also becomes difficult to calculate and the nanoparticles cannot be constructed with the golden section spiral algorithm. While no lower bound exists for ϕ_b, nanoparticle constructed with small ϕ_b values will feature considerable void space between neighboring particles. This could present a problem in simulations featuring smaller species that could intercalate inside the nanoparticle sphere. It is advised in such systems to include a short range repulsive potential radiating from the nanoparticle center to avoid this problem.

Interactions involving pseudo-atoms of CG nanoparticles are governed by a potential with a Mie functional form:

$$U(r) = C\varepsilon\left[\left(\frac{\sigma}{r}\right)^n - \left(\frac{\sigma}{r}\right)^m\right] \tag{6.1}$$

where the pre-factor C relates to the exponents n and m, where $C = \left(\frac{n}{n-m}\right)\left(\frac{n}{m}\right)^{\frac{m}{n-m}}$. This function reduces to the familiar 12-6 Lennard-Jones form when n and m equal 12 and 6, respectively. For interactions between pseudo-atoms, σ in Eq. 6.1 is equivalent to σ_b, while for cross-interactions between pseudo-atoms and other moieties σ is included in the optimization. Preliminary work revealed co-dependency between the parameters ε, n, and m in Eq. 6.1, supporting the concept of Mie potential degeneracy that has been noted elsewhere in the literature.[50] As such, for all interactions (both those between pseudo-atoms and all cross-interactions) the value of n has been fixed at 35, which was found to provide reasonable parameter sets, and helps capture the excluded volume of the nanoparticle core. However, the parameters ε and m are then dependent on the values of σ_b and ϕ_b used to construct a given nanoparticle. The work herein describes the optimization of these two parameters, such that the collective interaction between the pseudo-atoms of two nanoparticles matches data obtained for atomistically-detailed nanoparticles.

6.2.2 Atomistic Target Data

Atomistic nanoparticles were constructed by carving spheres from an amorphous silica bulk. Bulk amorphous silica was generated using a procedure that closely mimics the approach of Litton and Garofalini[51]; however, with the ReaxFF force field[21] used to describe Si and O interactions[52], as in the work of Refs. 53,54. Briefly, a 5nm $\times$ 5nm $\times$ 5nm simulation box was filled with a stoichiometric mixture of Si and O atoms at a density of $2.2\frac{\text{g}}{\text{mL}}$ and heated to 10,000K over 20ps to obtain a fluid. Stepwise annealing was performed to cool the system to room temperature, through 10ps isothermal-isochoric runs at 8000, 6000, 4000, 3000, 2000, 1000, and 300K. A 0.5fs timestep was used, and charge equilibration was performed at each timestep making use of the implementation by Aktulga et al..[55] Temperature was controlled using a Nose-Hoover thermostat[56,57] using the LAMMPS molecular dynamics simulation engine.[58,59]

Nanoparticles were carved from the bulk amorphous silica by including all atoms within

a spherical region of a specified diameter (further details are provided in Appendix E.2.2). Fig. 6.2a shows the result of this procedure for a nanoparticle with a diameter of 10nm. The silica bulk was replicated when necessary for the creation of large nanoparticles. Note that although a strict 2:1 stoichiometric ratio of oxygen atoms to silicon atoms was not enforced (although the bulk is stoichiometric, so these values are close), the force field chosen to evaluate nanoparticle-nanoparticle interactions did not include partial charges (discussed later), so there were no concerns with charge neutrality. More rigorous models allowing for the presence of an outer oxygen layer (mimicking expected oxidation) and relaxation of the nanoparticles were also examined; however, it was found that the inclusion of these more "realistic" features did not appreciably alter the nanoparticle-nanoparticle interaction energy (see Appendix E.2.3 for further details), and thus they were excluded for computational efficiency.

Force field parameters for silicon and oxygen, used in calculating the interaction potential between atomistic nanoparticles, were obtained from the hybrid COMPASS force field[60,61], which has been shown to yield good agreement in thermophysical properties with experiment for systems of silica nanoparticles.[38] Further details on the choice of the hybrid COMPASS force field and a comparison to the OPLS[62] and DREIDING[63] force fields for the calculation of nanoparticle-nanoparticle interaction potentials can be found in Appendix E.2.3. Non-bonded interactions are defined by a 9-6 Class2 Lennard-Jones-like potential,

$$U(r) = \varepsilon_{ij}\left[2\left(\frac{\sigma_{ij}}{r}\right)^9 - 3\left(\frac{\sigma_{ij}}{r}\right)^6\right] \tag{6.2}$$

and a 6th-order mixing rule[64] is used for cross-interactions. Atoms do not feature partial charges, as previous work has shown partial charges to have a negligible impact on themophysical properties in similar systems[38], and their exclusion aids in the reduction of computational cost. Additional information concerning the role of partial charges on nanoparticle-nanoparticle interaction energy is included in Appendix E.2.3.

Target data is obtained for nanoparticles with diameters of d=4, 6, 8, 10, 12, 14, 16,

18, and 20nm. To gauge transferability to larger nanoparticles sizes, data has also been collected for an all-atom nanoparticle with a diameter of 50nm. Additionally, for tests of force field transferability to systems featuring two distinct nanoparticle sizes, interaction potential data was collected between two nanoparticles with diameters of 8 and 16nm.

Energy profiles were obtained by binning interaction energy values into histograms over a range of center-of-mass separations, using a consistent number of 100 bins (providing higher resolution for smaller nanoparticles). An even sampling was performed across the entire range of inter-particle separations, although it should be noted that larger nanoparticles featured reduced sampling as variability in interaction potential at a given separation is reduced for particles of larger size; this also reduces computational cost. Sampling involved iteratively choosing random rotations and translations for one of the two nanoparticles such that the final energy profiles yielded an average over many configurations within each bin. An overlap criterion was applied, such that configurations featuring any two atoms closer than 0.8σ were excluded; where we note that rejected configurations were not counted towards our uniform sampling. However, it was ultimately found during the optimization of the pseudo-atom interactions that overlaps in the regime of smaller center-of-mass separations prevented reasonable fits. The data was then pruned to remove values at center-of-mass separations below $d + 0.40323\text{nm} \times 0.8$, where 0.40323nm represents the diameter of silica, to resolve this issue. Additional details on the sampling procedure are provided in Appendix E.2.4.

Target data was also collected for the interaction between an atomistic nanoparticle with $d = 10$nm and several united-atom (UA) alkane moieties. Specifically, the interaction potential was calculated over a range of center-of-mass separations between the atomistic nanoparticle and both CH_2 and CH_3 pseudo-atoms. Collection of nanoparticle-alkane target data followed the same procedure as that used for collecting the nanoparticle-nanoparticle target data; howevere, bin spacing was reduced in the region of the potential well to provide better definition. Specific details are provided in Appendix E.2.5. In-

teractions between silica and UA pseudo-atoms featured a 12-6 Lennard-Jones potential with parameters obtained from Ionescu et al. who followed the work of Frischknecht and Curro.[38,65] While the error in the target data was found to be large at low separations, it was found that inclusion of data points on both sides of the potential minimum was necessary to yield a proper fit. Target data was sanitized to ensure, from low to high separations, that interaction potentials were monotonically decreasing until the potential minimum, and monotonically increasing afterwards (removing data points that did not fit this criterion).

6.2.3 Alkane-Grafted Nanoparticles

Alkane-grafted nanoparticles are considered in this work as a means of validating the force field derivation process and demonstrating its utility. For both all-atom and coarse-grained nanoparticle models, chains are placed in an evenly distributed spherical array (again using a golden section spiral algorithm), extending normal to the nanoparticle surface. Chains are attached to the nanoparticle core by fixing the terminal polymer bead closest to the nanoparticle and treating the entire unit of the core plus these terminal beads as a singular rigid body (i.e., no physical bonds are defined between chains and the nanoparticle core). Experimentally, nanoparticles often feature polymer coatings as a means of preventing aggregation, and thus coatings should be sufficiently dense. Considering this, a dense surface density of 3.0 chains/nm^2 has been chosen for this study.

Nanoparticle cores are modeled using both atomistic and coarse-grained representations, constructed using the procedures outlined in the preceding sections. Polymer grafts feature a UA representation for both CG and atomistic models, where interactions between polymer chains are described by the TraPPE force field and cross-interactions with the all-atom core are obtained from Ionescu et al..[38]. Interactions between UA polymer grafts and pseudo-atoms of CG nanoparticle cores take the form of Eq. 6.1 and are derived through a potential-matching approach analogous to that used to obtain interactions between the CG nanoparticle cores themselves, as described in Section 6.4. Note, that the only difference

between the CG and atomistic systems is the nanoparticle core, allowing the quality of the derived CG interactions to be directly tested (i.e., chain-chain interactions do not change). Simulations of alkane-grafted nanoparticles are performed using the HOOMD-blue simulation engine.[66,67] Single alkane-grafted nanoparticles, with chain lengths of 12, 24, 36, and 72 carbons, are considered, where integration is performed only on the alkane tethers (excluding the end beads closest to the nanoparticle core). The presence of an implicit solvent is accounted for by truncating chain-chain interactions at the potential minimum (thus leading to a purely repulsive interaction), and through integration using Langevin dynamics, in a manner similar to that of Peters et al.[8] It should be noted that in this work, nanoparticle core-chain interactions are *not* truncated at the potential minimum (thay are instead truncated at 2.0nm for systems featuring an all-atom core, and at 2.0nm + $\sigma_b/2$ for systems featuring a CG core), so as to provide a means of fully validating the cross-interaction parameters. Following a brief energy minimization, systems are equilibrated for 10ns, the final 2ns of which are used for sampling. Simulations are performed at a temperature of 300K and use a timestep of 2fs.

As shown in Fig. 6.2d, CG nanoparticle models may feature void space between beads, particularly at low values of ϕ_b, which may cause issues with intercalation of chain particles into the nanoparticle core. To prevent this in our grafted nanoparticle systems, a short-range repulsive potential is utilized radiating from the nanoparticle center featuring a 12-6 Lennard-Jones potential with ε=5 kcal/mol and both σ and r_{cut} equal to the nanoparticle radius. This was found to be sufficient to prevent intercalation of chain particles into the nanoparticle core with minimal impact on film structure.

6.2.4 Force Field Optimization

Derivation of pairwise interactions between coarse-grained pseudo-atoms is achieved through potential-matching, whereby parameters in Eq. 6.1 are optimized such that the collective interaction potential between two CG nanoparticles as a function of center-of-

mass separation matches the corresponding results from all-atom nanoparticles, through minimization of the residual:

$$e = \frac{\sum |U_{\mathrm{aa}}(r_{\mathrm{com}}) - U_{\mathrm{cg}}(r_{\mathrm{com}})|}{\sum |U_{\mathrm{aa}}(r_{\mathrm{com}})| + |U_{\mathrm{cg}}(r_{\mathrm{com}})|} \tag{6.3}$$

Here, U_{aa} and U_{cg} represent the nanoparticle-nanoparticle interaction potential for the all-atom and CG models respectively at a given center-of-mass separation, r_{com}. Normalization is used to provide an even weighting of the energy scales across all values of r_{com}. We use the term "interaction potential" in place of the more common "potential of mean force" as potential values for each center-of-mass distance are not Boltzmann weighted; however, these values are shown to feature negligible orientational dependence. The inset in Fig. 6.3a shows the all-atom interaction potential for nanoparticles with $d = 7$nm overlayed by results from the CG model for $\sigma_{\mathrm{nm}} = 1.0$nm and $\phi_{\mathrm{b}} = 0.5$.

We have developed a Python package, NanoOpt, to perform these optimizations. This package relies on tools available from the scientific Python stack (most heavily SciPy[68]) and is hosted on Github at Ref. 69. Optimizations are performed via the following multi-stage process (outlined in Fig. 6.3):

1. A brute-force optimization over a coarse multi-dimensional grid spanning a wide parameter range. (see Fig. 6.3a)

2. A second brute-force optimization over a fine multi-dimensional grid spanning a

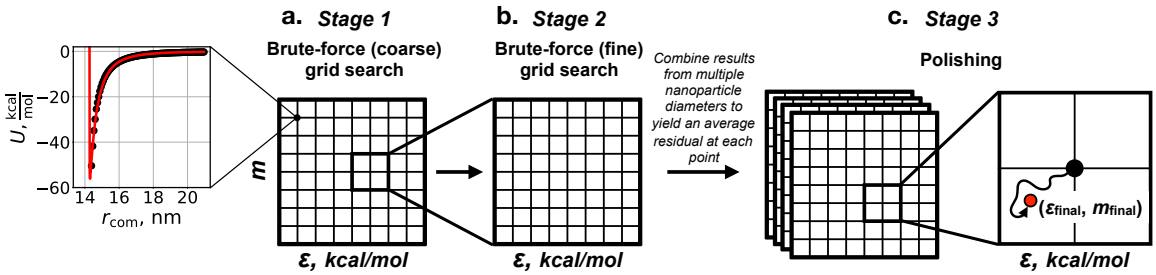

Figure 6.3: Overview of the workflow for optimizing coarse-grained nanoparticle parameters

narrow parameter range. (see Fig. 6.3b)

3. A polishing stage. The starting point for this stage is chosen from the results of the second brute-force optimization for a range of nanoparticle sizes (to ensure the creation of a transferable parameter set). An additional optimization is performed from this starting point using a Nelder-Mead simplex algorithm.[70,71] (see Fig. 6.3c)

Initial attempts at optimization included only the final stage and led to traps in local minima. As a result, Stage 2 was added to provide greater likelihood that the global minimum is reached. Stage 1 was added such that optimized parameter sets could be generated without the need to hand-pick bounds for each set.

Nanoparticle diameters of d=4, 6, 8, 10, 12, 14, 16, 18, and 20nm are considered in the optimizations. To yield a parameter set that is transferable across a range of nanoparticle diameters, these diameters are considered simultaneously in Stage 3 of the optimization, where the total residual simply becomes the sum of the individual residuals for each nanoparticle diameter.

6.3 Parameterization of Nanoparticle-Nanoparticle Core Interactions

Interaction parameters between CG pseudo-atoms, as defined by Eq. 6.1, are inherently dependent on the diameter of the CG beads (i.e., σ_b). These parameters will additionally be dependent on the volume fraction of beads included within the spherical annulus (i.e., ϕ_b). Furthermore, discrete parameters sets could be obtained for different nanoparticle sizes (i.e., d). However, such parameter sets would limit the scope and usability of the force field. Here, our goal is to define a force field where parameters may be obtained for nanoparticles featuring arbitrary values of d, σ_b, and ϕ_b. Independence of d is achieved as described in the preceding section, by including data from many nanoparticles sizes in Stage 3 of the optimization (Fig. 6.3c). Additionally, to support arbitrary values of σ_b and ϕ_b, we attempt to describe parameters as *functions* of these two variables.

To achieve this, Stages 1 and 2 of the optimization scheme were performed for all nanoparticles described by:

- d (nm): 4, 6, 8, 10, 12, 14, 16, 18, 20
- σ_b (nm): 0.5, 0.6, 0.7, 0.8, 0.9, 1.0, 1.1, 1.2, 1.3, 1.4, 1.5, 1.6, 1.7, 1.8, 1.9, 2.0
- ϕ_b: 0.25, 0.30, 0.35, 0.40, 0.45, 0.50, 0.55, 0.60

Note that 49 of the 1152 possible state points were excluded due to models featuring intersections between three CG beads, as ϕ_b can not be easily calculated in such cases.

Stage 3 of the optimization (the polishing stage) was then performed for each σ_b and ϕ_b combination, including data from multiple radii simultaneously. In order to be able to include multiple radii, the grid points used in Stage 2 for all radii must be identical. As such, when the grid bounds were determined for Stage 2, they were determined so as to be the same for all radii for a given combination of σ_b and ϕ_b.

For the two parameters included in the optimization, ε and m, the results of Stage 3 for each value of ϕ_b were examined as a function of σ_b, as shown in Fig. 6.4a and b. From Fig. 6.4a it is observed that ε increases as σ_b is increased. This result is sensible, as nanoparticles featuring larger bead sizes will also feature a lower total number of beads, thus ε must increase to yield the same collective interaction energy. Likewise, ε is found to increase as ϕ_b is decreased, along similar reasoning. Fig. 6.4b shows that as σ_b increases, m also increases. This reflects a softening of the potential as the nanoparticle model becomes further coarse-grained. Interestingly, m is found to be independent of ϕ_b, as Fig. 6.4b shows all curves collapsing onto the same line.

From Fig. 6.4a and b it appears the ε features a second-order dependence on σ_b, while m features a linear dependence. As such, the following general equations can be used to describe ε and m as a function of σ_b:

$$\varepsilon = A\sigma_b^2 \tag{6.4}$$

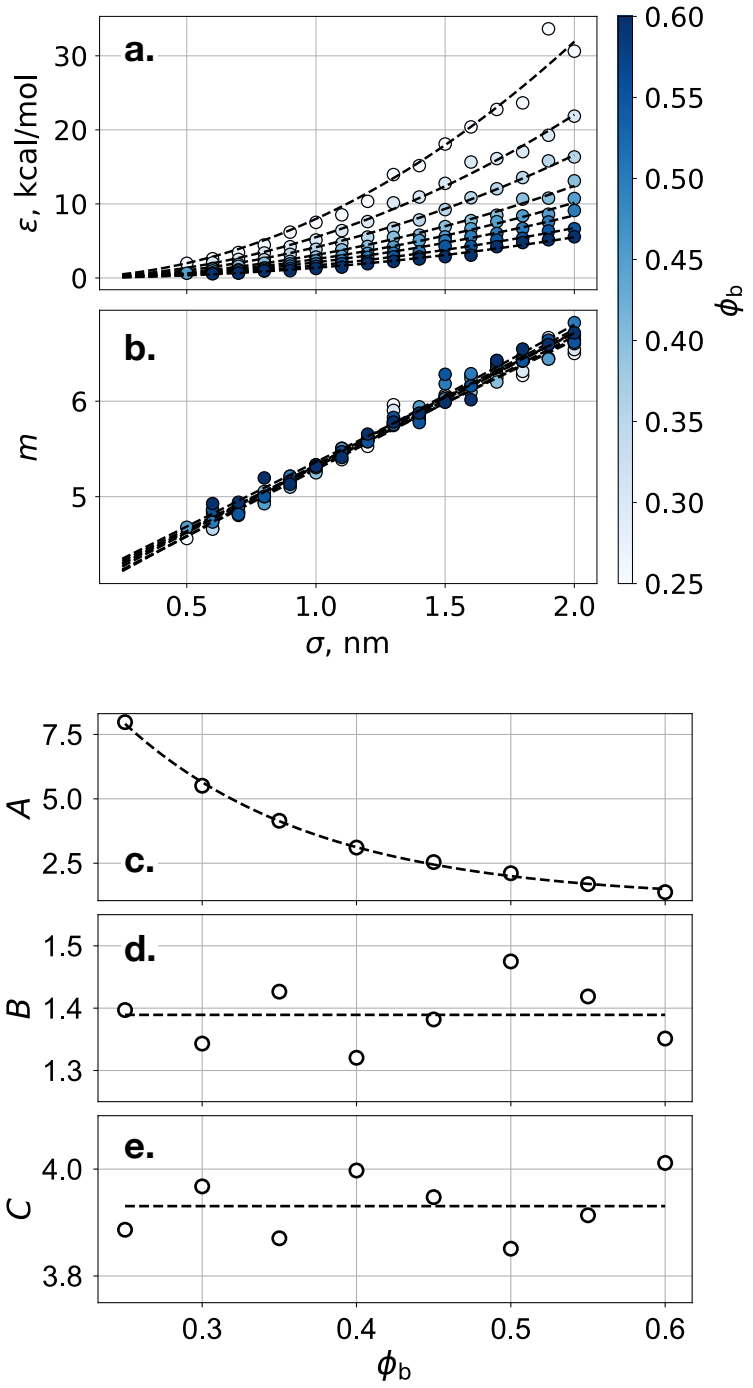

Figure 6.4: Optimized a. ε and b. m values as a function of σ_b. Dashed lines represent a. 2nd-order and b. 1st-order fits to the data. In c., d., and e., values for the fitting parameters A, B, and C are respectively shown as functions of ϕ. Dashed lines represent c. 2nd-order, d-e. 0th-order fits to the data.

$$m = B\sigma_b + C \tag{6.5}$$

Fig. 6.4c-e shows the coefficients A, B, and C from Eqs. 6.4 and 6.5 obtained for discrete values of ϕ_b by performing fits to the data in Fig. 6.4a and b. Both second-order and exponential functions are found to provide good fits to the data for A shown in Fig. 6.4c, where A is shown to decrease (and thus ε is reduced) as ϕ_b increases. However, the fit using an exponential function was slightly better than using a second-order function, so this is the function that was chosen to obtain the coefficient A as a function of ϕ_b. As expected from the results shown in 6.4b, the coefficients B and C from Eq. 6.5 appear from Fig. 6.5d and e to be independent of the value of ϕ_b. As a result, these coefficients can be obtained by taking a simple average of the values obtained for the various values of ϕ_b. From these fits, ε and m can be described in terms of σ_b and ϕ_b through the following relations:

$$\varepsilon = (51.417 \cdot \exp(-8.081\phi_b) + 1.095)\sigma_b^2 \tag{6.6}$$

$$m = 1.389\sigma_b + 3.931 \tag{6.7}$$

Using these relations, values for ε and m can be generated for arbitrary values of σ_b and ϕ_b.

Fig. 6.5 shows the nanoparticle-nanoparticle interaction energy obtained for atomistic nanoparticles compared to that calculated between CG nanoparticles using the results of Eqs. 6.6 and 6.7. It is shown that the CG results compare reasonably well to the all-atom data for several combinations of σ_b and ϕ_b. These fits are especially good in the long-range region, which is of particular importance as nanoparticles will typically featuring some sort of surface coating in practical simulations, which will nullify the effects of the short-range region. The quality of the fits does appear to feature some dependence on the nanoparticle size, as well as σ_b and ϕ_b, which is explored further in the following section.

6.3.1 Transferability

The goal of the derivation of Eqs. 6.6 and 6.7, relating ε and m from Eq. 6.1 to σ_b and ϕ_b, was to obtain functions that would be transferable across a wide range of σ_b, ϕ_b, and d values. To test this transferability, parameters obtained using these equations were used to calculate the interaction energy between CG nanoparticles and the result was compared to all-atom data using Eq. 6.3. Fig. 6.6 shows these results in the form of heatmaps for various

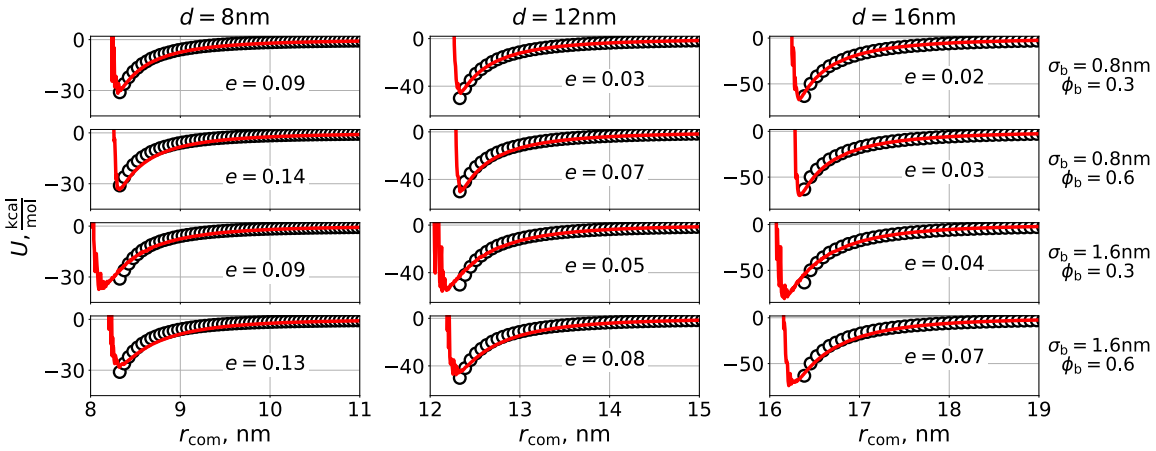

Figure 6.5: Interaction energy profiles calculated between nanoparticles with diameters of 8, 12, and 16nm. Circles represent all-atom data, while lines represent results for coarse-grained nanoparticles with parameters derived from Eqs. 6.6 and 6.7. Data is shown for several combinations of σ_b and ϕ_b.

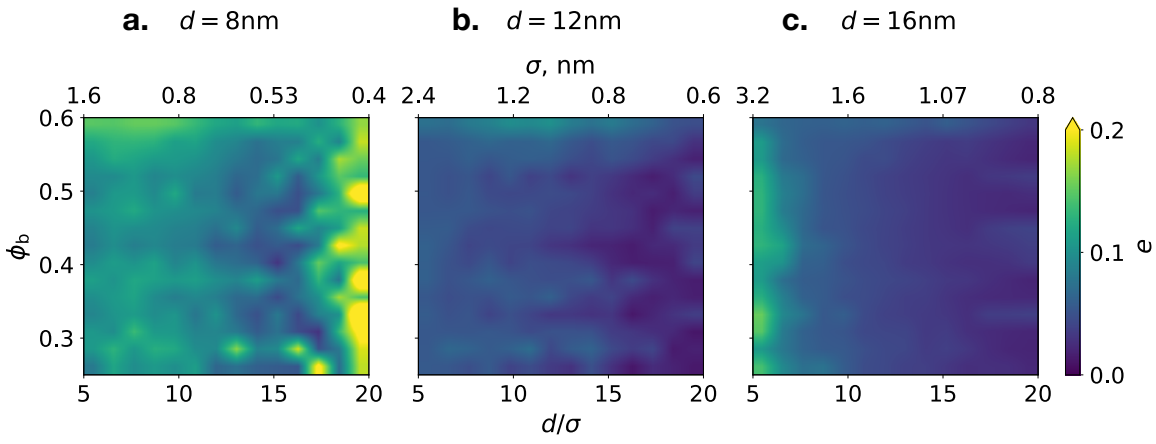

Figure 6.6: Heatmaps showing the interaction energy residual from Eq. 6.3 as a function of coarse-grained particle size (represented by the normalized and absolute values d/σ and σ respectively) and ϕ_b for nanoparticles with diameters of a. 8nm, b. 12nm, and c. 16nm.

σ_b and ϕ_b values for nanoparticles with diameters of 8, 12, and 16nm. From Fig. 6.6, it is found that the parameters obtained from Eqs. 6.6 and 6.7 well describe nanoparticles with a wide range of different σ_b, ϕ_b, and d values. Interestingly, the normalized value d/σ_b appears to have very little influence on the performance of these parameters. Additionally, the ability for the CG model to fit to the all-atom data appears to be independent of ϕ_b. As a result, the fit seems only dependent on the value of σ_b itself, where fits are found to be worse when $\sigma_b <\sim 0.45\,\text{nm}$ and when $\sigma_b >\sim 3.0\,\text{nm}$. The poor fits for low values of σ_b are likely due to its similarity in size to the "diameter" of silica itself (0.40323nm, from earlier). As such, the "coarse-grained" model approaches the same length scale as the atomistic model, and features of the atomistic model that could be averaged into larger CG pseudo-atoms are not well-described by the smaller beads. On the other end of the spectrum, the poorer fits that begin to occur (although it should still be noted that residual values are less than 0.2 even at $\sigma_b \approx 3.2\,\text{nm}$) as σ_b increases beyond 3.0nm are likely a simple result of the reduced fidelity of the model. In this regime, the model becomes more and more coarse-grained and with this comes some loss of accuracy. Furthermore, as these σ_b values are larger than any included in the target data for the optimization, any error in the fitting will become increasingly pronounced as σ_b increases further beyond the target data limit.

The results in Fig. 6.6 are encouraging and suggest transferability of the CG parameters across a range of d, σ_b, and ϕ_b values. However, we note this range matches what was used to optimize the potential, and examination of larger nanoparticle diameters, not included in the optimization, would provide considerable insight into whether or not the model parameters are in fact transferable. To this end, Fig. 6.7a shows residuals calculated using 6.3 from all-atom data for a nanoparticle where $d = 50$nm and CG data for various values of σ_b and ϕ_b. As might be expected in extrapolating the parameters to such a large nanoparticle size, the error is higher than for the smaller nanoparticles used in obtaining the parameters; however, there are still regions where the parameters from Eqs. 6.6 and 6.7 perform quite

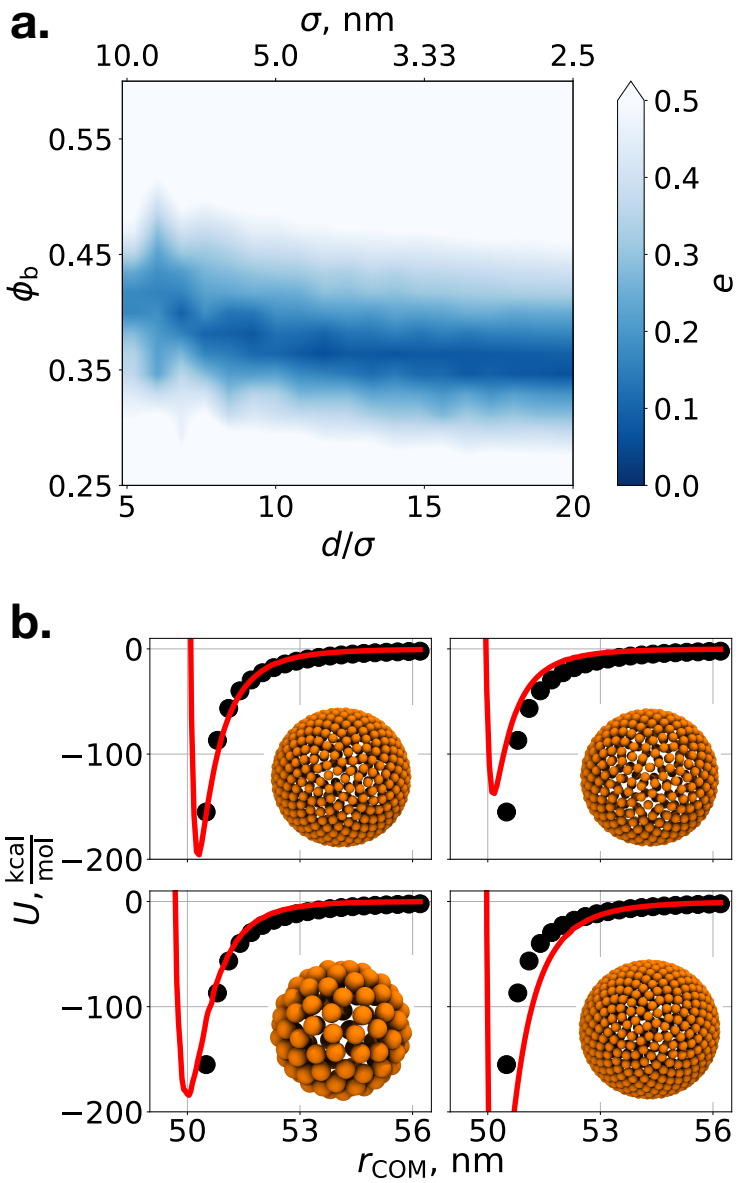

Figure 6.7: a. Heatmap showing the interaction energy residual from Eq. 6.3 as a function of coarse-grained particle size (represented by the normalized and absolute values d/σ and σ respectively) and ϕ_b between nanoparticles with $d = 50$nm, and b. a comparison of the all-atom interaction energy profile (black circles) with that of coarse-grained nanoparticles (red lines) constructed using (clockwise starting from the top-left) 1. $\sigma_b = 3.17$nm, $\phi_b = 0.36$ (corresponding to the lowest residual in the heatmap, $e = 0.07$), 2. $\sigma_b = 3.17$nm, $\phi_b = 0.31$(e=0.29), 3.$\sigma_b = 3.17$nm, $\phi_b = 0.41$ ($e = 0.27$), 4. $\sigma_b = 6.5$nm, $\phi_b = 0.36$ ($e = 0.17$). Snapshots of each of the coarse-grained nanoparticles are also provided.

well. The lowest residual (e=0.06) is observed where $\sigma_b = 3.17$nm and $\phi_b = 0.36$, and a comparison between the interaction energy profile between nanoparticles constructed us-

ing these values with the all-atom system is shown in Fig. 6.7b, visually demonstrating good agreement. Also shown in Fig. 6.7b are interaction energy profiles for several other combinations of σ_b and ϕ_b to provide a sense of the sensitivity to these parameters. Interestingly, the error for these system is nearly independent of σ_b, and instead is highly dependent on ϕ_b. As shown in Fig. 6.7b, slight increases or decreases in ϕ_b (± 0.05) from the optimal value (0.36) result in significant deviations in the depth of the potential well as well as the shape of the curve. However, increasing σ_b from 3.17nm to 6.5nm results in only a slight change in the interaction potential curve. Interestingly, the region in Fig. 6.7a where the error is lowest occurs where ϕ_b is slightly below 0.4, corresponding closely to the asymptotic value found for ϕ_b as nanoparticle radius is increased for nanoparticles constructed in a manner of maximum packing (where the largest number of pseudo-atoms are used to construct nanoparticles without overlaps, see Appendix E.1.2). This suggests that the presence of overlaps between beads at high values of ϕ_b and gaps between beads at low values of ϕ_b may present issues with transferability for larger nanoparticle sizes. In all, the results of Fig. 6.7 are encouraging that accurate interaction potential curves exist for our CG mdoel, at least for certain parameter combinations. Furthermore, the $d = 50$nm nanoparticle is likely larger than would be utilized in most studies using this child-particle approach, and the results of Fig. 6.6 suggest that these parameters derived as part of this work should be sufficient for most systems of interest.

To this point, all interaction energies considered have been between two nanoparticles that each feature the same diameter. It is not clear then whether or not parameters obtained through Eqs. 6.6 and 6.7 would be transferable to systems featuring nanoparticles of different sizes. Furthermore, as varying degrees of coarse-graining may be desired for such systems (i.e., reduced fidelity for larger nanoparticles to reduce particle count), it would be useful if nanoparticles constructed from beads with different values of σ_b could be used together. One possible route to deriving these cross-interactions would be to perform the same procedure shown in Fig. 6.3 using the interaction potential between two all-atom

nanoparticles of different sizes as target data. However, a simpler solution would be the use of mixing rules to obtain these interactions. Fig. 6.8 shows a comparison of all-atom and CG data for the interaction potential between two nanoparticles where one nanoparticle has a diameter of 8nm, a σ_b of 0.6nm, and a ϕ_b of 0.4, while the other nanoparticle features a diameter of 16nm, with various values of σ_b and ϕ_b examined for this second nanoparticle. The all-atom data shown in this plot was not included in any optimization

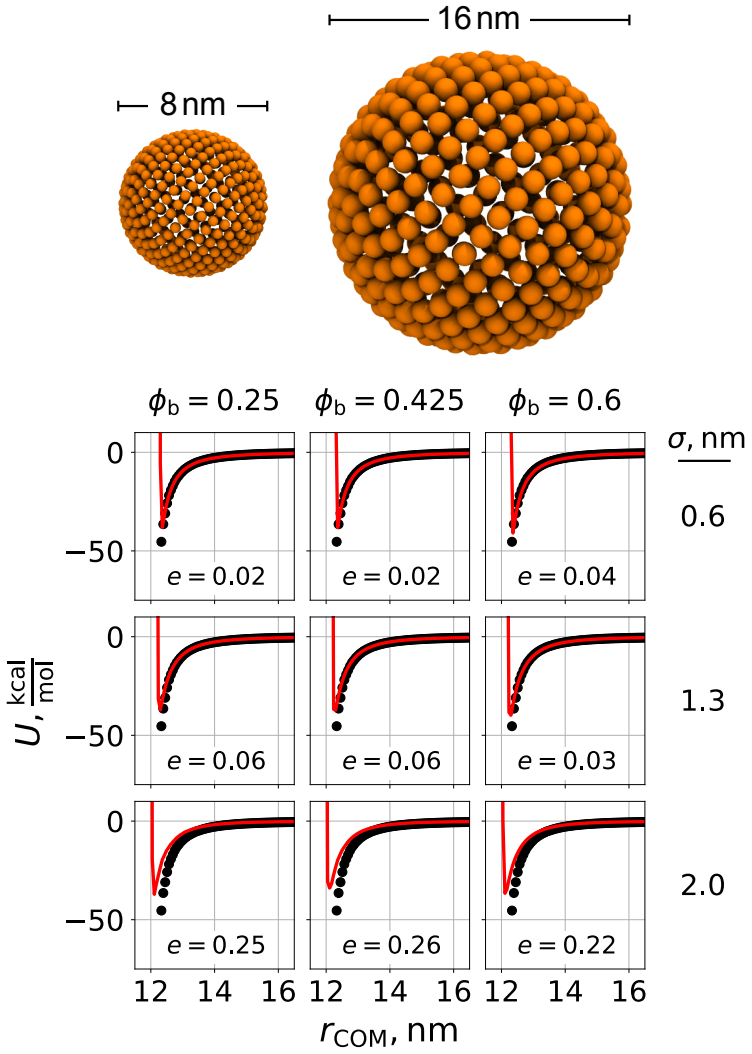

Figure 6.8: Interaction potential between a nanoparticle with $d = 8$nm, $\sigma_b = 0.6$nm, and $\phi = 0.4$ and a nanoparticle with $d = 16$nm, $\sigma_b = 0.6$, 1.3 and 2.0nm, and $\phi = 0.25$, 0.425, and 0.6. Points represent all-atom data and lines represent CG data using parameters obtained from Eqs. 6.6 and 6.7 and the mixing rules detailed in the text.

and is simply present for comparison only. Cross interactions between the two nanoparticles were obtained using geometric mixing rules for σ and ε and an arithmetic mixing rule for m. It is observed that the results parameters lead to excellent fits between the CG and all-atom data when σ_b of the larger nanoparticle is 0.6nm and 1.3nm. As the diameter of the pseudo-atoms within the second nanoparticle is further increased to 2.0nm the error is shown to increase, although the curves still feature the same general features. In all cases, fits appear to be independent of ϕ_b. As parameters here were obtained using simple mixing rules, it is unsurprising that fits begin to deviate as the difference in σ_b between the two nanoparticles becomes large; however, the results of Fig. 6.8 are still encouraging that parameters obtained using Eqs. 6.6 and 6.7 can be used for systems of nanoparticle with multiple sizes and multiple fidelities.

6.4 Parameterization of Cross-Interactions

The same general potential-matching procedure outlined in Fig. 6.3 can also be used to derive interactions between coarse-grained nanoparticles and other species (e.g., atom types/moieties from existing polymer force fields). This becomes powerful as it facilitates use of the coarse-grained silica model presented in this work beyond simple systems of silica nanoparticles in vacuum, and allows for more complex systems such as polymer-grafted nanoparticles and nanoparticles in a solvent. While the use of Mie mixing rules could be one approach to obtaining these cross interactions, large differences in both σ_b and the exponent values would likely result in poor accuracy.

Table 6.1 shows parameters obtained for the interaction between pseudo-atoms of a

Table 6.1: Optimized interaction parameters between coarse-grained nanoparticle beads ($\sigma_b = 1.3$nm, $\phi_b = 0.4$) and CH_2, CH_3 united-atom beads

Cross Interaction	σ, nm	ε, $\frac{\text{kcal}}{\text{mol}}$	n	m
NP-CH_2	0.7581	1.2809	35	6.9256
NP-CH_3	0.7435	1.6871	35	6.3843

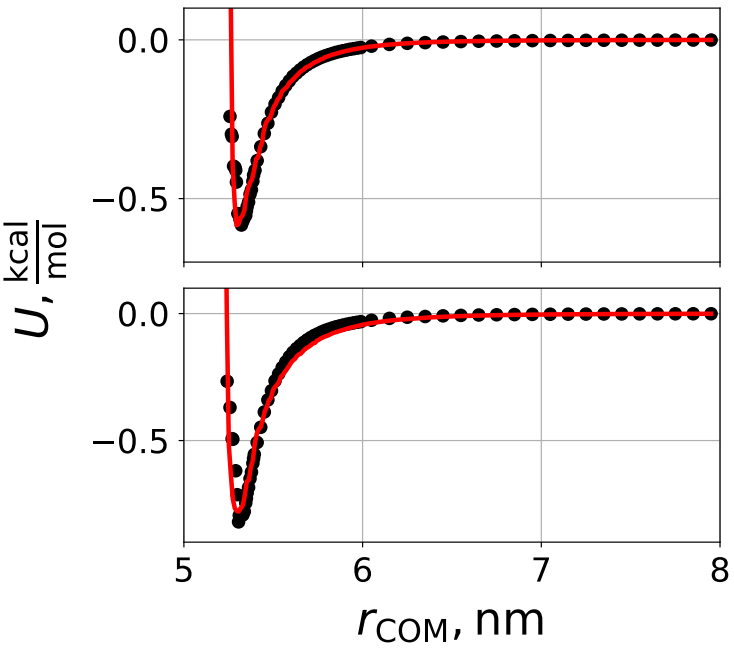

Figure 6.9: Interaction energy profiles calculated between a nanoparticle with $d = 10$nm and a. CH_2 and b. CH_3 united-atom moieties. Circles represent all-atom target data, while lines represent results for coarse-grained nanoparticles with $\sigma_b = 1.3$nm and $\phi_b = 0.4$.

CG nanoparticle ($\sigma_b = 1.3$nm, $\phi_b = 0.4$, $d = 10$nm) and both CH_2 and CH_3 united-atom moieties. Note that the parameters in Table 6.1 are not guaranteed to be transferable to CG nanoparticles with arbitrary values of σ_b, ϕ_b, and d. Our focus here is to demonstrate how cross-interactions with other particle types can be obtained rather than the presentation of a more general cross-interaction parameter set. The parameters in Table 6.1 provide an excellent match to the all-atom target data for the two cross-interactions, as shown in Figure 6.9. As in Figure 6.5, target data for long-range interactions has been included to ensure this portion of the potential curve is properly captured in the CG model. Additionally, as the cross-interactions feature a (relatively) softer potential compared to the interactions between the pseudo-atoms of nanoparticle cores, target data was also able to be obtained for the interaction at short-range, providing definition to the potential well. It was found that the inclusion of this short-range data was essential in the derivation of cross-interactions with a properly located potential minimum.

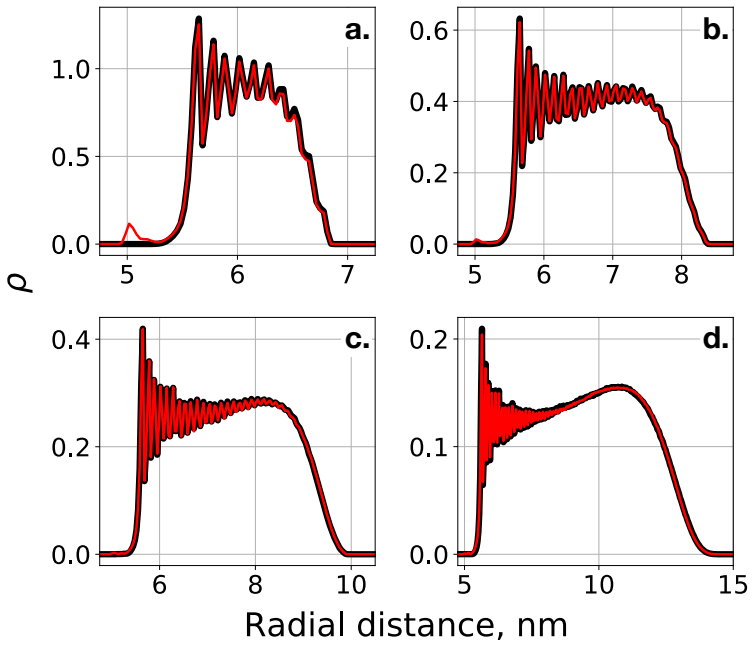

Figure 6.10: Radial mass density (ρ) of alkane tethers with chain lengths of a. 12, b. 24, c. 36, and d. 72 carbons attached at a density of 3.0 chains/nm^2 to a silica nanoparticle with $d = 10$nm. Results obtained for an all-atom nanoparticle core are shown in black, while results for a coarse-grained core (using parameters from Table 6.1 with $\sigma_b = 1.3$nm) are shown in red. Contributions to ρ from the two CH_2 beads closest to the nanoparticle surface (the nearest most of which has a fixed position) are excluded for clarity.

To validate the cross interactions in Table 6.1, alkane-grafted nanoparticles are constructed with both all-atom and CG cores and where the alkane coating is allowed to reach a steady state; the radial mass density profiles of the chains are calculated as a measure of parameter effectiveness. Figure 6.10 shows the radial mass density profiles for nanoparticles with alkane grafts featuring chain lengths of 12, 24, 36, and 72 carbons. It can be observed that for all chain lengths, the systems with the CG nanoparticle core closely match the film structure of those with an all-atom core, with the results nearly indistinguishable. The potential curves are found to become smoother further from the nanoparticle surface (most evident in Fig. 6.10d.), as the radial volume increases. At distances near the nanoparticle surface, the available volume for chains to explore is quite low, particularly at a high chain density of 3.0 chains/nm^2, and large peaks are present indicating the locations of individual CH_2 moieties along the chain backbone. These features of the mass density

profiles are well-captured by the CG model. The only notable difference between the film structures of the two models is a small peak located near the nanoparticle surface (at a radial distance of 5nm) that is present for the C12 and C24 coatings shown in Fig. 6.10a and b. This peak corresponds to chains that have intercalated into regions between neighboring pseudo-atoms of the CG nanoparticle core. While a pseudo hard-sphere potential is utilized to prevent chains from intercalating into the nanoparticle itself (which would otherwise be possible as a result of "gaps" between neighboring pseudo-atoms, see Fig. 6.2d), this does not prevent chains from exploring the region around the nanoparticle surface that is made rough by the large size of the pseudo-atoms. However, this effect is shown to be quite minor in Fig. 6.10 with little effect on the overall film structure and becomes unnoticeable at chain lengths of 36 and 72 carbons.

6.5 Discussion

The model and associated force field presented herein for CG nanoparticles provides a means to create systems of amorphous silica nanoparticles with user-specified fidelity. Cross-interactions with particles from other force fields are also obtainable through this approach. However, while the utility of such a generalized force field should not go unstated, a comparison with the existing silica force field of Lee and Hua[1] is also useful. Figure 6.11 shows a comparison of the nanoparticle-nanoparticle interaction potential between CG nanoparticles using parameters from Eqs. 6.6 and 6.7 and between point-particles using parameters obtained from the work of Lee and Hua (the exact equations used are provided in Appendix E.3), alongside atomistic data. The parameters from this work yield a CG nanoparticle-nanoparticle interaction potential that closely matches the shape of the all-atom data, which is to be expected as atomistic data was used to fit these parameters. Comparing to the potential curve obtained using parameters from the work of Lee and Hua, both potentials provide a similar value for the well depth, however, the Lee and Hua potentials shows a much sharper character, particularly for larger nanoparticle diameters, where

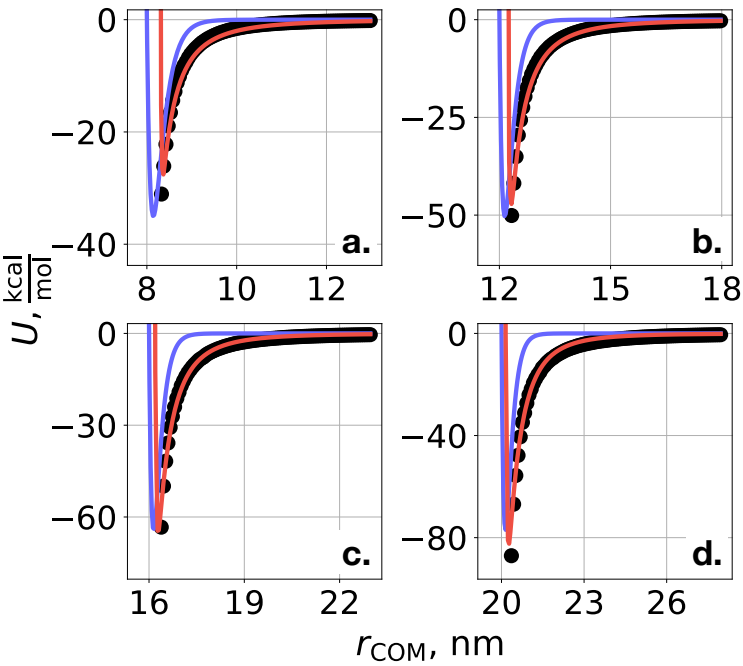

Figure 6.11: Interaction energy profiles calculated between nanoparticles with diameters of a. 8nm, b. 12nm, c. 16nm, and d. 20nm. Data is shown for nanoparticles featuring all-atom representations (black circles), the coarse-grained model described in this text with $d/\sigma_b = 12.5$ and $\phi_b = 0.5$ (red lines), and c. parameters from Fig. 6 of Ref. 1 (blue lines).

the interaction potential increases to nearly zero at a center-of-mass separation of only 1nm beyond the nanoparticle diameter. This shorter range behavior in the Lee and Hua potential is likely related to the use of the 12-6 Lennard Jones potential to model the pseudo-atom interactions. From Eq. 6.6, our work predicts that for a pseudo-atom with a matching diameter to Lee and Hua (0.62 nm) the attractive exponent of the Mie potential corresponds to a value of 4.79 (note this appears independent of the surface density of the pseudo-atoms), resulting in longer-ranged interactions than the standard 12-6 potential. This lack of long-range attraction may have effects on the dynamics, assembly, and supra-molecular structure of bulk systems.

It is important to note that, although the interaction potential values in this long-range region are small relative to the very strong short-range interaction, these may still be quite large relative to interactions with other constituents in the system. For example, considering the grafted alkane example, if a rather standard interaction cutoff of $\frac{1}{60}\varepsilon$ were to be

applied to the interaction between pseudo atoms that make up the nanoparticle core particles for $d = 10$nm, the nanoparticle-nanoparticle interaction energy would be truncated at a value on the order of 1 kcal/mol, where we note that this is on the same energy scale as the well depth of the nanoparticle-CH_x interaction (shown in Fig. 6.9), and an order of magnitude larger than the well depth of the CH_x-CH_x interaction (0.1 kcal/mol). Again, this considerable heterogeneity in the energy scales could result in significant changes to the dynamics, assembly, and structure of the systems if cutoffs are not appropriately chosen to capture this longer-range behavior.

Finally, an additional advantage of the model and force field presented herein should be discussed, namely, the ability to derive cross-interactions between polymer pseudo-atoms for which no all-atom interaction parameters are available. As an example, consider a coarse-grained alkane with a 3:1 mapping (3 CH_2/CH_3) units mapped into a single bead. While several such force fields exist[72,73], to the best of our knowledge, none contain interaction parameters with silica nanoparticles. In the approach presented herein, one could use as target data the interaction between, e.g., a CH_2-CH_2-CH_2 trimer (i.e., the underlying structure of the CG bead) and an all-atom nanoparticle core and then simply fit the parameters for the interaction between a CG core and a CG alkane moiety to this target data, similar to the united atom alkane examples. As a result, any polymer that can be mapped to the atomistic level is compatible with our CG nanoparticle model and procedure.

6.5.1 Application to Nanoscale Lubrication

The force field and general optimization scheme derived herein should have utility in molecular simulations for many applications. One application area in particular that should benefit from the use of this force field is nanoscale lubrication. Nanoparticle-based lubricants have received attention recently as a possible solution to the nanoscale lubrication problem through the introduction of lowered friction via ball-bearing-like rolling mechanisms.[2–6] However, similar to the single-asperity systems described in Chapter 4, systems

featuring nanoparticles confined between surfaces will likely require large system sizes to avoid artifacts from periodic boundaries (particularly if these surfaces also feature a monolayer surface coating). Thus, the use of a coarse-grained model may have utility in analysis of some of the fundamental mechanisms of such systems.

Furthermore, the parameters and general optimization scheme derived in this study should be readily applicable to planar surfaces. Further testing will be required to see if the parameters derived from Eqs. 6.6 and 6.7 can be used *as is* for planar systems; however, even if agreement with all-atom surface interaction data is not achieved, re-derivation of these parameters should be straightfoward through use of the same general optimization scheme shown in Fig. 6.3.

6.6 Conclusions

In this work, a coarse-grained force field has been derived for amorphous silica nanoparticles, modeled as spheres of evenly-distributed pseudo-atoms, via matching interaction potentials to all-atom data. The optimization scheme considers target data for multiple nanoparticle sizes simultaneously to yield parameters that are size-independent. Interactions between pseudo-atoms utilize a Mie functional form, where the value σ is equivalent to the diameter of the pseudo-atoms, the value of the repulsive exponent, n, is fixed, and the parameters ε and m are dependent on both pseudo-atom size and the volume fraction of beads within the spherical shell of the coarse-grained nanoparticle. Through parameter optimization for a variety of pseudo-atom sizes and volume fractions, functions are provided for ε and m such that parameters may be obtained for arbitrary nanoparticle models. These parameters are shown to feature transferability across a wide range of nanoparticles sizes, pseudo-atom diameters, and volume fractions. It is also shown that a similar approach can be used to obtain cross-interaction parameters between pseudo-atoms and other moieties, here specifically CH_2 and CH_3 united-atom moieties. This allows the model and force field presented herein to have utility towards grafted nanoparticle systems and systems of

nanoparticles in solvent. By including long-range target data in the force field optimization, the model presented herein is shown to improve upon prior CG silica nanoparticle models from the literature. This work should help facilitate, among others, studies of nanoparticle self-assembly, with minimal loss of chemical fidelity. The model and optimization scheme should be easily extensible to non-silica based nanoparticles, as well as silica structures that are non-spherical such as interfaces.

6.7 Bibliography

[1] Lee, C. K.; Hua, C. C. Nanoparticle interaction potentials constructed by multiscale computation. *The Journal of Chemical Physics* **2010**, *132*, 224904.

[2] Matsumoto, N.; Joly-Pottuz, L.; Kinoshita, H.; Ohmae, N. Application of onion-like carbon to micro and nanotribology. *Diamond and Related Materials* **2007**, *16*, 1227–1230.

[3] Joly-Pottuz, L.; Bucholz, E. W.; Matsumoto, N.; Phillpot, S. R.; Sinnott, S. B.; Ohmae, N.; Martin, J. M. Friction Properties of Carbon Nano-Onions from Experiment and Computer Simulations. *Tribology Letters* **2009**, *37*, 75–81.

[4] Bucholz, E. W.; Phillpot, S. R.; Sinnott, S. B. Molecular dynamics investigation of the lubrication mechanism of carbon nano-onions. *Computational Materials Science* **2012**, *54*, 91–96.

[5] Hu, X.; Martini, A. Atomistic simulation of the effect of roughness on nanoscale wear. *Computational Materials Science* **2015**, *102*, 208–212.

[6] Ko, S.-D.; Seo, M.-H.; Yoon, Y.-H.; Han, C.-H.; Lim, K.-S.; Kim, C.-K.; Yoon, J.-B. Investigation of the Nanoparticle Electrical Contact Lubrication in MEMS Switches. *Journal of Microelectromechanical Systems* **2017**, *26*, 1417–1427.

[7] Shim, J.-H.; Lee, B.-J.; Cho, Y. W. Thermal stability of unsupported gold nanoparticle: a molecular dynamics study. *Surface Science* **2002**, *512*, 262–268.

[8] Peters, B. L.; Lane, J. M. D.; Ismail, A. E.; Grest, G. S. Fully Atomistic Simulations of the Response of Silica Nanoparticle Coatings to Alkane Solvents. *Langmuir* **2012**, *28*, 17443–17449.

[9] Hong, D.-J.; Lee, E.; Jeong, H.; Lee, J.-k.; Zin, W.-C.; Nguyen, T.; Glotzer, S.; Lee, M. Solid-State Scrolls from Hierarchical Self-Assembly of T-Shaped Rod-Coil Molecules. *Angewandte Chemie* **2009**, *121*, 1692–1696.

[10] Van Lehn, R. C.; Alexander-Katz, A. Structure of Mixed-Monolayer-Protected Nanoparticles in Aqueous Salt Solution from Atomistic Molecular Dynamics Simulations. *The Journal of Physical Chemistry C* **2013**, *117*, 20104–20115.

[11] Jenkins, S.; Kirk, S. R.; Persson, M.; Carlen, J.; Abbas, Z. Molecular dynamics simulation of nanocolloidal amorphous silica particles: Part I. *The Journal of Chemical Physics* **2007**, *127*, 224711.

[12] Jenkins, S.; Kirk, S. R.; Persson, M.; Carlen, J.; Abbas, Z. Molecular dynamics simulation of nanocolloidal amorphous silica particles: Part II. *The Journal of Chemical Physics* **2008**, *128*, 164711.

[13] Jenkins, S.; Kirk, S. R.; Persson, M.; Carlen, J.; Abbas, Z. Molecular dynamics simulation of nanocolloidal amorphous silica particles: Part III. *The Journal of Chemical Physics* **2009**, *130*, 134702.

[14] Koparde, V. N.; Cummings, P. T. Molecular Dynamics Simulation of Titanium Dioxide Nanoparticle Sintering. *The Journal of Physical Chemistry B* **2005**, *109*, 24280–24287.

[15] Xia, Y.; Nguyen, T. D.; Yang, M.; Lee, B.; Santos, A.; Podsiadlo, P.; Tang, Z.; Glotzer, S. C.; Kotov, N. A. Self-assembly of self-limiting monodisperse supraparticles from polydisperse nanoparticles. *Nature Nanotechnology* **2011**, *6*, 580–587.

[16] Zhang,; Tang,; Kotov, N. A.; Glotzer, S. C. Simulations and Analysis of Self-Assembly of CdTe Nanoparticles into Wires and Sheets. *Nano Letters* **2007**, *7*, 1670–1675.

[17] Hattemer, G. D.; Arya, G. Viscoelastic Properties of Polymer-Grafted Nanoparticle Composites from Molecular Dynamics Simulations. *Macromolecules* **2015**, *48*, 1240–1255.

[18] Meng, D.; Kumar, S. K.; D. Lane, J. M.; Grest, G. S. Effective interactions between grafted nanoparticles in a polymer matrix. *Soft Matter* **2012**, *8*, 5002.

[19] Ethier, J. G.; Hall, L. M. Modeling individual and pairs of adsorbed polymer-grafted nanoparticles: structure and entanglements. *Soft Matter* **2018**, *14*, 643–652.

[20] Chevigny, C.; Dalmas, F.; Di Cola, E.; Gigmes, D.; Bertin, D.; Boue, F.; Jestin, J. Polymer-Grafted-Nanoparticles Nanocomposites: Dispersion, Grafted Chain Conformation, and Rheological Behavior. *Macromolecules* **2011**, *44*, 122–133.

[21] Chenoweth, K.; van Duin, A. C. T.; Goddard, W. A. ReaxFF Reactive Force Field for Molecular Dynamics Simulations of Hydrocarbon Oxidation. *The Journal of Physical Chemistry A* **2008**, *112*, 1040–1053.

[22] Pryamtisyn, V.; Ganesan, V.; Panagiotopoulos, A. Z.; Liu, H.; Kumar, S. K. Modeling the anisotropic self-assembly of spherical polymer-grafted nanoparticles. *The Journal of Chemical Physics* **2009**, *131*, 221102.

[23] Ndoro, T. V. M.; Voyiatzis, E.; Ghanbari, A.; Theodorou, D. N.; Bohm, M. C.; Muller-Plathe, F. Interface of Grafted and Ungrafted Silica Nanoparticles with a Polystyrene Matrix: Atomistic Molecular Dynamics Simulations. *Macromolecules* **2011**, *44*, 2316–2327.

[24] Goyal, S.; Escobedo, F. A. Structure and transport properties of polymer grafted nanoparticles. *The Journal of Chemical Physics* **2011**, *135*, 184902.

[25] Glotzer, S. C.; Horsch, M. A.; Iacovella, C. R.; Zhang, Z.; Chan, E. R.; Zhang, X. Self-assembly of anisotropic tethered nanoparticle shape amphiphiles. *Current Opinion in Colloid Interface Science* **2005**, *10*, 287–295.

[26] Lamm, M. H.; Chen, T.; Glotzer, S. C. Simulated Assembly of Nanostructured Organic/Inorganic Networks. *Nano Letters* **2003**, *3*, 989–994.

[27] Kumar, S. K.; Krishnamoorti, R. Nanocomposites: Structure, Phase Behavior, and Properties. *Annual Review of Chemical and Biomolecular Engineering* **2010**, *1*, 37–58.

[28] Akcora, P.; Liu, H.; Kumar, S. K.; Moll, J.; Li, Y.; Benicewicz, B. C.; Schadler, L. S.; Acehan, D.; Panagiotopoulos, A. Z.; Pryamitsyn, V.; et al., Anisotropic self-assembly of spherical polymer-grafted nanoparticles. *Nature Materials* **2009**, *8*, 354–359.

[29] Kumar, S. K.; Jouault, N.; Benicewicz, B.; Neely, T. Nanocomposites with Polymer Grafted Nanoparticles. *Macromolecules* **2013**, *46*, 3199–3214.

[30] Lane, J. M. D.; Ismail, A. E.; Chandross, M.; Lorenz, C. D.; Grest, G. S. Forces between functionalized silica nanoparticles in solution. *Physical Review E* **2009**, *79*.

[31] Phillips, C. L.; Iacovella, C. R.; Glotzer, S. C. Stability of the double gyroid phase to nanoparticle polydispersity in polymer-tethered nanosphere systems. *Soft Matter* **2010**, *6*, 1693.

[32] Liu, J.; Gao, Y.; Cao, D.; Zhang, L.; Guo, Z. Nanoparticle Dispersion and Aggregation in Polymer Nanocomposites: Insights from Molecular Dynamics Simulation. *Langmuir* **2011**, *27*, 7926–7933.

[33] Jayaraman, A. Polymer grafted nanoparticles: Effect of chemical and physical heterogeneity in polymer grafts on particle assembly and dispersion. *Journal of Polymer Science Part B: Polymer Physics* **2013**, *51*, 524–534.

[34] Lafitte, T.; Kumar, S. K.; Panagiotopoulos, A. Z. Self-assembly of polymer-grafted nanoparticles in thin films. *Soft Matter* **2014**, *10*, 786–794.

[35] Haley, J. D.; Iacovella, C. R.; Cummings, P. T.; McCabe, C. Examining the aggregation behavior of polymer grafted nanoparticles using molecular simulation and theory. *The Journal of Chemical Physics* **2015**, *143*, 054904.

[36] Striolo, A.; McCabe, C.; Cummings, P. T.; Chan, E. R.; Glotzer, S. C. Aggregation of POSS Monomers in Liquid Hexane: A Molecular-Simulation Study. *The Journal of Physical Chemistry B* **2007**, *111*, 12248–12256.

[37] Song, X.; Sun, Y.; Wu, X.; Zeng, F. Molecular dynamics simulation of a novel kind of polymer composite incorporated with polyhedral oligomeric silsesquioxane (POSS). *Computational Materials Science* **2011**, *50*, 3282–3289.

[38] Ionescu, T. C.; Qi, F.; McCabe, C.; Striolo, A.; Kieffer, J.; Cummings, P. T. Evaluation of force fields for molecular simulation of polyhedral oligomeric silsesquioxanes. *Journal of Physical Chemistry B* **2006**, *110*, 2502–2510.

[39] Klein, C.; Sallai, J.; Jones, T. J.; Iacovella, C. R.; McCabe, C.; Cummings, P. T. A Hierarchical, Component Based Approach to Screening Properties of Soft Matter. *Molecular Modeling and Simulation* **2016**, 79–92.

[40] Iacovella, C. R.; Horsch, M. A.; Glotzer, S. C. Local ordering of polymer-tethered nanospheres and nanorods and the stabilization of the double gyroid phase. *The Journal of Chemical Physics* **2008**, *129*, 044902.

[41] Zhang,; Horsch, M. A.; Lamm, M. H.; Glotzer, S. C. Tethered Nano Building Blocks: Toward a Conceptual Framework for Nanoparticle Self-Assembly. *Nano Letters* **2003**, *3*, 1341–1346.

[42] Chan, E. R.; Zhang, X.; Lee, C.-Y.; Neurock, M.; Glotzer, S. C. Simulations of Tetra-Tethered Organic/Inorganic NanocubePolymer Assemblies. *Macromolecules* **2005**, *38*, 6168–6180.

[43] in' t Veld, P. J.; Horsch, M. A.; Lechman, J. B.; Grest, G. S. Liquid-vapor coexistence for nanoparticles of various size. *The Journal of Chemical Physics* **2008**, *129*, 164504.

[44] Girifalco, L. A.; Hodak, M.; Lee, R. S. Carbon nanotubes, buckyballs, ropes, and a universal graphitic potential. *Physical Review B* **2000**, *62*, 13104–13110.

[45] Izvekov, S.; Violi, A.; Voth, G. A. Systematic Coarse-Graining of Nanoparticle Interactions in Molecular Dynamics Simulation. *The Journal of Physical Chemistry B* **2005**, *109*, 17019–17024.

[46] Chan, E. R.; Striolo, A.; McCabe, C.; Cummings, P. T.; Glotzer, S. C. Coarse-grained force field for simulating polymer-tethered silsesquioxane self-assembly in solution. *The Journal of Chemical Physics* **2007**, *127*, 114102.

[47] Moore, T. C.; Iacovella, C. R.; McCabe, C. Derivation of coarse-grained potentials via multistate iterative Boltzmann inversion. *The Journal of Chemical Physics* **2014**, *140*, 224104.

[48] Tóth, G. Effective potentials from complex simulations: a potential-matching algorithm and remarks on coarse-grained potentials. *Journal of Physics: Condensed Matter* **2007**, *19*, 335222.

[49] MoSDeF Github:. http://github.com/mosdef-hub.

[50] Ramrattan, N.; Avendaño, C.; Müller, E.; Galindo, A. A corresponding-states framework for the description of the Mie family of intermolecular potentials. *Molecular Physics* **2015**, *113*, 932–947.

[51] Litton, D. A.; Garofalini, S. H. Modeling of hydrophilic wafer bonding by molecular dynamics simulations. *Journal of Applied Physics* **2001**, *89*, 6013–6023.

[52] Fogarty, J. C.; Aktulga, H. M.; Grama, A. Y.; van Duin, A. C. T.; Pandit, S. A. A reactive molecular dynamics simulation of the silica-water interface. *The Journal of Chemical Physics* **2010**, *132*, 174704.

[53] Black, J. E.; Iacovella, C. R.; Cummings, P. T.; McCabe, C. Molecular Dynamics Study of Alkylsilane Monolayers on Realistic Amorphous Silica Surfaces. *Langmuir* **2015**, *31*, 3086–3093.

[54] Summers, A. Z.; Iacovella, C. R.; Cummings, P. T.; MCabe, C. Investigating Alkylsilane Monolayer Tribology at a Single-Asperity Contact with Molecular Dynamics Simulation. *Langmuir* **2017**, *33*, 11270–11280.

[55] Aktulga, H.; Fogarty, J.; Pandit, S.; Grama, A. Parallel reactive molecular dynamics: Numerical methods and algorithmic techniques. *Parallel Computing* **2012**, *38*, 245–259.

[56] Nose, S. A unified formulation of the constant temperature molecular dynamics methods. *The Journal of Chemical Physics* **1984**, *81*, 511–519.

[57] Hoover, W. G. Canonical dynamics: Equilibrium phase-space distributions. *Physical Review A* **1985**, *31*, 1695–1697.

[58] Plimpton, S. Fast Parallel Algorithms for Short-Range Molecular Dynamics. *Journal of Computational Physics* **1995**, *117*, 1–19.

[59] LAMMPS web page:. http://lammps.sandia.gov.

[60] Sun, H. Ab initio calculations and force field development for computer simulation of polysilanes. *Macromolecules* **1995**, *28*, 701–712.

[61] Sun, H.; Rigby, D. Polysiloxanes: ab initio force field and structural, conformational and thermophysical properties. *Spectrochimica Acta Part A: Molecular and Biomolecular Spectroscopy* **1997**, *53*, 1301–1323.

[62] Lorenz, C.; Webb, E.; Stevens, M.; Chandross, M.; Grest, G. Frictional dynamics of perfluorinated self-assembled monolayers on amorphous SiO2. *Tribology Letters* **2005**, *19*, 93–98.

[63] Mayo, S. L.; Olafson, B. D.; Goddard, W. A. DREIDING: a generic force field for molecular simulations. *The Journal of Physical Chemistry* **1990**, *94*, 8897–8909.

[64] Waldman, M.; Hagler, A. New combining rules for rare gas van der waals parameters. *Journal of Computational Chemistry* **1993**, *14*, 1077–1084.

[65] Frischknecht, A. L.; Curro, J. G. Improved United Atom Force Field for Poly(dimethylsiloxane). *Macromolecules* **2003**, *36*, 2122–2129.

[66] Anderson, J. A.; Lorenz, C. D.; Travesset, A. General purpose molecular dynamics simulations fully implemented on graphics processing units. *Journal of Computational Physics* **2008**, *227*, 5342–5359.

[67] Glaser, J.; Nguyen, T. D.; Anderson, J. A.; Lui, P.; Spiga, F.; Millan, J. A.; Morse, D. C.; Glotzer, S. C. Strong scaling of general-purpose molecular dynamics simulations on GPUs. *Computer Physics Communications* **2015**, *192*, 97–107.

[68] Jones, E.; Oliphant, T. E.; Peterson, P. SciPy: Open source scientific tools for Python. http://www.scipy.org/.

[69] NanoOpt: Deriving potentials for coarse-grained nanoparticles via potential matching:. http://github.com/mosdef-hub/nanoparticle_optimization.

[70] Nelder, J. A.; Mead, R. A Simplex Method for Function Minimization. *The Computer Journal* **1965**, *7*, 308–313.

[71] Wright, M. In *Numerical analysis*; Griffiths, D., Watson, G., Eds.; Addison-Wesley, 1996; pp 191–208.

[72] Nielsen, S. O.; Lopez, C. F.; Srinivas, G.; Klein, M. L. A coarse grain model for n-alkanes parameterized from surface tension data. *Journal of Chemical Physics* **2003**, *119*, 7043–7049.

[73] Maerzke, K. A.; Siepmann, J. I. Transferable potentials for phase equilibria-coarse-grain description for linear alkanes. *The journal of physical chemistry. B* **2011**, *115*, 3452–65.

CHAPTER 7

CONCLUSIONS AND FUTURE WORK

7.1 Conclusions

The functionalization of surfaces by chemisorbed monolayer films presents a promising solution to the tribological barriers present for sliding surfaces with nanoscale dimensions. Although poor durability has to-date prevented monolayers from becoming the quintessential lubricant for MEMS/NEMS devices, the chemical tunability of monolayer films provides optimism that these materials can be designed to overcome this obstacle. Computational studies continue to prove essential in developing a comprehensive understanding of the friction and wear mechanisms present in these materials, particularly in how these mechanisms relate to monolayer chemistry, and will be a critical piece of the workflow for optimizing better-performing films. In this thesis, a number of insights related to the friction and wear of monolayer lubricants have been made through molecular simulation, and the groundwork is established for more comprehensive screening of these materials in future studies.

In Chapter 3, the wear of monolayer films was analyzed by MD through the pre-desorption of chains, whereby the mobility of these desorbed chains was used to quantify monolayer stability. It was found that surface structure plays a key role in the stability of monolayers, whereby the disordered nature of chain attachment sites (i.e., less hexagonal) was found to directly correlate with wear propensity. This provides further evidence that amorphous silica, featuring disordered chain attachment sites and atomic-scale roughness, should be preferred over crystalline silica for simulations of monolayer films. Furthermore, the crystalline silica surfaces were shown to yield unrealistically ordered films that reduced degradation. Increasing chain length was found to act as a buffer towards some of these surface effects, agreeing with experiment that this can be used as a way to prolong monolayer

lifetimes.

In addition to atomic-scale roughness, surfaces of MEMS/NEMS devices are also likely to feature roughness on the nanoscale in the form of surface asperities. Contact at these asperity sites will localize the normal load and will likely act as focal points for monolayer wear. In Chapter 4, we have examined a model single-asperity contact through MD to attain a better understanding of the friction mechanisms involved and to analyze the sensitivity of these mechanisms to the density of the monolayer film. It was found that, counter to expectations, denser monolayer films yielded *higher* COFs under contact by an asperity than sparser films. This was found to be the result of a molecular plowing mechanism, whereby penetration of the asperity into the monolayer film allows the asperity to induce localized defects in monolayer chains during shear. The chains of sparser films were found to be more liquid-like, providing less resistance to displacement by the asperity. As such, liquid-like films appear to be important for monolayer survival at asperity contacts.

One of the chief barriers to the computational screening of monolayer films has been a lack of the necessary software tools to allow facile exchange of chemical components. The Molecular Simulation and Design Framework provides a solution to this problem. In Chapter 5, MoSDeF was used to perform screening of functionalized monolayer films to examine relationships between terminal group chemistry and tribology and to provide a template for future screening. A comparison of systems featuring chemically-identical and chemically-dissimilar monolayer films revealed that although mixing chemistries does not appear to provide a route to directly lowering the COF, combining polar and nonpolar terminal group chemistries yields low adhesion forces and can provide a route towards achieving more favorable lubrication. Through the derivation of QSPR models, it was found that COF is most sensitive to the terminal group shape, and that small, planar or linear terminal groups provide the lowest COF values. These models also revealed that adhesive forces are dominated by terminal group charge distribution, with the polar surface area and hydrogen-bonding ability of terminal groups found to be strong predictors of the force of

adhesion. The development of a workflow for monolayer screening opens the door towards screening over a much larger and more complex parameter space. The models generated in this chapter were developed to require only a SMILES representation of a terminal group as an input, facilitating their use for narrowing and focusing of the monolayer parameter space in future screening studies. With minor modifications, this workflow could also be utilized for optimizing monolayer chemistry for other applications, such as biofouling, which is important in the field of bioMEMS.[1]

Finally, while the advent of MoSDeF and workflows for monolayer screening provide an avenue for complex monolayer design, large-scale studies such as these come at significant computational cost. The use of more simplified models, if still effectively capturing the necessary behavior, may provide a more efficient route for such studies. In Chapter 6, a coarse-grained model for amorphous silica is developed, along with cross-interactions with alkane chains. This force field is derived with respect to silica nanoparticles, where the use of all-atom data in parameter derivation, as well as exposing parameters as functions of pseudo-atom size, makes this model more robust than prior models found in the literature. Thus, this force field should find application in any MD study involving the simulation of silica nanoparticles where atomistic representations are not required. The optimization scheme and accompanying software package should facilitate a simple extension of this coarse-grained silica model for application to planar geometries, such as interfaces, which would enable this model to be utilized in coarse-grained simulations of alkylsilane monolayers. Furthermore, nanoparticles themselves have been considered as a possible solution to the issue of nanoscale lubrication through ball-bearing type mechanisms and redistribution of load-bearing sites of contact, and the model developed in this work should aid in further exploration of such systems.

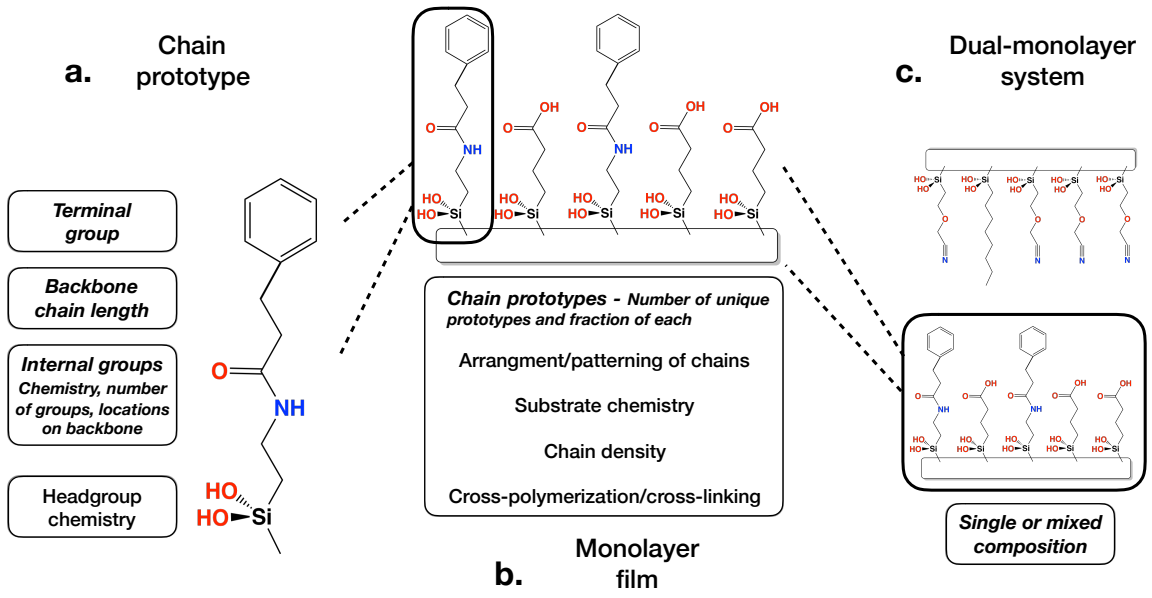

Figure 7.1: An overview of the parameter space afforded by monolayer films, highlighting the ability for monolayer chemistry to be altered a. at the level of the chain prototype, b. at the level of the monolayer film, and c. at the level of the dual-monolayer system.

7.2 Recommended Future Work

7.2.1 Multi-Component Monolayer Screening

The work in this thesis suggests that increases in chain length only facilitate marginal improvements in monolayer durability and friction. The alteration of terminal group chemistry provides another route for tuning monolayer chemistry to alter the tribological response; however, the small range of COF values observed for the pool of 16 terminal groups in Chapter 5 suggests this will only yield modest improvements in this area. The use of chemically-dissimilar monolayer lubrication also does not appear to be sufficient for further reduction of COF, although adhesion forces can be reduced by including at least one nonpolar monolayer. Thus, it appears further improvements to monolayer tribology must come from more complex monolayer compositions, such as multi-component monolayer films, that may elicit different friction mechanisms under shear. This is supported by several studies in the literature, such as the work of Jones et al. who found that in-

tercalation of 3-phenyl-1-propanol into C18 monolayers enhanced durability at asperity contacts.[2] A similar finding was made by Lewis et al. who showed that films containing a mixture of short fluorinated chains and long hydrogenated chains featuring frictional forces lower than either pure system, due to the presence of a liquid-like layer at the interface.[3] Despite these findings of favorable monolayer tribology using multi-component monolayer films, this parameter space remains mostly unexplored - likely a result of the difficulty in constructing and comparing such systems in a systematic manner. The advent of MoSDeF should alleviate this problem, and the work of Chapter 5 should be readily extensible to the screening of multi-component monolayer films. Considering the fractional composition of various chain types within a monolayer, in addition to terminal group chemistry, backbone functionality, and chain length, yields a parameter space that is near infinite, and where examination of all systems is intractable. Thus, an efficient sampling scheme will be required to properly examine this parameter space; yet the examination of such complex monolayer systems provides likely the best route towards the discovery of monolayer films with improved lubricity.

7.2.2 Multiple Asperity MD Simulations

Nanoscale asperities present on the surfaces of MEMS/NEMS likely act as focal points for the failure of monolayer films. Thus, a better understanding of the friction mechanisms involved under these conditions, as well as how changes in monolayer chemistry and structure influence these mechanisms in addition to the durability of the films, is essential towards the design of successful monolayer lubricants. Single-asperity contacts, such as those analyzed in Chapter 4 and analyzed experimentally via AFM, provide a simplified representation of these conditions and can help in this regard. However, understanding the response of monolayer films under conditions where two asperities come into contact may provide even greater insight, as this scenario likely represents the most extreme conditions which monolayer films must endure, and are expected to induce additional mechanisms of

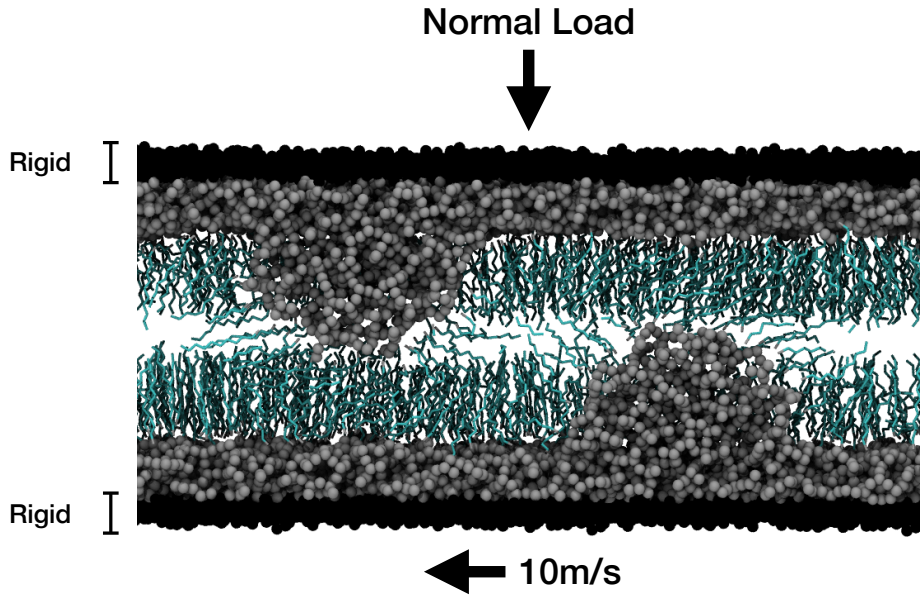

Figure 7.2: A 2D snapshot from an MD simulation of two alkylsilane-coated surfaces featuring asperities prior to contact. Alkylsilane chains are drawn in a bond representation, while grey and black atoms represent atoms of the silica surface. Black atoms are held rigid, while grey atoms are modeled using the BKS potential.

energy dissipation, such as ratcheting.[4] For monolayers to become a viable lubricant, they must be able to withstand these harsh environments.

Preliminary work suggests that MD simulation can be utilized to examine the contact of two monolayer-coated asperities. Several interesting challenges are present in these simulations, including the need to consider surface deformation. Contact areas at the point of asperity-asperity contacts will be very small, resulting in high local pressures that may deform the underlying surface. Classical MD force fields prohibit bond breaking, thus, alternative approaches will be necessary to handle this phenomenon. One possibility is through the use of a hybrid force field, where interactions between surface atoms are modeled using a nonbonded force field, such as the silica force field developed by van Beest et al.[5], and interactions involving monolayer chains are modeled through a classical force field such as OPLS. Fig. 7.2 shows a 2D snapshot from an MD simulation of two alkylsilane-coated surfaces featuring asperties prior to contact, using this approach. To analyze monolayer durability under these conditions, interfacial bonds between chains and surface can be sev-

ered if they exceed a threshold value, and the desorption of chains as well as surface deformation can be used as metrics to evaluate the efficacy of a particular monolayer film. Screening-type studies of such systems in relation to monolayer chemistry may provide insights into the ideal films for lubrication of MEMS/NEMS.

7.2.3 Coarse-Grained MD Simulations

Structure-property screening of monolayer films is essential to optimizing monolayer chemistry for tribological applications, yet the scope of the parameter space makes this a difficult task. Computational cost is increased further as systems become more complex such as through the introduction of asperties, presenting of significant barrier to screening. The coarse-grained model developed in Chapter 6 may provide a route towards overcoming this problem. As discussed in Chapter 6, the potential matching procedure used to derive interactions for coarse-grained silica beads of amorphous nanoparticles should be adaptable for use with silica surfaces. This would require only the attaining of all-atom interaction potential data between two atomistic surfaces and parameterization of bead-bead interactions to match the interaction potential profile for the coarse-grained surface. It is possible this procedure may not even be necessary, and the parameters from Eqs. 6.6 and 6.7 of Chapter 6 may be usable without rederivation.

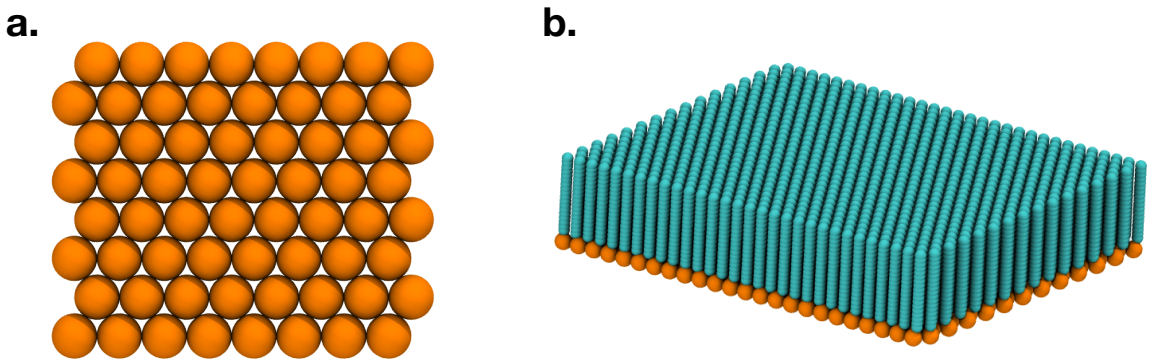

Figure 7.3: a. A coarse-grained silica surface (viewed in the surface plane) and b. a coarse-grained silica surface functionalized by a united-atom alkane monolayer.

Fig. 7.3 shows how a CG silica surface and a united-atom functionalized CG surface might look. While some chemical fidelity is certainly lost in the use of coarse-grained models (such as hydrogen bonding), more sophisticated models exist that attempt to recoup some of this behavior (e.g. anisotropic united-atom models, models with "sticky spots"). However, these coarse-grained monolayers may be better served at determining more general trends related to friction mechanisms, particularly in relationship to asperities. Chain-chain interactions can be toggled (through altering σ and ε) to examine general trends, and simple studies in this area include screening how the effects of the chain-chain σ and ε influence friction as a single-asperity contact, while more complicated studies could look at the effects of multi-component films.

7.3 Bibliography

[1] Grayson, A.; Shawgo, R.; Johnson, A.; Flynn, N.; Li, Y.; Cima, M.; Langer, R. A BioMEMS Review: MEMS Technology for Physiologically Integrated Devices. *Proceedings of the IEEE* **2004**, *92*, 6–21.

[2] Jones, R. L.; Harrod, B. L.; Batteas, J. D. Intercalation of 3-Phenyl-1-proponal into OTS SAMs on Silica Nanoasperities to Create Self-Repairing Interfaces for MEMS Lubrication†. *Langmuir* **2010**, *26*, 16355–16361.

[3] Lewis, J. B.; Vilt, S. G.; Rivera, J. L.; Jennings, G. K.; McCabe, C. Frictional Properties of Mixed Fluorocarbon/Hydrocarbon Silane Monolayers: A Simulation Study. *Langmuir* **2012**, *28*, 14218–14226.

[4] Vilt, S. G.; Caswell, C. J.; Tuberquia, J. C.; McCabe, C.; Jennings, G. K. Effect of Roughness on the Microscale Friction of Hydrocarbon Films. *The Journal of Physical Chemistry C* **2012**, *116*, 21795–21801.

[5] van Beest, B. W. H.; Kramer, G. J.; van Santen, R. A. Force fields for silicas and aluminophosphates based onab initiocalculations. *Physical Review Letters* **1990**, *64*, 1955–1958.

Appendix A

OPLS-AA Force Field

The OPLS force field uses the following contributions to the total potential[1]:

$$E_{\text{non-bonded}} = \sum_i \sum_{j>i} \left[\frac{q_i q_j e^2}{r_{ij}} + 4\varepsilon_{ij} \left[\left(\frac{\sigma_{ij}}{r_{ij}} \right)^{12} - \left(\frac{\sigma_{ij}}{r_{ij}} \right)^{6} \right] \right] \tag{A.1}$$

$$E_{\text{bond}} = \sum_{\text{bonds}} K_r (r - r_0)^2 \tag{A.2}$$

$$E_{\text{angle}} = \sum_{\text{angles}} K_\theta (\theta - \theta_0)^2 \tag{A.3}$$

$$E_{\text{torsion}} = \sum_{\text{torsions}} \frac{1}{2} \left[K_1 (1 + \cos\phi) + K_2 (1 - \cos 2\phi) + K_3 (1 + \cos 3\phi) - K_4 (1 - \cos 4\phi) \right] \tag{A.4}$$

where q_i and q_j are the partial charges on particles i and j, e is Coulomb's constant, r_{ij} is the inter-particle separation, ε and σ are interaction-specific Lennard-Jones parameters, K_r, K_θ, and $K_{1,2,3,4}$ are force constants, r_0 is the equilibrium bond distance, θ_0 is the equilibrium angle, and ϕ is the torsion angle.

For certain molecules, such as aromatics and alkenes, improper torsions are necessary to enforce planarity. The OPLS force field primarily utilizes improper parameters from the AMBER family of force fields, where impropers have the following potential form:

$$E_{\text{impropers}} = \sum_{\text{impropers}} \frac{1}{2} K_\phi [1 + \cos(n\phi - \gamma)] \tag{A.5}$$

where ϕ is the torsion angle, K_ϕ is the force constant, n is the multiplicity, and γ is the phase angle.

OPLS uses geometric mixing rules for cross-interactions:

$$\sigma_{ij} = (\sigma_{ii}\sigma_{jj})^{\frac{1}{2}} \tag{A.6}$$

$$\varepsilon_{ij} = (\varepsilon_{ii}\varepsilon_{jj})^{\frac{1}{2}} \tag{A.7}$$

Additionally, non-bonded interactions are excluded for particles separated by one or two bonds. For particles separated by three bonds, non-bonded interactions are scaled by 0.5.

Detailed below are the OPLS parameters utilized in this work. For Chapters 3 & 4, only a small subset of OPLS parameters are utilized as all systems feature methyl-functionalized alkylsilane chains. These parameters are provided first. For Chapter 5, sixteen unique terminal group chemistries are considered, resulting in a large number of required OPLS parameters. These parameters are provided after that standard alkylsilane parameters, where they have been separated by terminal group chemistry.

Alkylsilanes and Silica

Nonbonded parameters						
Atom type	Element	Charge	Sigma, nm	Epsilon, kcal/mol	Reference	Notes
opls_135	C	-0.18	0.35	0.066	1	-
opls_136	C	-0.12	0.35	0.066	1	-
opls_140	H	0.06	0.25	0.03	1	-
opls_1001	O	-0.43	0.3	0.17	2	-
opls_1002	Si	0.86	0.4	0.1	2	-
opls_1003	Si	0.745 (0.53)	0.4	0.1	2, 3	[1]
opls_1004	C	-0.12	0.35	0.066	1	-
opls_1005	O	-0.683	0.312	0.17	1	-
opls_1006	H	0.418	0	0	1	-
opls_1007	O	-0.215 (-0.43)	0.3	0.17	2, 3	[1]
opls_1008	O	-0.215	0.3	0.17	2	-
opls_1009	H	0.215	0.0	0	n/a	[2]

[1] Values in parentheses were used in Chapter 3, following the work of Lewis et al.[3] to maintain charge neutrality. Models were adjusted in Chapters 4 and 5 to allow use of all charges from Lorenz et al.[2] while maintaining system charge neutrality.

[2] Parameters for hydroxyl surface caps on silica surfaces are not available in the OPLS force field. We have used the same σ and ε values as the standard OPLS hydroxyl parameters and use a charge of 0.215 to maintain charge neutrality in the system.

Bond parameters					
Bond	Elements	k, kcal/mol^{-1} Å ^{2}	r_0, nm	Reference	Notes
opls_135-opls_136	C-C	268	0.1529	1	-
opls_135-opls_140	C-H	340	0.109	1	-
opls_136-opls_140	C-H	340	0.109	1	-
opls_136-opls_1004	C-C	268	0.1529	1	-
opls_1004-opls_140	C-H	340	0.109	1	-
opls_1004-opls_1003	C-Si	200	1.85	2	-
opls_1003-opls_1005	Si-O	300	1.65	2	-
opls_1005-opls_1006	O-H	553	0.945	1	-
opls_1003-opls_1007	Si-O	300	1.65	2	1
opls_1007-opls_1002	O-Si	300	1.65	2	-
opls_1001-opls_1002	O-Si	300	1.65	2	-
opls_1002-opls_1008	Si-O	300	1.65	2	-
opls_1008-opls_1009	O-H	553	0.945	1	-

[1] In Chapter 4, the Si-O interfacial bonds are modeled using a Morse potential, fit to the energy curve obtained for bond dissociation using the ReaxFF force field with parameters from Fogarty et al.[4], yielding the following potential:

$$E_{\text{bond}} = 147.13\left[1 - e^{-1.61(r-1.65)}\right]^2 \tag{A.8}$$

where E_{bond} is in kcal/mol. This was done to provide a platform for future studies of monolayer wear; however, for the current study, the depth of the potential well yields a behavior indistinguishable to that of the standard harmonic bond.

Angle parameters					
Angle	Elements	k, kcal/mol^{-1} deg^2	θ_0, deg	Reference	Notes
opls_135-opls_136-opls_136	C-C-C	58.35	112.7	1	-
opls_136-opls_136-opls_136	C-C-C	58.35	112.7	1	-
opls_136-opls_136-opls_1004	C-C-C	58.35	112.7	1	-
opls_140-opls_135-opls_140	H-C-H	33	107.8	1	-
opls_140-opls_136-opls_140	H-C-H	33	107.8	1	-
opls_140-opls_1004-opls_140	H-C-H	33	107.8	1	-
opls_140-opls_135-opls_136	H-C-C	37.5	110.7	1	-
opls_140-opls_136-opls_136	H-C-C	37.5	110.7	1	-
opls_140-opls_136-opls_1004	H-C-C	37.5	110.7	1	-
opls_136-opls_1004-opls_1003	C-C-Si	30.47	120	2	-
opls_140-opls_1004-opls_1003	H-C-Si	37.5	110.7	n/a	1
opls_1004-opls_1003-opls_1005	C-Si-O	60	100	2	-
opls_1004-opls_1003-opls_1007	C-Si-O	60	100	2	-
opls_1005-opls_1003-opls_1005	O-Si-O	60	110	2	-
opls_1005-opls_1003-opls_1007	O-Si-O	60	110	2	-
opls_1003-opls_1005-opls_1006	Si-O-H	23.7764	122.888	2	-
opls_1003-opls_1007-opls_1002	Si-O-Si	20	145	2	-
opls_1007-opls_1002-opls_1001	O-Si-O	60	110	2	-
opls_1002-opls_1001-opls_1002	Si-O-Si	20	145	2	-
opls_1001-opls_1002-opls_1001	O-Si-O	60	110	2	-
opls_1001-opls_1002-opls_1008	O-Si-O	60	110	2	-
opls_1002-opls_1008-opls_1009	Si-O-H	23.7764	122.888	2	-

[1] H-C-Si parameters do not exist in OPLS. In the work of Lorenz et al.[2] F-C-C angle parameters were also used for F-C-Si angles. Following this approach, H-C-C angle parameters have been used for H-C-Si angles.

Dihedral parameters							
Dihedral	Elements	k1, kcal/mol	k2, kcal/mol	k3, kcal/mol	k4, kcal/mol	Reference	Notes
opls_135-opls_136-opls_136-opls_136	C-C-C-C	1.3 (1.74)	-0.05 (-0.157)	0.2 (0.279)	0.0 (0.0)	5 (1)	1
opls_136-opls_136-opls_136-opls_136	C-C-C-C	1.3 (1.74)	-0.05 (-0.157)	0.2 (0.279)	0.0 (0.0)	5 (1)	1
opls_136-opls_136-opls_136-opls_1004	C-C-C-C	1.3 (1.74)	-0.05 (-0.157)	0.2 (0.279)	0.0 (0.0)	5 (1)	1
opls_140-opls_135-opls_136-opls_136	H-C-C-C	0.0 (0.0)	0.0 (0.0)	0.3 (0.366)	0.0 (0.0)	5 (1)	1
opls_140-opls_136-opls_136-opls_136	H-C-C-C	0.0 (0.0)	0.0 (0.0)	0.3 (0.366)	0.0 (0.0)	5 (1)	1
opls_140-opls_136-opls_136-opls_135	H-C-C-C	0.0 (0.0)	0.0 (0.0)	0.3 (0.366)	0.0 (0.0)	5 (1)	1
opls_140-opls_136-opls_136-opls_1004	H-C-C-C	0.0 (0.0)	0.0 (0.0)	0.3 (0.366)	0.0 (0.0)	5 (1)	1
opls_140-opls_1004-opls_136-opls_136	H-C-C-C	0.0 (0.0)	0.0 (0.0)	0.3 (0.366)	0.0 (0.0)	5 (1)	1
opls_140-opls_135-opls_136-opls_140	H-C-C-H	0.0 (0.0)	0.0 (0.0)	0.3 (0.318)	0.0 (0.0)	5 (1)	1
opls_140-opls_136-opls_136-opls_140	H-C-C-H	0.0 (0.0)	0.0 (0.0)	0.3 (0.318)	0.0 (0.0)	5 (1)	1
opls_140-opls_136-opls_1004-opls_140	H-C-C-H	0.0 (0.0)	0.0 (0.0)	0.3 (0.318)	0.0 (0.0)	5 (1)	1
All torsions containing silicon	X-Si-X-X, Si-X-X-X	0	0	0	0	2	2

[1] Parameters for C-C-C-C, H-C-C-C, and H-C-C-H dihedrals were updated in Ref. 5. In Chapter 3, the older dihedrals of Ref. 1 were used, following the work of Lewis et al.[3]. However, the updated parameters were used in Chapters 4 and 5.

[2] Any torsion containing a silicon atom is treated as a null torsion.

Methyl

Nonbonded parameters						
Atom type	Element	Charge	Sigma, nm	Epsilon, kcal/mol	Reference	Notes
opls_135	C	-0.18	0.35	0.066	1	-
opls_140	H	0.06	0.25	0.03	1	-

Bond parameters					
Bond	Elements	k, kcal/mol^{-1} Å ^{2}	r_0, nm	Reference	Notes
opls_135-opls_136	C-C	268	0.1529	1	-
opls_135-opls_140	C-H	340	0.109	1	-

Angle parameters					
Angle	Elements	k, kcal/mol^{-1} deg^2	θ_0, deg	Reference	Notes
opls_136-opls_136-opls_135	C-C-C	58.35	112.7	1	-
opls_136-opls_135-opls_140	C-C-H	37.5	110.7	1	-
opls_140-opls_135-opls_140	H-C-H	33	107.8	1	-

Dihedral parameters							
Dihedral	Elements	k1, kcal/mol	k2, kcal/mol	k3, kcal/mol	k4, kcal/mol	Reference	Notes
opls_136-opls_136-opls_136-opls_135	C-C-C-C	1.3	-0.05	0.2	0.0	5	-
opls_136-opls_136-opls_135-opls_140	C-C-C-H	0.0	0.0	0.3	0.0	5	-
opls_140-opls_136-opls_135-opls_140	H-C-C-H	0.0	0.0	0.3	0.0	5	-

Acetyl

Nonbonded parameters						
Atom type	Element	Charge	Sigma, nm	Epsilon, kcal/mol	Reference	Notes
opls_135	C	-0.18	0.35	0.066	1	-
opls_282	H	0.06	0.242	0.015	1	-
opls_280	C	0.47	0.375	0.105	1	-
opls_281	O	-0.47	0.296	0.21	1	-

Bond parameters					
Bond	Elements	k, kcal/mol^{-1} Å ^{2}	r_0, nm	Reference	Notes
opls_135-opls_282	C-H	340	0.109	1	-
opls_135-opls_280	C-C	317	0.1522	6	-
opls_280-opls_281	C-O	570	0.1229	6	-
opls_280-opls_136	C-C	317	0.1522	6	-

Angle parameters					
Angle	Elements	k, kcal/mol^{-1} deg^2	θ_0, deg	Reference	Notes
opls_282-opls_135-opls-282	H-C-H	33	107.8	1	-
opls_282-opls_135-opls_280	H-C-C	35	109.5	6	-
opls_135-opls_280-opls_281	C-C-O	80	120.4	6	-
opls_135-opls_280-opls_136	C-C-C	70	116.0	N/A	[1]
opls_281-opls_280-opls_136	O-C-C	80	120.4	6	-
opls_280-opls_136-opls_282	C-C-H	35	109.5	6	-
opls_280-opls_136-opls_136	C-C-C	63	111.1	6	-
opls_282-opls_136-opls_136	H-C-C	37.5	110.7	1	-
opls_136-opls_136-opls_140	C-C-H	37.5	110.7	1	-
opls_136-opls_136-opls_136	C-C-C	58.35	112.7	1	-

[1] No reference found. Parameters used from GROMACS *as is*.

Dihedral parameters							
Dihedral	Elements	k1, kcal/mol	k2, kcal/mol	k3, kcal/mol	k4, kcal/mol	Reference	Notes
opls_282-opls_135-opls_280-opls_281	H-C-C-O	0.0	0.0	0.0	0.0	1	-
opls_282-opls_135-opls_280-opls_136	H-C-C-C	0.0	0.0	0.275	0.0	1	-
opls_135-opls_280-opls_136-opls_136	C-C-C-C	1.454	-0.144	-0.775	0.0	1	-
opls_135-opls_280-opls_136-opls_282	C-C-C-H	0.0	0.0	0.275	0.0	1	-
opls_281-opls_280-opls_136-opls_136	O-C-C-C	-0.277	1.228	-0.694	0.0	1	-
opls_281-opls_280-opls_136-opls_282	O-C-C-H	0.0	0.0	0.0	0.0	1	-
opls_280-opls_136-opls_136-opls_136	C-C-C-C	-1.697	-0.456	0.585	0.0	1	-
opls_280-opls_136-opls_136-opls_140	C-C-C-H	0.0	0.0	-0.076	0.0	1	-
opls_282-opls_136-opls_136-opls_136	H-C-C-C	0.0	0.0	0.3	0.0	5	-
opls_282-opls_136-opls_136-opls_140	H-C-C-H	0.0	0.0	0.3	0.0	5	-

Improper parameters						
Improper	Elements	γ, degrees	K_ϕ, kcal/mol	n	Reference	Notes
opls_281-opls_280-opls_135-opls_136	O-C-C-C	180	21.0	2	6	-

Amino

Nonbonded parameters						
Atom type	Element	Charge	Sigma, nm	Epsilon, kcal/mol	Reference	Notes
opls_909	H	0.36	0	0	7	-
opls_900	N	-0.9	0.33	0.17	7	-
opls_906	C	0.06	0.35	0.066	7	-
opls_911	H	0.06	0.25	0.015	7	-

Bond parameters					
Bond	Elements	k, kcal/mol^{-1} Å ^{2}	r_0, nm	Reference	Notes
opls_909-opls_900	H-N	434	0.101	7	-
opls_900-opls_906	N-C	382	0.1448	7	-
opls_906-opls_911	C-H	340	0.109	7	-
opls_906-opls_136	C-C	268	0.1529	7	-

Angle parameters					
Angle	Elements	k, kcal/mol^{-1} deg^2	θ_0, deg	Reference	Notes
opls_909-opls_900-opls_909	H-N-H	43.6	106.4	7	-
opls_909-opls_900-opls_906	H-N-C	35	109.5	7	-
opls_900-opls_906-opls_911	N-C-H	35	109.5	7	-
opls_900-opls_906-opls_136	N-C-C	56.2	109.47	7	-
opls_911-opls_906-opls-911	H-C-H	33	107.8	1	-
opls_911-opls_906-opls_136	H-C-C	37.5	110.7	1	-
opls_906-opls_136-opls_140	C-C-H	37.5	110.7	1	-
opls_906-opls_136-opls_136	C-C-C	58.35	112.7	1	-

Dihedral parameters							
Dihedral	Elements	k1, kcal/mol	k2, kcal/mol	k3, kcal/mol	k4, kcal/mol	Reference	Notes
opls_909-opls_900-opls_906-opls_911	H-N-C-H	0.0	0.0	0.4	0.0	7	-
opls_909-opls_900-opls_906-opls_136	H-N-C-C	-0.19	-0.417	0.418	0.0	7	-
opls_900-opls_906-opls_136-opls_136	N-C-C-C	2.392	-0.674	0.55	0.0	7	-
opls_900-opls_906-opls_136-opls_140	N-C-C-H	-1.013	-0.709	0.473	0.0	7	-
opls_911-opls_906-opls_136-opls_136	H-C-C-C	0.0	0.0	0.3	0.0	5	-
opls_911-opls_906-opls_136-opls_140	H-C-C-H	0.0	0.0	0.3	0.0	5	-
opls_906-opls_136-opls_136-opls_136	C-C-C-C	1.3	-0.05	0.2	0.0	5	-
opls_906-opls_136-opls_136-opls_140	C-C-C-H	0.0	0.0	0.3	0.0	5	-

Carboxyl

Nonbonded parameters						
Atom type	Element	Charge	Sigma, nm	Epsilon, kcal/mol	Reference	Notes
opls_270	H	0.45	0	0	1	-
opls_268	O	-0.53	0.3	0.17	1	-
opls_267	C	0.52	0.375	0.105	1	-
opls_269	O	-0.44	0.296	0.21	1	-

Bond parameters					
Bond	Elements	k, kcal/mol^{-1} Å ^{2}	r_0, nm	Reference	Notes
opls_270-opls_268	H-O	553	0.0945	6	-
opls_268-opls_267	O-C	450	0.1364	6	-
opls_267-opls_269	C-O	570	0.1229	6	-
opls_267-opls_136	C-C	317	0.1522	6	-

Angle parameters					
Angle	Elements	k, kcal/mol^{-1} deg^2	θ_0, deg	Reference	Notes
opls_270-opls_268-opls_267	H-O-C	35	113	6	-
opls_268-opls_267-opls_269	O-C-O	80	121	8	-
opls_268-opls_267-opls_136	O-C-C	70	108	8	-
opls_269-opls_267-opls_136	O-C-C	80	120.4	6	-
opls_267-opls_136-opls_140	C-C-H	35	109.5	6	-
opls_267-opls_136-opls_136	C-C-C	63	111.1	6	-

Dihedral parameters							
Dihedral	Elements	k1, kcal/mol	k2, kcal/mol	k3, kcal/mol	k4, kcal/mol	Reference	Notes
opls_270-opls_268-opls_267-opls_269	H-O-C-O	0.0	5.5	0.0	0.0	N/A	1
opls_270-opls_268-opls_267-opls_136	H-O-C-C	1.5	5.5	0.0	0.0	N/A	1
opls_268-opls_267-opls_136-opls_136	O-C-C-C	1.0	0.546	0.45	0.0	8	-
opls_268-opls_267-opls_136-opls_140	O-C-C-H	0.0	0.0	0.0	0.0	8	-
opls_269-opls_267-opls_136-opls_140	O-C-C-H	0.0	0.0	0.0	0.0	8	-
opls_269-opls_267-opls_136-opls_136	O-C-C-C	0.0	0.546	0.0	0.0	8	-
opls_269-opls_267-opls_136-opls_136	C-C-C-C	-2.06	-0.313	0.315	0.0	1	-
opls_267-opls_136-opls_136-opls_140	C-C-C-H	0.0	0.0	-0.1	0.0	1	-

[1] No reference found. Parameters used from GROMACS *as is*.

Improper parameters						
Improper	Elements	γ, degrees	K_ϕ, kcal/mol	n	Reference	Notes
opls_269-opls_267-opls_268-opls_136	O-C-O-C	180	21.0	2	6	-

Nitrile

Nonbonded parameters						
Atom type	Element	Charge	Sigma, nm	Epsilon, kcal/mol	Reference	Notes
opls_753	N	-0.56	0.32	0.17	5	-
opls_754	C	0.46	0.33	0.066	5	-
opls_756	C	-0.02	0.33	0.066	5	-
opls_759	H	0.06	0.25	0.15	5	-

Bond parameters					
Bond	Elements	k, kcal/mol^{-1} Å ^{2}	r_0, nm	Reference	Notes
opls_753-opls_754	N-C	650	0.1157	5	-
opls_754-opls_756	C-C	385	0.1458	5	1
opls_756-opls_759	C-H	340	0.109	1	-
opls_756-opls_136	C-C	268	0.1529	1	-

[1] GROMACS parameters differ from the literature. Parameters from Ref. 5 have been used.

Angle parameters					
Angle	Elements	k, kcal/mol^{-1} deg^2	θ_0, deg	Reference	Notes
opls_753-opls_754-opls_756	N-C-C	150	180	5	-
opls_754-opls_756-opls_759	C-C-H	35	108.5	5	-
opls_754-opls_756-opls_136	C-C-C	58.35	112.7	5	-
opls_759-opls_756-opls_759	H-C-H	33	107.8	1	-
opls_759-opls_756-opls_136	H-C-C	37.5	110.7	1	-
opls_756-opls_136-opls_140	C-C-H	37.5	110.7	1	-
opls_756-opls_136-opls_136	C-C-C	58.35	112.7	1	-

Dihedral parameters							
Dihedral	Elements	k1, kcal/mol	k2, kcal/mol	k3, kcal/mol	k4, kcal/mol	Reference	Notes
opls_753-opls_754-opls_756-opls_136	N-C-C-C	0.0	0.0	0.0	0.0	5	-
opls_753-opls_754-opls_756-opls_759	N-C-C-H	0.0	0.0	0.0	0.0	5	-
opls_754-opls_756-opls_136-opls_136	C-C-C-C	1.3	-0.05	0.2	0.0	N/A	1
opls_754-opls_756-opls_136-opls_140	C-C-C-H	0.0	0.0	0.366	0.0	5	-
opls_759-opls_756-opls_136-opls_136	H-C-C-C	0.0	0.0	0.3	0.0	5	-
opls_759-opls_756-opls_136-opls_140	H-C-C-H	0.0	0.0	0.3	0.0	5	-
opls_756-opls_136-opls_136-opls_136	C-C-C-C	1.3	-0.05	0.2	0.0	5	-
opls_756-opls_136-opls_136-opls_140	C-C-C-H	0.0	0.0	0.3	0.0	5	-

[1] Parameters don't exist in GROMACS or the literature. Parameters for alkane C-C-C-C dihedrals have been used.

Cyclopropyl

Nonbonded parameters						
Atom type	Element	Charge	Sigma, nm	Epsilon, kcal/mol	Reference	Notes
opls_140	H	0.06	0.25	0.03	N/A	1
opls_711	C	-0.12	0.35	0.066	N/A	1
opls_712	C	-0.06	0.35	0.066	N/A	1

[1] No reference found. Parameters used from GROMACS *as is*.

Bond parameters					
Bond	Elements	k, kcal/mol^{-1} Å ^{2}	r_0, nm	Reference	Notes
opls_711-opls_140	C-H	340	0.1088	N/A	1
opls_711-opls_712	C-C	260	0.1509	N/A	1
opls_712-opls_140	C-H	340	0.1088	N/A	1
opls_712-opls_136	C-C	280	0.151	N/A	1

[1] No reference found. Parameters used from GROMACS *as is*.

Angle parameters					
Angle	Elements	k, kcal/mol^{-1} deg^2	θ_0, deg	Reference	Notes
opls_140-opls_711-opls_140	H-C-H	35	114.3	N/A	1
opls_140-opls_711-opls_711	H-C-C	37.5	117.2	N/A	1
opls_140-opls_711-opls_712	H-C-C	37.5	117.2	N/A	1
opls_711-opls_711-opls_712	C-C-C	30	60	N/A	1
opls_711-opls_712-opls_711	C-C-C	30	60	N/A	1
opls_711-opls_711-opls_140	C-C-H	37.5	117.2	N/A	1
opls_711-opls_712-opls_140	C-C-H	37.5	117.2	N/A	1
opls_711-opls_712-opls_136	C-C-C	37.5	117.2	N/A	1
opls_140-opls_712-opls_136	H-C-C	35	114.3	N/A	1
opls_712-opls_136-opls_136	C-C-C	58.35	112.7	N/A	2
opls_712-opls_136-opls_140	C-C-H	37.5	110.7	N/A	1

[1] No reference found. Parameters used from GROMACS *as is*.

[2] Parameters not found in GROMACS or the literature. Alkane C-C-C parameters have been used.

Dihedral parameters							
Dihedral	Elements	k1, kcal/mol	k2, kcal/mol	k3, kcal/mol	k4, kcal/mol	Reference	Notes
opls_140-opls_711-opls_711-opls_140	H-C-C-H	0.0	0.0	0.3	0.0	N/A	1
opls_140-opls_711-opls_711-opls_712	H-C-C-C	0.0	0.0	0.3	0.0	N/A	1
opls_140-opls_711-opls_712-opls_711	H-C-C-C	0.0	0.0	0.3	0.0	N/A	1
opls_140-opls_711-opls_712-opls_140	H-C-C-H	0.0	0.0	0.3	0.0	N/A	1
opls_140-opls_711-opls_712-opls_136	H-C-C-C	0.0	0.0	0.3	0.0	N/A	1
opls_711-opls_711-opls_712-opls_140	C-C-C-H	0.0	0.0	0.3	0.0	N/A	1
opls_711-opls_711-opls_712-opls_136	C-C-C-C	1.3	-0.05	0.2	0.0	N/A	1
opls_711-opls_712-opls_711-opls_140	C-C-C-H	0.0	0.0	0.3	0.0	N/A	1
opls_711-opls_712-opls_136-opls_136	C-C-C-C	1.3	-0.05	0.2	0.0	N/A	2
opls_711-opls_712-opls_136-opls_140	C-C-C-H	0.0	0.0	0.3	0.0	N/A	1
opls_140-opls_712-opls_136-opls_136	H-C-C-C	0.0	0.0	0.3	0.0	N/A	3
opls_140-opls_712-opls_136-opls_140	H-C-C-H	0.0	0.0	0.3	0.0	N/A	4
opls_712-opls_136-opls_136-opls_136	C-C-C-C	1.3	-0.05	0.2	0.0	N/A	2
opls_712-opls_136-opls_136-opls_140	C-C-C-H	0.0	0.0	0.3	0.0	N/A	3

[1] No reference found. Parameters used from GROMACS *as is*.

[2] Parameters not found in GROMACS or the literature. Parameters for alkane C-C-C-C dihedrals have been used.

[3] Parameters not found in GROMACS or the literature. Parameters for alkane C-C-C-H dihedrals have been used.

[4] Parameters not found in GROMACS or the literature. Parameters for alkane H-C-C-H dihedrals have been used.

Vinyl

Nonbonded parameters						
Atom type	Element	Charge	Sigma, nm	Epsilon, kcal/mol	Reference	Notes
opls_144	H	0.115	0.242	0.03	1	-
opls_143	C	-0.23	0.355	0.076	1	-
opls_142	C	-0.115	0.355	0.076	1	-

Bond parameters					
Bond	Elements	k, kcal/mol^{-1} Å ^{2}	r_0, nm	Reference	Notes
opls_144-opls_143	C-H	340	0.108	6	-
opls_143-opls_142	C-C	549	0.134	6	-
opls_142-opls_144	C-H	340	0.108	6	-
opls_142-opls_136	C-C	317	0.151	6	-

Angle parameters					
Angle	Elements	k, kcal/mol^{-1} deg^2	θ_0, deg	Reference	Notes
opls_144-opls_143-opls_144	H-C-H	35	117	N/A	1
opls_144-opls_143-opls_142	H-C-C	35	120	9	
opls_143-opls_142-opls_136	C-C-C	70	124	N/A	1
opls_143-opls_142-opls_144	C-C-H	35	120	9	
opls_144-opls_142-opls_136	H-C-C	35	117	N/A	1
opls_142-opls_136-opls_136	C-C-C	63	111.1	6	
opls_142-opls_136-opls_140	C-C-H	35	109.5	6	

[1] No reference found. Parameters used from GROMACS *as is*.

Dihedral parameters							
Dihedral	Elements	k1, kcal/mol	k2, kcal/mol	k3, kcal/mol	k4, kcal/mol	Reference	Notes
opls_144-opls_143-opls_142-opls_136	H-C-C-C	0.0	14.0	0.0	0.0	N/A	1
opls_144-opls_143-opls_142-opls_144	H-C-C-H	0.0	14.0	0.0	0.0	N/A	1
opls_143-opls_142-opls_136-opls_136	C-C-C-C	0.346	0.405	-0.904	0.0	N/A	1
opls_143-opls_142-opls_136-opls_140	C-C-C-H	0.0	0.0	-0.372	0.0	1	-
opls_144-opls_142-opls_136-opls_136	H-C-C-C	0.0	0.0	0.3	0.0	N/A	2
opls_144-opls_142-opls_136-opls_140	H-C-C-H	0.0	0.0	0.318	0.0	N/A	1
opls_142-opls_136-opls_136-opls_136	C-C-C-C	1.3	-0.05	0.2	0.0	N/A	1
opls_142-opls_136-opls_136-opls_140	C-C-C-H	0.0	0.0	0.366	0.0	N/A	1

[1] No reference found. Parameters used from GROMACS *as is*.

[2] Parameters not found in GROMACS or the literature. Parameters for alkane C-C-C-H dihedrals have been used.

Improper parameters						
Improper	Elements	γ, degrees	K_ϕ, kcal/mol	n	Reference	Notes
opls_142-opls_143-opls_144-opls_144	C-C-H-H	180	21.0	2	N/A	1
opls_143-opls_142-opls_144-opls_136	C-C-H-C	180	30.0	2	N/A	1

[1] No reference found. Parameters used from GROMACS *as is*.

Fluorophenyl

Nonbonded parameters						
Atom type	Element	Charge	Sigma, nm	Epsilon, kcal/mol	Reference	Notes
opls_719	F	-0.22	0.285	0.061	10	-
opls_718	C	0.22	0.355	0.07	10	-
opls_145	C	-0.115	0.355	0.07	1	-
opls_146	H	0.115	0.242	0.03	1	-
opls_149	C	-0.005	0.35	0.066	1	-
opls_140	H	0.06	0.25	0.03	1	-

Bond parameters					
Bond	Elements	k, kcal/mol^{-1} Å ^{2}	r_0, nm	Reference	Notes
opls_719-opls_718	F-C	420	0.1354	11	-
opls_718-opls_145	C-C	469	0.14	6	-
opls_145-opls_146	C-H	367	0.108	12	-
opls_145-opls_145	C-C	469	0.14	6	-
opls_145-opls_149	C-C	317	0.151	6	-
opls_149-opls_140	C-H	340	0.109	1	-
opls_149-opls_136	C-C	268	0.1529	1	-

Angle parameters					
Angle	Elements	k, kcal/mol^{-1} deg^2	θ_0, deg	Reference	Notes
opls_719-opls_718-opls_145	F-C-C	80	120	11	-
opls_718-opls_145-opls_146	C-C-H	35	120	6	-
opls_718-opls_145-opls_145	C-C-C	63	120	7	-
opls_146-opls_145-opls_145	H-C-C	35	120	6	-
opls_145-opls_718-opls_145	C-C-C	63	120	7	-
opls_145-opls_145-opls_145	C-C-C	63	120	7	-
opls_145-opls_145-opls_149	C-C-C	70	120	6	-
opls_145-opls_149-opls_136	C-C-C	63	114	6	-
opls_145-opls_149-opls_140	C-C-H	35	109.5	6	-
opls_149-opls_136-opls_136	C-C-C	58.35	112.7	1	-
opls_149-opls_136-opls_140	C-C-H	37.5	110.7	1	-
opls_140-opls_149-opls_140	H-C-H	33	107.8	1	-

Dihedral parameters							
Dihedral	Elements	k1, kcal/mol	k2, kcal/mol	k3, kcal/mol	k4, kcal/mol	Reference	Notes
opls_719-opls_718-opls_145-opls_145	F-C-C-C	0.0	7.25	0.0	0.0	7	-
opls_719-opls_718-opls_145-opls_146	F-C-C-H	0.0	7.25	0.0	0.0	7	-
opls_718-opls_145-opls_145-opls_145	C-C-C-C	0.0	7.25	0.0	0.0	7	-
opls_718-opls_145-opls_145-opls_146	C-C-C-H	0.0	7.25	0.0	0.0	7	-
opls_146-opls_145-opls_718-opls_145	H-C-C-C	0.0	7.25	0.0	0.0	7	-
opls_146-opls_145-opls_145-opls_146	H-C-C-H	0.0	7.25	0.0	0.0	7	-
opls_146-opls_145-opls_145-opls_145	H-C-C-C	0.0	7.25	0.0	0.0	7	-
opls_146-opls_145-opls_145-opls_149	H-C-C-C	0.0	7.25	0.0	0.0	7	-
opls_145-opls_145-opls_145-opls_145	C-C-C-C	0.0	7.25	0.0	0.0	7	-
opls_145-opls_145-opls_145-opls_149	C-C-C-C	0.0	7.25	0.0	0.0	7	-
opls_145-opls_718-opls_145-opls_145	C-C-C-C	0.0	7.25	0.0	0.0	7	-
opls_145-opls_145-opls_149-opls_136	C-C-C-C	0.0	0.0	0.0	0.0	1	-
opls_145-opls_145-opls_149-opls_140	C-C-C-H	0.0	0.0	0.0	0.0	1	-
opls_145-opls_149-opls_136-opls_136	C-C-C-C	1.3	-0.05	0.2	0.0	N/A	1
opls_145-opls_149-opls_136-opls_140	C-C-C-H	0.0	0.0	0.462	0.0	1	-

[1] No reference found. Parameters used from GROMACS *as is*. GROMACS uses same parameters as alkane C-C-C-C.

Improper parameters						
Improper	Elements	γ, degrees	K_ϕ, kcal/mol	n	Reference	Notes
opls_719-opls_718-opls_145-opls_145	F-C-C-C	180	2.2	2	7	-
opls_146-opls_145-opls_718-opls_145	H-C-C-C	180	2.2	2	7	-
opls_146-opls_145-opls_145-opls_145	H-C-C-C	180	2.2	2	7	-
opls_149-opls_145-opls_145-opls_145	C-C-C-C	180	2.2	2	7	-

Hydroxyl

Nonbonded parameters						
Atom type	Element	Charge	Sigma, nm	Epsilon, kcal/mol	Reference	Notes
opls_155	H	0.418	0	0	1	-
opls_154	O	-0.683	0.312	0.17	1	-
opls_157	C	0.145	0.35	0.066	1	-
opls_140	H	0.06	0.25	0.03	1	-

Bond parameters					
Bond	Elements	k, kcal/mol^{-1} Å ^{2}	r_0, nm	Reference	Notes
opls_155-opls_154	H-O	553	0.0945	6	-
opls_154-opls_157	O-C	320	0.141	6	-
opls_157-opls_140	C-H	340	0.109	1	-
opls_157-opls_136	C-C	268	0.1529	1	-

Angle parameters					
Angle	Elements	k, kcal/mol^{-1} deg^2	θ_0, deg	Reference	Notes
opls_155-opls_154-opls_157	H-O-C	55	108.5	6	-
opls_154-opls_157-opls_136	O-C-C	50	109.5	6	-
opls_154-opls_157-opls_140	O-C-H	35	109.5	6	-
opls_140-opls_157-opls_140	H-C-H	33	107.8	1	-
opls_140-opls_157-opls_136	H-C-C	37.5	110.7	1	-
opls_157-opls_136-opls_136	C-C-C	58.35	112.7	1	-
opls_157-opls_136-opls_140	C-C-H	37.5	110.7	1	-

Dihedral parameters							
Dihedral	Elements	k1, kcal/mol	k2, kcal/mol	k3, kcal/mol	k4, kcal/mol	Reference	Notes
opls_155-opls_154-opls_157-opls_136	H-O-C-C	-0.356	-0.174	0.492	0.0	1	-
opls_155-opls_154-opls_157-opls_140	H-O-C-H	0.0	0.0	0.45	0.0	1	-
opls_154-opls_157-opls_136-opls_136	O-C-C-C	1.711	-0.5	0.663	0.0	1	-
opls_154-opls_157-opls_136-opls_140	O-C-C-H	0.0	0.0	0.468	0.0	1	-
opls_140-opls_157-opls_136-opls_136	H-C-C-C	0.0	0.0	0.3	0.0	5	-
opls_140-opls_157-opls_136-opls_140	H-C-C-H	0.0	0.0	0.3	0.0	5	-
opls_157-opls_136-opls_136-opls_136	C-C-C-C	1.3	-0.05	0.2	0.0	5	-
opls_157-opls_136-opls_136-opls_140	C-C-C-H	0.0	0.0	0.3	0.0	5	-

Isopropyl

Nonbonded parameters						
Atom type	Element	Charge	Sigma, nm	Epsilon, kcal/mol	Reference	Notes
opls_140	H	0.06	0.25	0.03	1	-
opls_135	C	-0.18	0.35	0.066	1	-
opls_137	C	-0.06	0.35	0.066	1	-

Bond parameters					
Bond	Elements	k, kcal/mol^{-1} Å ^{2}	r_0, nm	Reference	Notes
opls_140-opls_135	H-C	340	0.109	1	-
opls_135-opls_137	C-C	268	0.1529	1	-
opls_137-opls_140	C-H	340	0.109	1	-
opls_137-opls_136	C-C	268	0.1529	1	-

Angle parameters					
Angle	Elements	k, kcal/mol^{-1} deg^2	θ_0, deg	Reference	Notes
opls_140-opls_135-opls_140	H-C-H	33	107.8	1	-
opls_140-opls_135-opls_137	H-C-C	37.5	110.7	1	-
opls_135-opls_137-opls_135	C-C-C	58.35	112.7	1	-
opls_135-opls_137-opls_140	C-C-H	37.5	110.7	1	-
opls_135-opls_137-opls_136	C-C-C	58.35	112.7	1	-
opls_140-opls_137-opls_136	H-C-C	37.5	110.7	1	-
opls_137-opls_136-opls_136	C-C-C	58.35	112.7	1	-
opls_137-opls_136-opls_140	C-C-H	37.5	110.7	1	-

Dihedral parameters							
Dihedral	Elements	k1, kcal/mol	k2, kcal/mol	k3, kcal/mol	k4, kcal/mol	Reference	Notes
opls_140-opls_135-opls_137-opls_140	H-C-C-H	0.0	0.0	0.3	0.0	5	-
opls_140-opls_135-opls_137-opls_135	H-C-C-C	0.0	0.0	0.3	0.0	5	-
opls_140-opls_135-opls_137-opls_136	H-C-C-C	0.0	0.0	0.3	0.0	5	-
opls_140-opls_137-opls_136-opls_136	H-C-C-C	0.0	0.0	0.3	0.0	5	-
opls_140-opls_137-opls_136-opls_140	H-C-C-H	0.0	0.0	0.3	0.0	5	-
opls_135-opls_137-opls_136-opls_136	C-C-C-C	1.3	-0.05	0.2	0.0	5	-
opls_135-opls_137-opls_136-opls_140	C-C-C-H	0.0	0.0	0.3	0.0	5	-
opls_137-opls_136-opls_136-opls_136	C-C-C-C	1.3	-0.05	0.2	0.0	5	-
opls_137-opls_136-opls_136-opls_140	C-C-C-H	0.0	0.0	0.3	0.0	5	-

Methoxy

Nonbonded parameters						
Atom type	Element	Charge	Sigma, nm	Epsilon, kcal/mol	Reference	Notes
opls_185	H	0.03	0.25	0.03	1	-
opls_181	C	0.11	0.35	0.066	1	-
opls_180	O	-0.4	0.29	0.14	1	-
opls_182	C	0.14	0.35	0.066	1	-

Bond parameters					
Bond	Elements	k, kcal/mol^{-1} Å ^{2}	r_0, nm	Reference	Notes
opls_185-opls_181	H-C	340	0.109	1	-
opls_181-opls_180	C-O	320	0.141	6	-
opls_180-opls_182	O-C	320	0.141	6	-
opls_182-opls_185	C-H	340	0.109	1	-
opls_182-opls_136	C-C	268	0.1529	1	-

Angle parameters					
Angle	Elements	k, kcal/mol^{-1} deg^2	θ_0, deg	Reference	Notes
opls_185-opls_181-opls_185	H-C-H	33	107.8	1	-
opls_185-opls_181-opls_180	H-C-O	35	109.5	6	-
opls_181-opls_180-opls_182	C-O-C	60	109.5	6	-
opls_180-opls_182-opls_136	O-C-C	50	109.5	6	-
opls_180-opls_182-opls_185	O-C-H	35	109.5	6	-
opls_185-opls_182-opls_185	H-C-H	33	107.8	1	-
opls_185-opls_182-opls_136	H-C-C	37.5	110.7	1	-
opls_182-opls_136-opls_136	C-C-C	58.35	112.7	1	-
opls_182-opls_136-opls_140	C-C-H	37.5	110.7	1	-

Dihedral parameters							
Dihedral	Elements	k1, kcal/mol	k2, kcal/mol	k3, kcal/mol	k4, kcal/mol	Reference	Notes
opls_185-opls_181-opls_180-opls_182	H-C-O-C	0.0	0.0	0.76	0.0	1	-
opls_181-opls_180-opls_182-opls_136	C-O-C-C	0.65	-0.25	0.67	0.0	1	-
opls_181-opls_180-opls_182-opls_185	C-O-C-H	0.0	0.0	0.76	0.0	1	-
opls_180-opls_182-opls_136-opls_136	O-C-C-C	1.711	-0.5	0.663	0.0	1	-
opls_180-opls_182-opls_136-opls_140	O-C-C-H	0.0	0.0	0.468	0.0	1	-
opls_185-opls_182-opls_136-opls_136	H-C-C-C	0.0	0.0	0.3	0.0	5	-
opls_185-opls_182-opls_136-opls_140	H-C-C-H	0.0	0.0	0.3	0.0	5	-
opls_182-opls_136-opls_136-opls_136	C-C-C-C	1.3	-0.05	0.2	0.0	5	-
opls_182-opls_136-opls_136-opls_140	C-C-C-H	0.0	0.0	0.3	0.0	5	-

Nitro

Nonbonded parameters						
Atom type	Element	Charge	Sigma, nm	Epsilon, kcal/mol	Reference	Notes
opls_761	O	-0.37	0.296	0.17	5	-
opls_760	N	0.54	0.325	0.12	5	-
opls_764	C	0.08	0.35	0.066	5	-
opls_763	H	0.06	0.25	0.015	5	-

Bond parameters					
Bond	Elements	k, kcal/mol^{-1} Å ^{2}	r_0, nm	Reference	Notes
opls_761-opls_760	O-N	550	0.1225	5	-
opls_760-opls_764	N-C	375	0.149	5	-
opls_764-opls_763	C-H	340	0.109	1	-
opls_764-opls_136	C-C	268	0.1529	1	-

Angle parameters					
Angle	Elements	k, kcal/mol^{-1} deg^2	θ_0, deg	Reference	Notes
opls_761-opls_760-opls_761	O-N-O	80	125	5	-
opls_761-opls_760-opls_764	O-N-C	80	117.5	5	-
opls_760-opls_764-opls_763	N-C-H	35	105	5	-
opls_760-opls_764-opls_136	N-C-C	63	111.1	5	-
opls_763-opls_764-opls_763	H-C-H	33	107.8	1	-
opls_763-opls_764-opls_136	H-C-C	37.5	110.7	1	-
opls_764-opls_136-opls_136	C-C-C	58.35	112.7	1	-
opls_764-opls_136-opls_140	C-C-H	37.5	110.7	1	-

Dihedral parameters							
Dihedral	Elements	k1, kcal/mol	k2, kcal/mol	k3, kcal/mol	k4, kcal/mol	Reference	Notes
opls_761-opls_760-opls_764-opls_136	O-N-C-C	0.0	0.4	0.0	0.0	5	-
opls_761-opls_760-opls_764-opls_763	O-N-C-H	0.0	0.0	0.0	0.0	5	-
opls_760-opls_764-opls_136-opls_136	N-C-C-C	-1.54	-0.214	0.0	0.0	5	1
opls_760-opls_764-opls_136-opls_140	N-C-C-H	0.0	0.0	-0.225	0.0	5	-
opls_763-opls_764-opls_136-opls_136	H-C-C-C	0.0	0.0	0.3	0.0	5	-
opls_763-opls_764-opls_136-opls_140	H-C-C-H	0.0	0.0	0.3	0.0	5	-
opls_764-opls_136-opls_136-opls_136	C-C-C-C	1.3	-0.05	0.2	0.0	5	-
opls_764-opls_136-opls_136-opls_140	C-C-C-H	0.0	0.0	0.3	0.0	5	-

[1] Parameters did not exist in GROMACS. Parameters from Ref. 5 have been used.

Nitrophenyl

Nonbonded parameters						
Atom type	Element	Charge	Sigma, nm	Epsilon, kcal/mol	Reference	Notes
opls_761	O	-0.37	0.296	0.17	5	-
opls_767	N	0.65	0.325	0.12	5	-
opls_768	C	0.09	0.355	0.07	5	-
opls_145	C	-0.115	0.355	0.07	1	-
opls_146	H	0.115	0.242	0.03	1	-
opls_149	C	-0.005	0.35	0.066	1	-
opls_140	H	0.06	0.25	0.03	1	-

Bond parameters					
Bond	Elements	k, kcal/mol^{-1} Å ^{2}	r_0, nm	Reference	Notes
opls_761-opls_767	O-N	550	0.1225	5	-
opls_767-opls_768	N-C	400	0.146	5	-
opls_768-opls_145	C-C	469	0.14	7	-
opls_145-opls_146	C-H	367	0.108	12	-
opls_145-opls_149	C-C	317	0.151	6	-
opls_149-opls_140	C-H	340	0.109	1	-
opls_149-opls_136	C-C	268	0.1529	1	-

Angle parameters					
Angle	Elements	k, kcal/mol^{-1} deg^2	θ_0, deg	Reference	Notes
opls_761-opls_767-opls_761	O-N-O	80	125	5	-
opls_761-opls_767-opls_768	O-N-C	80	117.5	5	-
opls_767-opls_768-opls_145	N-C-C	85	120	5	-
opls_768-opls_145-opls_145	C-C-C	63	120	7	-
opls_768-opls_145-opls_146	C-C-H	35	120	6	-
opls_145-opls_768-opls_145	C-C-C	63	120	6	-
opls_146-opls_145-opls_768	H-C-C	35	120	6	-
opls_146-opls_145-opls_145	H-C-C	35	120	6	-
opls_145-opls_145-opls_145	C-C-C	63	120	7	-
opls_145-opls_145-opls_149	C-C-C	70	120	6	-
opls_145-opls_149-opls_136	C-C-C	63	114	6	-
opls_145-opls_149-opls_140	C-C-H	35	109.5	6	-
opls_140-opls_149-opls_140	H-C-H	33	107.8	1	-
opls_140-opls_149-opls_136	H-C-C	37.5	110.7	1	-
opls_149-opls_136-opls_136	C-C-C	58.35	112.7	1	-
opls_149-opls_136-opls_140	C-C-H	37.5	110.7	1	-

Dihedral parameters							
Dihedral	Elements	k1, kcal/mol	k2, kcal/mol	k3, kcal/mol	k4, kcal/mol	Reference	Notes
opls_761-opls_767-opls_768-opls_145	O-N-C-C	0.0	1.15	0.0	0.0	5	-
opls_767-opls_768-opls_145-opls_145	N-C-C-C	0.0	7.25	0.0	0.0	7	-
opls_767-opls_768-opls_145-opls_146	N-C-C-H	0.0	7.25	0.0	0.0	7	-
opls_768-opls_145-opls_145-opls_145	C-C-C-C	0.0	7.25	0.0	0.0	7	-
opls_768-opls_145-opls_145-opls_146	C-C-C-H	0.0	7.25	0.0	0.0	7	-
opls_146-opls_145-opls_768-opls_145	H-C-C-C	0.0	7.25	0.0	0.0	7	-
opls_146-opls_145-opls_145-opls_146	H-C-C-H	0.0	7.25	0.0	0.0	7	-
opls_146-opls_145-opls_145-opls_145	H-C-C-C	0.0	7.25	0.0	0.0	7	-
opls_146-opls_145-opls_145-opls_149	H-C-C-C	0.0	7.25	0.0	0.0	7	-
opls_145-opls_145-opls_145-opls_145	C-C-C-C	0.0	7.25	0.0	0.0	7	-
opls_145-opls_145-opls_145-opls_149	C-C-C-C	0.0	7.25	0.0	0.0	7	-
opls_145-opls_768-opls_145-opls_145	C-C-C-C	0.0	7.25	0.0	0.0	7	-
opls_145-opls_145-opls_149-opls_136	C-C-C-C	0.0	0.0	0.0	0.0	1	-
opls_145-opls_145-opls_149-opls_140	C-C-C-H	0.0	0.0	0.0	0.0	1	-
opls_145-opls_149-opls_136-opls_136	C-C-C-C	1.3	-0.05	0.2	0.0	N/A	1
opls_145-opls_149-opls_136-opls_140	C-C-C-H	0.0	0.0	0.462	0.0	1	-

[1] No reference found. Parameters used from GROMACS *as is*. GROMACS uses same parameters as alkane C-C-C-C.

Improper parameters						
Improper	Elements	γ, degrees	K_ϕ, kcal/mol	n	Reference	Notes
opls_767-opls_768-opls_145-opls_145	N-C-C-C	180	2.2	2	7	-
opls_146-opls_145-opls_768-opls_145	H-C-C-C	180	2.2	2	7	-
opls_146-opls_145-opls_145-opls_145	H-C-C-C	180	2.2	2	7	-
opls_149-opls_145-opls_145-opls_145	C-C-C-C	180	2.2	2	7	-

Perfluoromethyl

Nonbonded parameters						
Atom type	Element	Charge	Sigma, nm	Epsilon, kcal/mol	Reference	Notes
opls_965	F	-0.12	0.295	0.053	13	-
opls_961	C	0.36	0.35	0.066	13	-

Bond parameters					
Bond	Elements	k, kcal/mol^{-1} Å ^{2}	r_0, nm	Reference	Notes
opls_965-opls_961	F-C	367	0.1332	13	-
opls_961-opls_136	C-C	268	0.1529	13	-

Angle parameters					
Angle	Elements	k, kcal/mol^{-1} deg^2	θ_0, deg	Reference	Notes
opls_965-opls_961-opls_965	F-C-F	77	109.1	13	-
opls_965-opls_961-opls_136	F-C-C	50	109.5	13	-
opls_961-opls_136-opls_136	C-C-C	58.35	112.7	1	-
opls_961-opls_136-opls_140	C-C-H	37.5	110.7	1	-

Dihedral parameters							
Dihedral	Elements	k1, kcal/mol	k2, kcal/mol	k3, kcal/mol	k4, kcal/mol	Reference	Notes
opls_965-opls_961-opls_136-opls_136	F-C-C-C	0.0	0.0	0.463	0.0	14	1
opls_965-opls_961-opls_136-opls_140	F-C-C-H	0.0	0.0	0.29	0.0	14	1
opls_961-opls_136-opls_136-opls_136	C-C-C-C	0.104	-0.312	0.048	-0.083	14	1
opls_961-opls_136-opls_136-opls_140	C-C-C-H	0.0	0.0	0.133	0.0	14	1

[1] These parameters are not in GROMACS, as the GROMACS parameters do not distinguish between dihedrals for fluorinated and hydrogenated carbons.

Phenyl

Nonbonded parameters						
Atom type	Element	Charge	Sigma, nm	Epsilon, kcal/mol	Reference	Notes
opls_145	C	-0.115	0.355	0.07	1	-
opls_146	H	0.115	0.242	0.03	1	-
opls_149	C	-0.005	0.35	0.066	1	-
opls_140	H	0.06	0.25	0.03	1	-

Bond parameters					
Bond	Elements	k, kcal/mol^{-1} Å ^{2}	r_0, nm	Reference	Notes
opls_146-opls_145	H-C	367	0.108	12	-
opls_145-opls_149	C-C	317	0.151	6	-
opls_149-opls_140	C-H	340	0.109	1	-
opls_149-opls_136	C-C	268	0.1529	1	-
opls_145-opls_145	C-C	469	0.14	6	-

Angle parameters					
Angle	Elements	k, kcal/mol^{-1} deg^2	θ_0, deg	Reference	Notes
opls_146-opls_145-opls_145	H-C-C	35	120	6	-
opls_145-opls_145-opls_145	C-C-C	63	120	7	-
opls_145-opls_145-opls_149	C-C-C	70	120	6	-
opls_145-opls_149-opls_136	C-C-C	63	114	6	-
opls_145-opls_149-opls_140	C-C-H	35	109.5	6	-
opls_140-opls_149-opls_140	H-C-H	33	107.8	1	-
opls_140-opls_149-opls_136	H-C-C	37.5	110.7	1	-
opls_149-opls_136-opls_136	C-C-C	58.35	112.7	1	-
opls_149-opls_136-opls_140	C-C-H	37.5	110.7	1	-

Dihedral parameters							
Dihedral	Elements	k1, kcal/mol	k2, kcal/mol	k3, kcal/mol	k4, kcal/mol	Reference	Notes
opls_146-opls_145-opls_145-opls_146	H-C-C-H	0.0	7.25	0.0	0.0	7	-
opls_146-opls_145-opls_145-opls_145	H-C-C-C	0.0	7.25	0.0	0.0	7	-
opls_146-opls_145-opls_145-opls_149	H-C-C-C	0.0	7.25	0.0	0.0	7	-
opls_145-opls_145-opls_145-opls_145	C-C-C-C	0.0	7.25	0.0	0.0	7	-
opls_145-opls_145-opls_145-opls_149	C-C-C-C	0.0	7.25	0.0	0.0	7	-
opls_145-opls_145-opls_149-opls_136	C-C-C-C	0.0	0.0	0.0	0.0	1	-
opls_145-opls_145-opls_149-opls_140	C-C-C-H	0.0	0.0	0.0	0.0	1	-
opls_145-opls_149-opls_136-opls_136	C-C-C-C	1.3	-0.05	0.2	0.0	N/A	1
opls_145-opls_149-opls_136-opls_140	C-C-C-H	0.0	0.0	0.462	0.0	1	-

[1] No reference found. Parameters used from GROMACS *as is*. GROMACS uses same parameters as alkane C-C-C-C.

Improper parameters						
Improper	Elements	γ, degrees	K_ϕ, kcal/mol	n	Reference	Notes
opls_146-opls_145-opls_145-opls_145	H-C-C-C	180	2.2	2	7	-
opls_149-opls_145-opls_145-opls_145	C-C-C-C	180	2.2	2	7	-

Pyrrole

Nonbonded parameters						
Atom type	Element	Charge	Sigma, nm	Epsilon, kcal/mol	Reference	Notes
opls_547	H	0.118	0.242	0.03	12	-
opls_546	H	0.155	0.242	0.03	12	-
opls_544	C	-0.149	0.355	0.07	12	-
opls_543	C	-0.163	0.355	0.07	12	-
opls_542	N	-0.239	0.325	0.17	12	-
opls_545	H	0.317	0	0	12	-
opls_679	C	0.035	0.35	0.066	N/A	1
opls_140	H	0.06	0.25	0.03	1	-

[1] No reference found. Parameters used from GROMACS *as is*.

Bond parameters					
Bond	Elements	k, kcal/mol^{-1} Å ^{2}	r_0, nm	Reference	Notes
opls_547-opls_544	H-C	367	0.108	12	-
opls_544-opls_543	C-C	546	0.1367	12	-
opls_546-opls_543	H-C	367	0.108	12	-
opls_543-opls_542	C-N	427	0.1381	12	-
opls_542-opls_545	N-H	434	0.101	12	-
opls_544-opls_544	C-C	469	0.1424	12	-
opls_543-opls_679	C-C	317	0.1504	N/A	1
opls_679-opls_140	C-H	340	0.109	1	-
opls_679-opls_136	C-C	268	0.1529	1	-

[1] No reference found. Parameters used from GROMACS *as is*.

Angle parameters					
Angle	Elements	k, kcal/mol^{-1} deg^2	θ_0, deg	Reference	Notes
opls_546-opls_543-opls_544	H-C-C	35	132.1	12	-
opls_546-opls_543-opls_542	H-C-N	35	121.6	12	-
opls_543-opls_544-opls_547	C-C-H	35	125.7	12	-
opls_543-opls_544-opls_544	C-C-C	70	107.3	12	-
opls_543-opls_542-opls_545	C-N-H	35	120	12	-
opls_543-opls_542-opls_543	C-N-C	70	109.8	12	-
opls_547-opls_544-opls_544	H-C-C	35	127.5	12	-
opls_545-opls_542-opls_543	H-N-C	35	120	12	-
opls_542-opls_543-opls_544	N-C-C	70	107.7	12	-
opls_542-opls_543-opls_679	N-C-C	70	121.6	N/A	1
opls_544-opls_543-opls_679	C-C-C	70	132.1	N/A	1
opls_543-opls_679-opls_136	C-C-C	63	114	N/A	1
opls_543-opls_679-opls_140	C-C-H	35	109.5	N/A	1
opls_140-opls_679-opls_140	H-C-H	33	107.8	1	-
opls_140-opls_679-opls_136	H-C-C	37.5	110.7	1	-
opls_679-opls_136-opls_136	C-C-C	58.35	112.7	1	-
opls_679-opls_136-opls_140	C-C-H	37.5	110.7	1	-

[1] No reference found. Parameters used from GROMACS *as is*.

Dihedral parameters							
Dihedral	Elements	k1, kcal/mol	k2, kcal/mol	k3, kcal/mol	k4, kcal/mol	Reference	Notes
opls_546-opls_543-opls_544-opls_547	H-C-C-H	0.0	7.25	0.0	0.0	N/A	1
opls_546-opls_543-opls_544-opls_544	H-C-C-C	0.0	7.25	0.0	0.0	N/A	1
opls_546-opls_543-opls_542-opls_545	H-C-N-H	0.0	3.0	0.0	0.0	N/A	1
opls_546-opls_543-opls_542-opls_543	H-C-N-C	0.0	3.2	0.0	0.0	N/A	1
opls_543-opls_544-opls_544-opls_543	C-C-C-C	0.0	7.25	0.0	0.0	N/A	1
opls_543-opls_544-opls_544-opls_547	C-C-C-H	0.0	7.25	0.0	0.0	N/A	1
opls_543-opls_542-opls_543-opls_544	C-N-C-C	0.0	3.2	0.0	0.0	N/A	1
opls_543-opls_542-opls_543-opls_679	C-N-C-C	0.0	3.2	0.0	0.0	N/A	1
opls_544-opls_543-opls_542-opls_543	C-C-N-C	0.0	3.2	0.0	0.0	N/A	1
opls_544-opls_543-opls_542-opls_545	C-C-N-H	0.0	3.2	0.0	0.0	N/A	1
opls_544-opls_544-opls_543-opls_542	C-C-C-N	0.0	7.25	0.0	0.0	N/A	1
opls_544-opls_544-opls_543-opls_679	C-C-C-C	0.0	7.25	0.0	0.0	N/A	1
opls_547-opls_544-opls_543-opls_542	H-C-C-N	0.0	7.25	0.0	0.0	N/A	1
opls_545-opls_542-opls_543-opls_679	H-N-C-C	0.0	3.2	0.0	0.0	N/A	1
opls_542-opls_543-opls_679-opls_136	N-C-C-C	1.7	-0.6	0.0	0.0	N/A	1
opls_542-opls_543-opls_679-opls_140	N-C-C-H	0.0	0.0	0.42	0.0	N/A	1
opls_547-opls_544-opls_543-opls_679	H-C-C-C	0.0	7.25	0.0	0.0	N/A	1
opls_544-opls_543-opls_679-opls_136	C-C-C-C	0.0	0.0	0.0	0.0	N/A	1
opls_544-opls_543-opls_679-opls_140	C-C-C-H	0.0	0.0	0.0	0.0	N/A	1
opls_543-opls_679-opls_136-opls_136	C-C-C-C	1.3	-0.05	0.2	0.0	N/A	2
opls_543-opls_679-opls_136-opls_140	C-C-C-H	0.0	0.0	0.462	0.0	N/A	1
opls_140-opls_679-opls_136-opls_136	H-C-C-C	0.0	0.0	0.3	0.0	N/A	1
opls_140-opls_679-opls_136-opls_140	H-C-C-H	0.0	0.0	0.3	0.0	N/A	1
opls_679-opls_136-opls_136-opls_136	C-C-C-C	1.3	-0.05	0.2	0.0	N/A	1
opls_679-opls_136-opls_136-opls_140	C-C-C-H	0.0	0.0	0.3	0.0	N/A	1

[1] No reference found. Parameters used from GROMACS *as is*.

[2] Parameters don't exist in GROMACS or the literature. Parameters for C(aromatic)-C-C-C dihedrals have been used.

Improper parameters						
Improper	Elements	γ, degrees	K_ϕ, kcal/mol	n	Reference	Notes
opls_546-opls_543-opls_542-opls_544	H-C-N-C	180	2.2	2	7	-
opls_547-opls_544-opls_543-opls_544	H-C-C-C	180	2.2	2	7	-
opls_679-opls_543-opls_542-opls_544	C-C-N-C	180	2.2	2	7	-
opls_545-opls_542-opls_543-opls_543	H-N-C-C	180	2.0	2	6	-

A.1 Bibliography

[1] Jorgensen, W. L.; Maxwell, D. S.; Tirado-Rives, J. Development and Testing of the OPLS All-Atom Force Field on Conformational Energetics and Properties of Organic Liquids. *Journal of the American Chemical Society* **1996**, *118*, 11225–11236.

[2] Lorenz, C.; Webb, E.; Stevens, M.; Chandross, M.; Grest, G. Frictional dynamics of perfluorinated self-assembled monolayers on amorphous SiO2. *Tribology Letters* **2005**, *19*, 93–98.

[3] Lewis, J. B.; Vilt, S. G.; Rivera, J. L.; Jennings, G. K.; McCabe, C. Frictional Properties of Mixed Fluorocarbon/Hydrocarbon Silane Monolayers: A Simulation Study. *Langmuir* **2012**, *28*, 14218–14226.

[4] Fogarty, J. C.; Aktulga, H. M.; Grama, A. Y.; van Duin, A. C. T.; Pandit, S. A. A reactive molecular dynamics simulation of the silica-water interface. *The Journal of Chemical Physics* **2010**, *132*, 174704.

[5] Price, M. L. P.; Ostrovsky, D.; Jorgensen, W. L. Gas-phase and liquid-state properties of esters, nitriles, and nitro compounds with the OPLS-AA force field. *Journal of Computational Chemistry* **2001**, *22*, 1340–1352.

[6] Weiner, S. J.; Kollman, P. A.; Nguyen, D. T.; Case, D. A. An all atom force field for simulations of proteins and nucleic acids. *Journal of Computational Chemistry* **1986**, *7*, 230–252.

[7] Rizzo, R. C.; Jorgensen, W. L. OPLS All-Atom Model for Amines: Resolution of the Amine Hydration Problem. *Journal of the American Chemical Society* **1999**, *121*, 4827–4836.

[8] Price, D. J.; Roberts, J. D.; Jorgensen, W. L. Conformational Complexity of Succinic Acid and Its Monoanion in the Gas Phase and in Solution: Ab Initio Calculations and Monte Carlo Simulations. *Journal of the American Chemical Society* **1998**, *120*, 9672–9679.

[9] Cornell, W. D.; Cieplak, P.; Bayly, C. I.; Gould, I. R.; Merz, K. M.; Ferguson, D. M.; Spellmeyer, D. C.; Fox, T.; Caldwell, J. W.; Kollman, P. A. A Second Generation Force Field for the Simulation of Proteins, Nucleic Acids, and Organic Molecules. *Journal of the American Chemical Society* **1995**, *117*, 5179–5197.

[10] Jorgensen, W. L.; Ulmschneider, J. P.; Tirado-Rives, J. Free Energies of Hydration from a Generalized Born Model and an All-Atom Force Field. *The Journal of Physical Chemistry B* **2004**, *108*, 16264–16270.

[11] Jorgensen, W. L.; Schyman, P. Treatment of Halogen Bonding in the OPLS-AA Force Field: Application to Potent Anti-HIV Agents. *Journal of Chemical Theory and Computation* **2012**, *8*, 3895–3901.

[12] McDonald, N. A.; Jorgensen, W. L. Development of an All-Atom Force Field for Heterocycles. Properties of Liquid Pyrrole, Furan, Diazoles, and Oxazoles. *The Journal of Physical Chemistry B* **1998**, *102*, 8049–8059.

[13] Watkins, E. K.; Jorgensen, W. L. Perfluoroalkanes: Conformational Analysis and Liquid-State Properties from ab Initio and Monte Carlo Calculations. *The Journal of Physical Chemistry A* **2001**, *105*, 4118–4125.

[14] Pádua, A. A. H. Torsion Energy Profiles and Force Fields Derived from Ab Initio Calculations for Simulations of HydrocarbonFluorocarbon Diblocks and Perfluoroalkylbromides. *The Journal of Physical Chemistry A* **2002**, *106*, 10116–10123.

Appendix B

Analysis

B.1 Modified Amonton's Law

Monolayer tribology is evaluated via calculation of the coefficient of friction (COF) and adhesive force as defined by the Derjaguin form of Amontons' Law of Friction[1]:

$$F_f = F_0 + \mu \cdot Fn \tag{B.1}$$

where F_f, μ, and F_n represent the friction force, COF, and normal force, respectively. F_0 represents the friction force between the two surfaces under zero normal load. This term is often referred to as the adhesion term, offset term, or Derjaguin offset. In this thesis, F_0 is referred to interchangeably as the adhesion force or force of adhesion.

COF and the force of adhesion can be evaluated from B.1 through linear regression of friction force data obtained at a series of normal loads. This general procedure is utilized throughout the thesis, with normal load specifics detailed in the Methods sections of each chapter.

Friction forces in this work are obtained through summing all forces in the direction of shear (the x direction) for one of the two contacting bodies (surface + chains).

B.2 Nematic Order

As a metric of orientational ordering of monolayer chains, the nematic order, S_2, is measured for monolayer systems. Nematic order is calculated following,

$$S_2 = \left\langle \frac{3}{2}\cos^2\theta - \frac{1}{2} \right\rangle \tag{B.2}$$

where each θ represents the angle between a chain's characteristic vector, drawn through the chain's lowest moment of inertia, and the system director, obtained through an average of all characteristic vectors. A value of 1.0 represents a completely ordered monolayer, and a value of 0.0 represents isotropy. Values below 0.8 tend to indicate liquid-like behavior for monolayers on surfaces.[2]

B.3 Hexagonal Order

Global hexagonal order is quantified through the use of the two-dimensional hexagonal order parameter[3,4], ψ_6, the general form of which is provided in Eq. B.3.

$$\psi_6(i) = \frac{1}{2}\sum_{j}^{n} e^{i6\theta_j} \tag{B.3}$$

Here, n represents the number of sites within the nearest neighbor shell of particle i, θ_j the bond angle between i and its jth neighbor, and six is the Fourier coefficient. By projecting all neighbor shells onto a unit sphere, a single value of ψ_6 is obtained corresponding to the extent of long-range hexagonal order. As with the nematic order parameter, the hexagonal order parameter measures on a scale from 0 to 1, where perfect hexagonal ordering, as is the case for the crystalline substrates in this work, yields a value of 1, and deviations from ideality yield values trending toward 0.

B.4 Interdigitation

Interdigitation of chains from opposing monolayers is quantified following the procedure of Das et al.[5], where the overlap density, ρ_{ov}, is calculated in a series of bins along the z dimension (normal to the surfaces) as,

$$\rho_{ov}(z) = 4\frac{\rho_{top}(z) \times \rho_{bot}(z)}{[\rho_{top}(z) + \rho_{bot}(z)]^2} \tag{B.4}$$

$$\lambda_{ov} = \int_{z_{s,bot}}^{z_{s,top}} \rho_{ov}(z) dz \tag{B.5}$$

where ρ_{top} and ρ_{bot} represent the mass densities of the top and bottom monolayers, respectively. Integration is performed over all bins from the bottom surface level, $z_{s,bot}$, to the top surface level, $z_{s,top}$, to obtain a z-independent interdigitation parameter, λ_{ov} (Eq. B.5). In the absence of interdigitation, λ_{ov} will equal zero and increasing values signify greater overlap between monolayers.

B.5 Bibliography

[1] Clear, S. C.; Nealey, P. F. Chemical Force Microscopy Study of Adhesion and Friction between Surfaces Functionalized with Self-Assembled Monolayers and Immersed in Solvents. *Journal of Colloid and Interface Science* **1999**, *213*, 238–250.

[2] Guo, S.; Moore, T. C.; Iacovella, C. R.; Strickland, L. A.; McCabe, C. Simulation Study of the Structure and Phase Behavior of Ceramide Bilayers and the Role of Lipid Headgroup Chemistry. *Journal of Chemical Theory and Computation* **2013**, *9*, 5116–5126.

[3] Keys, A. S.; Iacovella, C. R.; Glotzer, S. C. Characterizing Structure Through Shape Matching and Applications to Self-Assembly. *Annual Review of Condensed Matter Physics* **2011**, *2*, 263–285.

[4] Keys, A. S.; Iacovella, C. R.; Glotzer, S. C. Characterizing complex particle morphologies through shape matching: Descriptors, applications, and algorithms. *Journal of Computational Physics* **2011**, *230*, 6438–6463.

[5] Das, C.; Noro, M. G.; Olmsted, P. D. Simulation Studies of Stratum Corneum Lipid Mixtures. *Biophysical Journal* **2009**, *97*, 1941–1951.

Appendix C

Appendix to Chapter 4

C.1 Details of calculations for monolayer structural metrics

Sampling window, obtaining averages and errors

As mentioned in Chapter 4, sampling of properties during shear is obtained during a window from 0.3ns through 1.3ns after the initiation of shear for systems featuring a single-asperity geometry. For systems featuring a planar geometry, the sampling window is defined from 0.75 through 1.5ns following the initiation of shear. The longer shear time prior to sampling in these systems is a result of a delay in reaching a steady-state friction force associated with the time required for all chains to become shear-aligned.

Mean values and errors for properties under shear are obtained through a block-averaging approach. Friction forces are sampled every 0.5ps, while structural properties are sampled every 1.0ps. Results are binned into 15 equally-sized blocks over the sampling window. Block averaging is performed by reporting the average of the means for each sub-window, with errors representing the standard deviation of the block means. The exception to this scheme is in the calculation of error for monolayer tilt angle. Here, an error in the average tilt angle is obtained for each frame in the simulation trajectory (every 1.0ps). The error reported for tilt angles (such as in Fig. 4.2 and Table 4.1) represents the standard deviation in the block means for these error values.

The procedure for calculating the mean and error for the equilibrium properties provided in Table 4.1 is described in a footnote in the text; however, to re-iterate here, equilibrium properties are evaluated from a window from 0.5ns through 1.0ns after the beginning of the equilibration run (prior to which films have reached an equilibrated state). Mean values reported for the nematic order, average tilt angle, and gauche defect fraction represent an average of all values collected over the sampling window (with individual values

obtained every 1.0ps). Error for nematic order represents one standard deviation of this mean, while error for the average tilt angle and gauche defects per chain is evaluated for each frame and the value reported in the table represents the mean of these error values (thus providing a measure of uniformity within the film as opposed to changes in the global property over time). Film thickness is estimated by voxelizing the surface into a 9x9 grid (where each voxel has an area of 2.78nm^2) where values for each frame equate to the average of the thickness within all voxels. The mean value reported in the table corresponds to the mean of these averages over the sampling window and the error represents the mean of the standard deviations to again allow for error propagation.

Film thickness

Film thickness is calculated by subtracting the monolayer height from the surface level. The monolayer height is calculated by generating a cumulative histogram of the positions of all carbon atoms in the monolayer in the z-dimension (i.e. normal to the surface), where the bin location corresponding to 95% of the carbon atoms is considered to represent the film height. The surface level is determined by calculating the average z-position of surface oxygens (i.e. those oxygens attached to either alkylsilane chains or hydrogen caps).

Penetration depth

Penetration depth is considered to be the distance between the monolayer height (see the Film thickness section for this definition) and the minimum z-position of the tip (i.e. the apex).

Nematic and orientational order

Nematic order is calculated by first computing the inertia tensor of each alkylsilane chain. The chain's director is then considered to be the eigenvector corresponding to the lowest eigenvalue of the inertia tensor. A system director is then computed which corre-

sponds to the average of all chain directors. For a simple measure of orientational order, the dot product of the chain director and the system director is computed. This is useful in the generation of heatmaps to examine local ordering, as this provides a value for each individual chain. For a measure of global orientational order, the nematic order parameter is calculated using Eq. B.2.

Gauche defects

A gauche defect is defined as a C-C-C-C dihedral angle that is larger than 270 degrees or lower than 90 degrees.

Inter-surface separation

Inter-surface separation is defined as the distance between the interface of the top surface (either planar or tip geometry) and the bottom surface. Surface levels for planar geometries are determined by the mean z-coordinate of surface oxygens (i.e. those oxygens attached to either alkylsilane chains or hydrogen caps). Surface level for tips is determined by the minimum z value (i.e. the tip apex).

C.2 Details on the sampling of friction forces

Fig. C.1 shows friction force trajectories for each system under a normal load of 25nN. It is shown that friction force features higher variation for lower densities, corresponding to the nonuniform film thickness. Statistical averaging occurs over the 1ns window from 0.3ns to 1.3ns of shear (shown in the above figure as the non-shaded region). Friction forces are sampled every 0.5ps and the results are placed into 15 blocks over the 1ns sampling window. Block averaging is performed by reporting the average of the means for each sub-window, with errors representing the standard deviation of the block means.

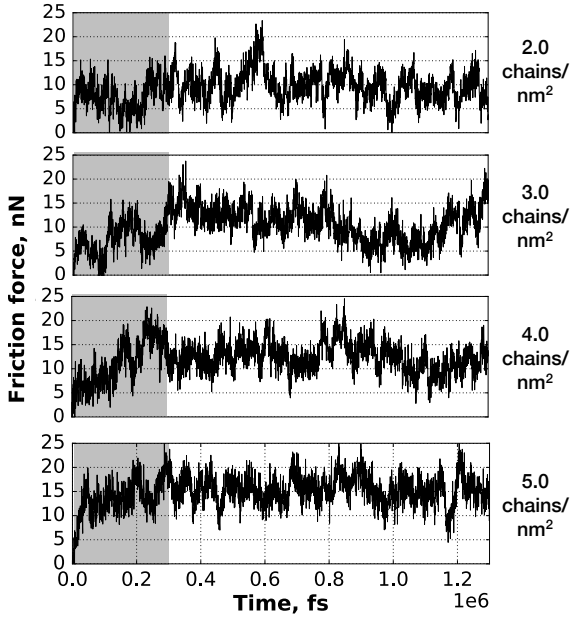

Figure C.1: Friction force trajectories for monolayers under shear with a 2nm hemispherical tip at a normal load of 25nN. Statistical averaging occurs over the 1ns window from 0.3ns to 1.3ns of shear, thus the shaded region is excluded.

C.3 Results for directional dependence of single-asperity shear

Fig. C.2 reveals that the trends in COF with monolayer density are independent of shear direction. The system with a monolayer density of 4.0 chains/nm^2 does feature a reduced COF when the surface is moved in the $+x$ direction as compared to the $-x$ direction (Fig. 4.1 in the main text); however, there is still a clear trend whereby the lowest density film (2.0 chains/nm^2) features the lowest COF and the highest density film (5.0 chains/nm^2) features the highest COF, a result of molecular plowing as shown in the main text.

C.4 Results for shear using a planar geometry

Fig. C.3 shows that the COF appears to be independent of monolayer density for the planar contact model used in this work. Linear regressions of the data in Fig. C.3 were used to obtain the values provided in Table 2.

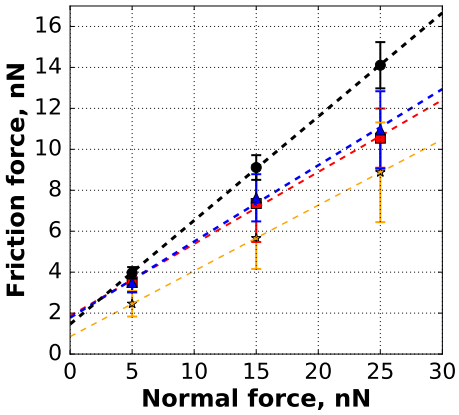

Figure C.2: Friction force vs. normal force for monolayers with densities of (in chains per nm^2) 5.0 (black, circles), 4.0 (blue, triangles), 3.0 (red, squares), and 2.0 (orange, stars) under shear with a 2nm hemispherical tip where the surface is moved in the $+x$ direction. Lines represent linear regressions and error bars represent one standard deviation.

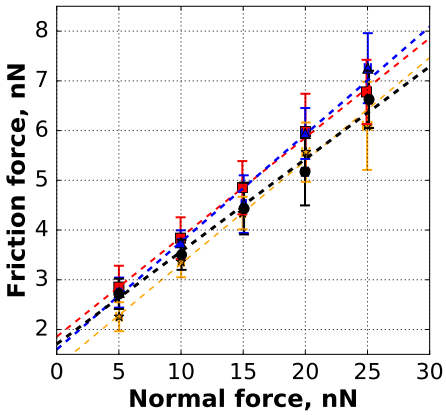

Figure C.3: Friction force vs. normal force for monolayers with densities of (in chains per nm^2) 5.0 (black, circles), 4.0 (blue, triangles), 3.0 (red, squares), and 2.0 (orange, stars) under shear with a planar, amorphous silica counter-surface. Lines represent linear regressions and error bars represent one standard deviation.

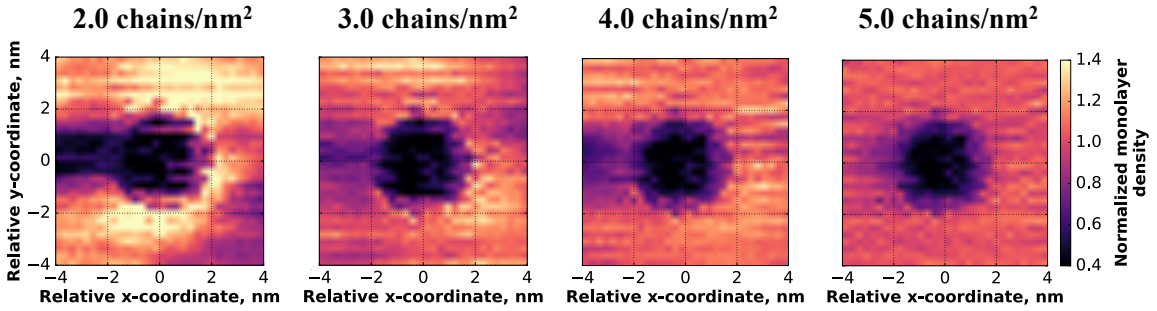

Figure C.4: Heatmaps of the number density of carbon atoms relative to the tip apex normalized by the bulk value, which corresponds to product of the number of carbons per chain (18) and the monolayer density, during shear under a normal load of 25nN. Note: Plot dimensions (-4nm, 4nm) to (-4nm, 4nm) represent a zoomed-in look at the region around the tip and do not represent the full substrate dimensions.

C.5 Heatmaps of monolayer density during shear

Fig. C.4 shows heatmaps for the time-averaged number density of carbon atoms in the monolayer region around the tip. For the film with a density of 2.0 chains/nm^2 and also somewhat for the film with a density of 3.0 chains/nm^2, a densified region of the film is apparent around the tip. This is similar to the result shown in Fig. 4.6 of the main text and is suggestive of the tip pushing/displacing chains to the side during shear, helping to explain the lack of additional induced gauche defects observed in Fig. 4.7.

C.6 Single asperity contact areas

Fig. C.5 shows the contact area for systems featuring an asperity geometry as a function of normal load for several monolayer densities. Contact area is observed to be relatively insensitive of monolayer density, which helps explain the similar values observed for the intercept calculated from the linear regressions in Fig. 4.4. Contact area is estimated via the approach of Ref. 1, whereby monolayer atoms that are within 0.5nm of any tip atom are considered to be in contact with the tip. The positions of all monolayer atoms in contact with the tip are projected onto the *xy*-plane (i.e. the surface plane) and a circle encompassing 95% of these atoms is considered to represent the contact area. It should

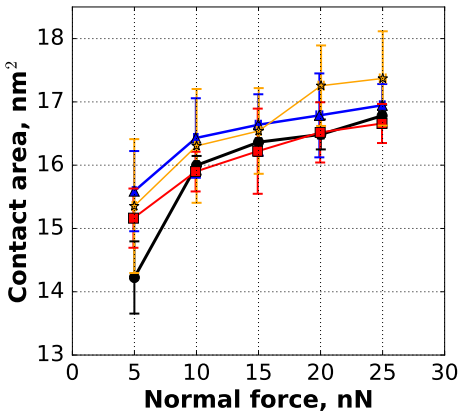

Figure C.5: Average contact area for tips under shear against monolayers with densities of (in chains per nm^2) 5.0 (black, circles), 4.0 (blue, triangles), 3.0 (red, squares), and 2.0 (orange, stars). Error bars represent one standard deviation and lines are provided only as a guide to the eye.

noted that this approach has been shown to under-estimate the contact area as compared to more rigorous force-based approaches[2,3]; however, for the purposes here we are interested only on the general trends so we utilize the simpler distance-based approach

C.7 Bibliography

[1] Chandross, M.; Lorenz, C. D.; Stevens, M. J.; Grest, G. S. Simulations of Nanotribology with Realistic Probe Tip Models. *Langmuir* **2008**, *24*, 1240–1246.

[2] Cheng, S.; Luan, B.; Robbins, M. O. Contact and friction of nanoasperities: Effects of adsorbed monolayers. *Physical Review E* **2010**, *81*.

[3] Cheng, S.; Robbins, M. O. Defining Contact at the Atomic Scale. *Tribology Letters* **2010**, *39*, 329–348.

Appendix D

Appendix to Chapter 5

D.1 Additional details on molecular descriptors

Molecular descriptor	Description	Category
Approximate Surface Area	Approximation of molecular surface area using the approach defined by Labute[1]	Size
Asphericity	Measure of molecular shape (from Baumgartner[2]); $A = 0$ for spherical shape, $A = 1$ for highly prolate shapes, and $A = 0.25$ for oblate shapes	Shape
Balaban *J*	Related to connectivity, degree of branching[3]	Complexity
Bertz C_T	Measure of molecular complexity through connectivity[4]	Complexity
Chi0, Chi1	Connectivity indices[5]	Complexity
Chi0n - Chi4n	Connectivity indices over various molecular fragments (0=atoms, 1=one bond fragments, 2=two bond fragments, etc.)[5]	Complexity
Chi0v - Chi4v	Valence connectivity indices (0=atoms, 1=one bond fragments, 2=two bond fragments, etc.)[5]	Complexity
Eccentricity	Shape descriptor calculated from the inertia matrix (0=spherical, 1=linear), from Arteca[6]	Shape
Hall-Kier alpha	Modifying term for kappa descriptors, related to shape/flexibility[7]	Shape
Hall-Kier kappa1	Alpha-modified topological shape descriptor; related to complexity/number of cycles (rings) in the bond graph[7]	Shape
Hall-Kier kappa2	Alpha-modified topological shape descriptor; related to degree of star-like bond graph vs. linearity[7]	Shape
Hall-Kier kappa3	Alpha-modified topological shape descriptor; related to ”centrality” of branching[7]	Shape
Hydrogen bond factor	Developed in this work; related to ability for formation of inter-monolayer hydrogen bonds	Charge distribution, Misc.
IPC	Complexity/connectivity descriptor estimated from adjacency matrix of bond graph[8]	Complexity

Molecular descriptor	Description	Category
Inertial shape factor	Characterization of molecular shape from principal moments of inertia ($pm_2/(pm_1 * pm_3)$, where pm1-3 are the three principal moments), from Todeschini and Consoni[7]	Shape
logP	Octanol - water partition coefficient estimated through the method of Wildman and Crippen[9]; measure of hydrophobicity	Charge distribution/Misc.
Molar refractivity	Estimation of molecular polarizability; calculated through the method of Wildman and Crippen[9]	Size
Molecular weight	-	Size
Molecular weight (heavy atoms)	Molecular weight excluding hydrogens	Size
Normalized principal moments ratios (NPR1, NPR2)	Used to characterize molecular shape, from Sauer and Schwarz[10]	Shape
Number of heavy atoms	Number of non-hydrogen atoms	Size
Number of rotatable bonds	-	Size/Shape
Number of valence electrons	-	Size
Plane of best fit	Measure of molecular planarity (0=planar, increasing with less planarity)[11]	Shape
Principal moments of inertia (PMI1, PMI2, PMI3)	Three principal moments of inertia for the molecule (1=smallest, 3=largest)	Shape
Radius of gyration	(From Arteca[6]) Characterizes molecular shape, specifically elongation	Shape/Size
Spherocity	Measure of molecular shape (0=spherical, 1=flat), from Robinson et al.[12]	Shape
Topological polar surface area	Estimation of surface area of only polar atoms, from Ertl et al.[13]	Charge distribution

Molecular descriptor	Description	Category
Total hydrophobic VSA	Sum of SA contributions from atoms with $-0.20 \leq q < 0.20$	Charge distribution
Total negative van der Waals surface area (VSA)	Sum of SA contributions from atoms with $q < 0.0$	Charge distribution
Total negative polar VSA	Sum of SA contributions from atoms with $q < -0.20$	Charge distribution
Total polar VSA	Sum of SA contributions from atoms with $\|q\| > 0.20$	Charge distribution
Total positive VSA	Sum of SA contributions from atoms with $q > 0.0$	Charge distribution
Total positive polar VSA	Sum of SA contributions from atoms with $q \geq 0.20$	Charge distribution
Fractional hydrophobic VSA	Total hydrophobic VSA / Total VSA	Charge distribution
Fractional negative VSA	Total negative VSA / Total VSA	Charge distribution
Fractional negative polar VSA	Total negative polar VSA / Total VSA	Charge distribution
Fractional polar VSA	Total polar VSA / Total VSA	Charge distribution
Fractional positive VSA	Total positive VSA / Total VSA	Charge distribution
Fractional positive polar VSA	Total positive polar VSA / Total VSA	Charge distribution

D.2 Plots of COF, F_0, and S_2 for chemically-identical systems

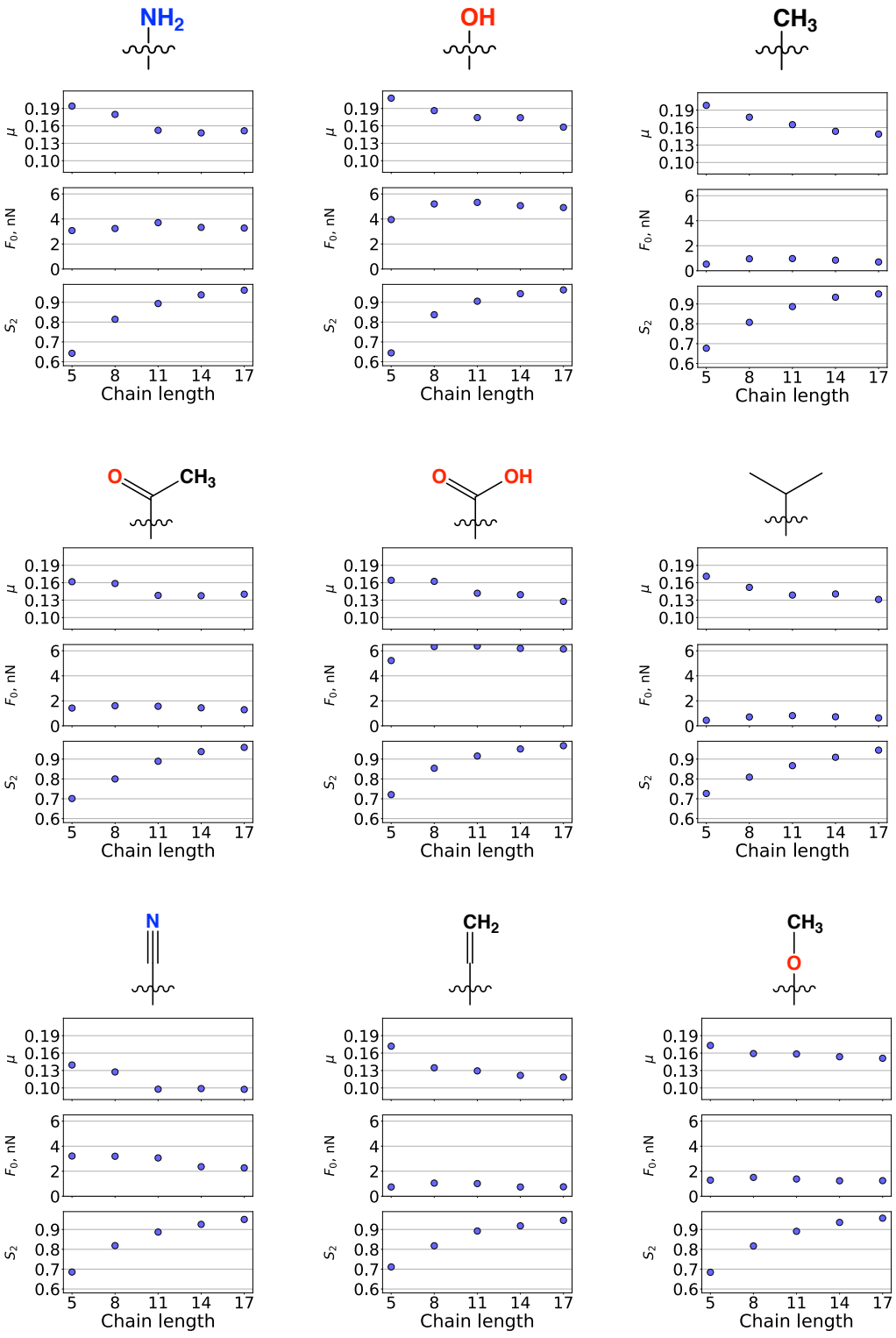

Figure D.1: COF, adhesive force, and nematic order of monolayers with select terminal groups as a function of chain length.

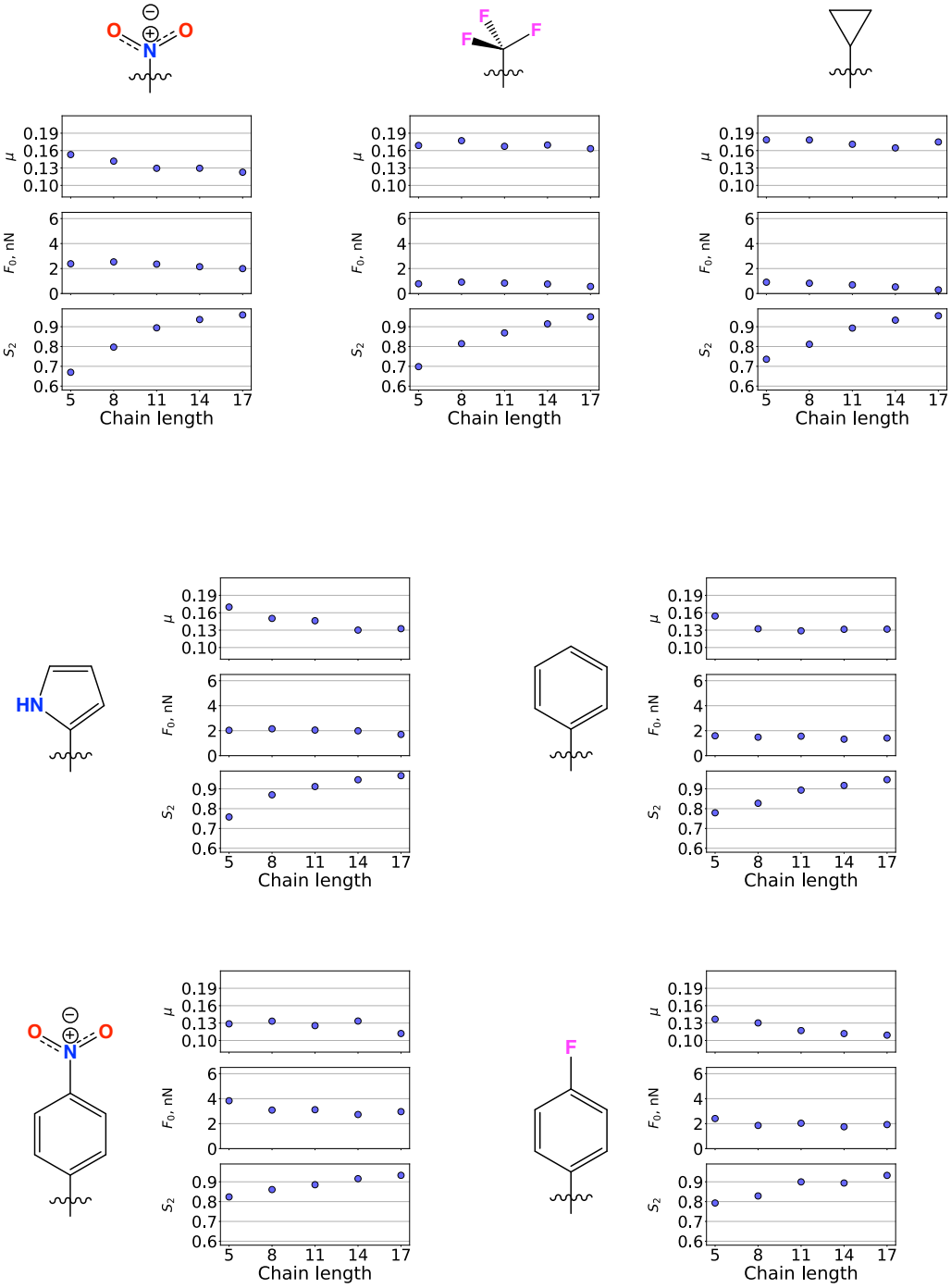

Figure D.2: COF, adhesive force, and nematic order of monolayers with select terminal groups as a function of chain length.

D.3 Bibliography

[1] Labute, P. A widely applicable set of descriptors. *Journal of Molecular Graphics and Modelling* **2000**, *18*, 464–477.

[2] Baumgärtner, A. Shapes of flexible vesicles at constant volume. *The Journal of Chemical Physics* **1993**, *98*, 7496–7501.

[3] Balaban, A. T. Highly discriminating distance-based topological index. *Chemical Physics Letters* **1982**, *89*, 399–404.

[4] Bertz, S. H. The first general index of molecular complexity. *Journal of the American Chemical Society* **1981**, *103*, 3599–3601.

[5] Hall, L. H.; Kier, L. B. The Molecular Connectivity Chi Indexes and Kappa Shape Indexes in Structure-Property Modeling. *Reviews in Computational Chemistry* **2007**, 367–422.

[6] Arteca, G. A. Molecular Shape Descriptors. *Reviews in Computational Chemistry* **2007**, 191–253.

[7] Todeschini, R.; Consonni, V. Handbook of Molecular Descriptors. *Methods and Principles in Medicinal Chemistry* **2000**,

[8] Bonchev, D.; Trinajstić, N. Information theory, distance matrix, and molecular branching. *The Journal of Chemical Physics* **1977**, *67*, 4517–4533.

[9] Wildman, S. A.; Crippen, G. M. Prediction of Physicochemical Parameters by Atomic Contributions. *Journal of Chemical Information and Computer Sciences* **1999**, *39*, 868–873.

[10] Sauer, W. H. B.; Schwarz, M. K. Molecular Shape Diversity of Combinatorial Libraries: A Prerequisite for Broad Bioactivity. *Journal of Chemical Information and Computer Sciences* **2003**, *43*, 987–1003.

[11] Firth, N. C.; Brown, N.; Blagg, J. Plane of Best Fit: A Novel Method to Characterize the Three-Dimensionality of Molecules. *Journal of Chemical Information and Modeling* **2012**, *52*, 2516–2525.

[12] Robinson, D. D.; Barlow, T. W.; Richards, W. G. Reduced Dimensional Representations of Molecular Structure. *Journal of Chemical Information and Computer Sciences* **1997**, *37*, 939–942.

[13] Ertl, P.; Rohde, B.; Selzer, P. Fast Calculation of Molecular Polar Surface Area as a Sum of Fragment-Based Contributions and Its Application to the Prediction of Drug Transport Properties. *Journal of Medicinal Chemistry* **2000**, *43*, 3714–3717.

Appendix E

Appendix to Chapter 6

E.1 Additional details on the CG nanoparticle model

E.1.1 Golden section spiral algorithm

The golden section spiral algorithm used to distribute pseudo-atoms into a spherical shell is included within the mBuild Python package.[1,2] The algorithm itself was adapted from a thread on the numpy-discussion list.[3]

$\phi = \frac{1}{2}(1+\sqrt{5})$

$l_{\text{incr}} = 2\pi/\phi$

$d_z = 2/n$, where $n =$ the number of pseudo-atoms

bands $= 0, 1, ..., n-1, n$

$z = \text{bands} \cdot d_z - 1 + (d_z/2)$

$r = \sqrt{1-z^2}$

$a_z = \text{bands} \cdot l_{\text{incr}}$

$x = r \cdot \cos a_z$

$y = r \cdot \sin a_z$

x, y, and z are vectors containing values of each coordinate for each point in the model.

E.1.2 Maximum packing model, $\phi_{\text{b}}(d, \sigma_{\text{b}})$

Preliminary nanoparticle models featured a maximum packing algorithm, where ϕ_{b} was maximized without allowing overlap between neighboring beads. Fig. E.1 shows that ϕ_{b} for nanoparticles constructed in this manner is dependent both on the nanoparticle diameter, d, and the pseudo-atom diameter, σ_{b}. However, the inset of Fig. E.1 reveals that ϕ_{b} is equivalent for values of d/σ_{b}. As d/σ_{b} increases, ϕ_{b} increases, reaching an asymp-

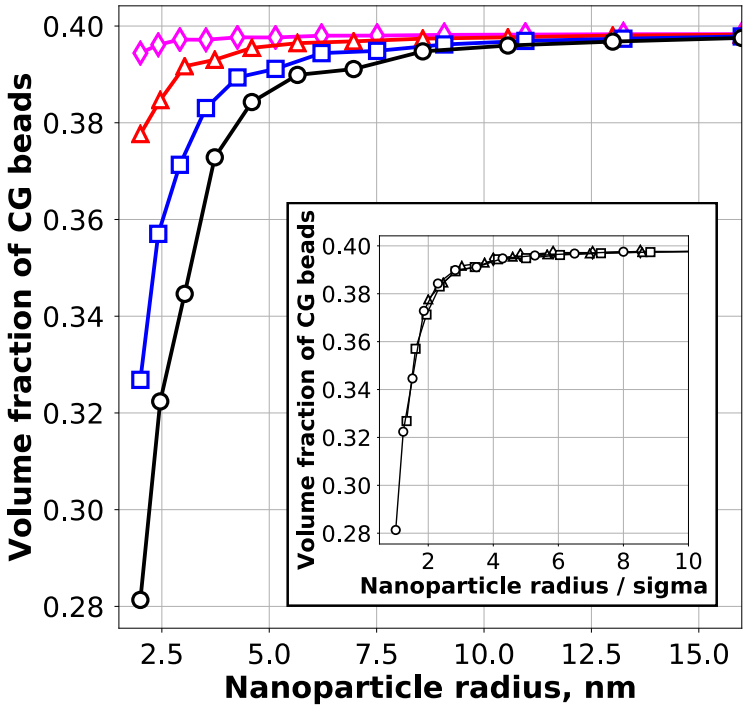

Figure E.1: Using a maximum packing model, volume fraction of coarse-grained beads within the spherical nanoparticle shell as a function of nanoparticle radius for σ_b values of 0.5 (magenta), 1.0 (red), 1.5 (blue), and 2.0nm (black). The inset shows the same data with the nanoparticle radius normalized by σ_b, where the four curves collapse onto a single line.

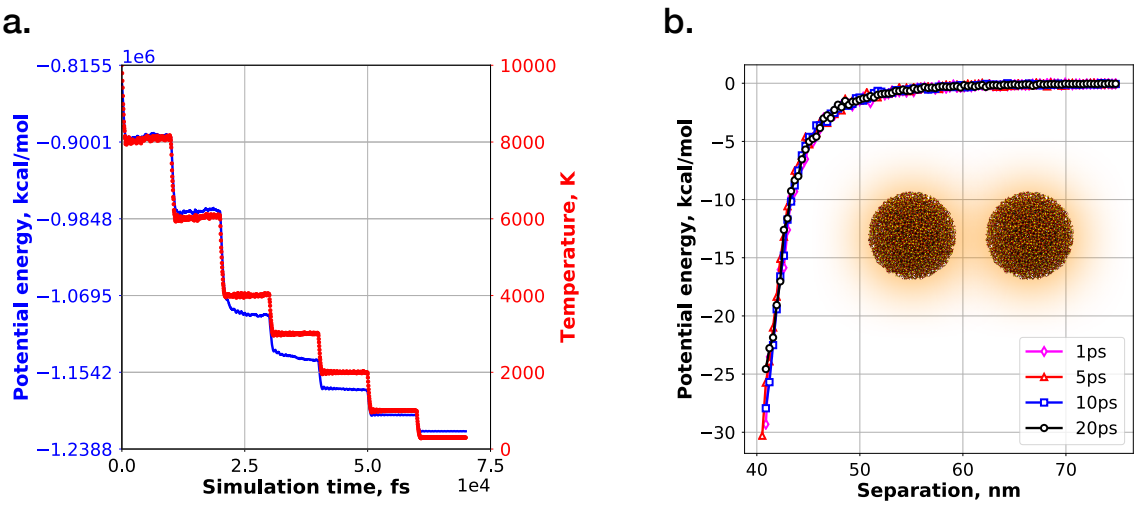

Figure E.2: a. Total potential energy (blue) and system temperature (red) during the stepwise annealing of the amorphous silica bulk with 10ps spent at each temperature stage. b. Interaction energy between two nanoparticles (d=4nm) carved from bulk silica annealed using times of 1, 5, 10, and 20ps spent at each temperature stage.

totic value of roughly 0.4. This phenomenon has profound effects on the transferability of interaction parameters derived for nanoparticles designed using the maximum packing model. Parameters are likely to be transferable between nanoparticles featuring equivalent (or nearly equivalent) values for ϕ_b. Thus, parameters would likely be transferable only for nanoparticles with d/σ_b values above about 5. Furthermore, if nanoparticles with lower values of d/σ_b are included during the optimization, the resulting parameter set will likely have reduced accuracy.

E.2 Additional details on the collection of atomistic target data

E.2.1 Bulk silica equilibration procedure

As described in the main text, the amorphous silica bulk from which atomistic nanoparticles were carved was generated through the procedure described by Litton and Garofalini, where a stoichiometric mixture of Si and O is heated to 10,000K and quenched to 300K through a series of intermediate temperatures, using the ReaxFF force field. The tempera-

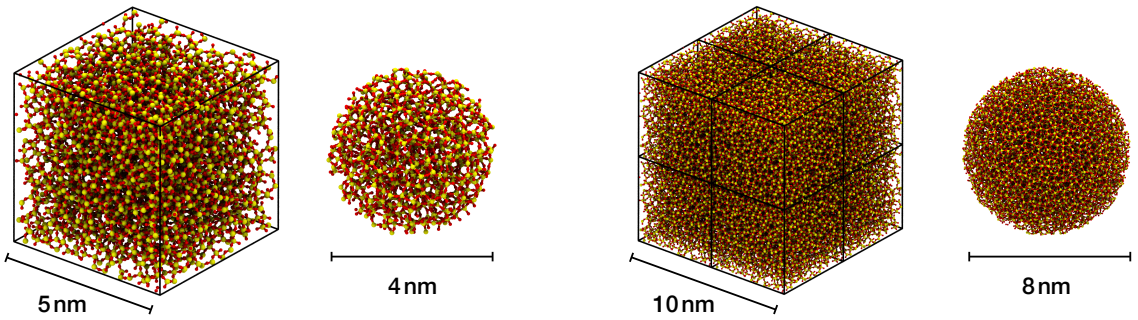

Figure E.3: Diagrams of the nanoparticles and the corresponding silica bulk used to carve them for nanoparticles with diameters of 4 and 8nm. For nanoparticles with a diameter larger than 5nm, the silica bulk is replicated.

ture profile of the system through the quenching procedure is shown in Fig. E.2a, alongside the potential energy of the system (which is shown to equilibrate quickly at each stage). At each stage the system is held at this temperature for 10ps before advancing to the next stage (directly following the procedure of Litton and Garofalini). We have examined the influence of the time spent at each stage by equilibrating the silica bulk where this time is set to 1, 5, 10, and 20ps and examining the interaction potential between two nanoparticles carved from each bulk. As shown in Fig. E.2b, the quench rate appears to have negligible influence on the interaction potential over the range studied here, providing further confidence that the chosen 10ps is appropriate.

E.2.2 Carving of nanoparticles from bulk silica

Nanoparticles are carved from the bulk silica as spheres of a user-defined radius (i.e. all atoms within *R*nm from the center of the box are included in the nanoparticle). As the dimensions of the silica box are 5nm x 5nm x 5nm, nanoparticles with radii larger than 2.5nm necessitate replication of the box for carving (Fig. E.3b).

Nanoparticles carved directly from bulk as perfect spheres certainly represent an idealized model, where in reality one would expect silica nanoparticles to feature some asphericity and a hydroxylized outer layer. The influence of an outer oxygen layer is examined by

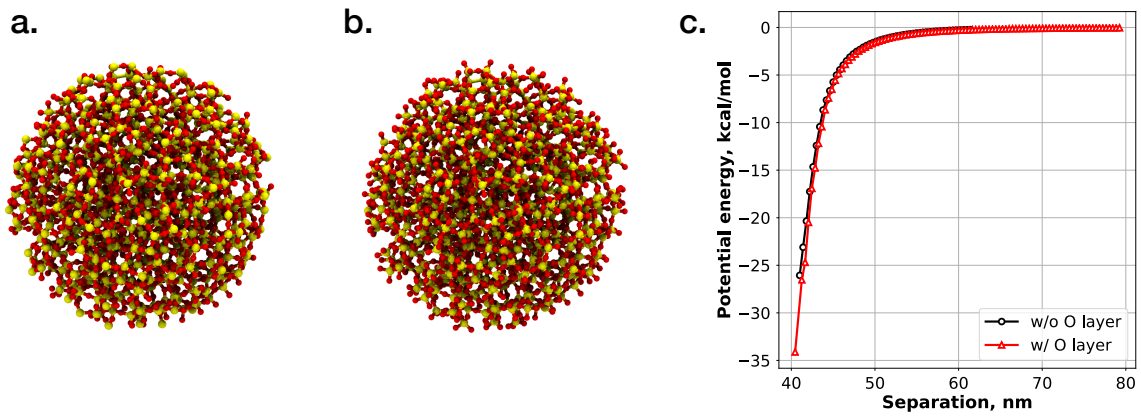

Figure E.4: Silica nanoparticles with a diameter of 4nm a. without and b. with a surface oxygen layer. c. The interaction energy between two nanoparticles without (black) and with (red) a surface oxygen layer.

calculating the interaction potential between two nanoparticles, comparing the model described in the main text (Fig. E.4a, where nanoparticles are carved ”as is” without an outer oxygen layer) with a model where an additional buffer of oxygen atoms (0.275nm) is included (Fig. E.4b). For the model that includes oxygen atoms, Si-O bonds were generated between all atoms within 0.20419nm and any atoms that are left un-bonded are removed from the system. The interaction potential calculated using these two models is shown in Fig. E.4c, where it should be noted that we have shifted the curve for the second model (w/ oxygen atoms) by a value of -0.55nm (twice the oxygen buffer) to account for the difference in radii. From Fig. E.4c we observe that the presence of an oxygen layer does not appreciably influence the nanoparticle-nanoparticle interaction potential. This helps provide further justification for the use of the simpler, idealized model we have utilized for the target data in the main text.

Concerning asphericity, in earlier trials of our nanoparticle optimizations we utilized target data obtained from nanoparticles that had been equilibrated for 50ps using the ReaxFF force field. For small nanoparticles (e.g. R=2nm) considerable asphericity was observed which resulted in difficulty obtained coarse-grained parameters that fit to the all-atom target data, as the coarse-grained nanoparticles are constructed as perfect spheres. Fig. E.5 shows

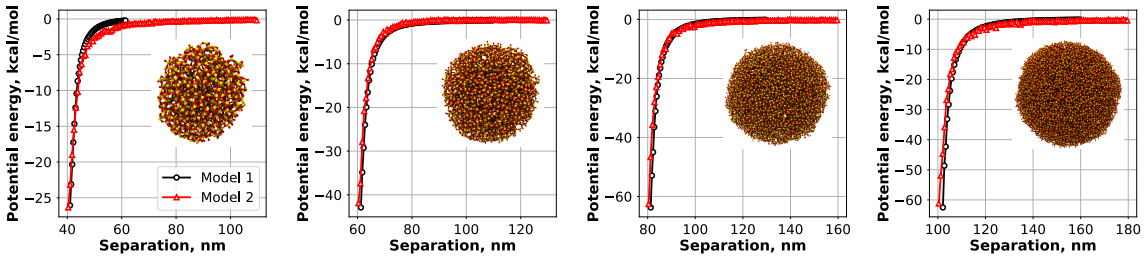

Figure E.5: The interaction energy between nanoparticles with diameters of 4, 6, 8, and 10nm using two different model. In black is the model used in the main text, where nanoparticles are carved directly from bulk silica. In red are nanoparticles that are equilibrated after carving.

the interaction potential between two nanoparticles, comparing results obtained using two nanoparticle models:

- **Model 1**: The model described in the main text, where nanoparticles are carved directly from bulk silica as (nearly) perfect spheres with no additional adjustments.
- **Model 2**: After carving from bulk silica, nanoparticles are equilibrated for 50ps under the ReaxFF force field. The interaction potential between two nanoparticles is calculated using DREIDING force field and includes a Coulomb term that uses charges from the ReaxFF charge equilibration.

It can be observed that for nanoparticles with radii of 3, 4, and 5nm the interaction potential is nearly identical between the two models. For the smallest nanoparticle size (R=2.5nm) deviation between the two models is observed, likely due to the asphericity of the nanoparticle in Model 2 (pictured as an inset). The agreement observed between these two models further supports the use of the idealized model (Model 1) for target data collection in the main text, and suggests that asphericity effects are negligible for radii ? 3nm.

E.2.3 Choice of atomistic force field

Nanoparticle-nanoparticle interaction potential *considering VDW interactions only* is examined using LJ parameters from three force fields: hybrid COMPASS, DREIDING,

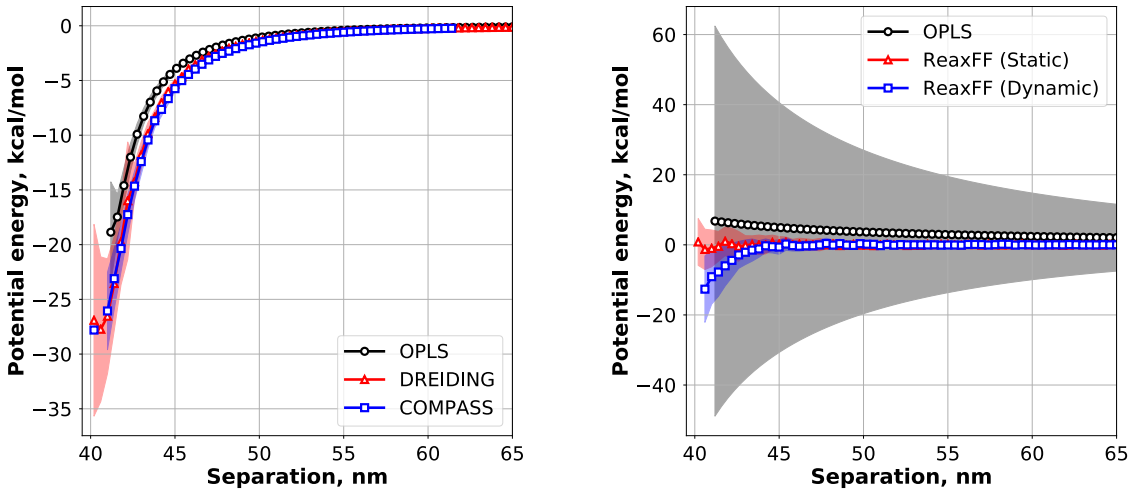

Figure E.6: a. The interaction energy *considering VDW interactions only* between two nanoparticles with d=4nm using the OPLS (black circles), DREIDING (red triangles), and COMPASS (blue squares) force fields. b. The interaction energy *considering electrostatic interactions only* using OPLS charges (black circles), charges obtained from ReaxFF charge equilibration (red triangles), and ReaxFF charges updated at each timestep (blue squares).

and OPLS. Details on the hybrid COMPASS LJ parameters are located in the main text.[4,5] Both the OPLS and DREIDING force fields describe VDW interactions through a 12-6 LJ potential, using Lorentz-Berthelot mixing rules for cross interactions. OPLS LJ parameters for silicon are $\sigma = 4.0$Å and $\varepsilon = 0.10\frac{\text{kcal}}{\text{mol}}$, and for oxygen are $\sigma = 3.0$Å and $\varepsilon = 0.17\frac{\text{kcal}}{\text{mol}}$.[6] DREIDING LJ parameters for silicon are $\sigma = 3.804$Å and $\varepsilon = 0.310\frac{\text{kcal}}{\text{mol}}$, and for oxygen are $\sigma = 3.033$Å and $\varepsilon = 0.096\frac{\text{kcal}}{\text{mol}}$.[7] The VDW contribution to the interaction potential is shown in Fig. E.6 for nanoparticles with a diameter of 4nm. Interaction potentials calculated using the DREIDING and COMPASS force fields are shown to be nearly identical, whereas the OPLS curve is shown to be slightly smoother. As both the DREIDING and COMPASS force fields have been utilized in the literature in studies of silica nanoparticles, it was determined that one of these should be chosen for our study. Interactions potentials were calculated slightly quicker using the COMPASS force field, so this is the one that was ultimately chosen.

Nanoparticle-nanoparticle interaction potential *considering electrostatic interactions*

only is examined using three sets of partial charges: OPLS, partial charges obtained through ReaxFF charge equilibration (QEq-static), and partial charges obtained through ReaxFF charge equilibration that are updated at each configuration (QEq-dynamic). OPLS charges for silicon and oxygen are 0.86 and -0.43 respectively.[6] Charge equilibration was performed in LAMMPS using the implementation by Aktulga et al..[8] The electrostatic contribution to the interaction potential is shown in Fig. E.6a for nanoparticles with a diameter of 4nm. The electrostatic contribution to the interaction potential using OPLS charges is shown to yield large error bars and deviates to slightly positive values at smaller separations. This is expected, as fixed charges without a charge equilibration are likely to yield a non-uniform charge distribution, and the lack of considering nanoparticle charge neutrality during carving is likely to provide each nanoparticle with a slight charge that will lead to repulsion. The electrostatic contribution to the interaction potential using dynamic charge equilibration is shown to be negligible at long range, and reveals attraction at short range. However, as mentioned in the main text, silica nanoparticles typically feature a polymer coating to prevent aggregation, so we are not concerned with the short range behavior, thus, the influence of charge appears to be negligible as has been found in previous work comparing the influence of various force fields on silica nanoparticle self-assembly.[9] This is further supported by examining the electrostatic contribution to the interaction potential using charges obtained through a single charge equilibration. Here, the influence of charge is shown to be negligible even at short range.

E.2.4 Procedure for collection of target data for nanoparticle-nanoparticle interaction energy

Target data used in force field optimization consists of values of interaction potential between two bodies calculated over a range of center-of-mass separations. For optimization of nanoparticle-nanoparticle parameters, the two bodies involved in target data collection are atomistic nanoparticles. Target data collection is not included within the NanoOpt

Python package, as we opted for scripting in C++ for this portion of the development for ease of parallelization and improved performance. A template of the script used in the collection of target data is provided in the NanoOpt repository.[10] The procedure used to collect target data can be broken down as:

1. Load in the atomic positions from an XYZ file
2. Define limits of center-of-mass separations to examine
    - **Min**: $20 \times R$
    - **Max**: $20 \times R + 40 + 10 \times (\text{ceil}(R/2) - 1)$
    - This does not represent the range of the final data, as pruning is performed to remove values at short separations (with the VDW volume), described in further detail below.
3. Initialize a histogram with 100 bins (higher resolution is therefore provided for smaller nanoparticles)
4. Choose a starting separation within the range of (Min, Max)
5. Evaluate the interaction energy and add the value to the appropriate bin in the histogram
    - Note: An overlap criterion is considered whereby if any two atoms are of a distance $\leq 0.8\sigma$ the two nanoparticles are considered to be overlapping and this configuration is skipped. This helps to avoid contributions from high-energy, overlapping configurations at small center-of-mass separations that systems would be unlikely to adopt.
6. Generate a new configuration by randomly rotating and randomly translating one of the nanoparticles

7. Continue to repeat steps 5 & 6 until an even sampling of all bins is achieved (excluding the first 5 bins, where our overlap criterion inhibits even sampling)

After target data is collected, the data is pruned to remove values at center-of-mass separations below $0.40323\text{nm} \times 0.8$, again as an overlap criterion, where 0.40323nm represents the diameter of silica. This removes data at center-of-mass separations where VDW radii would be overlapping, which hinders optimization of coarse-grained parameters.

It should also be noted that the number of configurations sampled per bin is not equal for all nanoparticle radii; however, standard deviations in interaction potential for all radii and center-of-mass separations are $< 10\%$ and are closer to $< 2\%$ for values other than at the shortest few center-of-mass separations. This supports the notion that a sufficient number of configurations were sampled per bin for all nanoparticle sizes. As follows are the mean number of configurations per bin, along with the standard deviation, for each of the radii examined in this work (3nm-10nm) is as follows:
3nm: 86.8 ± 9.2, 4nm: 69.5 ± 10.1, 5nm: 22.4 ± 4.2, 6nm: 66.1 ± 9.7, 7nm: 33.6 ± 5.2, 8nm: 19.1 ± 3.5,
9nm: 25.6 ± 4.2, 10nm: 13.9 ± 3.8

E.2.5 Procedure for collection of target data for nanoparticle-alkane cross-interactions

Target data was also collected for the interaction between spherical silica nanoparticles of various radii and united-atom alkane moieties (CH_2, CH_3). Data collection used the same procedure as for the target data collected for the potential between two nanoparticles, evaluating the interaction energy at a series of center-of-mass separations. Target data collection proceeding using the following general procedure:

1. Load the atomic positions of the nanoparticle from an XYZ file
2. Define a single point to represent united-atom CH2 or CH3 moiety
3. Define limits of center-of-mass separations to examine

- **Min**: $d/2$
- **Max**: $d/2+3$
- This does not represent the range of the final data, as pruning was performed to remove data with large error bars in the short-range region and additional data was collected to provide additional fidelity to the region of the potential well. See further explanation below.

4. Initialize a histogram with 50 bins
5. Choose a starting separation within the range of (Min, Max)
6. Evaluate the interaction energy and add the value to the appropriate bin in the histogram.
    - Note: An overlap criterion is considered whereby if any two atoms are of a distance $\leq 0.8\sigma$ the configuration is considered to be overlapping and this configuration is skipped. This helps to avoid contributions from high-energy, overlapping configurations at small center-of-mass separations that systems would be unlikely to adopt.
7. Generate a new configuration by randomly rotating and randomly translating the nanoparticle
8. Continue to repeat steps 5 & 6 until an even sampling of all bins is achieved (excluding the first 10 bins, which end up getting pruned off post-collection)

E.3 Equations used from the literature for CG model comparison

To compare the CG model developed in this work with available models in the literature, Fig. 6.11 in Chapter 6 provides plots showing interaction potential curves for several nanoparticle sizes calculated using the model developed in this work and using equations

provided in Fig. 6 of the work by Lee and Hua.[11] In their work, a general interaction potential was used for the interaction between two point nanoparticles of the form:

$$U(r) = 4\varepsilon \left[\left(\frac{\sigma}{r} \right)^{2\alpha} - \left(\frac{\sigma}{r} \right)^{\alpha} \right] \tag{E.1}$$

where σ is the nanoparticle diameter and ε and α are derived through fitting. The equations derived via fitting (along with reduced forms of ε and σ) for these last two parameters are:

$$\varepsilon_r = \frac{\varepsilon}{\varepsilon_0} \tag{E.2}$$

$$\sigma_r = \frac{\sigma}{\sigma_0} \tag{E.3}$$

$$\varepsilon_r = 286[1 - \exp(-0.014\sigma_r)] \tag{E.4}$$

$$\alpha = 0.226 + 2.983\sigma_r \tag{E.5}$$

where σ_0 and ε_0 correspond to 0.62nm and 3.10 kJ/mol, respectively. The values for σ_0 and ε_0 correspond to the parameters used in the interaction between pseudo-atoms of a coarse-grained nanoparticle model similar to that used in our work; however, in the work of Lee and Hua, pseudo-atoms were fixed to a given size (0.62nm in diameter) and interactions were governed by a 12-6 Lennard-Jones potential. The equations above for point particle interactions have been used in Chapter 6 (Figure 6.11) to compare nanoparticle-nanoparticle interaction potential curves with our model.

E.4 Bibliography

[1] Klein, C.; Sallai, J.; Jones, T. J.; Iacovella, C. R.; McCabe, C.; Cummings, P. T. A Hierarchical, Component Based Approach to Screening Properties of Soft Matter. *Molecular Modeling and Simulation* **2016**, 79–92.

[2] mBuild: a component-based molecule builder tool that relies on equivalence relations for component composition. http://mosdef-hub.github.io/mbuild/.

[3] Colbert, C. http://mail.scipy.org/pipermail/numpy-discussion/2009-July/043811.html.

[4] Sun, H. Ab initio calculations and force field development for computer simulation of polysilanes. *Macromolecules* **1995**, *28*, 701–712.

[5] Sun, H.; Rigby, D. Polysiloxanes: ab initio force field and structural, conformational and thermophysical properties. *Spectrochimica Acta Part A: Molecular and Biomolecular Spectroscopy* **1997**, *53*, 1301–1323.

[6] Lorenz, C.; Webb, E.; Stevens, M.; Chandross, M.; Grest, G. Frictional dynamics of perfluorinated self-assembled monolayers on amorphous SiO2. *Tribology Letters* **2005**, *19*, 93–98.

[7] Mayo, S. L.; Olafson, B. D.; Goddard, W. A. DREIDING: a generic force field for molecular simulations. *The Journal of Physical Chemistry* **1990**, *94*, 8897–8909.

[8] Aktulga, H.; Fogarty, J.; Pandit, S.; Grama, A. Parallel reactive molecular dynamics: Numerical methods and algorithmic techniques. *Parallel Computing* **2012**, *38*, 245–259.

[9] Ionescu, T. C.; Qi, F.; McCabe, C.; Striolo, A.; Kieffer, J.; Cummings, P. T. Evaluation of force fields for molecular simulation of polyhedral oligomeric silsesquioxanes. *Journal of Physical Chemistry B* **2006**, *110*, 2502–2510.

[10] NanoOpt: Deriving potentials for coarse-grained nanoparticles via potential matching:. http://github.com/mosdef-hub/nanoparticle_optimization.

[11] Lee, C. K.; Hua, C. C. Nanoparticle interaction potentials constructed by multiscale computation. *The Journal of Chemical Physics* **2010**, *132*, 224904.